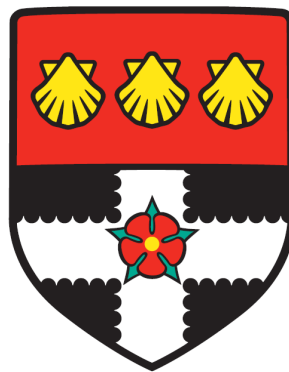


UNIVERSITY OF READING

Department of Meteorology



# **The Lifecycle of Storm Tracks**

Lenka Novak

A thesis submitted for the degree of Doctor of Philosophy

January 2016

# Declaration

I confirm that this is my own work and the use of all material from other sources has been properly and fully acknowledged.

Lenka Novak

# Abstract

Local periodic behaviour of storm tracks is found in the North Atlantic, the North Pacific, and in an aquaplanet global circulation model. Such periodicity is suggested to be a result of baroclinic instability that is characterised by nonlinear interactions between eddy fluxes and the mean-flow structure. This periodicity is associated with different processes at the beginning and end parts of the storm track.

The beginning part exhibits maxima in both storm track activity and its growth rate, both of which oscillate temporarily in intensity akin to a predator-prey relationship. A nonlinear oscillator model is proposed to describe this relationship quantitatively, yielding a good agreement with atmospheric observations. It is predicted and observed that on average stronger storm events occur less frequently but are triggered more rapidly. Examination of the associated energetics suggests additional importance of the mean overturning circulation and the transport of mean available potential energy from polar latitudes, neither of which were included in the present model.

Towards the end of the storm track, the dynamics are characterised more by variability in eddy momentum fluxes and transient jets, the latter often exhibiting periodic latitudinal fluctuations. It is suggested that the above effect of cycling baroclinicity and heat flux induces changes in eddy anisotropy which are responsible for the periodic jet deflections further downstream. On average, low heat flux is associated with an equatorward deflection of the jet, and vice versa. This jet-deflecting effect is characterised by a transfer of the system to a lower-frequency variability, and a mechanism to explain the observed preferred transitions of the North Atlantic jet is proposed.

The oscillations in the storm track activity, baroclinicity and eddy-driven jet are closely linked, and can be viewed as describing the spatio-temporal lifecycle of the storm track.

# Acknowledgements

First and foremost, I would like to thank my supervisors, Maarten Ambaum and Rémi Tailleux, for their invaluable guidance and their constant support and inspiration. I am also very grateful to my monitoring committee, Ted Shepherd and Jonathan Gregory, for their helpful comments and feedback during our meetings.

I am also thankful to Tim Woollings, Joaquim Pinto and Mike Blackburn for kindly taking the time to discuss aspects of my PhD work with me.

Many thanks also go to Deborah and Stephen for their reassurance and support whenever life got in the way. Finally, I would like to thank Tom for checking my thesis, (usually) avoiding mocking my mild obsession with thunderstorms, and devotedly keeping me supplied with coffee and white chocolate semolina pudding during the writing stage.

# Contents

<b>1</b>	<b>Introduction</b>	<b>1</b>
<b>2</b>	<b>Background</b>	<b>6</b>
2.1	Global Circulation . . . . .	6
2.2	Definition of Eddies . . . . .	8
2.3	Eddy Effect on the Mean Flow . . . . .	10
2.3.1	Direct Effect of Eddies . . . . .	10
2.3.2	Indirect Effect of Eddies . . . . .	16
2.3.3	Transformed Eulerian Mean . . . . .	18
2.4	Formation and Maintenance of Eddy-Driven Jets . . . . .	20
2.5	Eddy-driven Jet Variability . . . . .	24
2.6	Stationary Waves and Asymmetric Time-mean Flow . . . . .	30
2.7	Localised Storm Tracks and Jets on the Earth . . . . .	32
2.7.1	Spatial Setup of the Mid-latitude Jets . . . . .	32
2.7.2	Shifts in the Dominant Wave Breaking Type . . . . .	33
2.7.3	Observed Storm Track 3D Structure in the Steady State . . . . .	39
2.7.4	Temporal Variability of Storm Tracks and Jets . . . . .	40
2.8	Conclusion . . . . .	44
<b>3</b>	<b>Storm Track Activity and Its Nonlinear Oscillations</b>	<b>45</b>
3.1	Introduction . . . . .	45
3.2	Nonlinear Oscillator Model . . . . .	48
3.3	Properties of the Nonlinear Oscillator Model . . . . .	49
3.4	Datasets . . . . .	53
3.5	Construction of Phase Plots from Data . . . . .	55
3.6	The Nonlinear Oscillator in the North Atlantic Storm Track . . . . .	56
3.6.1	Composite Heat Flux Events . . . . .	57
3.6.2	Phase Space: Qualitative Comparison with the Model . . . . .	57
3.6.3	Phase Space: Quantitative Comparison with the Model . . . . .	61
3.7	Applicability of the Nonlinear Oscillator Model to other Measures and Storm Tracks	64
3.8	Summary and Discussion . . . . .	69
<b>4</b>	<b>Cyclical Variability of the North Atlantic Eddy-driven Jet</b>	<b>76</b>

4.1	Introduction . . . . .	76
4.2	Upstream Baroclinic Effect . . . . .	79
4.3	Downstream Barotropic Effect . . . . .	83
4.4	Sensitivity to the Choice of Frequency Bands to Define High-frequency Eddies . . . . .	94
4.5	Discussion and Conclusions . . . . .	95
<b>5</b>	<b>Energetics of the Storm Track Lifecycle</b>	<b>100</b>
5.1	Introduction . . . . .	100
5.2	Lorenz Energetics in Data . . . . .	108
5.3	Local Energy Terms: Method . . . . .	112
5.3.1	Definition . . . . .	112
5.3.2	Separation of APE Density into Eddy and Mean Components . . . . .	113
5.3.3	Local Evolution Equations . . . . .	114
5.4	Time-mean Spatial Distribution . . . . .	117
5.4.1	Globally Integrated Energetics . . . . .	118
5.4.2	Zonal-Mean View of the Energetics . . . . .	119
5.4.3	Three-dimensional Energetics . . . . .	125
5.4.4	Residual Diabatic and Frictional Terms . . . . .	128
5.5	Temporal Variability during the Storm Track Lifecycle . . . . .	132
5.5.1	The Nonlinear Oscillator of the Energetics: Theory . . . . .	133
5.5.2	PUMA Experiment: Zonal-mean Framework . . . . .	138
5.5.3	The North Atlantic: Transient Framework . . . . .	144
5.6	Summary and Conclusion . . . . .	158
<b>6</b>	<b>Conclusions</b>	<b>163</b>
6.1	Observed Periodic Behaviour of Storm Tracks . . . . .	163
6.2	Modelling the Predator-prey Relationship between Storm Track Activity and Its Growth Rate . . . . .	165
6.3	The Effect of the Periodic Variability of Storm Tracks on the Latitudinal Deflection of the Eddy-driven Jet . . . . .	167
6.4	Interaction of Storm Tracks with Other Global Regions . . . . .	169
6.5	Future Work . . . . .	170
	<b>Appendices</b>	<b>175</b>
A	Setup of the PUMA Experiment . . . . .	176
B	An Example Attempt to Justify the Nonlinear Oscillator Model Using Normal Mode Analysis . . . . .	180
C	Truncation of Thompson's (1987) Model . . . . .	182

D	The Connection to the Lorenz-84 Model . . . . .	185
E	Sensitivity of Oscillatory Properties to Kernel Phase-space Averaging . . . . .	186
F	Derivation of Lorenz Evolution Equations . . . . .	192
G	Methods for Calculating Reference Potential Temperature for the Local Framework	198
H	Local Energetics Evolution Equations in Spherical Coordinates . . . . .	202
I	Deriving the Energetics Nonlinear Oscillator Model Using the “Constant Vertical Tilt” Method . . . . .	204
J	Application of the Nonlinear Oscillator Model in the Oceans . . . . .	209
<b>References</b>		<b>214</b>

## Chapter 1

# Introduction

The term “storm tracks” or “storm zones” is commonly used for the regions of enhanced storminess, as well as the paths of individual storms. Storm tracks therefore provide a statistical measure of the overall properties of individual storms and their behaviour. Storms in this context are extratropical synoptic weather systems with horizontal scales of around 1000 km. These storms are baroclinic systems since they are generated when the mean flow becomes baroclinically unstable. Such a situation arises when surfaces of constant temperature (isotherms) become inclined relative to surfaces of constant pressure (isobars). The name “baroclinicity” is therefore given to the measure of this instability. Physically, baroclinicity is related to the amount of potential energy available for the generation of baroclinic systems. In the Northern Hemisphere the most baroclinic regions are situated in the mid-latitudes on the western sides of the oceans, as shown in figure 1.1. Collocated, though slightly more downstream, are the North Atlantic and North Pacific storm tracks which feed on the baroclinicity (figure 1.1). Associated with these storm tracks and areas of enhanced baroclinicity are maxima in the upper-level wind, known as the jet streams (figure 1.2a).

Downstream of the storm tracks in the Northern Hemisphere lie highly populated areas of western Europe and the west coast of North America. Most storms that impact these regions have their origins in the storm tracks (Hoskins and Hodges, 2002). Understanding the variability of the storm tracks is therefore crucial for weather forecasting, and for improving the assessment of probability of extreme events with a high risk of damage in these regions.

Furthermore, storm tracks cumulatively modify the kinetic energy of the large-scale flow and are thus involved in transitions between different low-frequency weather regimes that can persist for longer than the lifetime of an individual storm (Lau, 1988; Benedict *et al.*, 2004). Lower-frequency weather variability can also be induced as a result of storm tracks being a means of communicating flow anomalies between different global regions. For example, it has been pre-

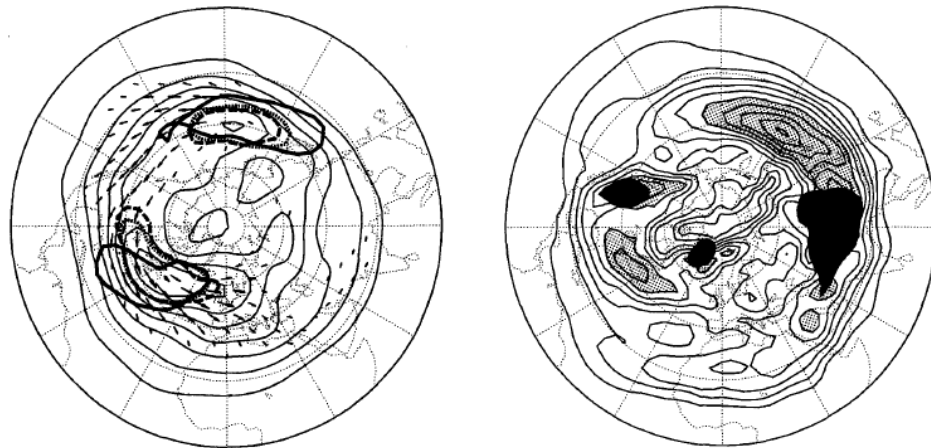


**Figure 1.1:** Time-mean (December-February of years 1979-84) view of the Northern Hemisphere of a) measures of storm track activity (left), including meridional heat flux at 700 hPa (thick dashed contour at  $10 \text{ K m s}^{-1}$ ), vertical heat flux at 700 hPa (thick dotted contour at  $0.2 \text{ K Pa s}^{-1}$ ), 250 hPa geopotential height variance (thin solid contour with an interval of  $15 \text{ m}^2$ ) and the mean diabatic heating (thick solid contour at  $50 \text{ W m}^2$ ); and b) baroclinicity at 780 hPa (measured by the max. Eady growth rate, with contour interval of  $0.1 \text{ day}^{-1}$  and stippling indicating values larger than  $0.6 \text{ day}^{-1}$ ). From Hoskins and Valdes (1990).

dicted that this year's enhanced El Niño will likely lead to a longer late winter in north-western Europe (Met Office News Blog, 2015). This is expected to occur via an alteration of the properties of the North Atlantic storm track (e.g. Li and Lau, 2012). Understanding storm tracks is therefore also central for enhancing the skill of medium-long range weather forecasting and prediction.

Similarly, storm tracks are a key player in the global circulation, because they transport heat, moisture and other chemical tracers. The long-term change of storm track properties can therefore have a key role in regional and global climate change, as well as the global chemistry composition distribution. For example, though this issue is still widely debated, some recent modelling studies (e.g. Meehl *et al.*, 2005; Yin, 2005; Mbengue and Schneider, 2013) suggest that storm tracks should move polewards in the future, which would be likely to shift the precipitation downstream of them polewards and make some regions wetter and some drier. Storm tracks are therefore central to the study of both climate change and weather variability, on a wide range of spatial and temporal scales.

Recent research into storm tracks has focused on their spatial variability and the dominant controls over their existence (e.g. Brayshaw *et al.*, 2009), or their long-term variability in the context of global warming (e.g. Mbengue and Schneider, 2013; Woollings *et al.*, 2012). However, the sub-seasonal temporal variability of storm tracks and the corresponding dominant processes are not

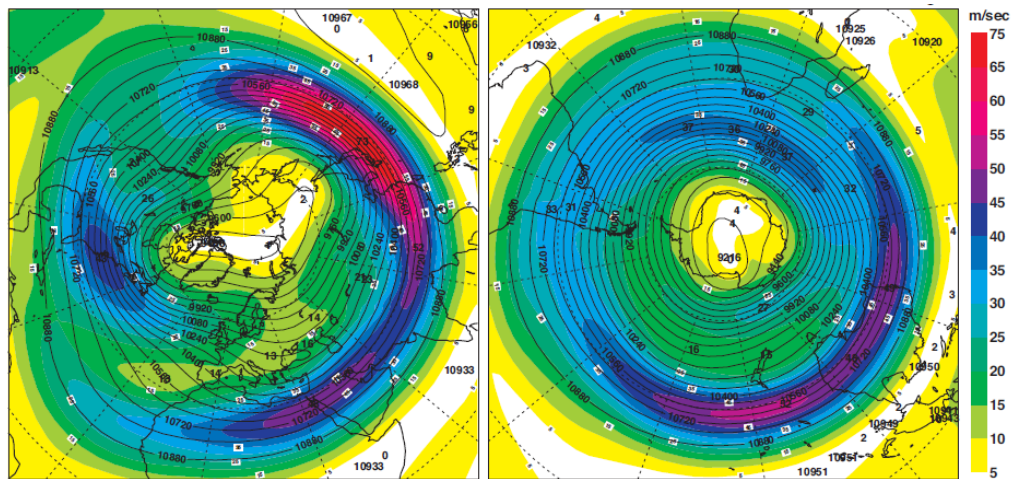


**Figure 1.2:** The upper-level (250 hPa) jet structure (zonal wind in colours) and geopotential height (contours) in the winter Northern Hemisphere (a) and the equivalent fields in the winter Southern Hemisphere (b). From the ERA-40 Atlas (Kållberg *et al.*, 2005).

widely studied, despite their importance for weather prediction as outlined above. One reason for this may be that the sub-seasonal variability is a “no-man’s land” between seasonal prediction and short-term numerical weather prediction. Another reason may be the complexity of the behaviour of the observed storm tracks at these scales, which is a result of a large number of external and internal forcings that affect them. Consequently, the higher-frequency behaviour of storm tracks is often regarded as chaotic (Osprey and Ambaum, 2011).

Nevertheless, theoretical and recent observational studies (Pedlosky, 1970; Thompson, 1987; Ambaum and Novak, 2014; Thompson and Woodworth, 2014) indicate that some periodicity may exist in both storm track activity and its effect on the mean flow. This periodicity is likely an internal property of the storm tracks that is related to competition between baroclinicity dissipation by eddies and baroclinicity generation by stationary forcings. Understanding of this internal periodic variability within the storm track system can help further the development of medium-range weather forecasting models.

In the light of the above discussion, this thesis aims to answer the following questions:

- Can a coherent periodic behaviour of storm tracks be observed in the Northern Hemisphere?
- What is the mechanism responsible for the periodic behaviour?
- Can the periodic behaviour be deduced from the governing equations of motion?

- Is this behaviour reproducible in medium-complexity models?
- Can storm tracks autonomously induce periodic shifts in the latitude of the eddy-driven jet?
- Is this periodic behaviour only a local phenomenon, or is it part of a hemispheric-scale annular mode variability?

The theoretical arguments in this study are supported by observational investigation of the ERA-40 and ERA-Interim reanalysis produced by the European Centre for Medium-range Weather Forecasts (Uppala *et al.*, 2005). Although the former dataset has a lower resolution and is based on an older-generation data assimilation technique than the latter dataset, it contains a longer time series and was therefore used in cases where a higher statistical confidence was of higher priority than resolution.

It should also be noted that although the Southern Hemisphere also exhibits an equivalent system of a storm track and an associated jet structure, its storm track is more zonally symmetric (along the latitude circle) due to a decreased interruption of the zonal flow by continents, as shown in figure 1.2b. When investigating the interaction between the mean flow and storms, it is often preferable to investigate the Southern Hemisphere where the use of simplifying methods, such as zonal averaging, can be more easily justified. However, this study aims to investigate the temporal, as well as spatial, variability of storm tracks. Since the beginning and end parts of the storm track in the Southern Hemisphere are less clearly definable, the variability of interest would be more obscured. The focus of the observational analysis here will therefore be on the Northern Hemisphere.

Additionally, in order to test that the observed behaviour is not case-specific to the Northern Hemisphere, a simplified dry-dynamical core global circulation model, PUMA, was used to create a single storm track by imposing a heating dipole in an aquaplanet mid-latitude atmosphere. The precise details of the model setup are shown in Appendix A.

All of the dynamics analysis used in this thesis is based on a dry framework. Although moisture is an important factor that enhances storm track activity (Hoskins and Valdes, 1990), amplifies the eddy feedback on the mean flow (Tamarin and Kaspi, in press), and strengthens the upper-level Hadley cell (Kim and Lee, 2001), the current study is not concerned with the mediation of the

flow due to these processes. Instead, the large-scale dynamics is studied here, for which the dry framework is sufficient. Nevertheless, it should be noted that the reanalysis datasets implicitly contain the dynamical effects of moisture because they are based on real observations.

This thesis is structured as follows. Chapter 2 briefly reviews the relevant theory and literature. Chapter 3 focuses on the variability of the storm track activity and proposes that a predator-prey type oscillatory relationship exists between baroclinicity and storm track activity. This relationship is linked to existing theoretical models of the eddy-mean flow interaction, and a two-dimensional nonlinear oscillator model is developed to describe these oscillations explicitly. An additional application of the steady state of this nonlinear oscillator model is also presented in the oceanic setting. Chapter 4 links the oscillatory behaviour of the storm track activity to downstream oscillations in the latitude of the jet, with a particular focus on the North Atlantic eddy-driven jet. Chapter 5 uses a local energetics framework to investigate the existence of the periodic storm track behaviour, in both the energy evolution equations and in the atmospheric observations. Chapter 6 summarises the findings and concludes that the observed periodic behaviour of the storm track and the associated eddy-driven jet is a general feature of all localised storm tracks.

## Chapter 2

# Background

The key concepts and literature for the following chapters are reviewed here. The Earth's global circulation is first described to emphasize the need for turbulent motion to help maintain it. This turbulent motion is then defined in terms of eddies. Subsequently, the direct effect of these eddies on the mean circulation is discussed in terms of the momentum and heat eddy fluxes expected from the eddy geometry, and in terms of the eddy fluxes expected from the baroclinic instability theory. The indirect effect of eddy activity, associated with an overturning meridional circulation and the need to maintain the thermal wind balance, is also considered. The chapter then proceeds by outlining the research on the ability of a collection of eddies to form, maintain and (quasi-)periodically modify zonal structures, such as jets, in a rotating fluid. Next, the localisation of eddy activity into storm tracks by stationary forcings is discussed. Finally, the literature on the observed characteristics of the spatial and temporal variability of storm tracks and their eddy-driven jets on the Earth is reviewed.

## 2.1 Global Circulation

Since the Sun is the ultimate source of energy on the Earth, its radiation forms the basis of the global motions in the atmosphere and the oceans. In particular, the enhanced heating at low latitudes and cooling at high latitudes induce meridional temperature gradients that cause the atmosphere to become (baroclinically) unstable and form a global circulation which equilibrates this instability. This global circulation is particularly strong in the winter season when the temperature gradients are the greatest. The winter circulation is the focus of this thesis and the discussion of this chapter will therefore be oriented towards it.

In the atmosphere of the Earth (and indeed other planets with a fluid atmosphere) the radiative

effects thermodynamically drive a meridional overturning circulation characterised by a large-scale ascent near the Equator and a large-scale descent in the polar regions. By mass conservation, one would expect poleward movement in the upper levels and equatorward movement in the lower levels to complete the circulation. However, the picture is complicated in the presence of planetary rotation.

Conservation of angular momentum implies that a parcel of fluid rotating at a low latitude will possess a higher zonal angular momentum than a parcel that is travelling at a higher latitude. Having risen in the tropics, poleward movement of parcels in the upper levels to higher latitudes therefore induces a Coriolis force which leads to the formation of upper-level zonal winds. These winds peak in the subtropics, forming the subtropical jet. By the conservation of mass, this jet must mark the edge of a thermally direct cell that rises in the tropics and subsides in the subtropics, called the Hadley cell. This axisymmetric tropical circulation is shown in figure 2.1a. The Hadley cell is stronger in the winter hemisphere and the associated subtropical jets can be seen in figure 2.1b, with their maxima close to 200 hPa. The meridional extent of a realistic Hadley cell can be relatively well estimated using the model of Held and Hou (1980) which is based on the angular momentum conservation and the thermal wind balance. A weak thermally direct circulation also occurs over the polar regions, called the polar cell (also apparent in figure 2.1a).

In the mid-latitudes however, the momentum conservation arguments are insufficient as the atmospheric motions are additionally affected by strong eddy heat and momentum fluxes that result from the strong baroclinic instability there. In the standard (Eulerian) zonal averaging displayed in figure 2.1, this forms a thermally indirect cell between the Hadley and polar cells, which acts as a sink of the mean kinetic energy supplied by the direct circulation. This mid-latitude circulation cell is referred to as the Ferrel cell. However, it should be noted that the Ferrel cell is a result of the Eulerian averaging. Parcel-following (Lagrangian) averaging methods yield a single thermally direct circulation in each hemisphere, reflecting the overall northward transport of air parcels (and other tracers) by the mid-latitude turbulent motions (e.g. Townsend and Johnson, 1985). The dynamics of these turbulent motions will be discussed in more detail in the next section.

For the sake of completeness, figure 2.1b also shows a westerly polar night jet (forming a polar vortex) in the winter stratosphere, whereas easterly flow appears in the summer hemisphere,

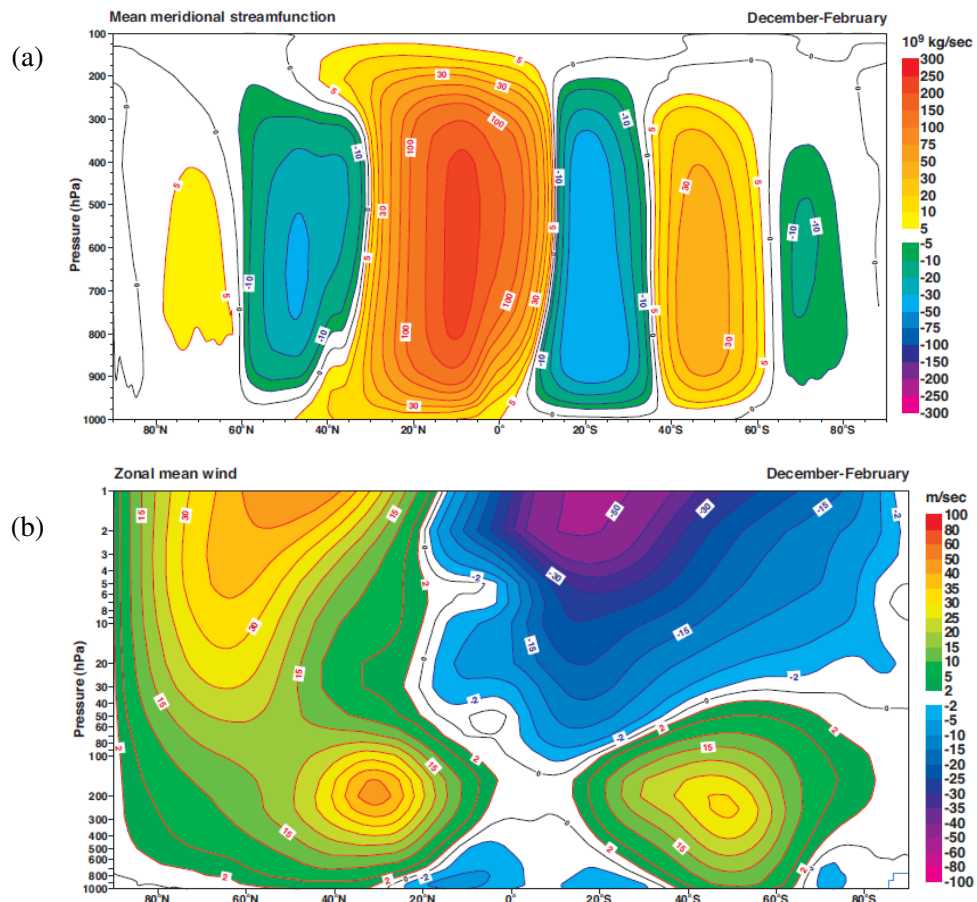


**Figure 2.1:** Zonal-mean meridional streamfunction (a) and zonal-mean wind (b) of the Northern Hemisphere winter from the ERA-40 Reanalysis Atlas (Kållberg *et al.*, 2005).

reflecting the stratospheric meridional temperature distribution.

## 2.2 Definition of Eddies

The turbulent motions that dominate the mid-latitude atmosphere are eddies which are defined here as perturbations from a mean of interest. This study mainly focuses on perturbations from the zonal mean (along the latitude circle) and the temporal mean. Although a synoptic storm would be captured in perturbations from both of these averages, it is noted that there are important differences between the two frameworks. For example, a steady-state meandering flow would yield eddies when using the zonal mean but none in the time mean. Throughout this thesis this difference will be highlighted.

The mean activity of eddies is measured by variances of meteorological variables, including geopotential height variance and a half of the sum of the horizontal velocity variances (corresponding to the eddy kinetic energy, EKE). Covariances with velocity components are also indicative of eddy activity and are referred to as eddy fluxes. Common examples include the meridional heat flux ( $\overline{v'T'}$ ) or the meridional zonal momentum flux ( $\overline{u'v'}$ ). When considering such mean eddy activity, the zonal and temporal averages are often combined to yield the following separation (James, 1994):

$$\overline{uv} = [\overline{u} \overline{v}] + [\overline{u^*} \overline{v^*}] + [\overline{u'v'}], \quad (2.1)$$

where the momentum flux was chosen as an example, the bars and primes represent time mean and perturbations thereof, and the square brackets and stars represent the zonal mean and its perturbations respectively. The first term represents the mean flow transport, the second term represents the time-mean stationary eddies and the last term represents mainly the transient eddies. Synoptic transient eddies define the baroclinic storms that form storm tracks. These synoptic transients are often represented using a 10-day Lanczos filter to separate them from the lower-frequency variability, the latter often being associated with different dynamics and spatial flow structures (e.g. Hoskins *et al.*, 1983; Blackmon *et al.*, 1984; Lorenz and Hartmann, 2001).

However, the mid-level streamfunction does not possess a pronounced spectral peak at 10 days due to synoptic-scale eddies, which are gradually replaced by planetary-scale waves at lower frequencies (Blackmon, 1976). The precise partition into the eddy and mean parts is therefore somewhat artificial, and it can be designed to yield the correct mean state for the particular context of interest. For example, the zonal mean-based partition is justified for a (nearly) zonally symmetric flow, such as that of the Southern Hemisphere. However, this partition is not ideal for the study of local variabilities of the zonally asymmetric North Atlantic and North Pacific storm tracks, as the two storm tracks would interfere with each other in the zonal mean. In addition, this framework includes the transient as well as stationary eddies and is not therefore solely representative of synoptic storms. Nevertheless, the zonal mean-based partition is the basis for many theoretical arguments as it allows cancellation of zonal differentials when periodic boundaries are applied. The time mean-based partition provides a three-dimensional view, but in order to represent the variability of transient eddies, a running mean or a weighted average (such as the Lanczos filter) with a 10 day cut-off is often used. These averaging techniques are not strictly commutative and would introduce additional complexity in the zonal-mean based theoretical arguments.

This thesis uses both types of averaging in conjunction. The zonal mean is used in most theoretical arguments and in the runs of a simplified aquaplanet general circulation model (GCM) with a single storm track, and the 10-day Lanczos filter is used for analysing Northern Hemispheric storm tracks. In the context of the spatio-temporal variability of storm tracks, it will be shown that both averaging methods yield comparable results.

The above averaging methods can therefore isolate the synoptic-scale baroclinic systems relatively well. These systems are observed to be meridionally stretched structures often tilted horizontally and vertically (Hoskins *et al.*, 1983; Blackmon *et al.*, 1984). They also tend to organise themselves into a series of alternately cyclonic and anticyclonic eddies, called a wavetrain, which gives them a wave-like structure. Thus linear wave theory can often be used to describe some of their properties and their effect on the mean flow, as discussed in the following sections.

## 2.3 Eddy Effect on the Mean Flow

This section outlines the direct effect of eddies on the baroclinic and barotropic structure of the mean flow, deduced from their geometry as well as from the wave theory. An indirect effect of the eddies, whereby the mean flow is adjusted by an ageostrophic circulation in order to maintain the thermal wind balance, is also discussed.

### 2.3.1 Direct Effect of Eddies

#### 2.3.1.1 Steady-state Perturbations: Baroclinic Eddy Shape

Following Hoskins *et al.* (1983), several properties of the effect of eddies on the mean flow can be deduced solely from the geometrical structure of the eddies. Consider a large-scale quasi-geostrophic flow (where pressure gradients almost balance the Coriolis force), where the zonal and meridional eddy velocities ( $u', v'$ ) can be expressed in terms of one or a sum of more complex Fourier modes. In such a case, the ratio of the variances of the two velocities can be written as the inverse ratio of their respective square wave numbers ( $k, l$ ) as follows:

$$\frac{\overline{v'^2}}{\overline{u'^2}} = \frac{k^2}{l^2}. \quad (2.2)$$

Hence, if the meridional velocity variance is greater than its zonal equivalent, then the associated eddy would be meridionally elongated. In terms of the momentum fluxes, the importance of this elongation becomes important when the eddies are tilted. Consider a simple example of a closed circulating eddy, as shown in figure 2.2a. From this figure it is evident that such tilting is associated with a positive meridional flow along the longer eddy axis when the easterly momentum is positive, and vice versa. This eddy therefore transports westerly momentum northwards and easterly momentum southwards, and so  $\overline{u'v'} > 0$ . Similarly, the momentum flux is negative when the tilt is opposite. The mathematical formulation of this geometrical argument can be found in James (1994). This argument of tilted eddy structures inducing horizontal momentum fluxes can be additionally supported by the wave theory as is shown in the next section. Eddies aligned around a jet as in figure 2.2b, will therefore tend to reinforce the jet barotropically (throughout the depth of the domain), as shown in figure 2.2c.

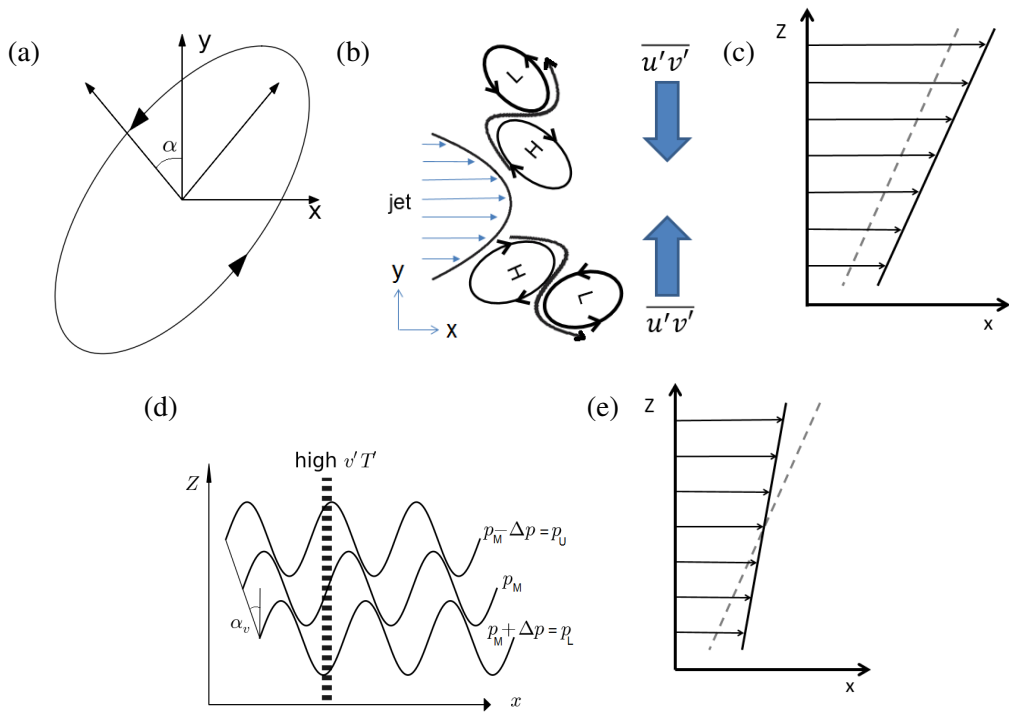


**Figure 2.2:** Barotropic eddy tilting in the horizontal (a), a typical arrangement of such tilted eddies around an accelerating jet (b), and the associated vertical zonal wind profile of the jet (c). Baroclinic eddy tilting in the vertical and the associated pressure surfaces (d), and the associated vertical profile of the zonal wind (e). The dashed and solid lines in (c) and (e) represent the wind profile before and after the eddy interaction, respectively. Panels a) and d) are reproduced from James (1994), and  $\alpha$  and  $\alpha_v$  relate to the horizontal and vertical phase angles respectively.

The properties of the mean flow can also be affected by the vertical structure of eddies. Following James (1994) and using the thermal wind balance on pressure coordinates, a geostrophically

and hydrostatically balanced meridional eddy velocity can be shown to be proportional to the horizontal gradient of the geopotential height anomaly,  $Z'$ , as follows:

$$v' = \frac{g}{f_0} \frac{\partial Z'}{\partial x}, \quad (2.3)$$

where  $g$  is the gravitational acceleration and  $f_0$  is the Coriolis parameter. In a simplified system of figure 2.2d, where geopotential height perturbations on pressure surfaces can be represented by sinusoidal functions in the zonal coordinate ( $x$ ), the eddy temperature in the middle layer can be written in terms of the geopotential height thickness ( $Z'_U - Z'_L$ ) as:

$$T'_M = \frac{g p_M}{R} \frac{Z'_U - Z'_L}{2 \Delta p}, \quad (2.4)$$

where the  $U$ ,  $M$  and  $L$  subscripts refer to the upper, middle and lower layers, respectively.  $R$  is the specific gas constant for dry air and  $p$  is pressure. It is readily apparent from the figure that, for such tilting, the eddy temperature is at its maximum where there is a maximum poleward velocity and minimum where there is an equatorward velocity. The heat flux is therefore positive. In the case of the opposite tilt, the heat flux is negative. These arguments imply that a zero eddy tilt is associated with a zero meridional eddy heat flux. This agrees with linear wave theory that topographically induced barotropic stationary waves (with no tilt) do not transport heat polewards (Derome and Wiin-Nielsen, 1971). These arguments are additionally supported by the linear theory of upward-tilted baroclinic waves in a westerly flow, as is shown below. The westward-upward vertical tilting therefore induces poleward temperature fluxes that reduce the meridional temperature gradient, which must be associated with reducing the vertical zonal wind shear (through the thermal wind balance), as shown in figure 2.2e.

It is therefore apparent that the vertical and horizontal tilting and stretching of baroclinic eddies, as depicted in figures 2.2c and d, is associated with zonal momentum extraction from upper levels outside of the jet to the lower levels under the jet core, which would in general reduce the vertical shear of the jet, thus making it more barotropic. The next section uses the baroclinic instability wave theory to describe how such tilts of baroclinic eddies occur, and how they evolve as eddies grow, mature and decay.

### 2.3.1.2 Baroclinic Eddy Evolution: Baroclinic Instability

Baroclinic instability, or the development of baroclinic eddies, occurs in flows that are dominated by strong temperature gradients and rotation. Theories of such baroclinic eddy development exist, many of which are based on simplification of the governing equations. For example, one of the simplest analytical models of baroclinic instability is that of Eady (1949), based on the quasi-geostrophic (QG) equations linearised around a zonal mean. Using a system of two rigid vertical boundaries with a constant background vertical zonal wind shear and a constant planetary vorticity, Eady simulated the initial stages of the development of baroclinic eddies. In his model, these eddies are represented by two coupled edge waves, one on each vertical boundary. The analytical solution of Eady's model yields a spatial structure of perturbations that tilt in the westward-upward direction. Examples of the related meridional temperature and meridional velocity profiles of the most unstable wavenumber are shown in figure 2.3 (left). It is apparent that such tilting will induce a positive heat flux, concurring with the geometric arguments above.

The Eady model predicts an exponential growth of the eddies in time, with the inverse timescale (or growth rate) varying with the meridional and zonal wavenumbers ( $l$  and  $k$ ) as displayed in figure 2.4. Beyond the dashed line, the growth rate vanishes and the waves are neutrally stable. There is therefore a short-wave cut-off, whereby sufficiently small waves at the vertical boundaries no longer interact with each other, and an example of such a neutral wave is shown in figure 2.3 (right). The growth rate of the most unstable (dominant) mode is given by:

$$\sigma = 0.31 \frac{f}{N} \frac{dU}{dZ}, \quad (2.5)$$

which is referred to as the “maximum Eady growth rate”. The growth rate of disturbances is therefore proportional to the ratio of the vertical shear (or meridional temperature gradients, by thermal wind balance) and the static stability (proportional to the vertical temperature gradients), and is thus related to the tilting of the isentropes and the amount of the potential energy of the mean flow that is available for conversion into eddy energy. It is therefore commonly used as a measure of baroclinicity.

A limitation of the Eady model is that it predicts that the disturbances would intensify to infinity, due to the constant vertical wind shear. This is not realistic, but the model still gives a good

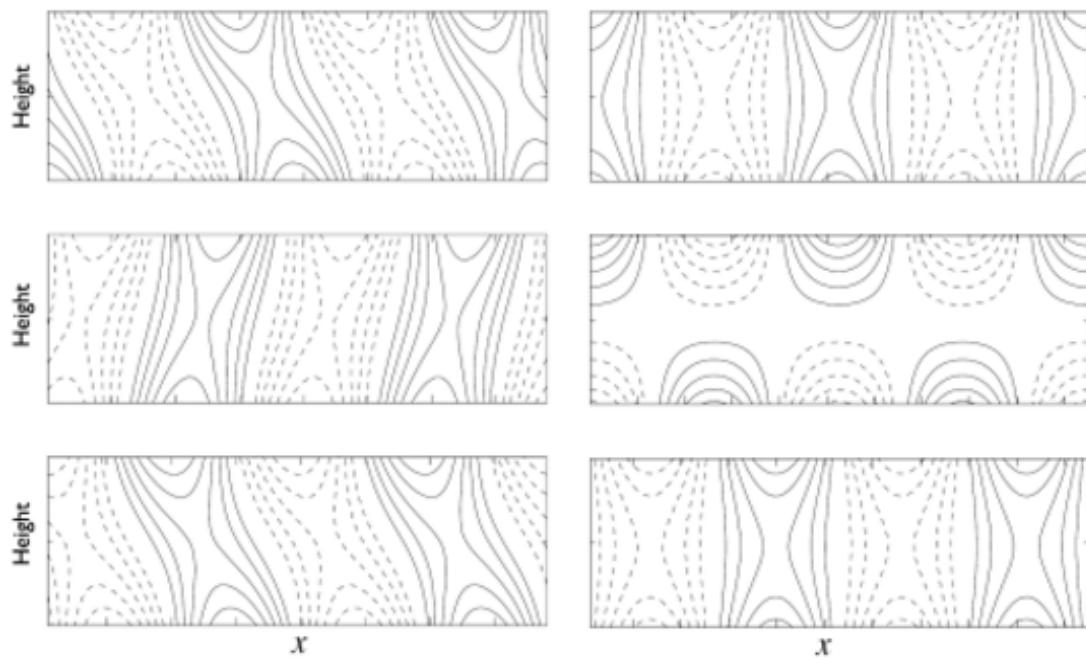


**Figure 2.3:** Solutions of the Eady model for the most unstable mode (left), and a decaying mode just beyond the short wave cut off (right). The variables displayed are the perturbations of streamfunction (top), temperature (middle) and meridional velocity with poleward being positive (bottom). Dashed contours represent negative values. From Vallis (2006), p. 260.

approximation of the initial growth. For example, using suitable mid-latitude parameters for  $f$  and  $N$  yields the wavelength of 4000 km and growth rate of  $0.5 \text{ day}^{-1}$ , which are comparable to the observed values (James, 1994).

Alternatively, Charney's (1947) linear model includes less drastic simplifications compared to Eady's (1949) model. For example, it includes a variable planetary vorticity with latitude which allows instability between the fluid interior and one (lower) vertical boundary, somewhat more similar to the observed atmosphere. The vertical scales are set by the  $\beta$  parameter ( $\beta = df/dy$ ), instead of the height of the upper boundary like in Eady's (1949) model. Despite these differences, both models yield a comparable behaviour and structures of their most unstable modes for Earth-like parameters.

Despite the usefulness of the above linearised models for the initial growth and structure of the heat fluxes, momentum fluxes are not considered, as the perturbations lack the horizontal tilting. The absence of these nonlinear interactions and the assumption of a constant vertical shear preclude any modification to the barotropic or baroclinic structure of the mean flow, no matter the size of the disturbances. When the perturbations reach larger amplitudes the linear theory

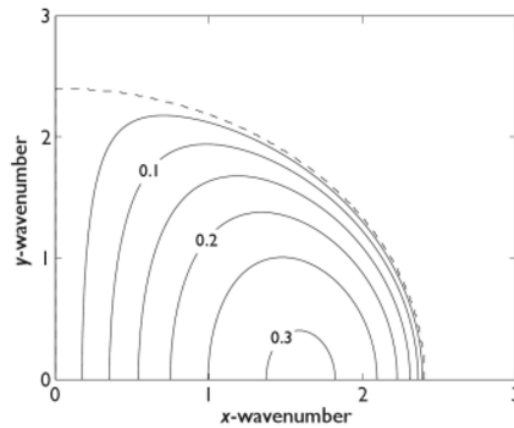


**Figure 2.4:** Structure of the non-dimensionalised Eady growth rate in the meridional ( $l$ ) - zonal ( $k$ ) wavenumber plane. From Vallis (2006) p. 270.

therefore clearly breaks down.

Analytical models of eddy evolution that include some nonlinear aspects and finite-amplitude considerations have been developed by various truncations of the primitive equations (e.g. Lorenz, 1963a; Pedlosky, 1970; Thompson, 1987; Killworth and McIntyre, 1985; Warn and Gauthier, 1989), or based on observations and heuristic arguments (e.g. Lorenz and Hartmann, 2001; Thompson and Woodworth, 2014). Such models include a nonlinear interaction whereby eddies interact with the baroclinic structure of the mean flow and thus their own growth rate, often leading to some oscillation between an eddy activity-dominated state and a mean flow-dominated state. As a result, the flow remains in a state of marginal stability (Farrell and Ioannou, 2009) with the wave amplitudes oscillating in time, as the nonlinear feedback precludes exponential eddy growth to infinity (as in the linear baroclinic instability theory).

Modelling of such eddy-mean flow nonlinear interaction is the primary focus of Chapter 3, and thus will be discussed there in more detail. However, it is noted here that the simplest analytical models mostly represent the oscillations between the growth rate and the amplitude of the eddies (associated with eddy heat fluxes and conversion of the mean available potential energy to eddy energy). In contrast, the interactions with the barotropic structure of the flow (associated with eddy momentum fluxes and conversion to the mean kinetic energy) are often neglected, as they have been observed to be significant only for larger wave amplitudes (e.g. Hart, 1979, and references therein).

As opposed to the purely analytical models, numerical integrations allow investigation of the fully nonlinear primitive equations. Eddy lifecycle experiments provide particularly enlightening insight into the growth, maturing and decay of baroclinic eddies. Particularly useful work is that of Simmons and Hoskins (1978) and Tanaka (1995) which shows how eddies draw on the available potential energy during their baroclinic growth stage, as is consistent with the linear theory. As the eddies mature and start decaying this energy is barotropically returned to the mean flow as zonal kinetic energy, and the eddies strengthen the flow. Similarly, Thorncroft *et al.* (1993) show such evolution from a more synoptic meteorological point of view, and will be discussed in more detail below.

The section discussed that baroclinic eddies initially grow in an almost exponential fashion when meridional heat fluxes dominate the eddy activity (as observed in the linear theory). Once eddies gain substantial amplitudes, nonlinear processes start to take over and they will affect first the baroclinic vertical shear and eventually the barotropic structure of the mean flow. The latter effect of the nonlinearity includes momentum fluxes which are associated with horizontal wave tilts. Lifecycle experiments show that as waves decay their vertical tilting decreases and so at this point the momentum fluxes start to dominate. It is therefore apparent that the nature of eddy-mean flow interaction changes throughout their lifecycle along with their evolving shape.

### 2.3.2 Indirect Effect of Eddies

Despite the findings of the last section, the presence of heat and momentum fluxes is not sufficient to induce changes to the zonal wind profile, because such changes can only occur as long as the thermal wind balance is maintained. This section examines the balance of eddy flux terms in the zonal-mean QG equations of motion, and the implication of the thermal wind balance, which (in the notation of Holton, 2004) is:

$$f_0 \frac{\partial \bar{u}}{\partial z} = - \frac{R}{H} \frac{\partial \bar{T}}{\partial y}, \quad (2.6)$$

where  $f_0$  is the Coriolis parameter,  $\bar{u}$  is the zonal-mean wind,  $\bar{T}$  is temperature,  $R$  is the specific gas constant for dry air and  $H$  is the depth scale of the troposphere ( $10^4$  km). This is a relatively stringent restriction as it limits the ability of the zonal wind and temperature to vary independently

in the following QG momentum and thermodynamic equations:

$$\frac{\partial \bar{u}}{\partial t} - f_0 \bar{v} = -\frac{\partial \overline{u'v'}}{\partial y} + \bar{X}, \quad (2.7)$$

$$\frac{\partial \bar{T}}{\partial t} + N^2 \frac{H}{R} \bar{w} = -\frac{\partial \overline{v'T'}}{\partial y} + \bar{J}/c_p, \quad (2.8)$$

where  $X$  denotes the frictional processes,  $J$  is the diabatic heating,  $N$  is the static stability, and  $c_p$  is the specific heat capacity at constant pressure. The thermal wind balance couples these equations, and so the alteration of the mean flow requires that both the heat fluxes and momentum fluxes change simultaneously. Without the mean overturning circulation ( $\bar{v}, \bar{w}$ ) and diabatic terms, independent variation of the eddy fluxes would violate the thermal wind balance.

In order to examine the mean meridional circulation induced by the eddy fluxes in a steady state, a mean meridional stream function is defined accordingly:

$$\rho_0 \bar{v} = -\frac{\partial \bar{\psi}}{\partial z}, \quad (2.9)$$

$$\rho_0 \bar{w} = \frac{\partial \bar{\psi}}{\partial y}, \quad (2.10)$$

so that equations 5.43 and 2.8 can be combined to eliminate the time derivatives as follows:

$$\frac{\partial^2 \bar{\psi}}{\partial y^2} + \frac{f_0^2}{N^2} \frac{\partial^2 \bar{\psi}}{\partial z^2} = -\frac{\rho_0 R}{N^2 H} \frac{\partial^2 \overline{v'T'}}{\partial z^2} - \frac{\rho_0}{N^2} f_0 \frac{\partial^2 \overline{u'v'}}{\partial y \partial z} + \frac{\rho_0 \kappa}{N^2 H} \frac{\partial \bar{J}}{\partial y} + \frac{\rho_0}{N^2} f_0 \frac{\partial \bar{X}}{\partial z}. \quad (2.11)$$

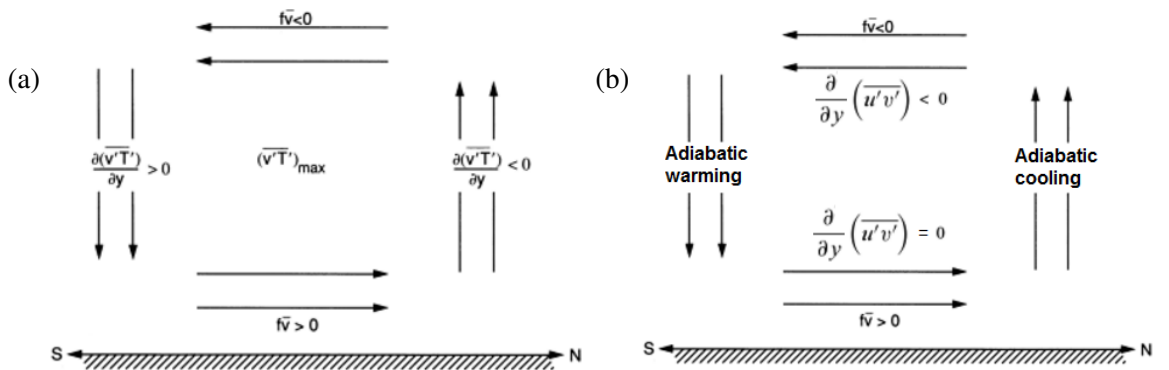


**Figure 2.5:** Schematic of the thermally indirect circulation induced by a) eddy heat flux, and b) eddy momentum flux in a typical atmospheric situation where an eddy induces a low to mid-level heat flux and an upper-level momentum flux convergence. Adapted from Holton (2004).

In the absence of diabatic effects, this elliptical equation states that the thermally indirect overturning circulation balances the action of the eddy fluxes, in order to assure the maintenance of the thermal wind balance. This balance therefore implies that a positive heat flux would induce a thermally indirect circulation, strengthening the temperature gradients and restoring the thermal wind balance (figure 2.5a). Similarly, an upper-level momentum flux convergence induces a thermally indirect circulation (figure 2.5b). The only way for the eddies to alter the zonal mean zonal flow in the time-varying picture without disturbing the thermal wind balance is for the eddy heat fluxes to vary simultaneously with the eddy momentum fluxes.

The magnitude of the individual eddy fluxes is therefore not sufficient for determining their resultant impact on the mean flow, as the eddy forcing can often be cancelled out by the overturning circulation. It is additionally noted that since the edges of the resulting Ferrel cell are also the edges of the Hadley and polar cells, there is a clear connection between the eddies in the mid-latitudes and other latitudinal regions.

### 2.3.3 Transformed Eulerian Mean

Andrews and McIntyre (1976) suggested an alternative way of viewing the eddy feedback on the mean flow, using a “transformed Eulerian mean” (TEM). A residual mean circulation ( $\bar{v}^*$ ,  $\bar{w}^*$ ) that is only associated with the diabatic forcing is defined so as to eliminate the large cancellation between the eddy fluxes and the adiabatic heating and cooling of the meridional overturning circulation. Retaining the notation and QG approximation of the previous section, the mean zonal wind and thermodynamic equations are:

$$\frac{\partial \bar{u}}{\partial t} - f_0 \bar{v}^* = \nabla \cdot \mathbf{F} + \bar{X}, \quad (2.12)$$

$$\frac{\partial \bar{T}}{\partial t} + N^2 \frac{H}{R} \bar{w}^* = +\bar{J}/c_p, \quad (2.13)$$

where  $\mathbf{F}$  is the Eliassen-Palm (EP) flux defined as:

$$F_y = -\overline{u'v'}, \quad F_z = \frac{f_0}{N^2 H} \overline{v'T'}, \quad (2.14)$$

and the meridional and vertical mean residual velocities are respectively defined as:

$$\bar{v}^* = \bar{v} - \frac{R}{N^2 H} \frac{\partial}{\partial z} \overline{v'T'}, \quad \bar{w}^* = \bar{w} + \frac{R}{N^2 H} \frac{\partial}{\partial y} \overline{v'T'}, \quad (2.15)$$

where the static stability ( $N$ ) is assumed to be constant. This framework states more explicitly that it is the combination of the convergences of the heat and momentum eddy fluxes that determines the evolution of the mean flow. In the time mean, the direct effect of the eddy fluxes dominates and a single more prolonged direct circulation cell can be observed in both the original QG TEM framework (figure 2.6), as well as in the isentropic EP-flux framework of Tanaka *et al.* (2004).

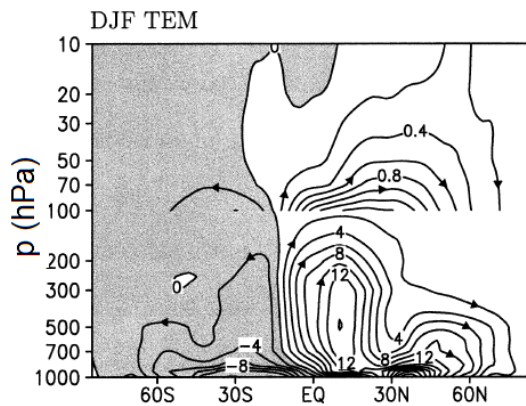


**Figure 2.6:** Winter (1990-2001) meridional mass transport streamfunction of the TEM framework from Tanaka *et al.* (2004). Units are  $10^{10} \text{ kg s}^{-1}$ , and negative values are shaded. ©American Meteorological Society. Used with permission.

Furthermore, combining the above equations and using the conservation of the zonal mean QG potential vorticity ( $\bar{q}$ ), it can be shown that:

$$\frac{\partial \bar{q}}{\partial t} = -\frac{\partial}{\partial y} \overline{v'q'} = -\frac{\partial}{\partial y} (\nabla \cdot \mathbf{F}), \quad (2.16)$$

where the last equality is called Taylor identity (Taylor, 1915; Bretherton, 1966). Thus the eddy forcing on the mean flow can be summarised as the potential vorticity flux. Although the TEM framework is useful for showing the direct influence of eddies, its boundary conditions are more complicated.

For small-amplitude perturbations, “wave activity” can be defined as the enstrophy divided by the mean QG potential vorticity gradient ( $A = 1/2\bar{q}^2 / (\partial\bar{q}/\partial y)$ ). Using the perturbation potential vorticity equation, the wave activity evolution equation under adiabatic conditions can be defined

as:

$$\frac{\partial A}{\partial t} + \nabla \cdot \mathbf{F} = 0, \quad (2.17)$$

where the Taylor identity was used. A more general equivalent version for finite amplitude was obtained by Killworth and McIntyre (1985) and Haynes (1988). Subsequent finite-amplitude theoretical and numerical studies of barotropic shear turbulence focused on bounding the growth of the initially exponentially growing wave (e.g. Shepherd, 1987b; Ishioka and Yoden, 1996).

For (almost) plane Rossby waves, it can be shown that the EP flux can be written as the product of the wave activity and group velocity ( $c_g$ ),

$$\mathbf{F} = \mathbf{c}_g A, \quad (2.18)$$

so the vector  $\mathbf{F}$  indicates the direction of propagation of the wave packet and thus wave activity (e.g. Vallis, 2006), i.e.  $\overline{u'v'} \propto -c_{gy}$  and  $\overline{v'T'} \propto c_{gz}$ . It has been further shown by McIntyre and Shepherd (1987) that this relationship exists for the finite-amplitude wave activity and its flux. This relationship shows that southward propagating waves will tend to induce a northward zonal momentum flux, and upward tilting waves will tend to be associated with a positive meridional heat flux, concurring with the geometrical arguments above.

## 2.4 Formation and Maintenance of Eddy-Driven Jets

Having reviewed the theory of barotropic and baroclinic modification of the mean flow by eddies in the zonal mean framework, this section touches on a selection of the relevant theories about the ability of a homogeneously (isotropically) spread collection of eddies to drive heterogeneous (anisotropic) changes in the mean flow.

Eddy-driven jets exist on the Earth and other planets with fluid atmospheres where turbulent motions occur. The Earth's general circulation is rather complex and variable, with the subtropical jet and eddy-driven jets often merging. Such a setting, together with the zonally asymmetric topography and ocean heat transport, yields a rather convoluted picture for the study of purely eddy-driven jets. Jupiter and other real (or idealised) planets with similar conditions, on the other hand, are convenient case studies for such research as their multiple jets in the mid-latitudes are

almost entirely driven by transient eddy activity that pumps momentum into the jet core (Salyk *et al.*, 2006; Ingersoll *et al.*, 1981). Studies of such phenomena will therefore be briefly reviewed here in order to indicate the importance of transient eddies in introducing structure to the mean flow.

The theoretical work on eddy-driven jets goes back to the papers of Phillips (1972) and Rhines (1975). Phillips (1972) discovered that homogeneous stirring in a stably stratified fluid can lead to inhomogeneous vertical mixing of the buoyancy gradient and therefore cause distinct layering of the vertical stratification, producing strongly stratified layers separated by well mixed regions. Such a phenomenon is caused by a positive feedback of the turbulent motions that encourages further stirring in the regions where stratification is already relatively weak and precludes it where stratification is stronger. This “Phillips effect” is widely studied, including laboratory work (e.g. Ruddick *et al.*, 1989), and has been used as an analogy for the horizontal mixing for the potential vorticity (PV) in the atmosphere (e.g. Dritschel and McIntyre, 2008).

Rhines (1975) originally showed that small-scale homogeneous two-dimensional barotropic decaying turbulence caused inhomogeneous mixing of PV gradients in a fluid on a  $\beta$ -plane, leading to the formation of anisotropic jets. He argued that small eddies coalesce until they become sufficiently large to allow planetary rotation to dominate so that nonlinear effects can transfer energy to the mean flow. This occurs at a critical scale of  $L_R = \sqrt{U/\beta}$  (with  $U$  being the eddy velocity scale), where the formation of Rossby waves becomes dominant over the advective effects of the smaller scales. This would impede the cascade of energy to larger scale turbulence. The structure of this critical length scale, expressed as the horizontal critical wavenumbers, is displayed in figure 2.7. The energy will tend to cascade to the largest scales outside the Rossby-wave dominated region. It is evident from the figure that such scales are at  $k_x \rightarrow 0$ , and so the eddy structures will become flattened and eventually form zonal flow. The presence of this anisotropic cascade was directly demonstrated by numerical experiments of Vallis and Maltrud (1993). In the presence of friction, dissipation removes energy from the large scale flow and, in combination with the Rhines scale, it can be used to determine the steady-state width of the jets (Vallis, 2006). The tendency of such  $\beta$ -plane turbulence to produce anisotropic structures was further confirmed by Shepherd (1987a) who quantified the transition from the advection-driven (turbulent) regime to a planetary rotation-driven wave-like regime observed by Rhines (1975).

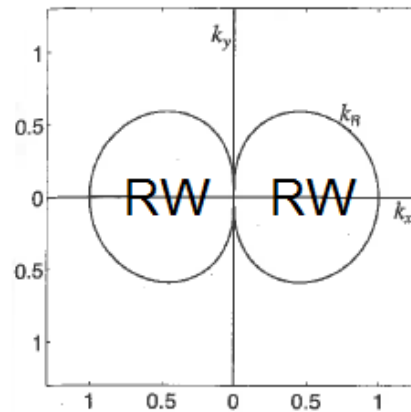


**Figure 2.7:** The critical wavenumber structure ( $k_R = 2\pi/L_R$ ) in the meridional-zonal wavenumber domain (normalised), related to the transition from isotropic turbulence to anisotropic wave structures. “RW” marks the regions that are dominated by the Rossby wave mechanism. Adapted from Vallis (2006), p.381.

The existence of the “Phillips effect” was also shown more systematically by Dritschel and McIntyre (2008) in a QG beta-plane barotropic channel model with an imposed homogeneous mixing. Using PV as a tracer, the authors revealed a Jupiter-like PV staircase reflecting the emergence of multiple jets (which are characterised by tightened PV gradients). These jets were found to be separated by isotropically turbulent mixing zones which exhibit lowered PV gradients. In time the jets eventually became almost impenetrable horizontal shear-dominated barriers between the mixing zones. It is also noted that the jets can be further sharpened by horizontal shearing and stretching of individual approaching eddies, which tilt in such a way as to supply momentum into the jet core. The eddy-driven jets are therefore characterised by eddies forming banana-shaped structures similar to that shown in figure 2.2c, which can be observed on Jupiter and other similar planets (figure 2.8).

An additional mechanism of maintaining the jet is through breaking of the Rossby waves that grow on the jet, which induces momentum fluxes in line with the theory described above. A complementary picture of this jet sharpening by breaking Rossby waves on the extra-tropical tropopause was presented by Ambaum (1997). Consider an area on an isentropic surface between two PV contours. This area is conserved under adiabatic flow. Upon irreversible wave breaking, some of this area will be advected away (and homogenised), and the two original PV contours rejoin. However, because of the decreased area between them, the contours will rejoin closer together so the PV gradients and the jet must sharpen (Ambaum, 1997). This view is reminiscent of the planetary wave variability observed in PV distribution near the Earth’s tropopause, as will be shown in the next section.

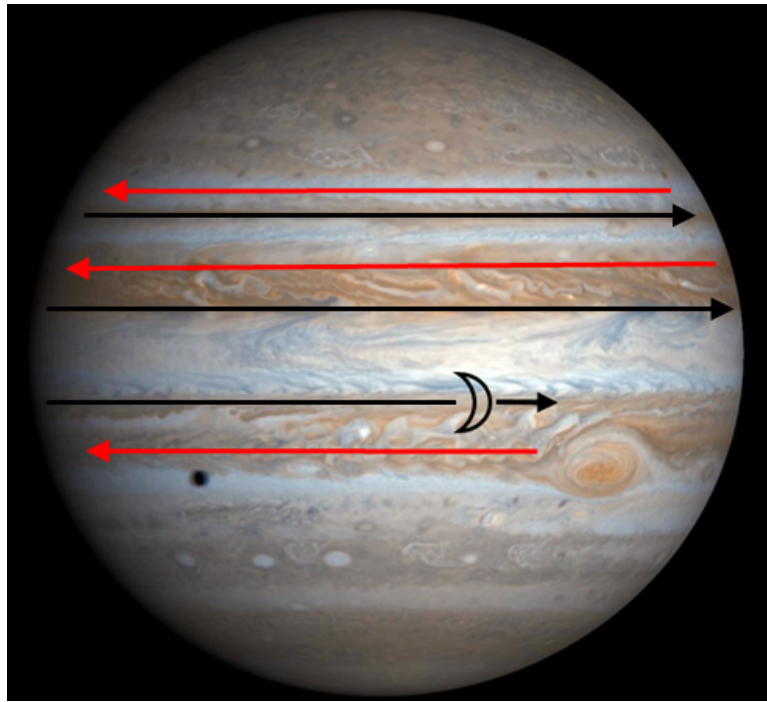


**Figure 2.8:** An image of Jupiter taken by NASA’s Cassini spacecraft (NASA/JPL; [www.nasa.gov](http://www.nasa.gov)), with the main westward jets being highlighted in red arrows, the main eastward jets in black arrows and an example of eddy tilting around a jet being marked by the moon-shaped segment.

The above studies focus on the barotropic interaction between the mean flow and eddies, assuming that baroclinic interaction is negligible. Baroclinic effects clearly add additional complications by making the turbulence three-dimensional. In that case it is necessary to consider other parameters related to the vertical structure, such as the baroclinic Rossby deformation radius  $L_D = NH/f$ , which is related to the vertical scale ( $H$ ) of the eddies relative to the balance of rotation and stratification. It was already shown above that a short wave cut-off exists for baroclinic instability, so for sufficiently small vertical (or large horizontal) scales barotropic turbulence dominates. Once the scales are in time increased to  $L_D$ , baroclinic energy will in turn be allowed to transform to barotropic energy which will then be cascaded to even larger scales, as discussed for the barotropic cascade case above. This conversion from the baroclinic to barotropic energy is called the “barotropisation” of the flow, and is summarised in figure 2.9. In this figure the energy input is the large-scale solar input rather than small-scale mixing. This mechanism of the baroclinic energy cascade has been obtained in numerical models even for weak baroclinicity (e.g. Kaspi and Flierl, 2007), and it helps to maintain the kinetic energy of the mean jets, which is then dissipated as boundary layer friction.

It should be noted that even barotropised flow can be influenced by the value of  $L_D$ . For example,

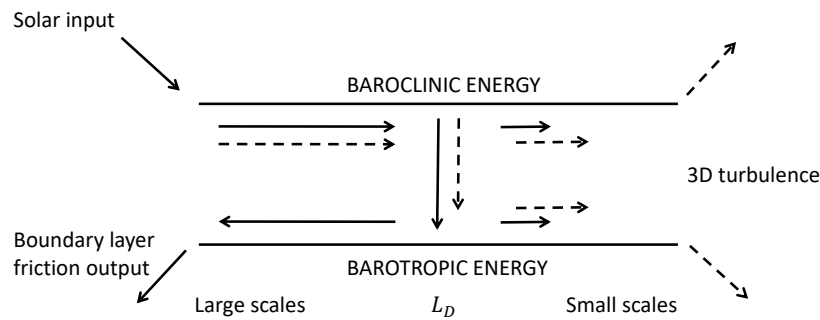


**Figure 2.9:** Two-layer baroclinic QG turbulence cascade. The horizontal axis denotes the horizontal wavenumber, increasing to the right. The two levels represent the baroclinic and barotropic flow, as indicated.  $K_R$  is the radius of deformation at which energy (solid) and enstrophy (dashed) flows are transferred into the barotropic mode. Reproduced from Salmon (1980).

Okuno and Masuda (2003) found that for very large values of  $L_D$  the  $\beta$ -effect becomes ineffective at interrupting the inverse energy cascade, so that the anisotropic jets do not develop and the flow behaves as if on an  $f$ -plane.

The arguments above indicate that the mean flow is energised by the eddies via an inverse cascade. However, a series of recent modelling studies (e.g. O’Gorman and Schneider, 2007; Thompson and Young, 2007; Berloff *et al.*, 2009) suggest that in fact baroclinic eddies interact directly with the mean flow, rather than merely supplying energy to the barotropic inverse cascade, the latter being deemed an insufficient and sometimes less preferred way of eddies interacting with the mean flow. Similarly, Schneider and Liu (2009) used a global circulation model (GCM) of Jupiter’s outer atmosphere to demonstrate that baroclinic eddies drive the jets that are beyond the equator. Baroclinic eddies can therefore dominate the maintenance of the mean flow directly through the nonlinear eddy-flux mechanism introduced in the previous section.

## 2.5 Eddy-driven Jet Variability

The previous section showed that baroclinic eddies can be the key ingredient in the formation and maintenance of zonal jets. However, eddy forcing is also likely responsible for driving the temporal and spatial variability of the mean flow. For example, Porco *et al.* (2003) present observations showing latitudinal shifting of Jupiter’s extratropical jets, and the associated Rossby waves. Williams’s (2003) modelling study of jovian jets suggests that such latitudinal jet migrating oc-

curs due to an asymmetric convergence of the eddy momentum flux. Similarly, observational and numerical studies focusing on more terrestrial conditions note that eddy fluxes are behind quasi-periodic changes in the strength and latitude of the eddy-driven jet (e.g. Lorenz and Hartmann, 2001; Robinson, 2000). This section briefly outlines the theory and mechanistic understanding behind such variability.

A prominent early study was that of Panetta (1991), who used a two-layer QG model to simulate multiple eddy-driven jets and studied their variability. Using a fixed background shear he was able to diagnose initial exponential growth of the eddies followed by a long period of equilibration. A subsequent low-frequency variability in the jets emerged as a result of the internal dynamics of the system (rather than the model parameters). In particular, the jets were observed to fluctuate independently in latitude, and autocorrelations of the potential and kinetic energies suggested long-term oscillations of the system. However, the authors concluded that the inverse energy cascade is insufficient to induce these low-frequency variations, implying a direct effect of the transient baroclinic eddies.

One way in which longer-term jet variability can be induced by high-frequency waves is associated with changes in the Rossby wave absorption-reflection properties, which is briefly outlined here. Waves that propagate outside of the jet will eventually reach a point where the wave phase speed approaches the speed of the mean flow. This would introduce singularity in the linearised governing equations of motion (e.g. Haynes, 2003). This problem can be partially solved by introducing a nonlinear critical layer, which includes effects (such as nonlinearity) that were neglected in the initial linearisation of the governing equations. A critical layer can be viewed as a mixing zone, which is separated from the Rossby waves of the meandering jet by a barrier, similar to that investigated by Dritschel and McIntyre (2008). The Rossby waves travelling from the jet can be either reflected, over-reflected or absorbed (associated with breaking) when approaching the critical layer on the equatorward side of the jet (e.g. Stewartson, 1981; Killworth and McIntyre, 1985). Reflection, over-reflection and absorption lead to zero, negative or positive poleward zonal momentum fluxes respectively. In either case the mixing region acts as a limiting boundary for wave propagation.

The absorption-reflection property of critical layers is related to the amount of mixing of the (conserved) PV within the critical layers. A cumulative absorption (or breaking) of waves propagating

from the jet into the critical layer would induce the PV in the critical layer to rearrange in such a way as to increase the reflective properties of the layer, and a further rearrangement would eventually lead to an over-reflection (emitting waves back towards the jet). Following this overturning, the critical layer would regain its ability to absorb waves again, resulting in a long-term oscillation in the momentum fluxes. An example of the three stages is shown in figure 2.10. In the presence of strong friction, one may expect that indefinite absorption of waves may occur, though such a behaviour is often not possible as wave absorptivity has been found to have a finite amplitude (Killworth and McIntyre, 1985). Though highly idealised, the above studies highlight the importance of systematic wave breaking on the lower-frequency temporal variability of momentum fluxes, which can induce corresponding fluctuations in the eddy-driven jets.

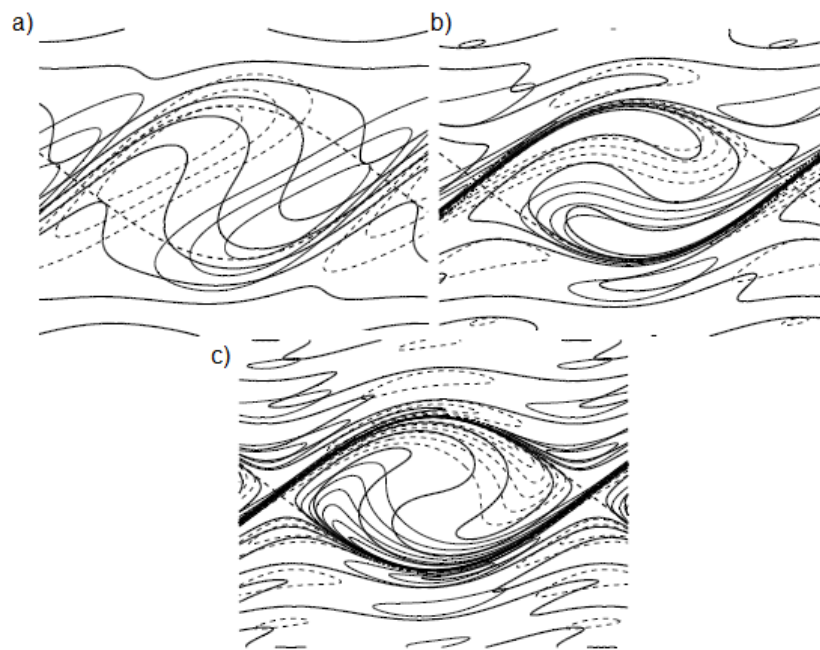


**Figure 2.10:** Vorticity rearrangement within a nonlinear critical layer, capturing the wave a) absorption, b) reflection, and c) over-reflection stages. The thick dotted contours represent the closed streamlines, and the thick solid contours are the absolute vorticity, whilst the thin contours are the relative vorticity (dashed lines represent negative values). From Haynes (2003).

Wave breaking is a very common phenomenon in the Earth's atmosphere. The schematic in figure 2.11 shows a typical structure of a flow on isentropic surfaces associated with a maturing baroclinic wave (or cyclonic synoptic system), looking northwards in the Northern Hemisphere. This structure comprises a rising flow that splits into a cyclonic branch and an anticyclonic branch. A similar but descending structure is evident to the west of the cyclone. This setting forms the basis of typical weather systems studied by synoptic meteorologists. As Thorncroft *et al.* (1993)

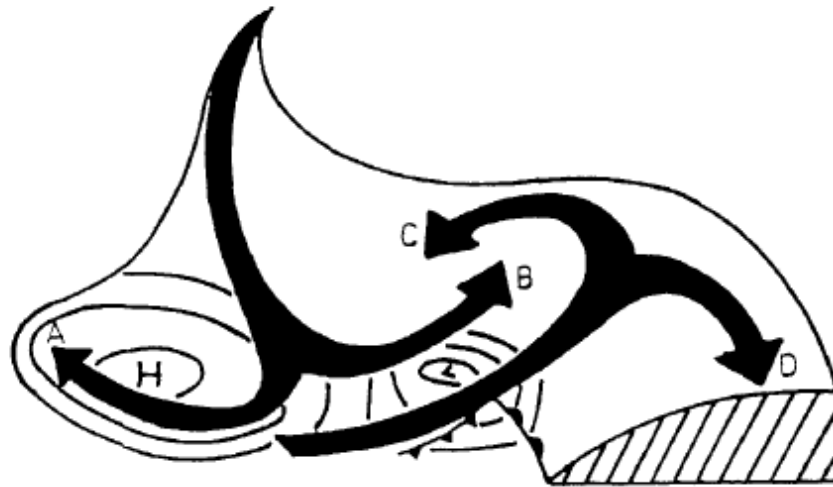


**Figure 2.11:** Schematic of isentropic flow within a maturing baroclinic wave (see text for details). From Thorncroft *et al.* (1993).

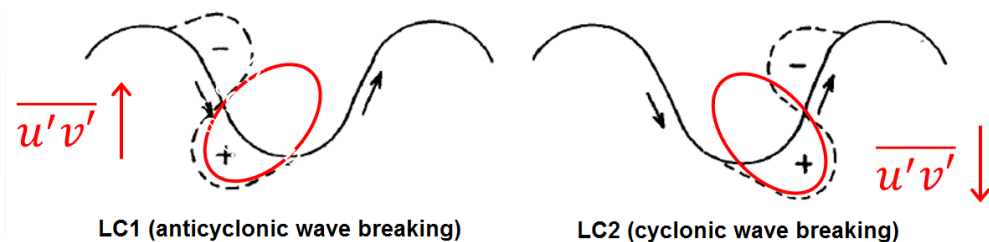


**Figure 2.12:** Schematic of the deformation of a theta-PV contour with an initial sine-wave structure during LC1 and LC2, with the flow being indicated by the black arrows. The eddy tilt and direction of the zonal momentum flux are indicated in red. Adapted from Thorncroft *et al.* (1993).

point out, two major types of behaviour occur when either the anticyclonic branches A and D dominate (stretching the cyclone), or when the cyclonic branches C and B dominate (where the cyclones stay compact and stretch the surrounding anticyclones). These types of behaviour are called anticyclonic and cyclonic wave breaking, respectively, and a schematic of their horizontal structure is shown in figure 2.12. For examples of real synoptic case studies, the reader is referred to Thorncroft *et al.* (1993), Reed and Albright (1986), Liberato *et al.* (2013) and references therein.

Thorncroft *et al.* (1993) investigated these two types of wave breaking by running an idealised experiment of wavenumber 6 with a different initial horizontal shear structure. They recovered two lifecycle paradigms: LC1 which is characterised by mainly anticyclonic wave breaking, and LC2 dominated by cyclonic breaking. By observing the evolution of the PV contours on isentropic surfaces, the authors linked the two lifecycle paradigms and their associated dominant wave breaking types to the critical layer theory, as follows.

LC1 exhibits a linear-like baroclinic development up to day 5, after which the lower layer saturates and releases an upward propagating Rossby wave activity into the westerly jet aloft. Unlike the baroclinic instability, the Rossby wave propagation is independent of low-level temperature gradients, and this stage is associated with additional bursts in the eddy kinetic energy. After about 2 days of the upward propagation, the upper levels saturate and release Rossby waves predominantly in the equatorward direction. The resulting irreversible mixing of subtropical PV and the thinning and stretching of cyclones on the equatorward flanks of the jet in the southwest-northeast direction are characteristic of absorption by the subtropical critical layer and the anticyclonic wave breaking. The corresponding momentum fluxes then shift the associated jet poleward.

LC2 displays similar characteristics to LC1 during the first stages of its evolution, until the waves start propagating to the upper levels. The propagation of the strongest disturbances to the equatorward sides of the jet (as in LC1) is suppressed in this case. The authors show that this is characteristic of a less absorptive upper level critical layer on the equatorward side of the jet associated with lower PV gradients (and thus reduced PV mixing) in this region. The poleward side of the jet is associated with a strong cyclonic wrap-up. Using Haynes's (1988) wave activity, the authors show that this steady vortical region cannot effectively absorb or radiate waves.

In addition to the lowered absorption reducing the amount of wave breaking on the equatorward side of the jet, the authors attribute the observed slight poleward migration of the waves to an upper-level minimum of a wave refractive index on the equatorward side of the jet. This refractive index relates to the extent to which the PV gradients are sufficient to support the Rossby wave propagation, and its minima partially deflect waves away (Matsuno, 1970, Rivière, 2009). This index is given by:

$$I_R = \sqrt{a^2 \frac{\partial \bar{q}}{\partial y} \overline{U} - c^2}, \quad (2.19)$$

where  $a$  is the Earth's radius,  $\bar{q}/\partial y$  is the zonal-mean QG PV meridional gradient,  $c$  refers to the wave phase speed,  $\overline{U}$  is the zonal mean zonal wind speed and  $m$  is the zonal wavenumber.

Lorenz (2014) further investigated the wave reflection (where  $I_R = 0$ ) in an idealised barotropic model with a zonal jet. He found that a wavenumber-selective reflection operates at the poleward flank of the jet, additionally to the absorption at the critical level. When phase speeds are increased, fewer waves are reflected and more absorbed at the poleward flank of the jet, which

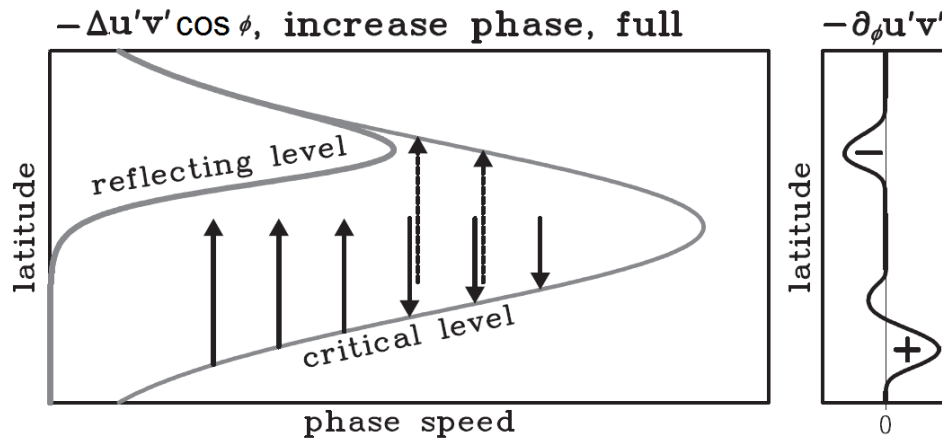


**Figure 2.13:** Schematic of the effect of increased phase speeds on both the reflection and absorption of waves. The left panel shows a latitude-phase speed plot, where the arrows represent the change in the meridional component of the EP flux in response to the increased phase speeds, with the dashed arrows marking the wave activity that is absorbed at the poleward critical level. The direction of the solid arrows reflects the change in the momentum fluxes as phase speed increases. The critical and reflecting levels are depicted by the grey lines. The panel on the right shows the corresponding changes in the net momentum convergence. These plots only correspond to one wavenumber, since  $I_R$  is wavenumber dependent. Adapted from Lorenz (2014). ©American Meteorological Society. Used with permission.

would oppose the poleward jet shift induced by the poleward movement of the subtropical critical line at the equatorward side of the jet (Thorncroft *et al.*, 1993; Chen *et al.*, 2007). These two effects are shown in figure 2.13. Despite this added complexity, Thorncroft *et al.*'s (1993) and Lorenz's (2014) studies provide a physical link between baroclinic eddies, Rossby wave breaking and forcing on the main flow.

The aforementioned default preference for the equatorward propagation of Rossby waves can be attributed to several factors on the Earth, most of which are related to the  $\beta$  parameter increasing at lower latitudes. First, the increased  $\beta$  parameter would increase the group velocity and make the linear propagation more efficient there (e.g. Vallis, 2006). Additionally, Schopf *et al.* (1981) studied the dispersion of oceanic internal Rossby waves, using the ray theory and the group velocity vector. They found that the theory predicts an equatorward turning of group velocity vectors of waves that were generated away from the Equator. The authors attribute such asymmetry in wave propagation to the latitudinal variability of the Rossby deformation radius. Furthermore, Balasubramanian and Garner (1997) found that the effect of spherical geometry leads to an alteration of the wave phase speeds that produces anticyclonic tilts, whereas in a Cartesian model the ageostrophic horizontal wind induces a cyclonic shear which tilts the waves the other way. The  $\beta$  parameter also affects the value of the refractive index (equation 2.19) as it appears in the

definition of the QGPV gradient, and so (in the case of a weak stretching term in equation 2.20 discussed in more detail below) the wave-repelling refractive index minimum will be located towards the higher latitudes. Furthermore, the critical layer in the subtropics is more definitely confined to where the zonal wind changes direction for high enough phase speeds. On the poleward side of the jet, on the other hand, the complex nature of  $I_R$  depends on the reversal of the mean PV gradient, the zonal wave number and the value of the phase speed (as implied by equation 2.19), neither of which is particularly latitudinally restricted.

## 2.6 Stationary Waves and Asymmetric Time-mean Flow

When considering the global circulation of the Earth, arguments based on the zonally symmetric framework need to be extended to the three-dimensional picture, where eddy activity is concentrated in localised storm tracks. The Southern Hemisphere is more zonally symmetric, but even there several localised storm tracks can be observed (Hoskins and Hodges, 2005). Nevertheless, the higher zonal symmetry of the Southern Hemisphere means that its storm tracks are dominated by transient eddies (wavenumber 4-7), whereas in the Northern Hemisphere stationary waves (wavenumber 1-3) dominate (Lorenz and Hartmann, 2003; Tanaka *et al.*, 2004). This section briefly outlines some of the issues associated with stationary waves and their forcings which can lead to formation of localised storm tracks, and potentially their variability.

Stationary waves can be approximately viewed as planetary-scale barotropic stationary Rossby waves, and their idealised structure can be induced from the dispersion relation of the latter (Holton, 2004). The relation shows that a point source produces two downstream stationary wavetrains, and an example of such features is shown in figure 2.14. The wave amplitudes are prevented from diminishing due to the energy supplied to the waves from their source, maintaining the group velocity. In light of the theory discussed above, the tilting apparent in this figure supplies momentum back towards the latitude of the wave maker (to compensate for the upstream mountain torque). The preferential propagation towards lower latitudes has been found to disappear in a flow that is linearised (Ringler and Cook, 1997). This asymmetric effect of the nonlinear system was attributed to its capacity to alter the background PV gradient which creates zonal asymmetries in the refractive index and thus the irregularity in the stationary wave structure.

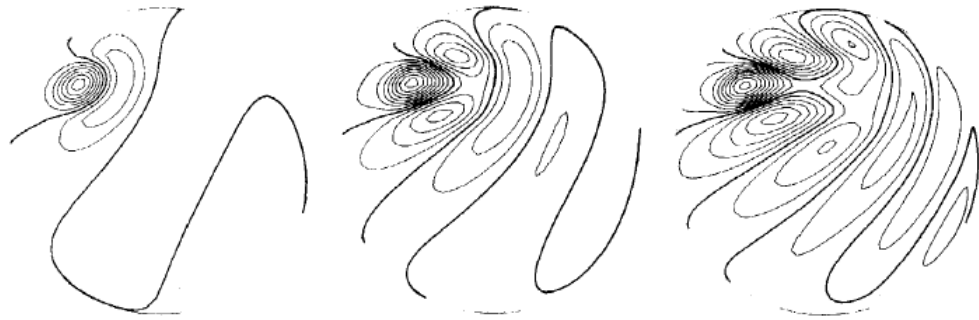


**Figure 2.14:** Vorticity pattern representing topographically generated idealised stationary Rossby wave trains on a sphere for 2 (left), 4 (middle) and 6 (right) days after switching on the forcing. From Hoskins (1983).

The stationary waves in the Northern Hemisphere are affected by this nonlinearity, but also by the numerous sources of the stationary waves, such as orography, land-sea contrast, sea surface temperatures and friction (Brayshaw *et al.*, 2009), which generates a less regular asymmetric flow pattern. The most important forcings that contribute to the time-mean flow of the Northern Hemisphere have been found to be extratropical diabatic heating and orography, though the relative importance of these is still being debated (Derome and Wiin-Nielsen, 1971; Chang, 2009). For example, stationary waves induced by both topography and diabatic heating were studied for a particular case study by Derome and Wiin-Nielsen (1971) using a linear QG model. They found that the topography forcing appears to be similar to the diabatic forcing, though the former produces larger amplitudes.

On the contrary, Chang's (2009) idealised GCM study implies that the extratropical diabatic heating in the Northern Hemisphere dominates the stationary flow pattern, while orography (i.e. the Rockies and the Tibetan plateau) merely helps to strengthen this effect. Similarly, Kaspi and Schneider (2013) showed that a heating dipole in an aquaplanet idealised model can produce flow asymmetries and strong localised storm tracks, similar to those observed in the Northern Hemisphere. The associated stationary waves were found to be the dominant driver that determines the beginning and end of the storm track, the length scale being given by the stationary Rossby length scale. This demonstrates that mountains are not necessary to create localised storm tracks.

Evidently, stationary Rossby waves are able to introduce prominent momentum fluxes and produce zonally asymmetric steady structures in the flow. There is, however, some evidence that stationary forcings can also contribute to a quasi-periodic temporal variability of the flow. For instance, Hogg and Blundell (2006) studied the effect of topography on low-frequency periodic

variability of baroclinicity in a simplified QG model of the Southern Ocean, with the wind stress forcing and dissipation being kept constant. They observed that the wind stress forcing increases the baroclinicity which in turn generates eddy activity. Eddies then tend to transfer momentum into deeper layers and drive deep ocean currents. The baroclinic instability will keep increasing until it reaches a point at which eddy activity induces a low-level cyclonic gyre, which is steered by topography and causes flow asymmetry in all layers. This in turn accelerates the enhancement of the baroclinic instability and eddy activity until the available potential energy is depleted. When the eddy activity and low-level circulation cease the cycle can repeat. Though this work is not directly related to storm tracks, it demonstrates that stationary forcing, such as orography, can be involved in low-frequency variability.

## 2.7 Localised Storm Tracks and Jets on the Earth

The previous sections reviewed some idealised studies that emphasize the strong interaction between the mean flow and baroclinic eddies, and its importance in setting the baroclinic and barotropic structure of the jet, as well as its temporal variability. This section outlines the more complex eddy-mean flow interaction on the Earth and its observed variability.

### 2.7.1 Spatial Setup of the Mid-latitude Jets

Eddy length scales on the Earth are relatively large compared to the size of the planet, and so each hemisphere exhibits only one eddy-driven jet with a relatively substantial amount of space around it that allows the jets to migrate substantially in latitude (e.g. Chemke and Kaspi, 2015). However, this meridional variability is somewhat constrained by the presence of the subtropical jet. Lee and Kim (2003) simulated a simplified setup of the subtropical and eddy-driven jets in a multilayer primitive equation model to show that if the subtropical jet is strong and northerly enough, it can induce sufficient baroclinic instability and merge with the eddy-driven jet. Otherwise the latter would normally develop in the baroclinic zone of the mid-latitudes. In analogy to the idealised flows discussed in the previous sections, the two jets will tend to be spaced far enough from each other to allow the most baroclinic waves to develop. However, if the jets are initiated closer together, they will be pushed closer together by the eddies developing on the outer edges of the jet couplet.

As mentioned above, stationary waves in the Northern Hemisphere result in sharpened meridional temperature gradients at the eastern mid-latitude edges of the Asian and North American continents. This (by thermal wind balance) strengthens the upper-level flow. Lee and Kim (2003) suggest that this is the reason for the observed different jet merging in the two storm tracks as follows. The Pacific eddy-driven and subtropical jets are more merged due to the lower latitude of the baroclinic area established by the stationary forcings. Conversely, the stationary forcings in the North Atlantic enhance baroclinicity further north from the subtropical jet, so the jet splitting is more common. The authors suggest that due to the North Atlantic eddy-driven jet being consequently more free to move meridionally, its wave activity is allowed to develop further and so the storm track activity is comparable in strength to the Pacific, despite the North Atlantic being associated with a weaker jet. Consistent with this view point, the first mode of jet variability in the North Atlantic is linked to the latitudinal shifting, whereas in the Pacific it is linked to the jet intensity or pulsing (Woollings *et al.*, 2010).

### 2.7.2 Shifts in the Dominant Wave Breaking Type

In accordance with the theory outlined above, it is observed that when the Earth's eddy-driven jets become baroclinically unstable, they develop Rossby waves which eventually deform and break. Some of the wave breaking produces isolated vortices which sharpens the jet and these vortices are eventually sheared out and homogenised (as in Ambaum, 1997; Dritschel and McIntyre, 2008). Such features can be observed particularly well in the potential temperature field on the 2 PVU surface, as is shown in figure 2.15. This field is usually studied as the potential temperature is conserved and represents the dynamical tropopause in the mid-latitudes at around 315 K (which marks the location of the upper-level jets). Tilting large-scale meanders evidently wrap up and break, as suggested above. In the light of the discussion above, this wave breaking is associated with different absorptivity and reflection of Rossby waves at critical layers. The nonlinear critical layer theory is too simple to explain the Earth's wide critical breaking zones precisely (Haynes, 2003), but it can be used qualitatively to indicate the basic components behind such variability.

It should be noted that only an intermediate range of eddy scales (wavenumbers 6-7) are observed to break both ways, with higher wavenumbers predominantly breaking cyclonically and lower wavenumbers breaking anticyclonically (e.g. Hartmann, 2007). However, the intermediate scales include some of the most unstable baroclinic modes in the atmosphere, and their evolution is

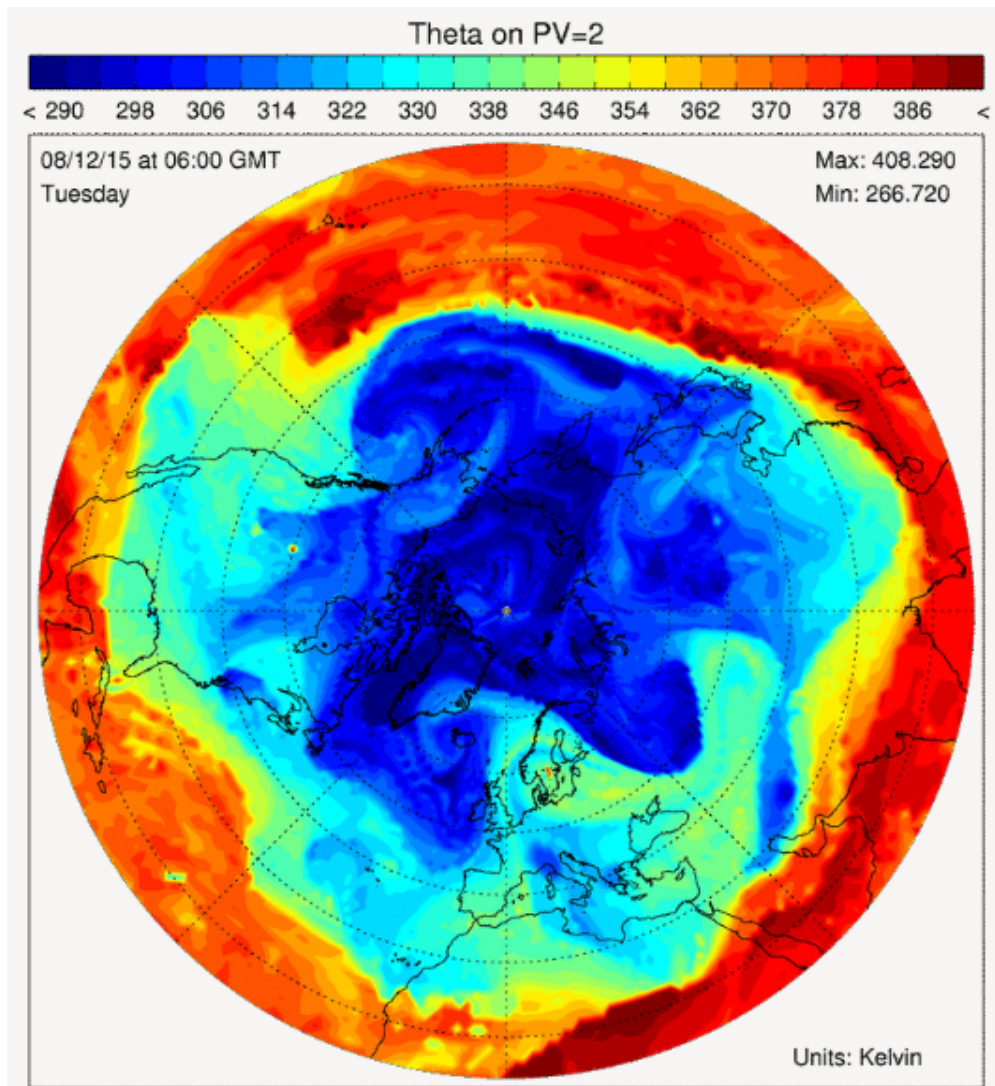


**Figure 2.15:** A snapshot of potential temperature on the 2 PVU surface from the ECMWF operational analyses (courtesy of Dr Nick Klingaman).

therefore crucial to the large-scale development of the flow.

It is evident from the previous sections that the mean meridional PV gradient plays a pivotal role in the variability of the westerly mid-latitude jets. In the context of wave breaking and jet latitude shifting, Rivière (2009) analysed the mean meridional QG PV gradient:

$$\frac{\partial \bar{q}}{\partial y} = \underbrace{\beta + \frac{\partial \bar{\zeta}}{\partial y}}_{\text{abs. vort.}} - \underbrace{f^2 \frac{\partial}{\partial p} \left[ \left( \frac{\rho g}{N} \right)^2 \frac{\partial \bar{u}}{\partial p} \right]}_{\text{stretching}}, \quad (2.20)$$

where  $\rho$  is the density and  $\bar{\zeta}$  is the relative vorticity. The author points out that if variations in  $f$  are accounted for, the competition between the absolute vorticity and the stretching terms can

result in the dominance of different wave breaking via changes in the refractive index (equation 2.19). The absolute vorticity increases the refractive index at the equatorward flank of the jet and promotes anticyclonic wave breaking in the upper levels. This upper-level effect is partially opposed by the stretching term, which additionally induces a tendency to break more cyclonically in the lower levels. The author also presents a number of primitive equation model runs that simulate the theoretically deduced behaviour. He finds that a low-latitude initial jet supports more cyclonic wave breaking (where the stretching term is more effective) and a zonal flow structure further downstream, whereas a more poleward initial jet tends to break anticyclonically (due to the absolute vorticity effect dominating) supporting a more poleward flow further downstream. The author then compares this behaviour to the more northerly location of the North Atlantic eddy-driven jet which is dominated by anticyclonic wave breaking, and the North Pacific jet which exhibits more cyclonic wave breaking (Martius *et al.*, 2007) as it is situated at a lower latitude. These findings complement those of Lee and Kim (2003) mentioned above.

Changes in the PV gradient are therefore capable of triggering the transitions between the dominant types of wave breaking. It was already mentioned above that such changes to the PV gradient can be induced by introducing a horizontal shear (Thorncroft *et al.*, 1993). However, it should be noted that too much horizontal shear can inhibit baroclinic eddy generation altogether by suppressing the region between the critical layers (James, 1987). This was called the “barotropic governor” mechanism (James and Gray, 1986), and is said to be responsible for the enhanced mid-winter Pacific minimum (Nakamura, 1992; Nakamura and Sampe, 2002).

Changes in the low-level tropospheric vertical wind shear can also affect wave breaking. For example, Chen *et al.* (2007) observe a transition from cyclonic to anticyclonic wave breaking due to reduced surface friction resulting in increased phase speeds of the most unstable waves and a poleward migration of the critical layer.

Another proposed mechanism that can induce changes in the dominant wave breaking type is through the vertical shear in the stratosphere (Wittman *et al.*, 2007). The authors discovered that for a single (intermediate) wavenumber experiment, an increase in the lower stratospheric wind shear and the consequent increase in the phase speeds caused a shift from LC1 to LC2. This is not consistent with Chen *et al.*'s (2007) mechanism for movement of the critical layer, which would require lower phase speeds in this case. It is more likely that Lorenz's (2014) selective

wavenumber reflection is of greater importance here, whereby the higher phase speed can reduce the amount of equatorward propagating waves by increasing their absorption at the poleward critical level.

Ambaum and Hoskins (2002) additionally found that the tropospheric-stratospheric connection includes a positive feedback, whereby altered refractive index in the upper-level troposphere affects the polar vortex strength which induces the tropospheric flow below. It is likely that the resulting tropospheric flow would in turn feedback on the properties of the breaking waves. This would concur with the results of Polvani and Kushner (2002) who found that forcing in the stratosphere in a relatively simple GCM could reproduce major shifts in the tropospheric jets, recovering similar patterns to the observed dominant modes of variability in the atmosphere. Furthermore, the coupling between the stratosphere and troposphere via the balance between the tropospheric meridional circulation and the stratospheric wave drag of stratospheric planetary waves (called “downward control”) as suggested by Haynes *et al.* (1991), has been observed to have a substantial imprint in the troposphere (Ambaum and Hoskins, 2002; Hitchcock and Simpson, 2014).

Stratospheric influence on the tropospheric flow and its wave breaking can also induce quasi-periodic variability. For example the polar-night jet oscillation on seasonal timescales (Hitchcock *et al.*, 2013) is communicated into the lower troposphere (Hitchcock and Simpson, 2014). Likewise, the quasi-biennial oscillation, characterised by periodically changing the sign in the tropical stratospheric winds, has been observed to imprint on the mid-latitude variability (Kidston *et al.*, 2015).

Furthermore, forcings from the tropics can come into play. For instance, tropical heating can trigger external Rossby waves in the subtropical westerlies via advection of the low-latitude vorticity (Sardeshmukh and Hoskins, 1988). Similarly, heating directly in the subtropics has been found to be effective at generating poleward propagating Rossby waves (e.g. Hoskins and Karoly, 1981). These external Rossby waves affect the momentum flux that acts on the mid-latitude eddy-driven jet core, and tend to act against the forcing of the high-frequency baroclinic eddy forcing (e.g. Lorenz and Hartmann, 2001).

As an example, quasi-periodic variability can be induced by such low-latitude forcings. For ex-

ample, the El Niño-Southern Oscillation (ENSO, related to the variability of the sea surface temperatures in the tropical eastern Pacific) introduces low-frequency variability in different wave-breaking types in the North Pacific storm track (Straus and Shukla, 1997; Orlanski, 2003), as well as the North Atlantic storm track through downstream development of transient North Pacific eddies (e.g. Li and Lau, 2012). Li and Lau (2013) propose an additional stratospheric pathway mechanism through which ENSO can affect the North Atlantic wave breaking by modifying the strength of the polar vortex and the refraction of the upper-tropospheric planetary waves. These studies demonstrate the complicated global forcing on the storm tracks due to a localised low-latitude source. Other low-latitude sources of mid-latitude variability also include the sub-seasonal Madden-Julian Oscillation, characterised by a periodical intensification of the tropical convection in the Indian Ocean and western Pacific (Kim *et al.*, 2006).

Finally, the effect of low-level tropospheric baroclinicity has been studied by Orlanski (2003). Instead of the QG theory, Orlanski (2003) considers a shallow-water primitive equation model, whilst simulating a baroclinic forcing. His findings were somewhat complementary to those of Rivière (2009). He found that a large stretching term (in this case related to high low-level baroclinicity rather than a lower latitude of the jet) is associated with a shift to cyclonic wave breaking. Alternatively, for lower values of low-level baroclinicity anticyclonic wave breaking occurs. The author attributes the difference to the observed asymmetry between the maximum possible strength of cyclones and anticyclones, which can be summarised as follows. Under PV conservation, the maximum negative (anticyclonic) relative vorticity,  $\zeta$ , was observed to be achieved when the absolute vorticity and PV vanish (and so does the baroclinic forcing term), so that  $\zeta = -f$ . However, positive (cyclonic) relative vorticity centres do not possess such a bound and so they can grow much stronger than the anticyclones under high baroclinic forcing. Thus in order to maintain mass balance and the Kelvin circulation theorem, the strong cyclones are concentrated in a smaller but more intense centre than the weaker and more diffuse anticyclones (Hart, 1979). This would imply dominance of the cyclones in meridional eddy flux statistics (no matter what type of breaking occurs). When the baroclinic forcing is large, the cyclones become sufficiently strong to stretch the anticyclones whilst themselves staying compact (figure 2.16), similar to the wrap-up structures in Thorncroft *et al.*'s (1993) LC2 case. On the other hand, when the baroclinic forcing is weak, the asymmetry due to the Earth's sphericity leads to the anticyclones becoming more dominant over the cyclones, the latter being sheared and stretched anticyclonically (figure 2.16), forming shapes reminiscent of LC1. This is in agreement with Rivière's (2009) aforemen-

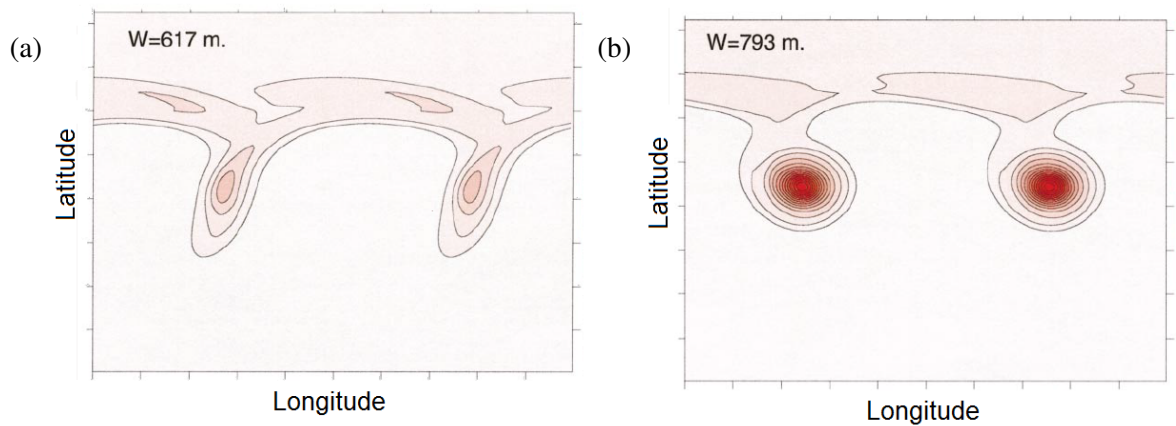


**Figure 2.16:** PV contours marking flow induced by a moderate (a) and large (b) forcing of low-level baroclinicity. From Orlandi (2003). ©American Meteorological Society. Used with permission.

tioned QG theory-based finding that a higher baroclinicity (or stretching term) will lead to more cyclonic wave breaking and vice versa. However, the QG theory does not allow asymmetries between cyclones and anticyclones, so the mechanisms involved in these two theories are different but equally plausible.

In the light of the QG critical layer theory, increased low-level baroclinicity could be expected to replicate the effect of increased low-level friction, as in both cases the low-level wind shear is enhanced (under the thermal wind balance). The decreased phase speeds and the more equatorward subtropical critical layer would reduce the amount of waves propagating and breaking equatorwards, as in LC2. Both mechanisms of Orlandi (2003) and the QG critical layer theory therefore predict that larger values of baroclinicity will likely lead to a shift to a regime that is similar to the LC2 and a more southward jet, and vice versa.

It is evident from the above studies that there are competing mechanisms that can lead to temporal jet fluctuations through changes in different types of wave breaking within the storm tracks. The forcing of low-level baroclinicity is of particular interest, as it directly generates the storm track activity, as well as being directly eroded by the latter. This interaction implies that the timescales of the baroclinicity variability should be closely linked to that of the storm track activity.

In contrast, the stationary and external forcings do not necessarily have the same scale of variability as the transient motions studied here. For example, oceanic heating is slower compared to the timescales of the atmospheric transient motions (Czaja, 2003) and so it is unlikely to be

responsible for the jet transitions that are of interest here. As suggested by the theory, the relationship between baroclinicity and storm track activity should additionally provide a mechanism for obtaining quasi-periodic variability within the storm track, as long as baroclinicity is allowed to replenish. Whether or not such an internal variability in storm track activity exists and whether it can influence the observed changes in the jet latitude is the main focus of this thesis.

However, in order to investigate the possibility of the two baroclinic (characterised by oscillations in storm track activity) and barotropic (characterised by oscillations in jet latitude) types of internal variability of the storm track, the observed three-dimensional structure of the storm tracks, as well as the different timescales involved in their temporal evolution must be considered. These two issues are briefly discussed in the next two sections.

### 2.7.3 Observed Storm Track 3D Structure in the Steady State

As mentioned above, stationary waves in the Northern Hemisphere result in sharpened meridional temperature gradients at the eastern mid-latitude edges of the Asian and North American continents, forming zonally asymmetric regions of intense baroclinicity. These regions become baroclinically unstable and mark the beginning of the North Atlantic and North Pacific storm tracks (see figure 1.1). The ageostrophic wind associated with the steady state jets forms a thermally direct circulation at the jet entrance (beginning of the storm track) and a thermally indirect circulation at the jet exit. Note that in this context the “downstream of the end” of the storm track is defined as the location of maximum eddy momentum flux convergence, where the eddy-driven jet fluctuates markedly in latitude.

The storm tracks have also been suggested to be self-maintaining. For example, Hoskins and Valdes (1990) argue that the wind stress curl associated with the eddy-driven jet accelerates the oceanic western boundary currents, providing additional heat to the storm track. Storms additionally flux energy to downstream development of storms, extending the storm track laterally (Orlanski and Katzfey, 1991). Additionally, Robinson (2000) suggests a positive feedback of the transient eddies, whereby the strengthening of the eddy-driven jet by eddy momentum fluxes, in combination with substantial surface drag, leads to an enhanced higher vertical wind shear (and thus baroclinicity and storm tracks) in the steady state.

In this setting the transient eddies grow at the beginning of the storm track and start decaying once they leave the region of high baroclinicity towards the downstream end of the storm track. This upstream to downstream change in the spatial storm track characteristics is a reflection of the different parts of the storm track being dominated by different stages of the lifecycles of storms. A statistically consistent temporal evolution of a number of downstream-propagating storms generated in the same location can therefore be translated into a steady state spatial variability of a storm track, which is observed as follows.

At the beginning of the storm track, the baroclinic instability could be assumed to be almost linear with an exponential growth rate (Chang and Orlanski, 1993) and dominated by heat fluxes and upward propagation of waves (Hoskins *et al.*, 1983). At the downstream end of the storm track the dominance of the heat fluxes and baroclinicity is replaced by the barotropisation of the storm track with enhanced momentum fluxes and horizontal wave breaking. Using Orlanski's (2003) argument, the beginning of the storm track can be viewed as predominantly controlled by a strong baroclinic forcing and cyclonic wrap-up, whereas the downstream end of the storm track can be viewed as dominated by stronger anticyclones that are conducive to cyclonic shearing and stretching. The large scale flow is consequently organised in a trough-ridge structure spanning along the storm track (Orlanski, 1998) which is characterised by a northward tilt (Chang *et al.*, 2002). Orlanski (1998) confirmed that eddy fluxes drive such structures in the North Atlantic and the North Pacific.

#### 2.7.4 Temporal Variability of Storm Tracks and Jets

The temporal variability of storm track activity (and the associated jets) is, however, not constant. For example, theoretical arguments outlined briefly above suggest potential for some nonlinear periodic behaviour. In addition, Messori and Czaja (2013) and Swanson and Pierrehumbert (1997) observed that heat fluxes occur in spikes, suggesting that eddy activity is highly variable and intermittent. However, raw observations are very noisy and storm tracks are often thought to be dominated by non-periodic (or chaotic) variability (e.g. Lorenz, 1963a; Lorenz, 1984).

On the other hand, the (quasi-)periodic variability of the jets is fairly well documented. For example, Namias (1950) documented cycling shifts in the zonal mean westerlies in both of the hemispheres which he called index cycles, where high index refers to a more northern and zonal

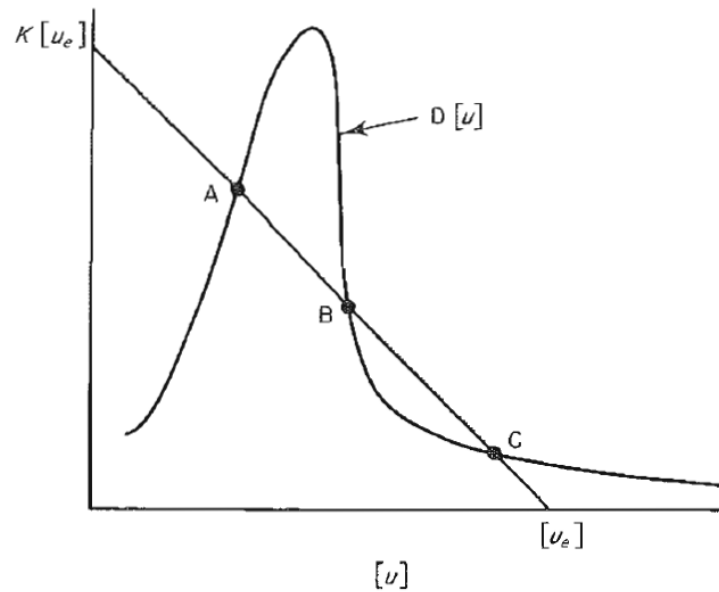


**Figure 2.17:** A schematic representation of the steady-state solution of Charney and DeVore's (1979) model.  $[u]$  represents the zonal wind, and  $D[u]$  and  $K[u]$  represent the nonlinear and linear terms that contribute to the deceleration and acceleration of the zonal wind, respectively. There is no acceleration of the zonal wind at the steady points A, B and C. From Held (1983).

jet, and vice versa. More locally, the North Atlantic was found to exhibit three preferred and persistent meridional locations of the jet, and a number of studies have attributed this to the persistence of different dominant types of wave breaking (e.g. Franzke *et al.*, 2004; Woollings *et al.*, 2008; Woollings *et al.*, 2010). A preferred sequence of transitions between these jet locations has been observed by Franzke *et al.* (2011), from south to middle, middle to north and north to south. Similarly, in the North Pacific and in the Southern Hemisphere the upper-level jets display a latitudinal migration of the associated eddy-driven jets, but with only two preferred locations corresponding to whether or not the eddy-driven jet merges with the subtropical one (Woollings *et al.*, 2010; Lee and Kim, 2003). The reason for the three North Atlantic positions and their apparently cycling transitions is not fully understood.

Such observations of preferred locations of the eddy-driven jet may be suggestive of the existence of multiple equilibrium states, or regimes, in the atmosphere. An example of a theoretical study of multiple atmospheric states is that of Charney and DeVore (1979), who use a simplified model to simulate a response to orographically damped Rossby waves. The solution based on a single meridional mode is shown in figure 2.17, where the two terms which contribute to the zonal mean wind acceleration are plotted with increasing zonal wind. Where the two terms meet, there is no acceleration to the zonal mean wind, so there are three steady-state solutions: A, B, and C.

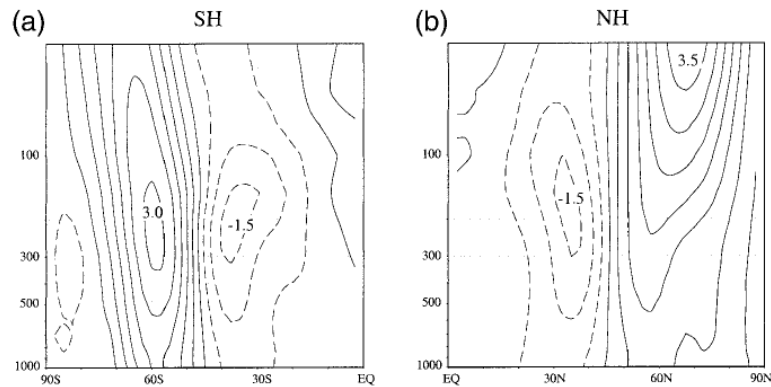


**Figure 2.18:** Zonal-mean geostrophic wind regressed on the standardised indices of the hemispheric annular modes for a) the Southern Hemisphere and b) the Northern Hemisphere, based on monthly data between January 1958 and December 1997. The vertical coordinate is in hPa and the contour interval is  $0.5\text{ m s}^{-1}$ . From Thompson and Wallace (2000). ©American Meteorological Society. Used with permission.

It is evident visually from the figure that solution B is unstable, whereas solutions A and C are stable. The two stable states were attributed to a low index (characterised by undulating flow and blocking) and a high zonal index (characterised by a more zonal flow).

Increasing the number of meridional modes in Charney and DeVore's (1979) model would produce additional structures characterised by oscillating solutions that are comparable to the observed patterns of the leading orthogonal modes of zonal-mean atmospheric variability (Holton, 2004), referred to as annular modes. Thompson and Wallace (1998) observed such annular modes in both hemispheres, using the principal component analysis (PCA) on geopotential height anomalies, with oppositely signed anomalies between the polar cap region and the mid-latitude ring surrounding it (figure 2.18). The barotropic oscillations in the Southern Hemisphere had been observed previously (Kidston, 1988), but their presence in the more zonally asymmetric Northern Hemisphere had not. The authors called the latter pattern the Arctic Oscillation. These results would suggest a hemispheric-wide pattern, and that the locally defined dominant modes of variability (or teleconnections), namely the North Atlantic Oscillation (NAO) and Pacific Northern Anomaly (PNA), are in fact strongly linked. However, Ambaum *et al.* (2001) argue that the Arctic Oscillation is in effect an artefact of the PCA analysis used to define it, and they show that the subpolar centres of action in the North Atlantic and the North Pacific are not significantly correlated. Cash *et al.* (2005) further demonstrate that zonal-mean anomalies tend to be determined by zonally localised bursts of storm track activity, rather than a zonally symmetric forcing. The latter two studies therefore imply that shifts in the eddy-driven jets in the Northern Hemisphere may be a local feature which is not systematically dependent on the changes outside of their regions of

origin.

In terms of the North Atlantic storm track, while it is indisputable that forcings from the western and other boundaries of the North Atlantic domain will affect the lower-frequency variability of the flow in the North Atlantic (e.g. Rivière and Orlandi, 2007; Drouard *et al.*, 2013; Drouard *et al.*, 2015), none of the above external forcings seem to exhibit a periodicity which could robustly explain the preferred cycling of the North Atlantic jet locations (which are related to the NAO). A more likely candidate behind such variability in the North Atlantic (and equivalently in the North Pacific), are the synoptic transients. The previous sections have already outlined some theoretical work on the ability of transient baroclinic eddies directly to induce lower-frequency variability of the associated eddy-driven jets. Observational studies agree with this finding. For example, Lorenz and Hartmann's (2003) lag regression study shows that transient eddy forcing leads the response of the mean flow by several days in the Northern Hemisphere, with both very low-frequency eddies and transient eddies acting to reinforce the zonal wind anomalies. The former dominate in the Northern Hemisphere and with intermediate frequency eddies (external barotropic Rossby waves) opposing this effect. It is noteworthy that the second mode of variability, which is associated with jet pulsing, did not involve such a feedback from transient eddies.

A number of studies suggest that synoptic transient eddies can also increase the persistence of zonal mean anomalies (e.g. Feldstein and Lee, 1998; Robinson, 2000). It was also noted by Hoskins (1983) that as blocking is established, a positive feedback occurs whereby the block itself tilts and stretches the disturbances. Moreover, Benedict *et al.* (2004) observed that cumulative wave breaking of synoptic waves induces and maintains changes in the NAO, agreeing with similar observations of Woollings *et al.* (2008) and Franzke *et al.* (2011). Furthermore, Athanasiadis and Ambaum (2010) found that although the low-frequency NAO variability is mainly due to the mean advection of PV (rather than a transient-eddy forcing), some events can be dominated by synoptic eddy activity.

Thus transient eddies seem to be crucial in understanding high- and mid- frequency feedbacks on the variability and persistence of the mean flow. It is of interest to explore whether these feedbacks are associated with a (most likely internally driven) cyclical variability of the storm track activity and the mean cycling of the preferred locations of the North Atlantic jet.

## 2.8 Conclusion

From the discussion above it is apparent that the transient eddy forcing is a key contributor to the temporal variability of mid-latitude storm tracks and the associated eddy-driven jet. In the Northern Hemisphere, the picture is complicated by the continents introducing stationary wave structures which determine the transient nature and the dominant modes of very-low frequency variability of the North Atlantic or the North Pacific storm tracks. However, transient eddies also play an important part, especially on somewhat shorter timescales. The net effect of these eddies is to mix temperature gradients and barotropise the jet. This is associated with the release of meridional heat and momentum fluxes, the latter being associated with Rossby wave breaking and modulation of the jet latitude. The steady-state spatial structure of storm tracks is relatively well known, and can be viewed as a superposition of the evolution lifecycles of multiple downstream-propagating storms. However, it is the temporal variability that is of interest in this thesis.

The storm track variability is influenced by many external factors. These include changes to the thermal structure of the Hadley cell, exciting external Rossby wave trains, vorticity advection from outside of the domain, lower stratospheric modulation, and the modulation of the low-level tropospheric polar flow due to a stratospheric vortex spin up. However, there is some expectation from theoretical arguments and observational evidence that storm tracks also exhibit an internal periodic variability, though the mechanism behind it is not fully understood. This will be addressed in Chapter 3.

Variability of the associated eddy-driven jets further downstream of the storm track maxima is partially related to the times when the eddy-driven jet is merged with the subtropical jet. However, the North Atlantic has three preferred positions, the reason for which is not yet fully explained. Chapter 4 investigates this issue further.

Chapter 5 unifies the oscillatory behaviour of storm track activity and that of the eddy-driven jet using a three-dimensional energetics approach using observations and a simple dry dynamical-core GCM. The results imply that the spatial and temporal internally-driven cycling found in the previous two chapters for the North Atlantic is a general feature of all zonally confined storm tracks. Such cycling can be viewed as the spatio-temporal lifecycle of the storm track.

## Chapter 3

# Storm Track Activity and Its Nonlinear Oscillations

*The work in this chapter was split into two publications. The nonlinear-oscillator model was first introduced by Ambaum and Novak (2014), and the examination of the detailed properties of the observed oscillatory behaviour and their agreement with the nonlinear oscillator model is planned to be published in Novak et al. (in review). Although the heuristic idea of the oscillatory (predator-prey) relationship was developed collaboratively between the author and her supervisors, the precise initial formulation of the nonlinear oscillator model was developed by the author's supervisor. The analysis of its properties and its comparison to the observed data was conducted by the author. The investigation using the idealised PUMA model was conducted as part of an MSc project the author co-supervised; only the preliminary results performed by the author are included in this thesis.*

## 3.1 Introduction

In the time-mean picture both baroclinicity and storm track activity are almost collocated with the areas of intensified meridional temperature gradients (Hoskins and Valdes, 1990). One may expect this, as baroclinicity can be measured by the sharpness of these gradients which are related to the available potential energy for eddies to grow. Baroclinicity is therefore a measure of the growth rate of storm track activity, explaining the partial spatial correlation of the two quantities in the time-mean (though there is a slight spatial offset since eddies move downstream as they develop and reach their maximum amplitude). Conversely, it is also known that as eddies increase in intensity, they mix the temperature down-gradient and thus reduce the baroclinicity, an idea which has led to low-order parametrisations of eddy heat fluxes (a measure of storm track activity) as

eddy diffusion (e.g. Griffies, 1998; Barry *et al.*, 2002), the latter being proportional to the negative temperature gradient (a measure of baroclinicity). Evidently, these two seemingly contradictory relationships between baroclinicity and storm track activity cannot hold simultaneously without some mutual interaction keeping them in balance.

There is substantial evidence that oscillations between the mean flow and the associated eddies exist in the governing equations of simplified atmospheric systems. It is evident that the traditional linear theory becomes insufficient as it assumes a constant mean vertical shear and produces an indefinitely exponential growth of eddies. The nonlinear interactions between the eddies and mean flow therefore need to be included. A common and successful technique is to simplify the atmospheric system to two layers with the associated perturbations being approximated by one or more dominant normal modes. For example, using a two-layer QG model with a small departure from the critical shear (beyond which instability occurs) and an asymptotic expansion of the perturbation therein, Pedlosky (1970) was able to study a weak nonlinear interaction between the mean flow and the primary wave for an inviscid case. This nonlinearity was shown to yield an oscillation of the perturbation amplitude due to it alternately changing the sign of the phase shift (i.e. reducing and increasing the overall wind shear) and thus alternately making the system too stable and too unstable, oscillating reversibly around a state of neutrality. Because this behaviour arises from the inertial properties of the interaction of the mean flow and the primary wave alone, these oscillations do not require any forcing or interacting harmonics to maintain them. However, it should be noted that Pedlosky (1982a) has found that for situations at the minimum critical shear the oscillatory behaviour is in fact more complex due to non-negligible resonant behaviour which makes the single-mode theory less applicable. Nevertheless, beyond the minimum critical shear, the resonant behaviour is less pronounced and the single-mode theory provides a good example of the mutual interaction between perturbations and the mean flow.

Thompson (1987) also used the two-layer model and found an oscillation between the mean flow and the primary wave in a truncated five-dimensional closed equation system. However, in this case the period of these oscillations was found to be directly proportional to the ratio between the square roots of heating and friction (Thompson, 1988), implying that those diabatic processes are essential for the existence of these oscillations. Realistic values of this diabatic forcing yielded a period of approximately 23 days. Similar oscillations in the two-layer model were recovered by Lorenz (1963b), who used a less severe truncation of the orthogonal functions of the model

variables to produce a 14-dimensional system. It was additionally found by the latter author that transitions of the system into different more stable or more chaotic regimes were possible, depending on the scale of the eddies and the magnitude of the imposed diabatic forcing. Smaller eddies and larger heating led to a less stable system and eventually chaos. Fleming (2014) found a similar result for Thompson's (1987) model, while observing that when chaos is approached the baroclinic instability is stronger and more explosive.

In the light of the theories above, it is apparent that some periodic or non-periodic temporal interaction between the mean flow and the eddies is expected in the atmosphere. Although laboratory experiments can replicate some of the predicted oscillatory behaviour above (e.g. Hide, 1953; Hide, 1958; Hart, 1972), the baroclinic behaviour of the atmosphere is often deemed to be too irregular and more characteristic of non-periodic chaotic behaviour (e.g. Lorenz, 1963a). Nevertheless, the present chapter will show some observational evidence and suggest a coherent mutual interaction between storm track activity and baroclinicity on various timescales. These results complement those of Thompson and Woodworth (2014) and Thompson and Li (2015) who independently studied the same relationship diagnosed using EOF analysis.

Since this forms a part of this thesis, the results will be discussed in more detail later. At this point it suffices to say that these studies heuristically indicate that a predator-prey type relationship exists between baroclinicity (prey) and heat flux (predator), where the build up of baroclinicity due to a stationary diabatic forcing (e.g. meridional insolation gradient, land-sea contrast, orography and ocean boundary currents) encourages eddy growth until eddies become so intense that they start mixing the temperature down-gradient (and therefore reducing baroclinicity) overriding the effect of the diabatic forcing. Once the baroclinicity is low enough to inhibit any further eddy generation, the storm track activity falls and allows the diabatic forcing to replenish the baroclinicity again and the cycle repeats.

These heuristic arguments are the basis of an idealised two-dimensional nonlinear oscillator model of storm track activity and baroclinicity variability developed as part of this thesis. This model is presented in section 3.2. Although the model is initially based on heuristic arguments, links are made with existing models (namely Thompson's (1987) and Lorenz's (1984) models) that can be truncated from the governing equations. The nonlinear oscillator model is a two-dimensional dynamical system and therefore lacks the potential to become chaotic (Hirsch and

Smale, 1974), which makes it an attractive system to investigate further. Its oscillatory properties are thus outlined in section 3.3, which includes the study of the model phase space (i.e. on the baroclinicity-storm track activity plane).

The model and its oscillatory properties are then compared to observed storm tracks. Section 3.4 discusses the datasets used in this study and section 3.5 outlines the method of constructing a filtered phase space plot from noisy observations. Section 3.6 investigates the existence of the predator-prey relationship between heat flux and baroclinicity within the North Atlantic storm track, and tests the agreement with the nonlinear oscillator model. Section 3.7 then investigates whether this agreement exists for the North Pacific storm track and for other measures of storm track activity. Preliminary results showing the existence of this oscillatory behaviour in an idealised dry-core global circulation model are also presented. The remaining section summarises the results and discusses the general implications for studying localised storm tracks.

## 3.2 Nonlinear Oscillator Model

As mentioned in Chapter 1, baroclinicity represents the effect of static stability and meridional temperature gradients. It can be shown that at the beginning of the storm track the variability of the temperature gradients dominates the static stability at the vertical level of interest (Hoskins and Valdes, 1990; also confirmed as part of the work for the next chapter). Baroclinicity can therefore be assumed to be directly proportional to the meridional temperature gradient:

$$s = -k \frac{dT}{dy}, \quad (3.1)$$

where  $k$  is a constant, and would be  $k = 0.31g/(NT_0)$  if  $s$  represented the maximum Eady growth rate (equation 2.5). The generation of baroclinicity by the mean-flow advection and diabatic forcing, including boundary currents, topography or the land-sea contrast (e.g. Brayshaw *et al.*, 2009), is parametrised as a constant forcing,  $F$ . The constancy of this forcing is a rather crude assumption, and its implications will be discussed later. Baroclinicity reduction is assumed to be primarily caused by baroclinic eddies due to their eroding effect of the temperature gradients.

The evolution equation of baroclinicity according to these arguments is thus:

$$\frac{ds}{dt} = F + k \frac{d^2 \overline{v'T'}}{dy^2} = F - f, \quad (3.2)$$

with the heat flux being scaled as  $f = kl^2 \overline{v'T'}$  which is proportional to the squared eddy amplitude. The meridional extent of the heat flux is dominated by a meridional wavenumber,  $l$ . The evolution of the scaled heat flux is justified using the definition of baroclinicity as the growth rate of the amplitude, giving:

$$\frac{df}{dt} = 2(s - s_0)f, \quad (3.3)$$

where  $s_0$  represents a constant eddy dissipation rate. Equations 3.2 and 3.3 therefore represent a closed two-dimensional system that describes nonlinear oscillations in  $f$  and  $s$ , as will be shown more explicitly in the next section.

Since this nonlinear oscillator model was initially constructed based on heuristic arguments, it would be more satisfactory to show its relation to first principles. Attempts using the normal mode analysis to justify this system have been made, and an example is shown in the Appendix B. This example shows that the nonlinear oscillator model can be derived using the normal-mode theory but only for a locally restricted domain. Similarly, it can be shown that this model can be obtained by truncating Thompson's (1987) model, which is also based on a local domain restricted to the area of maximum storm track intensity (Appendix C). Alternatively, this relationship may be obtained by simplification of the Lorenz-84 model (Appendix D).

It is noted that although the focus here is on storm track dynamics, the time mean of the nonlinear oscillator model can also be applied to the oceanic setting to explain a phenomenon called "eddy saturation" which was observed to occur in the Antarctic Circumpolar Current. Preliminary results on this aspect of work are discussed in Appendix J.

### 3.3 Properties of the Nonlinear Oscillator Model

A useful transformation of  $f$  as

$$y = \ln(f/F) \quad (3.4)$$

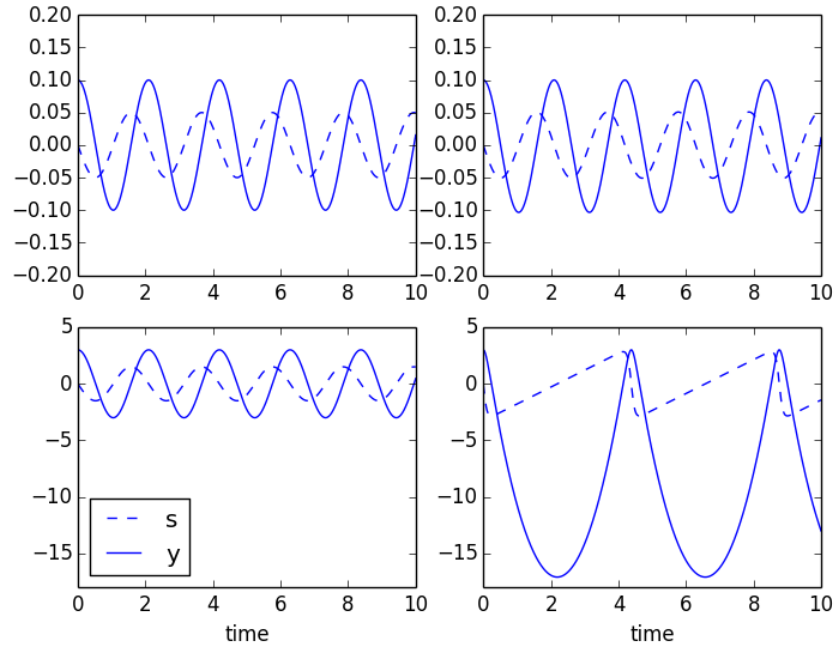


**Figure 3.1:** Numerical integration of the nondimensional linear oscillator (left) and the nonlinear oscillator (right), for amplitudes of 0.1 (top) and 3 (bottom). The time step is  $3 \times 10^{-4}$ , and the diabatic forcing is  $F = 0.5$ .

allows equations 3.2 and 3.3 to be written as:

$$\frac{dy}{dt} = 2(s - s_0), \quad (3.5)$$

$$\frac{ds}{dt} = F(1 - e^y), \quad (3.6)$$

which can be combined to form

$$\frac{d^2y}{dt^2} = 2F(1 - e^y). \quad (3.7)$$

This dynamical system is a nonlinear oscillator, which becomes linear at small amplitudes of  $y$ . The system linearises to  $d^2y/dt^2 = -2Fy$ , so that the natural frequency is  $\omega_0 = \sqrt{2F}$ . The intensity of the diabatic forcing would therefore determine the period of oscillation. At higher amplitudes, it is apparent that the nonlinear terms can no longer be neglected. The equation set can be simplified using a successive approximation method (Landau and Lifshitz, 1976) that

yields a correction to the natural frequency, which for a second order approximation is:

$$\omega = \omega_0 - \frac{1}{24}\omega_0 y_{\max}^2, \quad (3.8)$$

where  $y_{\max}$  is the amplitude of oscillations of the transformed heat flux. It is therefore expected that the time period of oscillation increases with amplitude of heat flux events due to the nonlinearity.

This effect of the nonlinearity is depicted in figure 3.1, where the model has been integrated for different amplitudes and compared to the linear harmonic oscillator (corresponding to approximating  $e^y \approx 1 + y$  in equation 3.7). It is apparent that the symmetry and frequency of the nonlinear oscillator change dramatically with increasing amplitude. The heat flux peaks become much more pronounced, more abrupt and less frequent, whereas in the linear case the shape and frequency are retained, with only the amplitude increasing. Furthermore, the baroclinicity in the nonlinear oscillator falls abruptly but recovers relatively slowly, whereas the symmetry is retained in the linear oscillator.

Another property of the nonlinear oscillator is that the amplitude of the perturbations is constant with time, as is evidenced by the zero time derivative of the Liapunov function:

$$E = \frac{1}{2}y^2 + V(y), \quad (3.9)$$

where  $dE/dt = 0$ , and  $V(y) = 2F(e^y - y - 1)$  is the potential of the system (using  $\dot{y} = -dV/dy$ ), so the system oscillates around its equilibria along limit cycles.

A further insight into this cycling behaviour can be gained by studying the phase space of the baroclinicity and heat flux. A phase space plot displays baroclinicity plotted against heat flux, using multiple timeseries obtained from equations 3.2 and 3.3 for multiple different amplitudes (i.e. different values of  $E$ ). A baroclinicity-heat flux phase space plot for the two non-dimensionalised variables is shown in figure 3.2a, with time running in the clockwise direction. The aforementioned predator-prey relationship emerges whereby baroclinicity increases at times of low heat flux and the subsequent bursts in the heat flux erode the baroclinicity to values at which the heat flux production is inhibited. The low heat flux then allows the baroclinicity to be replenished again. The aforementioned spiky nature of the heat flux is evident from the skewness of the con-

tours of high amplitudes (similar to Fleming, 2014). The thickness of the contours indicates the speed of propagation along the trajectories, and it shows that the speed of oscillation is faster for higher amplitude events, despite the longer time periods that were deduced in the previous section.

As per equation 3.4, this value of  $F$  is used to compute the transformed heat flux,  $y$ , which produces the phase space plot in figure 3.2b. The transformation is necessary as it is the  $y$  variable that allows the mathematical description of the system as an oscillator. It is this phase space that will be later used to study the quantitative oscillatory properties of the system, relative to the behaviour of the same variables in the ERA-Interim data. Due to the logarithm in its definition (equation 3.4), the negative part of the phase plot is stretched, and the central trajectories are almost circular, similar to those of a linear oscillator, agreeing with the analytical arguments above. The trajectories then become more skewed and variable in the speed of propagation as the amplitude of oscillations increases and the system becomes more nonlinear.

The nonlinear oscillator model predicts several properties of storm track activity and baroclinicity, which can be summarised as:

1. a spiky nature of the heat flux and a slow recovery of the baroclinicity, implying two timescales;
2. a clockwise oscillation in the baroclinicity-heat flux phase space which becomes more skewed with amplitude;
3. at small amplitudes the system becomes linear (with a given natural frequency proportional to the mean diabatic forcing);
4. a decrease of frequency with amplitude in a quadratic fashion; and
5. an increase of speed of the onset and termination of heat flux events with an increasing amplitude.

These predicted properties will be tested against the atmospheric observations in the sections below, by analysing the composited time series of heat flux and baroclinicity centred around the highest peaks of heat flux, and by exploring the baroclinicity-heat flux phase space.

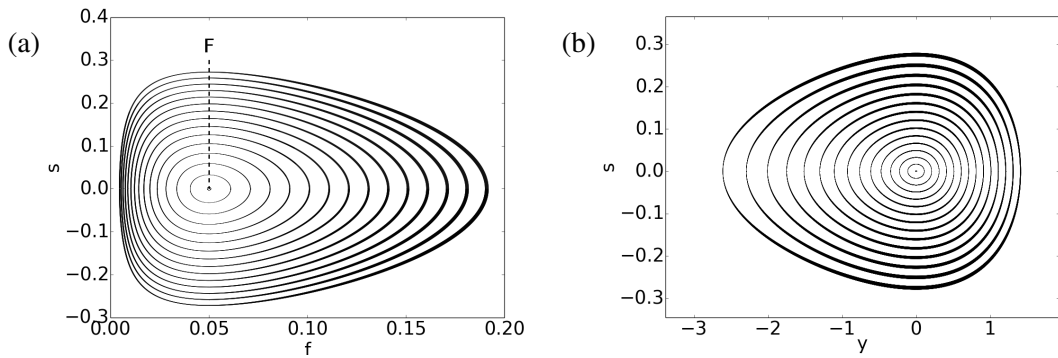


**Figure 3.2:** Phase plots for the numerically integrated nonlinear oscillator model for a) the instantaneous heat flux,  $f$ , and b) the corresponding transformed heat flux,  $y = \ln(f/F)$ , where  $F$  is the diabatic forcing and  $s$  is the baroclinicity. The system was scaled to be non-dimensional and parametrised using  $F = 0.05$  and  $s_0 = 0$ . The line thickness marks the speed of the oscillations, defined as  $\sqrt{s^2 + y^2}$ .

### 3.4 Datasets

The following two sections diagnose the existence of the oscillatory relationship between storm track activity and baroclinicity in the winter storm track of the North Atlantic, the North Pacific and a simplified aquaplanet GCM, and this section outlines some of the details of the data used.

Unless otherwise stated, the observations of the real atmosphere are based on the 6-hourly December-January (DJF) ERA-Interim reanalysis (Uppala *et al.*, 2005) produced by the European Centre for Medium-range Weather Forecasts. The default measure of storm track activity is the instantaneous meridional eddy heat flux ( $v'T'$ ), vertically averaged between 925 and 700 hPa and based on the 10-day Lanczos filter. Note that the Lanczos time filter (instead of zonal mean) has been used to compute the perturbations, since the focus of this study is on transient synoptic eddies. Although formally applying this technique would introduce additional terms in the equations that were used to justify the nonlinear oscillator model, it will be shown below that the time-filtered fluxes still behave in accordance with the zonal-mean ones predicted by the model. The baroclinicity is measured by the maximum Eady growth rate ( $s = 0.31f_0N^{-1}dU/dZ$ ) at 775 hPa, as per Hoskins and Valdes (1990).

To produce one-dimensional time series of each variable, spatial averaging over the beginning of the storm track was applied. In the North Atlantic the averaging sector spans between 35 - 50°N and 290 - 320°E for  $v'T'$ , and 30 - 50°N and 270 - 320°E for  $s$ . In these regions the

respective variables exhibit their maxima (figure 3.3), the latitude of which is fairly constant in time (as will be shown in the next chapter). In the North Atlantic, other measures of storm track activity have also been tested. These are eddy kinetic energy ( $1/2(u'^2 + v'^2)$ ) at 250 hPa and 850 hPa, meridional wind variance ( $v'^2$ ) at 250 hPa, potential vorticity variance ( $PV'^2$ ) at 315 K, geopotential height variance ( $Z'^2$ ) at 250 hPa and 500 hPa, and the mean sea-level pressure variance ( $MSLP'^2$ ). The same or similar averaging regions to that of the heat flux have been tested. For example, eddy kinetic energy at 250 hPa, which is discussed in more detail below, was averaged between 40-55°N and 290-330°E.

Figure 3.3 also shows the averaging sectors in the North Pacific, which for the lower-level meridional heat flux is 30 - 50°N and 150 - 195°E, and for the maximum Eady growth rate it is 25 - 45°N and 120-170°E. Note the larger spatial separation between the maxima of baroclinicity and heat flux in the North Pacific compared to those in the North Atlantic.

The Portable University Model of Atmosphere (PUMA, available from the Meteorological Institute of Hamburg University) was also used here to test whether the predator-prey relationship also occurs in simpler idealised settings. The model is the dry dynamical core of Hoskins and Simmons's (1975) spectral global circulation model, and it is set to be an aquaplanet (i.e. without orography) with a single localised storm track. This storm track is produced by imposing a heating dipole in the mid-latitudes. More details of the setup can be found in Appendix A. Because of the idealised setting of having one localised storm track, the storm track can be represented by eddy quantities defined as departures from the zonal mean. This would not be possible in the Northern Hemisphere, where the North Atlantic and North Pacific storm tracks would interfere with each other. Using PUMA therefore not only enables the examination of whether the predator-prey relationship applies to a model of medium-complexity, but also to use this zonal-mean averaging, which is what the theoretical framework of the nonlinear oscillator is based on. The daily data of the 24 winters of the low-level (vertically averaged between 925 and 700 hPa) zonal mean-based heat flux,  $[v^*T^*]$ , and the zonal-mean maximum Eady growth rate (at 775 hPa) are therefore used. Both fields are also spatially averaged between 20 and 80 °N. A wider averaging sector was used here as the idealised storm track appeared to be more transient than in the reanalysis data.

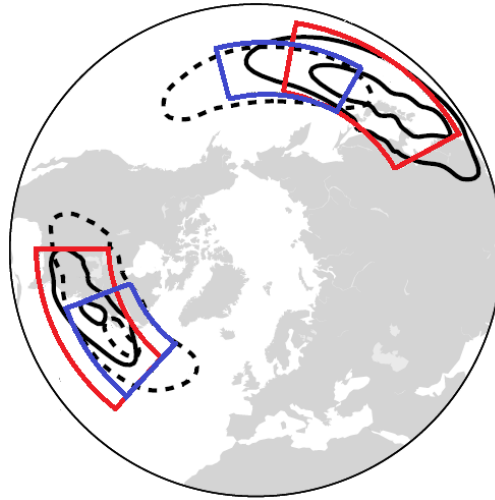


**Figure 3.3:** Time-mean DJF plots of heat flux (dashed black, displaying 10 and 20 K m s<sup>-1</sup>) and baroclinicity (solid black, displaying 0.5 and 0.6 day<sup>-1</sup>) calculated from the ERA-40 data. The averaging sectors for heat flux (blue) and baroclinicity (red) are also shown. Adapted from Ambaum and Novak (2014).

### 3.5 Construction of Phase Plots from Data

The next section analyses the phase space of the observed baroclinicity and heat flux time series, in order to help visualise the oscillatory behaviour of the reanalysis data and facilitate the comparison to the model described above. This section outlines the method employed to construct an averaged phase space plot from the relatively noisy time series of the observed data.

First, the system was scaled to its natural coordinates,

$$\frac{d\sigma}{d\tau} = 1 - e^y, \quad (3.10)$$

$$\frac{dy}{d\tau} = \sigma, \quad (3.11)$$

where  $\sigma = 2s/\sqrt{2F}$  is the scaled nondimensional baroclinicity and  $\tau = \sqrt{2F}t$  is the nondimensional time. The  $s_0$  offset can be absorbed into  $\sigma$ , so that the system oscillates around zero excess baroclinicity. The diabatic forcing is  $F = ck l^2 \langle v'T' \rangle$ , where the angle brackets denote a long time mean, and  $kl^2$  is a constant (the precise value of which will be discussed later).  $c$  is an empirically determined constant which adjusts  $F$ , so that the latter corresponds to the value  $f$  of the central point of the phase plot (i.e. if the  $f$  was Gaussian then  $F = kl^2 \langle v'T' \rangle$  and  $c = 1$ ).  $F/(kl^2)$  was therefore taken to be the central value of the untransformed heat flux-baroclinicity phase space.

Next the tendencies (change in time or phase space vectors) of each variable were obtained using the centred-difference method. These were then averaged for a  $30 \times 30$  grid, using two-dimensional Gaussian kernel averaging in the phase space (i.e. the closest points of each grid point were allocated the highest weights when averaging the tendencies). The coarseness of this averaging can be quantified by the standard deviation of the filtering kernel. Different standard deviations of this filter were tested. Using the resulting tendency vectors of each grid point, streamlines were plotted to construct the phase space plot, while ignoring the grid boxes that only contained 2 data points or less. The steps of this method are depicted in figure 3.4.

### 3.6 The Nonlinear Oscillator in the North Atlantic Storm Track

This section analyses the properties of the predator-prey relationship between the storm track activity and baroclinicity within the North Atlantic.

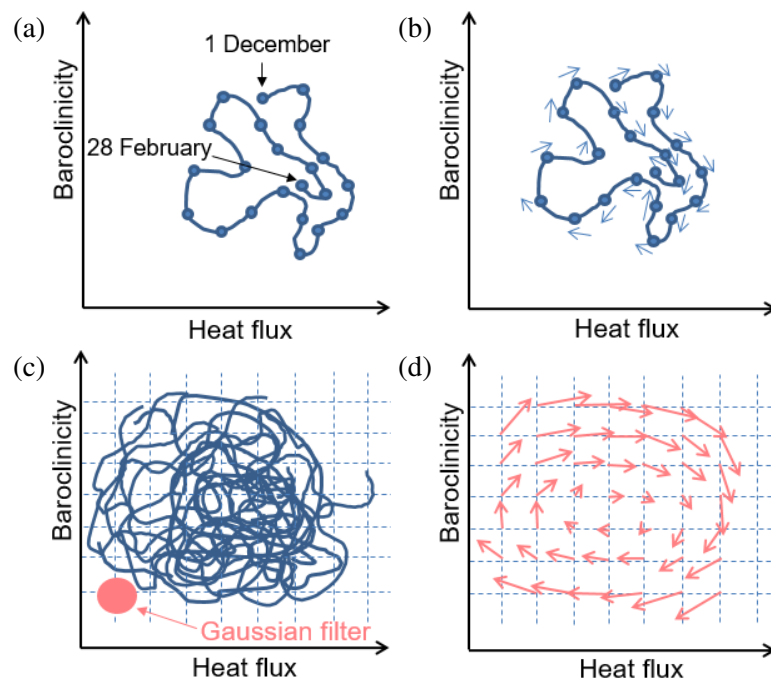


**Figure 3.4:** Schematic explaining the construction of the phase plot for the noisy observed data. The steps are to a) extract each DJF time series of baroclinicity and heat flux; b) calculate the tendencies in both variables, obtaining a vector in the phase space for each point of each time series; c) divide the phase space into a grid and apply a weighted Gaussian average to the phase space to obtain mean tendency vectors of all time series in the dataset; and d) use the averaged tendency field to plot stream lines.

### 3.6.1 Composite Heat Flux Events

The raw winter time series of the heat flux (examples shown in figure 3.5) contain several high spikes in each winter, as is confirmed by the analysis of Swanson and Pierrehumbert (1997) and Messori and Czaja (2013). In order to extract the average behaviour of baroclinicity around these spikes, the highest events (higher than  $30 \text{ K m s}^{-1}$ ) of the 35-winter ERA-I time series were composited with the 8-day window surrounding them in figure 3.6, where it is compared to the model solution for a reasonably high amplitude. A similarity is apparent between the two plots during the main event, with baroclinicity increasing preceding the event, dipping substantially during it and recovering afterwards. The data do not exhibit a coherent periodic oscillation of the two variables at larger lags, indicating that many different timescales are involved (as will be explored below) and that the behaviour is more quasi-periodic. Additionally, the saw-tooth pattern of baroclinicity is less apparent in the data due to the rapid (though only partial) recovery in the baroclinicity, suggesting that the recovery occurs at multiple timescales and probably due to different processes (discussed below). Nevertheless, these results suggest that the predator-prey relationship exists for the baroclinicity and heat flux, warranting further investigation.

### 3.6.2 Phase Space: Qualitative Comparison with the Model

Examples of the North Atlantic phase space plots are shown in figure 3.7, where the black arrows are the stream lines, their thickness indicates the speed in the nondimensional phase space ( $\sqrt{s^2 + y^2}$ ) and the shading is a two-dimensional histogram, with warmer colours representing a higher data density extracted from the raw time series data of the two variables. The phase space plots for the North Atlantic storm track for fine, medium and coarse (smoothing) filter sizes are shown in figure 3.7a, c and e, respectively. The skewed shape of these phase space plots, as well as the clockwise direction of propagation around a single point, is reminiscent of the phase space plot of the nonlinear oscillator model (figure 3.2a). Additionally, the skew towards high heat flux values reflects the spiky nature of the heat flux in the nonlinear oscillator model as well as in the observations (e.g. Swanson and Pierrehumbert, 1997; Messori and Czaja, 2013). Furthermore it is apparent that the speed of oscillation during the bursts in heat flux activity does increase with amplitude in the North Atlantic, agreeing with the nonlinear oscillator model.

However, there are also some marked differences between the data and the nonlinear oscillator

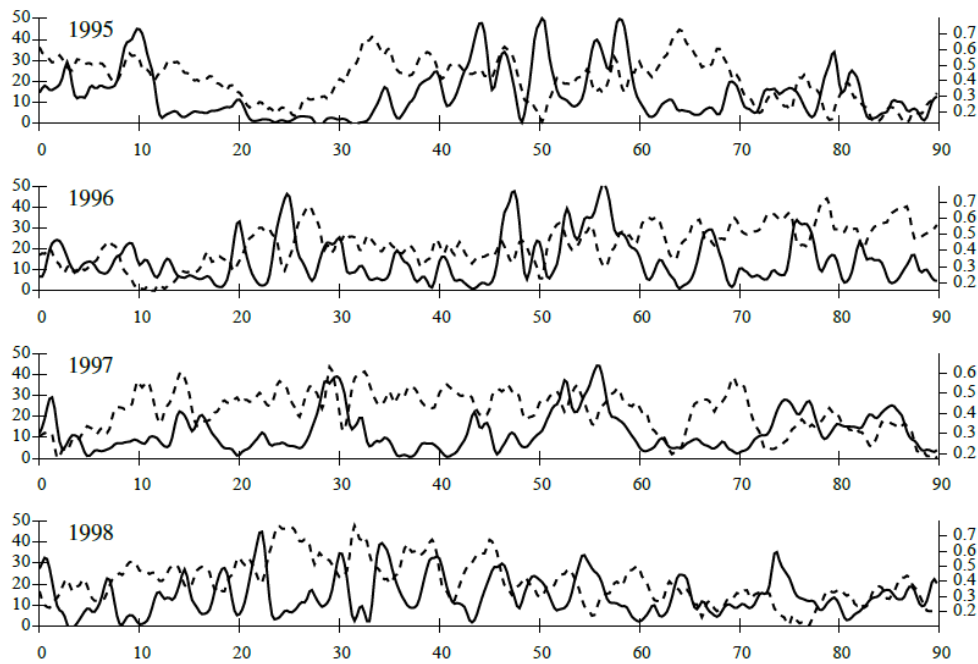


**Figure 3.5:** Timeseries of heat flux (solid, in  $\text{K m s}^{-1}$ , left axis) and baroclinicity (dashed, in  $\text{day}^{-1}$ , right axis) for a random selection of winters, with days from 1 December along the x-axis of the ERA-40 data. The variables were averaged over the upstream storm track region where they peak (figure 3.3). Adapted from Ambaum and Novak (2014).

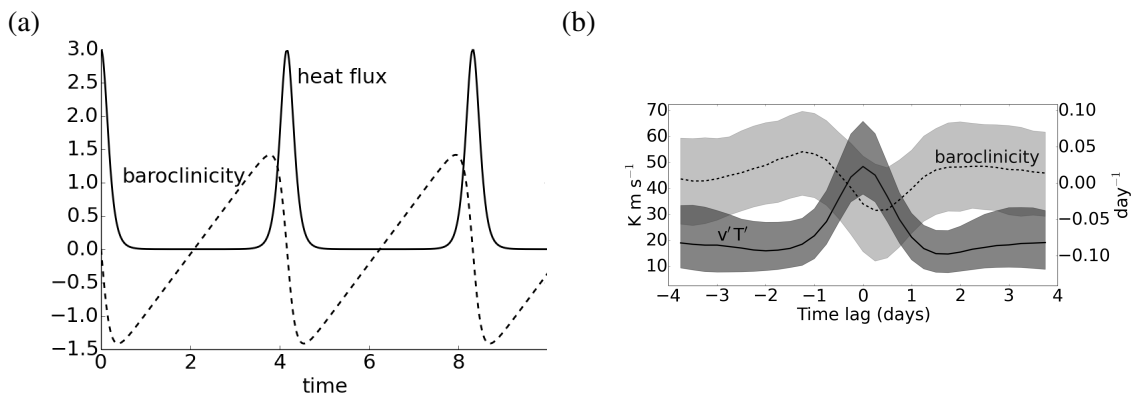


**Figure 3.6:** The heat flux (solid) and baroclinicity (dashed) time series of a) the nonlinear oscillator model numerical integrations (with nondimensional parameters of  $F=0.3$  and a nondimensional time step of 3), and b) the ERA-I median spike centred around the maxima (higher than  $30 \text{ K m s}^{-1}$ ) of the unfiltered heat flux (solid), and baroclinicity (dashed). Baroclinicity is the excess baroclinicity ( $s - s_0$ ) and with the mean offset  $s_0 = 0.57 \text{ rad day}^{-1}$ . A 1-2-1 filter was used to smooth the heat flux peaks. The shading shows the interquartile range.

model. For example, the model does not contain any negative heat flux values and thus its phase plot can be very suppressed near zero for extremely high amplitudes. On the other hand, the reanalysis data show some negative values and less skewness along the heat flux axis, especially for coarser smoothing. Although fine smoothing produces a more consistent general shape of the

observed phase plot compared to the model plot, the former also emerges with more fine-scale structures which are uncharacteristic of the model. It is shown in Appendix E that too little or too much filtering seems to cause a departure from the nonlinear oscillator model, and there is an optimal size of the smoothing filter, which produces desirably consistent results. However, the precise value of the size and shape of the filter is not known a priori.

In order to quantify some of the properties of the North Atlantic phase space plot, the heat flux was transformed into the  $y$  variable, and the corresponding phase space plots equivalent to those discussed above are shown in figure 3.7b, d and f, respectively. It should be noted that the occasional negative values of heat flux were ignored due to the natural logarithm used to transform the heat flux (equation 3.4). The phase space plots exhibit a similar shape to that of the idealised model, though again more structure is apparent for the finest smoothing. The histogram shows that all three cases oscillate around the maxima of the data density of both variables, with the smallest amplitudes exhibiting more regular oscillations. This agrees with the model prediction that smaller amplitude oscillations should be almost linear. The medium coarseness plot will be studied in more detail in the next subsection and its properties will be compared to those of the idealised model more quantitatively.

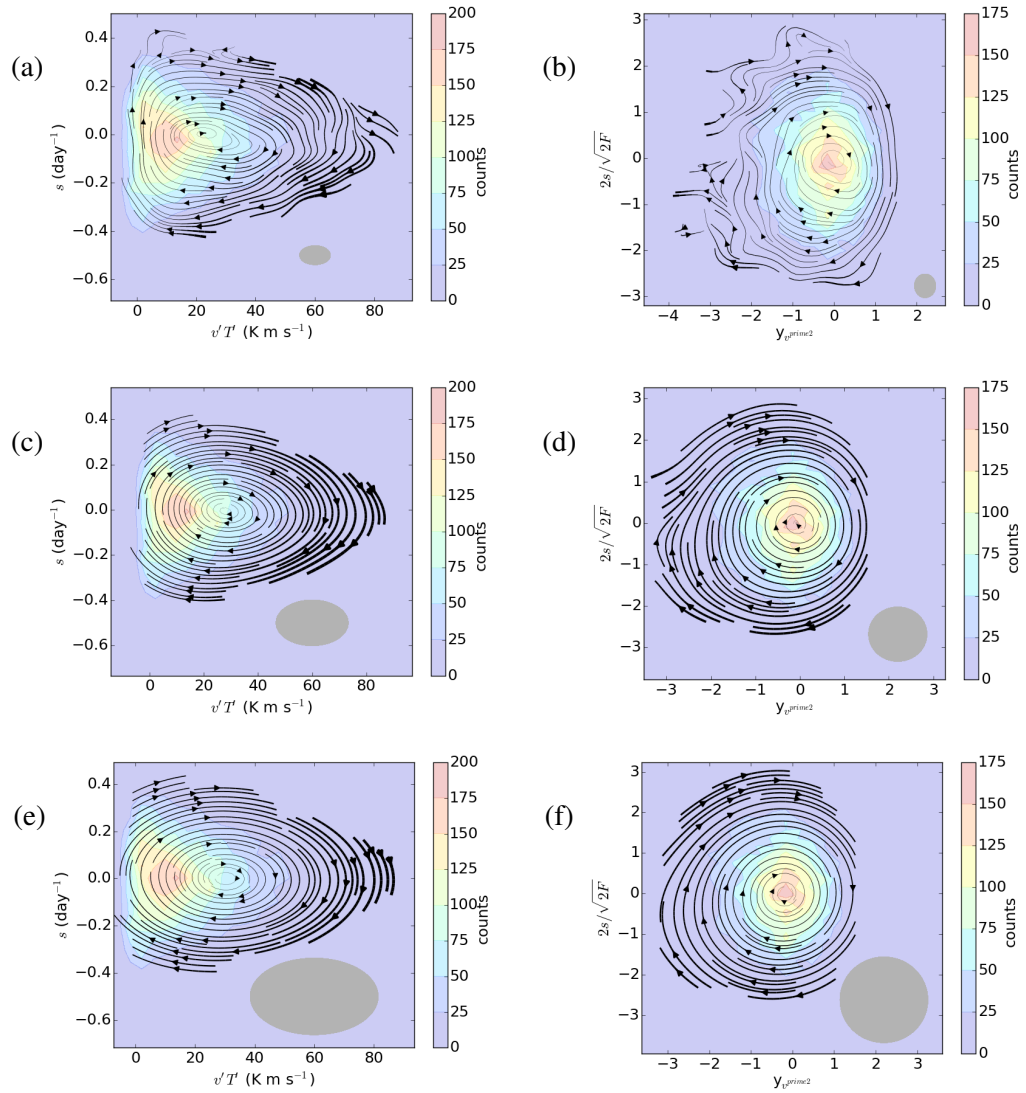


**Figure 3.7:** Phase plots for the observed instantaneous heat flux,  $f = kl^2v'T'$  (a, c, e) and the transformed heat flux,  $y = \ln(f/F)$  (b, d, f), where  $F$  is the diabatic forcing (in this case around  $28 \text{ K m s}^{-1}$ ) and  $s$  is the baroclinicity. Line thickness marks the speed of oscillation and the colours are the 2D histogram. The plots in the first row are averaged using a coarse filter (standard deviation: 1.05), while finer filters have been used for the second and third rows (0.65 and 0.25 respectively). The radii of the grey ellipses mark the standard deviations of the averaging Gaussian kernel in both directions.

### 3.6.3 Phase Space: Quantitative Comparison with the Model

The previous section qualitatively showed that, despite its simplified nature, the idealised non-linear oscillator model can replicate the general features of the reanalysis data. This section concentrates on the case with medium smoothing (with the standard deviation of the smoothing filter being 0.65 units of the scaled phase space) and the scaling factor of  $ckl^2 = 3.1 \times 10^{-13} \text{ K}^{-1} \text{ m}^{-1} \text{ s}^{-1}$ . The choice of these parameters yielded appropriate scaling of the baroclinicity as is discussed in Appendix E. The associated phase plots are shown in figure 3.7c and d.

In order to obtain the frequency of the North Atlantic oscillations for trajectories of different amplitudes, the smoothed (grid point) tendencies were first interpolated across the phase space (using a cubic spline interpolation) and the system was then numerically integrated in time (using the fourth-order Runge-Kutta method) from different starting amplitudes (at  $s=0$ ), until a full cycle was completed. The time period was obtained by summing up the number of the 6-hourly intervals it took for each trajectory to complete a cycle. In most cases the contours were not completely closed, so one cycle was defined as the second crossing of the zero baroclinicity line. The error bars were calculated using the same procedure but starting from different points along the semicircle of each trajectory in the region of positive  $y$  (between the highest and lowest points of baroclinicity). The interquartile range and median of the resulting values were then calculated and displayed in figure 3.8. The exact numerically integrated solution of the idealised model and its second order approximation (computed using equation 3.8) are also shown for comparison. The idealised model was parametrised using  $F$  obtained from the observed frequency of the smallest amplitude (assumed to be approximately equal to the natural frequency) and using  $F = 1/2\omega_0^2$ . The tendency of  $y$  at  $y = 0$  with increasing amplitude was additionally investigated, in order to quantify the speed of the onset and termination of heat flux events of different magnitudes.

Figure 3.8a shows that the frequency of oscillation is almost constant for the smallest amplitudes, approximately marking the natural frequency of the oscillator (which would be constant for all amplitudes if the oscillator was linear). As the amplitude increases further the frequency decreases and drops off sharply after approximately  $y_{\text{MAX}} = 1$ . The pattern of change agrees very well with the idealised model even at high amplitudes. In fact, the agreement is better between the data and the exact model solution than between the exact model solution and its second order approximation. This striking agreement also appears in the plot of the  $y$ -tendency at  $y = 0$ , which

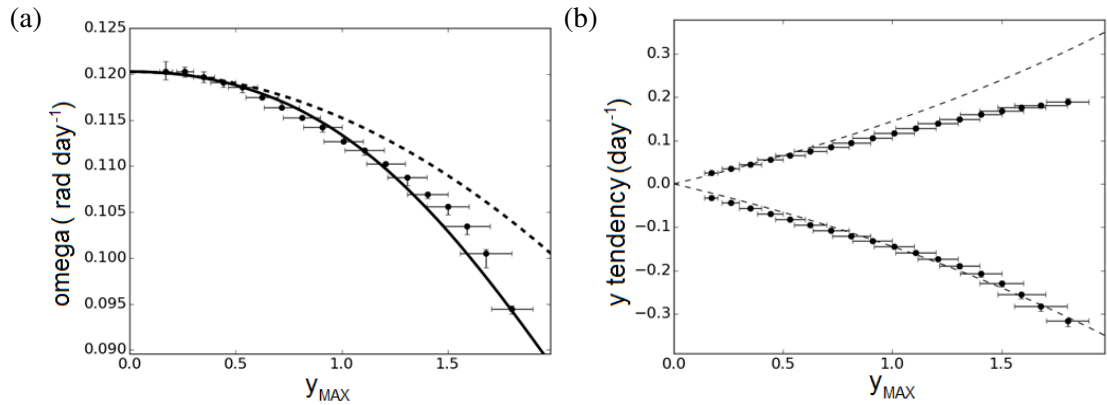


**Figure 3.8:** Change with increasing amplitude in a) the angular frequency ( $\omega$ ) of oscillation around the phase plot for the exact numerical model solution (solid line), the approximated second order model solution (dashed line) and the data (points); and b) the tendency of  $y$  at  $y = 0$  for the model (dashed line) and data (points).

increases in magnitude with increasing amplitude in an almost linear fashion. The agreement is less good for the positive branch of tendencies, most likely because at that point the trajectories had already been through the region of negative  $y$  on the phase space plot, where the values are less certain due to the neglected negative heat flux values mentioned above. However, since the system mostly lies below  $y_{MAX} = 1$  (as a result of the transformation in equation 3.4), it is concluded that the agreement is still very good.

The results above and the discussion in Appendix E imply that there is a preferred (natural) frequency of the system, though the averaging obscures its precise value. Power spectra of baroclinicity and heat flux, calculated using the original winter timeseries, should reveal any purely periodic behaviour of the system. These were constructed using the method of Thompson and Li (2015), by applying the Hanning window to reduce the effect of sampling, with the number of winters representing the number of independent (non-overlapping) spectra. The resultant spectra for baroclinicity and heat flux are displayed in figure 3.9 (thick lines). In order to determine whether the observed variability is significantly different from red noise, red noise timeseries were calculated using the lag-1 autocorrelations to produce red-noise spectra (thin solid lines) fitted to the baroclinicity and heat flux spectra. The 99 % confidence level (dashed lines) was calculated using the chi-squared statistic. Following Thompson and Li (2015), the red noise fit to heat flux is based on high-pass filtered timeseries to remove the dominant low-frequency variability, thus

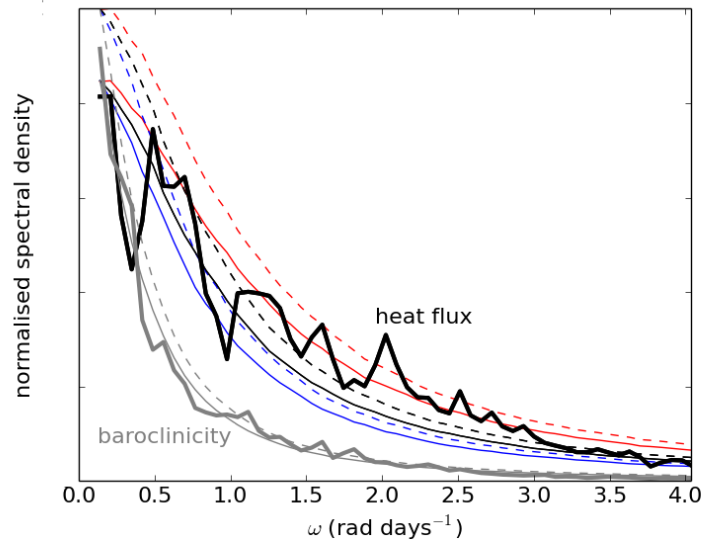


**Figure 3.9:** Power spectrum of the North Atlantic heat flux (thick black) and baroclinicity (thick grey) time series. Thin solid lines represent fitted red noise spectra for baroclinicity (grey), and for heat flux. The heat flux fits based on high-pass filtering using a 20-day window (blue solid), 30-day window (thin black solid) and 40-day window (red solid) were included. The statistical significance is indicated by the 99% confidence level marked by the dashed lines.

enhancing the fit to the observed power spectrum. However, the choice of the filtering window is not unique and the level of significance is sensitive to this choice. Quantitative analysis of the significance is therefore somewhat limited.

Nevertheless, the spectra still contain some useful qualitative information. Heat flux has several higher-frequency peaks that can be interpreted as (conditionally) significant, starting from angular frequency of  $0.5 \text{ rad day}^{-1}$  (corresponding to time period of about 13 days and lower). Baroclinicity does not exhibit such prominent higher frequency peaks. However, both baroclinicity and heat flux spectra do share a low-frequency increase in spectral density between  $0.14$  and  $0.25 \text{ rad day}^{-1}$  (i.e. time period of 25-45 days). Note that the very low frequencies are missing due to the restricted duration of the winter season.

Although this relatively low frequency peak is comparable to the natural frequency values found in the above phase space plots (especially when the fine filtering was applied), the shapes of these power spectra are similar to those of the red noise fits. However, this does not preclude the existence of the low-frequency oscillations or imply that the two timeseries are independent. In

fact, constructing the phase space plots for the two independent red noise timeseries (not shown) does not yield any circulating patterns consistent with the analysis above. The real system is thought to be quasi-periodic rather than purely periodic, in which case sharp peaks in the power spectra are not necessarily expected. However, it will be shown in the next section that the lack of dominance of this lower-frequency spectral peak is associated with a less clear agreement between the observations and the nonlinear oscillator model.

It is additionally noted that very similar spectra (not shown) were recovered for heat flux and baroclinicity independent of Lanczos filtering, for example when using the climatological or zonal mean to define the heat fluxes (not shown). Thus spectral leakage does not seem to be responsible for the lack of significant low-frequency peaks.

One could therefore view the system as being externally forced by essentially random forcings, which would give it features resembling to red noise. This is not characteristic of the nonlinear oscillator model (which assumes a constant forcing). However, the baroclinicity and heat flux still influence each other in accordance with the predator-prey relationship, resulting in quasi-periodic oscillations rather than a purely periodic behaviour. Nevertheless, despite the quasi-periodicity, this section has shown that the purely periodic nonlinear oscillator model still reproduces some of the quantitative behaviour of the real system very well.

### 3.7 Applicability of the Nonlinear Oscillator Model to other Measures and Storm Tracks

In order to investigate whether the above oscillating relationship in the North Atlantic applies to other measures of storm track activity, the identical analysis to the one above was performed for eddy kinetic energy ( $EKE = 1/2(u'^2 + v'^2)$ ) at 250 hPa and 850 hPa, meridional wind variance ( $v'^2$ ) at 250 hPa, potential vorticity variance ( $PV'^2$ ) at 315 K, geopotential height variance ( $Z'^2$ ) at 250 hPa and 500 hPa, and the mean sea-level pressure variance ( $MSLP'^2$ ). Note that, as before, these variables are the “unfiltered variances”, where the products of the perturbations were not averaged (as is the case in traditional covariance calculations). This last step was omitted in order to investigate the instantaneous variability rather than the 10-day filtered signal (the differences between the two are discussed in the next chapter). Because all the above storm track activity

measures yielded similar (or better) results, only the results from the upper-level EKE analysis are presented here.

The baroclinicity- $y_{(EKE)}$  phase space plot is shown in figure 3.10a. Qualitatively, the data concurs with the model; the phase space again exhibits an oscillating behaviour in the clockwise direction, with speed of oscillation increasing with amplitude during the onset and termination of high storminess events. This time however, the trajectories are less regular and are being suppressed in the negative  $y$  territory, where a second attracting node appears. Although the colour shading shows that most data are within the primary oscillation, the quantitative comparison between the data and the model is affected by this secondary node. The frequency change with amplitude (figure 3.10b) is sharper than that of the model and the natural frequency is estimated to be less than half of that estimated from the heat flux in the previous section. Inspecting the associated power spectrum (figure 3.10d) reveals that although there is an increase in spectral density at very low frequency values (between around 0.08 and 0.25 rad days<sup>-1</sup>) as it was in the heat flux case, this increase is no longer dominant. Instead, a larger peak appears around 0.6 rad days<sup>-1</sup>. This higher-frequency peak is also present in the spectral density of the heat flux, but its power is substantially weaker compared to the primary low-frequency peak.

Since the two dominant peaks of the EKE spectrum are where the baroclinicity spectrum is weak, it is not surprising that the phase plot is not as neat as it was in the case of the heat flux. As a result a coarser averaging was applied to filter out the undesired fine scale structure, leading to an underestimation of the natural frequency. The speed of oscillation at  $y = 0$  is simulated relatively well by the nonlinear oscillator model, though at large amplitudes the model departs from the observed error bars, particularly for the negative  $y$  tendencies. Because the trajectories at large amplitudes are more distorted by the secondary node and because they are associated with fewer data points, such discrepancies are not surprising.

It was found that the results improve if the sector used for spatial averaging of EKE is moved to a more upstream location over the region of maximum baroclinicity, rather than being centered over the EKE maximum (which was more downstream than that of the heat flux). Furthermore, if low-level EKE is used, results that are very similar to those obtained when using the heat flux were obtained, with a natural frequency of  $\omega_0 = 0.11$  rad day<sup>-1</sup> (not shown). Similar results apply for the MSLP analysis with  $\omega_0 = 0.13$  rad day<sup>-1</sup> (not shown).

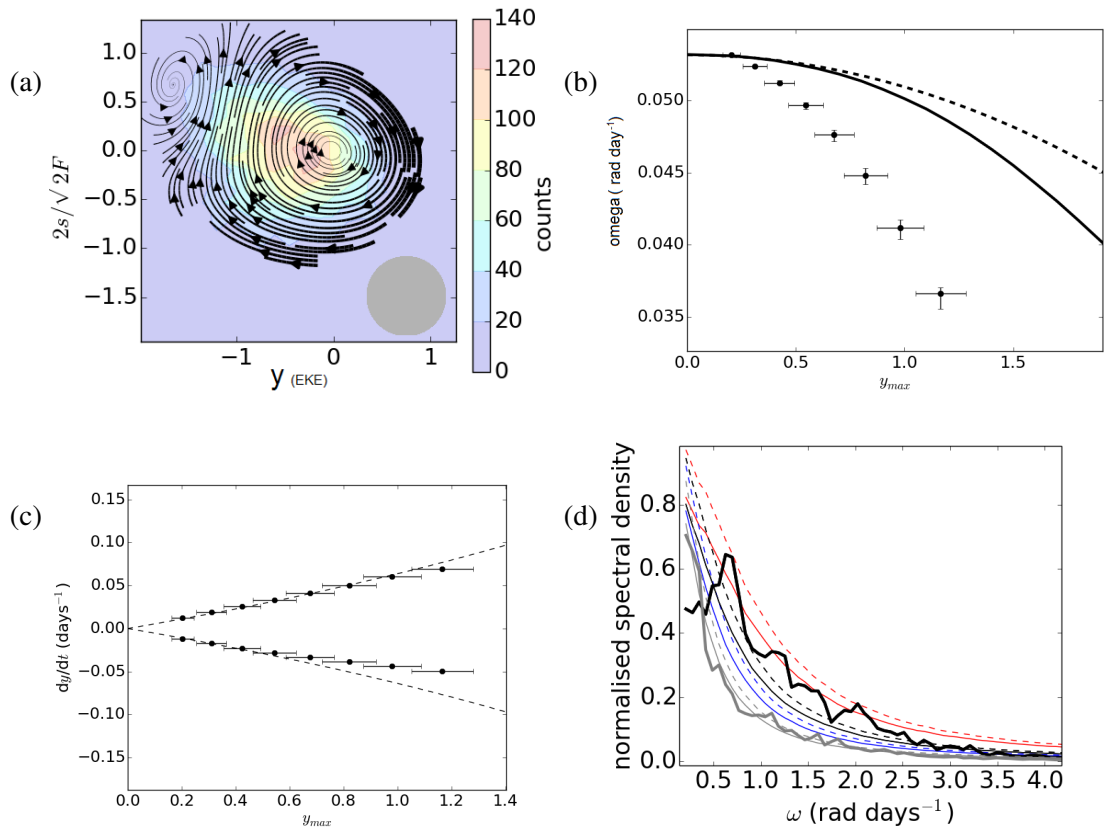


**Figure 3.10:** Analysis of the variability of baroclinicity and  $y_{EKE}$  (calculated at 250 hPa and averaged between 40–55°N and 290–330°E) in the Atlantic storm track, showing a) the phase space plot with the 2-D histogram (colours) and the filter standard deviation (grey ellipse), b) the angular frequency change with amplitude, c) the  $y_{EKE}$ -tendency change at  $y_{EKE} = 0$  with amplitude, and d) the power spectra of the raw baroclinicity and EKE time series, plotted as in figure 3.9.

Having seen that the North Atlantic exhibits an oscillatory behaviour with a period of around 25–45 days, it is of interest to investigate whether such behaviour exists in other storm tracks. Indeed periodicity in heat flux has been observed in both hemispheres by Thompson and Woodworth (2014) and Thompson and Li (2015). This analysis is restricted to the localised storm tracks of the Northern Hemisphere, and so the North Pacific storm track was additionally investigated. Its phase plot for baroclinicity and the transformed heat flux is shown in figure 3.11. The oscillations are less regular and not centered around the highest data density, and a secondary node appears in the region of negative  $y$  and positive excess baroclinicity. Nevertheless, the agreement between the model and data is still reasonable for both the frequency and the negative  $y$ -tendency analyses (figures 3.11b and c). However, the natural frequency is much lower than in the North Atlantic, even if the filtering is decreased to the smallest value that allows a coherent oscillation around the phase space.

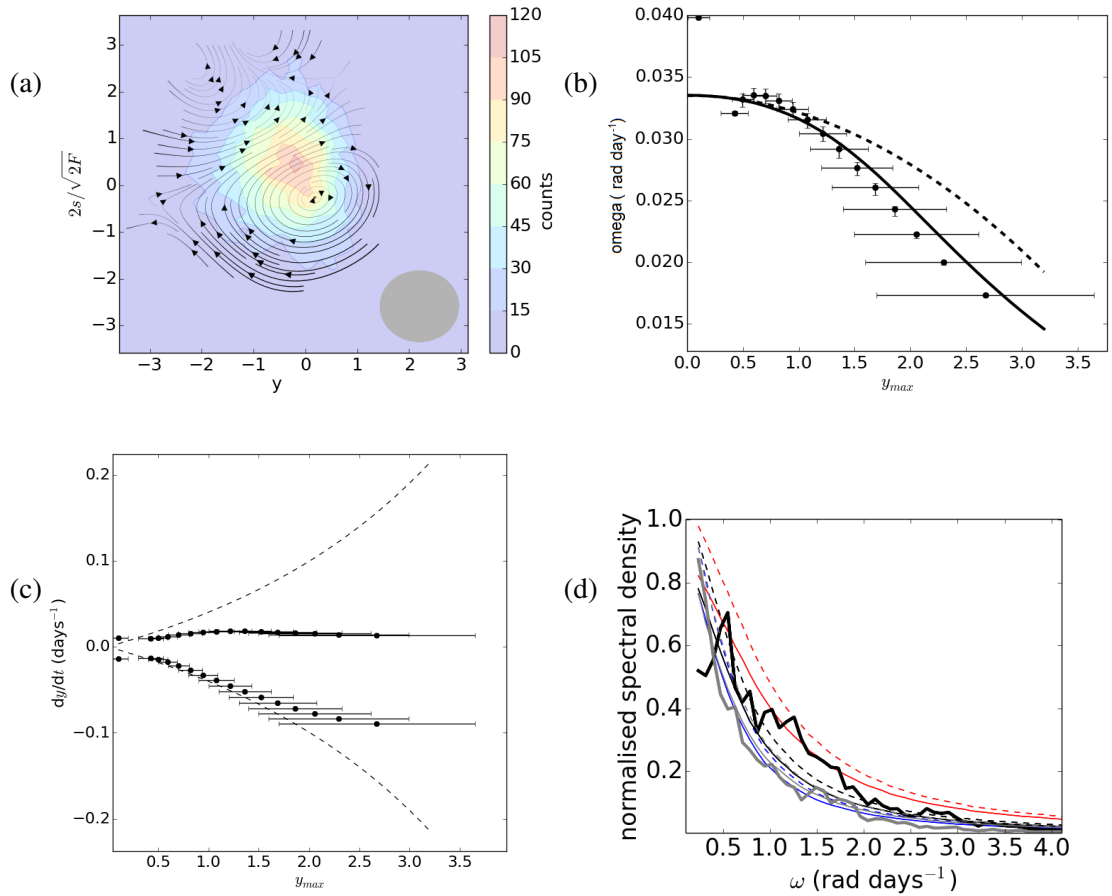


**Figure 3.11:** Analysis of the variability baroclinicity and  $y(v'T')$  (averaged using the sectors in figure 3.3) in the Pacific storm track, showing a) the phase space plot with the 2-D histogram (colours) and the filter standard deviation (grey ellipse), b) the angular frequency change with amplitude, c) the  $y$ -tendency change at  $y = 0$  with amplitude, and d) the power spectra of the raw baroclinicity and heat flux time series, plotted as in figure 3.9.

Again, investigating the power spectrum (figure 3.11d) reveals that the most dominant modes have a frequency of  $0.6 \text{ rad days}^{-1}$ , where the North Pacific baroclinicity spectrum is already relatively weak. The baroclinicity spectrum peaks at very low frequencies as in the North Atlantic, but in the North Pacific the low-frequencies no longer dominate the heat flux power spectrum. With there being additional higher-frequency heat flux variability that is not associated with the baroclinicity variations, the oscillating behaviour is not as well defined in the phase space. The quantitative analysis therefore yields somewhat less consistent results with the idealised model. This is additionally reflected in the positive  $y$ -tendency, which increases much less than as predicted by the model. The secondary circulation forces the trajectories to deform and enter the more central region of the phase plot, where lower  $y$ -tendencies persist (i.e. where the energy of

the oscillator is lower). It is known that the maximum of the storm track activity in the North Pacific is situated further downstream from the maximum of the baroclinicity (figure 3.3). As in the Atlantic upper-level EKE case, it is therefore plausible that the degraded spatial collocation between baroclinicity and heat flux introduces larger inconsistencies in the temporal behaviour of the phase space.

The above analysis of the properties of the average oscillations of the storm track activity and baroclinicity reveals a good agreement with the nonlinear oscillator model behaviour for small amplitude oscillations, i.e. when the system is weakly nonlinear. For larger amplitudes, the sampling error bars get larger and consistency between the data and the model is more difficult to prove, especially for upper-level variables that reach their maxima further downstream. Another factor worsening the agreement between the observations and the model at larger amplitudes is that there are fewer data points there. Nonetheless, the sign of change for reasonably scaled data is always well predicted by the model, with both the speed of oscillation during heat flux events, and the time period increasing with increasing amplitude (in a linear and quadratic-like fashion, respectively). This seems to apply for all measures of storm track activity tested in the North Atlantic as well as for the Pacific storm track. It is apparent that low-level variables that reach their maxima closest to the region of maximum baroclinicity yield a strikingly good agreement with the model.

Preliminary results of the PUMA experiment show that the nonlinear oscillator relationship also exists in medium complexity models, and for the zonal mean framework. The corresponding time lag composites around high heat flux peaks (larger than  $10 \text{ K m s}^{-1}$ ) and the baroclinicity-heat flux phase plot are displayed in figure 3.12. Note that the quantities were averaged between  $20$  and  $80^\circ \text{N}$ , and baroclinicity was calculated at  $775 \text{ hPa}$  and heat flux vertically averaged between  $925$  and  $700 \text{ hPa}$  (as previously). The baroclinicity clearly dips following a high heat flux event and there seems to be some sign of periodicity apparent in the lag composite. Consistent with this, the phase space plot again shows clockwise circulating trajectories around the highest data density. Though only preliminary, these results suggest that the predator-prey relationship between the transient eddies and baroclinicity is a general feature of storm tracks. A more detailed and highly-resolved study of the predator-prey relationship was conducted as part of an MSc project by Paolo Ghinassi, which further confirmed the results of this section. A more thorough examination, including a quantitative comparison with the nonlinear oscillator model, is a focus

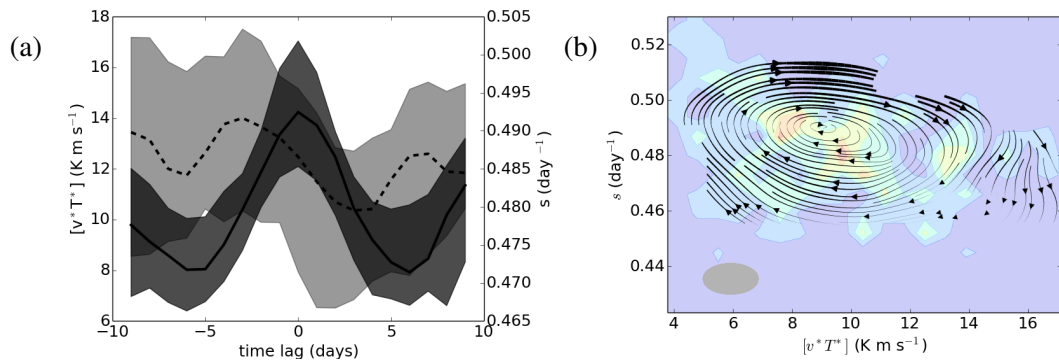


**Figure 3.12:** Nonlinear oscillator relationship in the PUMA experiment, indicated by a) a lag composite centered around high spikes in the heat flux of baroclinicity (dashed) and heat flux (solid), based on the zonal mean averaging; and b) the corresponding phase plot of the baroclinicity and heat flux.

of future work.

### 3.8 Summary and Discussion

It is apparent that both the North Atlantic and North Pacific storm tracks exhibit a predator-prey relationship between storm track activity and baroclinicity, irrespective of which measure of storm track activity is used. This relationship is based on the competing effects of high storm track activity eroding temperature gradients (and thus baroclinicity), and diabatic forcing enhancing them when storm track activity is low.

However, in the North Pacific this relationship was found to be less well defined. Nakamura and Sampe (2002) have found that as the East Asian winter monsoon intensifies, the enhanced westerlies trap the Pacific synoptic-scale eddies within the subtropical jet core and guide them southward and downstream, away from the maximum low-level baroclinicity and therefore reducing the interaction between the upper and lower levels which is essential for baroclinic growth (as is consistent with the barotropic governor mechanism discussed in the introduction). Consequently, the Pacific storm track is situated more downstream and is therefore less collocated with the maximum baroclinicity. This would move a substantial part of the eddy erosion of temperature gradients outside of the baroclinic domain of interest, where (instead of the diabatic heating sharpening temperature gradients and growing the eddies) downstream fluxing of recycled energy

from previous flow structures dominates eddy growth (Chang and Orlanski, 1993; Orlanski and Katzfey, 1991). This makes the predator-prey relationship less clear in the North Pacific compared to the North Atlantic.

In addition, some measures of storm track activity, such as PV variance, only produce the maximum over the North Atlantic in the winter time mean, because of this Pacific mid-winter minimum of storm track activity. It was therefore more difficult to identify the correct spatial averaging domain over the Pacific storm track. In contrast, the stationary forcing and weaker winds in the North Atlantic allow the storm track to be more locally defined and collocated with the maximum of baroclinicity so that any changes in one variable are immediately felt by the other. The classical theories of baroclinic instability are therefore more applicable in the North Atlantic storm track and the predator-prey behaviour is more detectable. This is why this storm track was the main focus of this chapter.

The results indicate that this predator-prey relationship exists on weekly to monthly timescales. The weekly timescales were observed in time lag composites, where a relatively slow baroclinicity growth (over around 3 days) is followed by baroclinicity decay during a two-day spike in storm track activity, which in turn is followed by a (partial) rapid recovery in the baroclinicity over approximately two days. The rapid recovery in baroclinicity may be a result of quick thermal damping of the low-level temperature to the underlying ocean surface temperature, which occurs on a timescale of approximately one day (Swanson and Pierrehumbert, 1997).

On the other hand, the thermal relaxation timescales of the atmospheric interior are longer, with values of around 10-20 days (Swanson and Pierrehumbert, 1997). This long-term relaxation may lead to lower-frequency cycling of baroclinicity and heat flux. In fact, averaging of the phase space of these two variables has yielded a natural time period of 25-45 days, with the lower value relating to less severe phase-space smoothing. The speed of the phase space plot trajectories indicates that the reason for the longer time period (compared to the time period extracted from the time lag composites) is due to a slower recovery in the baroclinicity rather than due to slower storm track activity events. A sensitivity analysis also revealed that these longer timescales are not a result of Lanczos averaging, though it is possible that the precise values of the quantitative results may be affected by the Lanczos filtering making the timeseries more Gaussian (Proistosescu *et al.*, 2016).

The existence of some degree of low-frequency periodicity is further supported by Thompson and Woodworth (2014) and Thompson and Li (2015), who found similar timescales (20-25 days) using the principal component analysis of eddy kinetic energy in both hemispheres. Their results suggest an annular structure of this variability, giving it its name: the Baroclinic Annular Mode (BAM). The BAM is primarily associated with a quasi-periodic development of baroclinic waves (Thompson and Woodworth, 2014), and is therefore closely related to the predator-prey relationship investigated here. However, it should be noted that time lag composites of the Northern Hemisphere (examples of which are presented and discussed in chapter 5) indicate that this cycling behaviour is confined to a particular storm track, rather than having an annular structure. It is therefore possible that the extreme events described by these composites are more identifiable as a local phenomenon.

Additionally, Thompson and Li (2015) have found that the BAM is stronger in winter but the spectral peak at the BAM frequency is not robustly different from red noise when compared to summer, agreeing with the results of this chapter. The winter season is generally more dynamically active and thus comprises more prominent background noise compared to the summer season, which may explain why extreme events dominate the heat transport more exclusively in the summer despite the heat transport being of a lower magnitude (Messori and Czaja, 2013). It is therefore possible that the additional noise in the winter makes the periodicity less pronounced. Nevertheless, the predator-prey relationship still applies, even if the behaviour is more quasi-periodic rather than purely periodic.

The analysis of the phase plots constructed using the reanalysis data revealed that the average time period of oscillation and speed of onset and termination of stormy events both increase with the amplitude of those events, implying that more extreme events occur more suddenly but less frequently. This may be of considerable use in the context of climate change studies. For example, modelling studies (e.g. Bengtsson *et al.*, 2009, Pinto *et al.*, 2009) have found that in warmer climates the North Atlantic storms will become less frequent but retain their current amplitude. This would suggest that the system would enter a new regime in the phase space with a lower value of steady-state heat flux which has been associated here with the diabatic forcing of the mean flow. This would be consistent with the idea that diabatic processes, such as boundary currents and land-sea contrast, would be less efficient at sharpening the low-level temperature gradient in a climate with a warmer Arctic (e.g. Barnes and Screen, 2015).

Another focus of this chapter was to develop a low-complexity model to simulate the observed predator-prey behaviour of storm track activity and baroclinicity. This nonlinear oscillator model is a two-dimensional dynamical system which assumes that baroclinicity is replenished by a constant diabatic forcing and eroded by storm track activity. The growth of storm track activity is assumed to be proportional to the product of the excess baroclinicity and storm track activity. Although this model was initially based on heuristic arguments, parallels can be drawn with Thompson's (1987) and Lorenz's (1984) models. The behaviour of this idealised model are periodic oscillations in both baroclinicity and heat flux, which manifest themselves as spikes in heat flux and a saw-tooth pattern in baroclinicity for large enough amplitudes.

Thompson and Barnes (2014) conducted a complementary study simultaneously with (but independently from) the present work. The authors also present a model that describes this predator-prey behaviour within storm tracks. Their model is based on empirically determined regression coefficients  $\alpha$  and  $\beta$  which describe the feedback between baroclinicity and heat fluxes. The model is as follows:

$$\frac{\partial \langle b \rangle}{\partial t} = \beta \langle v' T' \rangle - \frac{\langle b \rangle}{\tau} \quad (3.12)$$

$$\frac{\partial \langle v' T' \rangle}{\partial t} = -\alpha \langle b \rangle + \epsilon(t) \quad (3.13)$$

where  $b = dT/dy$  is the baroclinicity,  $v'T'$  is the heat flux,  $\epsilon$  is a stochastic noise,  $\tau$  is the baroclinicity damping timescale and the angled brackets denote the average over the Southern Hemisphere storm track. Although linear regression could be argued to be too simplistic to describe the feedbacks between baroclinicity and heat fluxes given the nonlinear nature of their variability discussed in this chapter, Thompson and Barnes's (2014) model describes essentially the same periodic interaction to that investigated in this chapter (simplified to a stochastically forced linear damped oscillator). This study therefore provides further support for the existence of oscillatory behaviour of both the storm track activity and baroclinicity due to their mutual interaction.

Returning to the nonlinear oscillator model developed here, despite some arguably substantial truncations used to justify it, this model was found to replicate the general behaviour of the observed data very well, exhibiting a clockwise circulation in the baroclinicity-heat flux phase space and showing an approximately quadratic increase of the oscillating period with amplitude and an approximately linear increase of the speed of onset and termination of heat flux events with amplitude. A more quantitative investigation showed some sensitivity to the size and shape of the

filter that was used to smooth the raw baroclinicity-heat flux phase space. Since the raw data series are relatively noisy, averaging is necessary to recover the overall behaviour, though it can also lead to damping of the desired structures. For an appropriate filter, a strikingly good agreement was found between the changes in the time period and the speed of the onset and termination of the heat flux events with increasing amplitude, with the agreement between the data and the exact numerical model solution being better than the agreement between the exact solution and its second order approximation. Even though the model lacks a large part of the complexity of the real system (such as the slight convergence or divergence of the circulating trajectories of the phase space), it still proved useful at reproducing the general behaviour and uncovering the links with the existing theories of the oscillatory behaviour of storm tracks.

It was also found that in general low-level measures of storm track activity produce a neater comparison. The upper levels may have more memory of the previous flow propagating from the upstream regions, which may introduce additional variability into the phase space. The clearest picture was found using low-level heat flux, low-level EKE and MSLP variance, averaged over the region of maximum baroclinicity.

The model also indicates that the recovery of the baroclinicity in the reanalysis data occurs slowly (with a timescale  $2\pi/\sqrt{F}$  between 30-70 days, corresponding to the range of natural frequencies found for different coarseness of averaging) relative to the eddy dissipation (with a timescale  $1/s_0$  of around 2 days), if the baroclinicity is scaled in a reasonable way. In other words, eddy dissipation dominates the system and so when high storm track activity occurs (and starts to override the effect of baroclinicity replenishment by diabatic forcing), it is quickly reduced by the eddy dissipation resulting in the short-lived burst-like nature of heat flux events (Messori and Czaja, 2013). The interaction of the short eddy dissipation and long-term baroclinicity replenishment is reflected in the multiple (weekly to monthly) timescales that characterise the predator-prey behaviour mentioned above.

It was additionally concluded from the phase space analysis that most of the reanalysis data lie within the near-linear regime, where the exact numerical and second-order approximated solutions only just start to depart. This observation strengthens the scope for using the weakly-nonlinear theory for the beginning of the storm track.

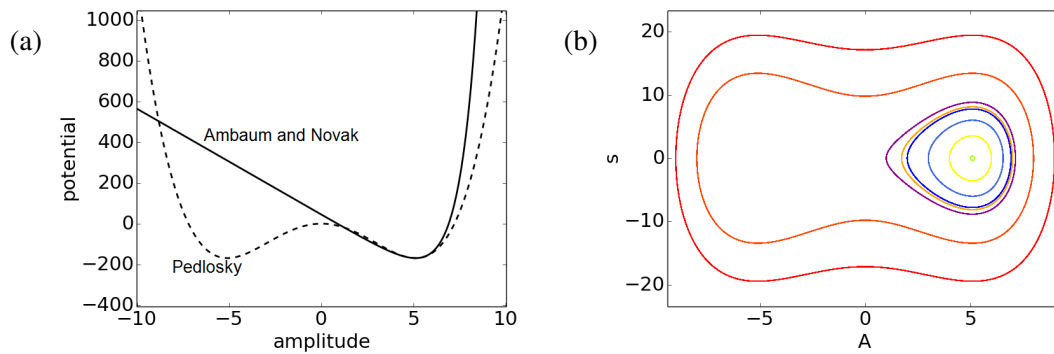


**Figure 3.13:** Comparison between the unforced inertial oscillatory system of Pedlosky (1970) and the diabatically forced system of Ambaum and Novak (2014), showing a) the nondimensional potentials of the two systems, with the natural frequency of the nonlinear oscillator tuned to the frequency of Pedlosky's (1970) model near the potential minimum; and b) the corresponding nondimensional phase plot of Pedlosky's (1970) system.  $A$  represents the amplitude of the baroclinic wave and  $s$  represents the  $dA/dt$  which relates to the vertical wind shear of the mean flow. The colours in panel b) emphasize different initial amplitudes, with warmer colours marking higher values. Note that the potential of the nonlinear oscillator in panel a) was shifted to coincide with one of the potential minima of Pedlosky's (1970) model for better comparison.

Furthermore, it should be also noted that the situation discussed here is different to that of Pedlosky (1970), who used the weakly-nonlinear theory to predict oscillatory behaviour between the perturbation amplitude and the underlying baroclinicity. In that study where resonant effects are neglected (Pedlosky (1982b)), the system is dependent on the overshooting of the eddy mixing effect (and thus phase angle reversal) which would allow eddies to return energy to the mean flow. Consequently the two quantities oscillate inertially whilst propagating downstream with the perturbation. On the other hand, the model used in this study (as well as that of Thompson, 1987) does not include such a continuous feedback. Once the eddies decay to almost zero values, their phase angle never attains negative values, and so the eddies do not have the ability to return energy back to the mean flow. This is where the necessity of the diabatic heating becomes apparent for the nonlinear oscillator model, as without it the baroclinicity would not be replenished. In other words, Pedlosky's (1970) eddies have a dual role of eroding baroclinicity when it is high, and replenishing it when it is below the critical value. On the other hand, the eddies of the nonlinear oscillator are only able to erode baroclinicity. The different potentials of the two systems can be compared in figure 3.13a. It is apparent that the two systems exhibit a similar behaviour near their steady state equilibria, where their potentials are at their minima and their oscillations are nearly linear (not shown). For larger values, the two systems differ significantly, as can be observed by studying their respective phase plots (figures 3.13b and 3.2b).

Finally, although the above analysis uses transient eddies as a measure of storm track activity, the behaviour of the real system is well simulated by the idealised nonlinear oscillator model (the formulation of which is based on the zonal-mean averaging). Using the zonal mean in the Northern Hemisphere would result in a mutual interference of the two storm tracks, which would be undesirable. To investigate the nonlinear oscillator problem in the more accurate zonal-mean framework, a preliminary investigation was conducted using an aquaplanet dry-core global circulation model, where a heating dipole was imposed and one localised storm track simulated. Despite the relatively large domain that was considered when spatially averaging the heat flux and baroclinicity, the results show a consistent picture with the above results, displaying a predator-prey relationship in composites of the raw data, as well as in the phase space. It can therefore be concluded that the predator-prey relationship of the nonlinearly oscillating baroclinicity and storm track activity is a general feature of all localised storm tracks.

## Chapter 4

# Cyclical Variability of the North Atlantic Eddy-driven Jet

*Most of the work in this chapter was published in Novak et al. (2015, ©American Meteorological Society, used with permission) and all of it was performed by the author.*

## 4.1 Introduction

The previous chapter suggests that localised storm tracks are characterised by a (quasi-) periodic behaviour of their activity. This behaviour occurs due to the internal competition between reduction of temperature gradients by baroclinic eddy activity and their strengthening by a stationary forcing. Given the arguments in the introduction, the storm track variability should imprint on the behaviour of the associated mean flow, which is the basis of the work in this chapter. Because the (quasi-) periodic behaviour is particularly pronounced there, this chapter will focus on the North Atlantic storm track and the associated variability of the mean flow. Such variability is quite different at the beginning of the storm track (which is dominated by baroclinic instability and eddy high heat fluxes) to that towards the middle and end parts of the storm track (which is dominated by the maximum convergence of horizontal momentum fluxes and barotropic latitudinal shifting of the jet). These different regions of the storm tracks will be referred to as the “upstream” and “downstream” regions, respectively, and their approximate location in the North Atlantic is shown in figure 4.1.

As outlined earlier, a key feature of terrestrial storm tracks is that they are generally accompanied by a deep tropospheric jet primarily driven by the momentum convergence produced by the storm tracks’ high-frequency baroclinic eddies (Hoskins *et al.*, 1983). This three-dimensional momen-

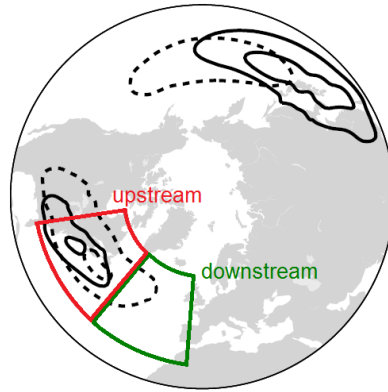


**Figure 4.1:** The location of the upstream and downstream parts of the North Atlantic storm track, relative to the winter time-mean baroclinicity (solid, 0.5 and 0.6 days<sup>-1</sup>) and heat flux (dashed, 10 and 20 K m s<sup>-1</sup>) calculated from the ERA-40 data. Adapted from Ambaum and Novak (2014).

tum convergence can be visualised using the divergence of the  $\mathbf{E}$ -vectors (Hoskins *et al.*, 1983). The  $\mathbf{E}$ -vector is analogous to the two-dimensional EP flux outlined in the introduction in that it also indicates the direction of eddy propagation (which is opposite to the direction of the westerly momentum transfer by eddies). In contrary to the EP flux however, the  $\mathbf{E}$ -vector framework enables the use of time averaging to define eddies and thus allows the additional exploration of eddy propagation in the zonal direction. The  $\mathbf{E}$ -vector is defined as

$$\mathbf{E} = \left( \overline{v'^2 - u'^2}, -\overline{u'v'}, \frac{f}{\partial\theta/\partial p} \overline{v'\theta'} \propto \overline{v'T'} \right), \quad (4.1)$$

where the first two terms are the horizontal barotropic components, and the last term is the vertical baroclinic component which is proportional to the lower-level meridional heat flux ( $\overline{v'T'}$ , referred to hereafter as ‘heat flux’). The bar indicates a time average and the prime denotes a perturbation from that average. Hoskins *et al.* (1983) observe that for high-frequency (with period of 10 days and lower) eddies the  $\mathbf{E}$ -vectors tend to point upwards at the beginning of the storm track and subsequently become more horizontal and meridionally divergent towards the middle of the storm track. This means that at the beginning of the storm track the eddies transfer momentum to lower levels reducing the vertical wind shear, whereas further downstream the eddies are responsible for a more barotropic variability in the jet. The authors also showed that the two horizontal  $\mathbf{E}$ -vector components are strongly dependent on eddy anisotropy, such as tilt and aspect ratio. The reader is referred to Hoskins *et al.* (1983) and Orlanski (1998) for more detailed description of these two components and their relationship with eddy anisotropy. Variability in the eddy anisotropy was further linked to different dominant types of wave breaking by the idealised experiments

of Rivière (2009) and Orlanski (2003), corroborating the observations of a northward jet during enhanced anticyclonic wave breaking on the equatorward side of the jet, and a southward jet during enhanced cyclonic wave breaking on the poleward side of the jet (Woollings *et al.*, 2008; Woollings *et al.*, 2010; Franzke *et al.*, 2011).

The above research suggests that transitions between different dominant types of wave breaking are crucial for altering the downstream course of the jet. Anticyclonic wave breaking is dominant on a sphere by default (e.g., Rivière, 2009), which can be seen by studying the structure of the terrestrial eddy-driven jets spiralling towards the poles. Several different mechanisms have been suggested for the transitions to the dominance of cyclonic breaking, including increasing the initial cyclonic barotropic shear of the jet (Thorncroft *et al.*, 1993), enhancing the vertical shear in the lower stratosphere (Wittman *et al.*, 2007) and strengthening the lower-level baroclinicity (Namias, 1950; Orlanski, 2003; Rivière, 2009).

The latter effect of lower-level baroclinicity is of interest as recent observational and conceptual studies (for example, Thompson and Birner, 2012; work in the previous chapter) have suggested that the upstream temperature gradient (and thus baroclinicity) is considerably reduced and replenished in time due to the fluctuations in the storm track activity itself. The previous chapter suggests a mechanism whereby a diabatic forcing (such as land-sea contrast, possibly enhanced by the presence of a western boundary current and orography (Brayshaw *et al.*, 2011)) continuously increases baroclinicity which provides favourable conditions for eddy growth leading to high storm track activity. As the storm track activity increases substantially, the baroclinicity starts to be eroded due to the reduction of the temperature gradients by vigorous eddies. Once baroclinicity reaches very low levels, further production of new eddies becomes limited. The resultant low storm track activity then allows the baroclinicity to increase again due to the diabatic forcing and the cycle repeats. This nonlinear relationship results in an oscillatory behaviour which is concealed in the time-mean picture and may not be initially obvious from the apparently unpredictable and chaotic behaviour of the system.

The above reasoning is used here to hypothesise that this cyclical variability in the storm track activity and baroclinicity should have a dual role in modifying the North Atlantic jet. The first (upstream) role is the erosion of temperature gradients by storm track activity leading to a fluctuating vertical shear (by thermal wind balance). The second (downstream) role is that the cyclical

variations in the upstream storm track activity cause a different wave breaking type to dominate, inducing latitudinal shifts in the downstream jet.

In order to test these hypotheses linking different properties of the storm track to the latitudinal variability in the jet, some observational characterisation of the latter needs to be defined. Recently, Woollings *et al.* (2010) and Franzke *et al.* (2011) demonstrated, based on the analysis of lower-level wind maxima in the ERA-40 reanalysis data, that the latitudinal variations of the eddy-driven jet in the North Atlantic region could be partitioned into three ‘persistent’ and ‘recurrent’ regimes, labelled south (S), middle (M) and north (N) regimes. As these regimes conveniently characterise the latitudinal variability of the eddy-driven jet, they are adopted here to study the spatio-temporal variability of the storm track and flow characteristics.

Section 4.2 investigates the direct effect of storm track activity variations during the jet regimes on baroclinicity and the associated baroclinic jet structure. Section 4.3 then explores the downstream effect of the upstream storm track activity and baroclinicity variations on the eddy structure, the associated horizontal **E**-vector components and the barotropic deflection of the jet. Section 4.4 indicates that the observation that different jet positions are associated with different values of heat flux applies to eddies of other frequencies that are shorter than a month. Section 4.5 combines these findings and reveals a sequence of different stages of a cyclic evolution, a lifecycle, of the storm track in space and time. It is proposed that this lifecycle is associated with a latitudinally-fixed upstream pulsation of storm track activity that drives downstream shifts in the latitude of the storm track and the associated jet. A discussion of the transition to lower-frequency timescales that leads to this lifecycle, as well as the extent to which this mechanism is local, is also provided in section 4.5, along with concluding remarks.

## 4.2 Upstream Baroclinic Effect

The analyses carried out in this and the following sections are all based on the daily-averaged DJF data from the ERA-40 (1957-2002) reanalysis dataset (as per Uppala *et al.*, 2005). This study uses Frame *et al.*’s (2011) K-means clustering of the latitudinal jet profiles (zonally and vertically averaged between 0 and 60°W and between 700 and 925 hPa) to partition the data into the three jet regimes. Note that since the eddy-driven jet is deep, the lower-level zonal wind is

used to identify its location and separate it from the shallow subtropical jet. This partitioning method is slightly different to that of Woollings *et al.* (2010) and Franzke *et al.* (2011), who used partitioning based on the latitudinal variability of the maximum low-frequency zonal wind. The former method was preferred because it does not require the large-scale flow variability to be based on low-frequency filtering, and because it is more robust when applied to different datasets (Frame *et al.*, 2011). This partition method yields 1174 days in the S regime, 1521 in the M regime and 1355 in the N regime. The reader is referred to Frame *et al.*'s (2011) study for further details of this partitioning method.

The meridional heat flux and the maximum Eady growth rate were used to investigate the variability in storm track activity and baroclinicity, respectively. The meridional heat flux, calculated using perturbations from a 10-day low-pass running mean based on Duchon's (1989) Lanczos filter of vertically averaged (between 700 and 925 hPa) meridional velocity and temperature, was used to represent the storm track activity that is associated with high-frequency eddies (Lorenz and Hartmann, 2003). The maximum Eady growth rate at 775 hPa ( $\sigma$ ), based on the vertical zonal wind shear and a variable static stability parameter (as in James, 1994), is defined as:

$$\sigma = 0.31 \frac{f}{N} \frac{\partial u}{\partial Z'} \quad (4.2)$$

where  $f$  is the Coriolis parameter,  $N$  is the static stability parameter and  $Z$  is the geopotential height. The static stability parameter for dry atmosphere was used as most of the variance across the regimes was found to be associated with changes in wind shear.

The partitioned heat flux and baroclinicity were then averaged for each jet regime to produce three composites (upper panel of figure 4.2). Neither the region of maximum heat flux nor the region of enhanced baroclinicity move latitudinally with the jet to any significant extent until the very downstream end of the storm track. This latitudinal confinement is displayed more explicitly in figure 4.3. In terms of intensity, these two quantities are clearly not proportional to each other as may be suggested by the time-mean picture discussed in many studies (e.g., Hoskins and Valdes, 1990; Orlanski, 1998). Instead, the heat flux intensity increases with the jet's latitude while the baroclinicity is most intense during the M regime and least intense during the N regime, as is evident from figure 4.3. Note that in figure 4.3a, the relative angular momentum represents latitudinally weighted lower-level zonal wind ( $r = ua \cos \phi$ ). In terms of the variability within

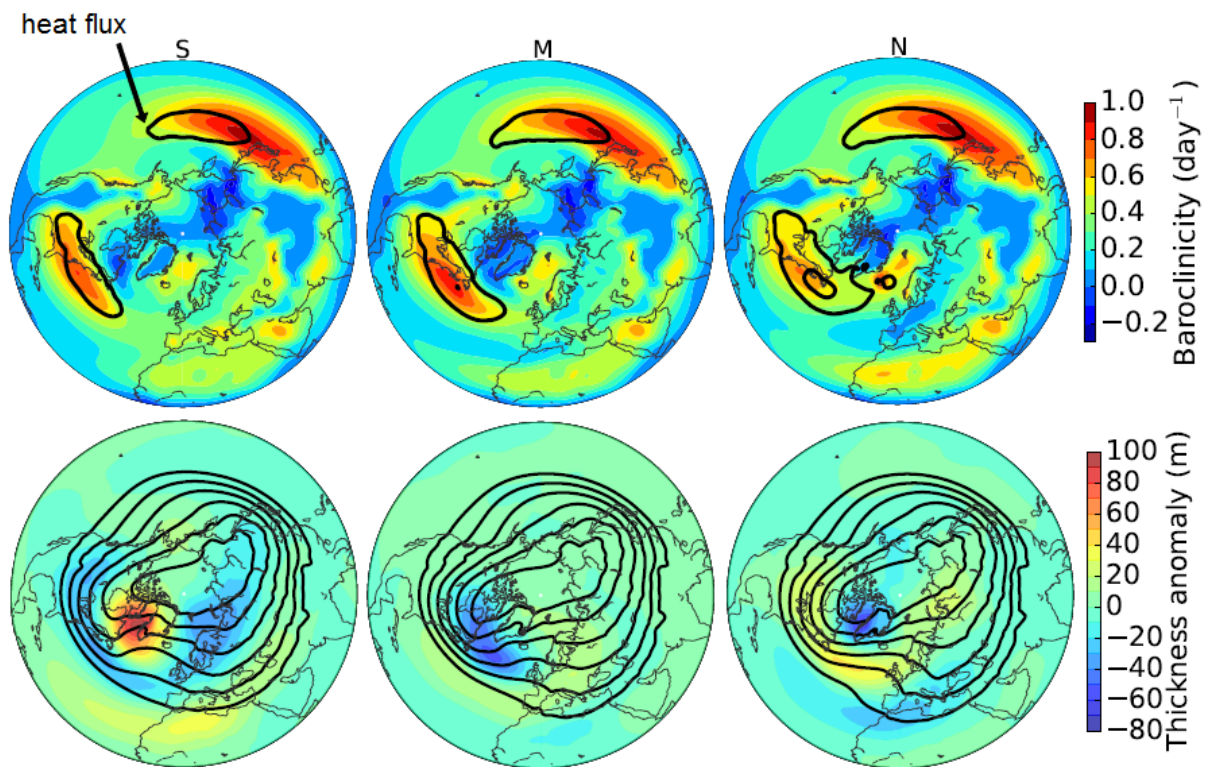


**Figure 4.2:** Hemispheric regime composites of baroclinicity (colours) and heat flux (black contours, displaying values of 10 and 20 K m s<sup>-1</sup>) for the S, M and N regimes (upper panels); and the associated 1000-500 hPa thickness (black contours, 100 m intervals from 4500 m) and thickness anomaly (colour) from the climatological (lower panels). From Novak *et al.* (2015).

the regimes, a closer inspection of the probability distribution functions (PDFs) of baroclinicity (not shown) and heat flux (investigated in the next section) has revealed that although all the regimes exhibit a wide range of both baroclinicity and heat flux values, the above variability between the regimes is still apparent and is not caused by sampling issues. Note that there is very little variability in both heat flux and baroclinicity outside of the North Atlantic region. Such lack of substantial external variability can be observed in other related quantities, such as the geopotential thickness anomalies from the climatological mean (corresponding to the virtual temperature anomalies as mentioned in the introduction), as shown in the bottom panel of figure 4.2. This aspect will be investigated further in the next section.

Franzke *et al.* (2011) propose that the preferred transitions between the jet regimes are from M to N, N to S and S to M regimes. Assuming this sequence of transitions, the above temporal relationship between heat flux and baroclinicity is reminiscent of the predator-prey behaviour proposed in the previous chapter. In the previous chapter a large but short-lived (lasting approximately 2 days)

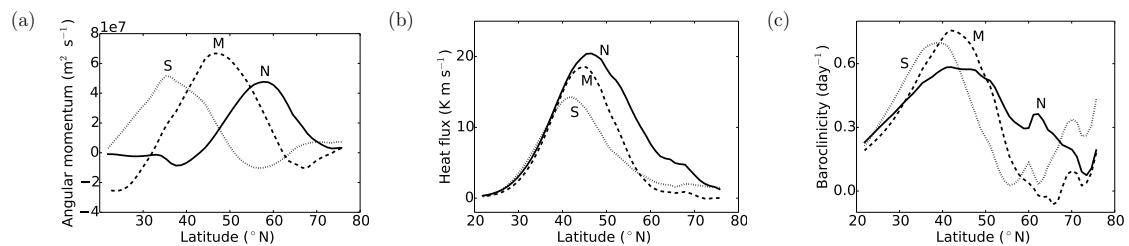


**Figure 4.3:** Composites of latitudinal profiles of the lower-level relative angular momentum (a, in  $\text{m}^2 \text{s}^{-1}$  and averaged between  $0$  and  $30^{\circ} \text{W}$ ), heat flux (b, in  $\text{K m s}^{-1}$  and averaged between  $40$  and  $70^{\circ} \text{W}$ ) and baroclinicity (c, in  $\text{day}^{-1}$  and averaged between  $30$  and  $90^{\circ} \text{W}$ ) for the S (dotted), M (dashed) and N (solid) regimes. From Novak *et al.* (2015).

heat flux event erodes baroclinicity, which eventually limits further baroclinic instability and the associated heat flux growth. The reduced heat flux then allows the continuous replenishment of baroclinicity by diabatic forcings to dominate until heat flux starts to increase again and the cycle repeats. It is suggested here that this nonlinear oscillator model can also assist in the interpretation of the variability of heat flux and baroclinicity on the longer timescale of the jet regimes. This issue of timescales will be further addressed in the next section. An additional difference is that while the previous chapter uses the instantaneous unfiltered  $v'T'$  to study short-lived spike-like heat flux events, this chapter uses its time-filtered value,  $\overline{v'T'}$ . The latter is proportional to the vertical  $\mathbf{E}$ -vector component and can therefore be easily related to the existing theoretical frameworks. The time-filtered heat flux can be viewed as an accumulation of smaller heat flux events or one particularly large event (this will be shown in the next section). It is therefore proposed that a mechanism exists whereby explosive rapidly deepening cyclones are initiated during the M regime due to its high baroclinicity (Sanders and Gyakum, 1980). The cyclones then develop further during the N regime while eroding the temperature gradients and therefore reducing baroclinicity to very low values. This is followed by a recovery of baroclinicity during the S regime when the eddy activity is limited (Rivi re and Orlanski, 2007). A similar mechanism, whereby slow-moving waves are associated with the strengthening and relaxation of the meridional temperature gradient (i.e. baroclinicity) in the storm track region, has been linked to the fluctuations in the zonal wind index in Namias' (1950) study. The next section explores whether this nonlinear oscillator mechanism can help to explain the existence of the jet regimes and the transitions between them.

### 4.3 Downstream Barotropic Effect

As outlined in Chapter 1, Rivière's (2009) and Orlandi's (2003) studies suggest that variations in baroclinicity can induce variations in eddy anisotropy and different dominant types of wave breaking that lead to shifts in the jet latitude. This section tests whether variations in these eddy and jet characteristics can be observed during the jet regimes and whether the above nonlinear oscillatory relationship between baroclinicity and heat flux can explain the preferred cycling between the jet regimes.

Orlandi's (2003) study proposes that anticyclonic breaking is dominant if the cyclonic eddies are more southwest-northeast (SW-NE) tilted and meridionally elongated, while cyclonic breaking is more characteristic of rounder cyclonic eddies tilted in the southeast-northwest (SE-NW) direction. Different types of wave breaking were thus identified here using Ertel PV on the 315 K isentrope, eddy tilt ( $\alpha$ ) and aspect ratio ( $\epsilon$ ) along the rotated coordinates relative to the eddy tilt. The two latter quantities were calculated for the 250 hPa level as per James (1994):

$$\alpha = \frac{1}{2} \tan^{-1} \left( \frac{2\overline{u'v'}}{\overline{v'^2} - \overline{u'^2}} \right), \quad (4.3)$$

$$\epsilon = \frac{\overline{(u'\sin\alpha + v'\cos\alpha)^2}}{\overline{(u'\cos\alpha - v'\sin\alpha)^2}}, \quad (4.4)$$

where the eddy tilt represents the angle between the minor axis of a meridionally elongated eddy and the circle of latitude, with positive values representing a SW-NE eddy tilt. The eddy aspect ratio represents the extent to which the meridionally elongated eddies are stretched and is a ratio between their major and minor axes.

As expected, figure 4.4 shows that eddies exhibit a SW-NE tilt (indicative of anticyclonic breaking) on the equatorward side and a SE-NW tilt (indicative of cyclonic breaking) on the poleward side of the storm track region, as the eddies supply momentum towards the jet core and accelerate it. However, it is clear that the SW-NE tilting of the N regime is most spatially extensive, especially in the eastern North Atlantic. The tilting patterns of the S and M regimes are more latitudinally constrained across the basin with the SE-NW tilting being more extensive during the S regime. The aspect ratio anomaly maximum moves more northwest towards the centre of the storm track with increasing jet latitude. It is thus likely that the low baroclinicity of the N regime

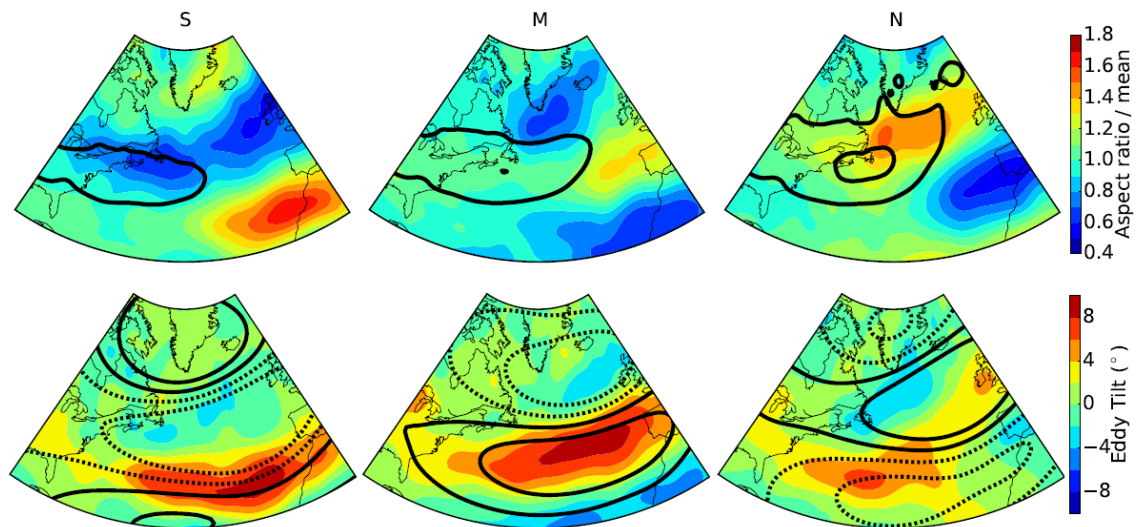


**Figure 4.4:** Composites of the upper-level (250 hPa) eddy aspect ratio anomaly (computed by dividing the aspect ratio by its climatological mean) for the S, M and N regimes (upper panel); and the upper-level (250 hPa) eddy tilt for the S, M and N regimes (lower panel). The black solid contours in the upper panel show the location of the storm track (measured by heat flux as in figure 4.2) for reference, and the black contours in the lower panel mark the 250 hPa stream function anomaly ( $-6 \times 10^6$ ,  $-2 \times 10^6$ ,  $2 \times 10^6$  and  $6 \times 10^6 \text{ m}^2 \text{ s}^{-1}$ ) with dashed being negative. From Novak *et al.* (2015).

is not sufficient to maintain coherent eddies, leading to eddy deformation and breaking further upstream. The high eddy stretching and extensive SW-NE tilting in the N regime are indicative of anticyclonic breaking. Conversely, in the M regime the eddies are less stretched in the region of the most intense storm track activity and baroclinicity, only beginning to deform considerably further downstream of the storm track maximum. The S regime exhibits even less stretched and more coherent eddies within the most intense part of the storm track as baroclinicity is being replenished in the absence of strong eddy mixing (as is evident from the low heat flux values). The reduced stretching and relatively extensive SE-NW tilting are indicative of cyclonic breaking. These patterns of eddy anisotropy therefore indicate that the N regime experiences anticyclonic breaking further upstream and more extensively than the other two regimes. The S regime has the most dominant cyclonic component with the two types of tilting being most symmetric about the latitude circle. The M regime appears to be strongly influenced by both types of wave breaking. These patterns are consistent with those found by Franzke *et al.* (2011).

In support of these interpretations, the large-scale flow pattern is shown in figure 4.5 using composites of the upper-level Ertel potential vorticity (PV) distribution and the zonal wind anomalies from the climatological mean at upper levels (250 hPa, therefore including anomalies associated

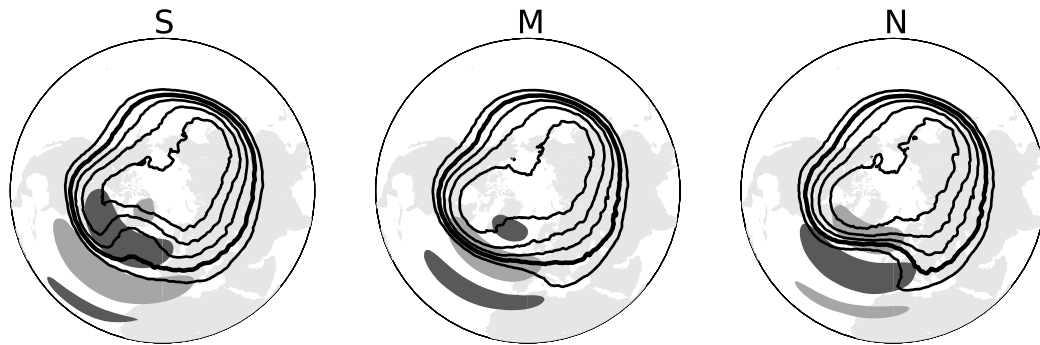


**Figure 4.5:** Composites (medians) of Ertel PV on the 315 K isentrope for the S, M and N regimes. Contours have an interval of 1 PVU and the thick line marks the 2 PVU contour. The shading represents upper-level (250 hPa) zonal wind anomalies from the climatological mean (light shading:  $5 \text{ m s}^{-1}$  and above; dark shading:  $-5 \text{ m s}^{-1}$  and below). A pattern correlation analysis of the PV distribution (not shown) confirmed that the averaged correlations between individual instances belonging to a particular regime are greater for that regime than those for the other regimes, confirming that these patterns are statistically robust. From Novak *et al.* (2015).

with the subtropical jet) for the three regimes. The median was used for the PV composites instead of the mean so as to retain the sharp PV gradient, making the composites more structurally correct. The 2 PVU line represents the dynamical tropopause and the sharpest PV gradient indicates the location of the upper-level jet. The S regime exhibits a fairly zonal jet and a strong easterly wind anomaly north of the jet. This indicates a strong trough over the western Atlantic with the ridge in the eastern Atlantic being stretched in the SE-NW direction relative to the latitude circle towards Greenland (corresponding to cyclonic wave breaking). On the other hand, the N regime exhibits a split flow and a more pronounced ridge downstream of the storm track, which tilts the trough-ridge structure in the opposite direction (corresponding to anticyclonic wave breaking). This figure also shows that PV patterns vary only weakly outside of the North Atlantic region, indicating statistical robustness in our results as well as the fact that the far upstream flow is not systematically linked to the persistence of these regimes. This is shown more quantitatively in tables 4.1 and 4.2, which show the spatial correlation scores (calculated as per von Storch and Zwiers, 1999) for PV anomalies (from the climatological mean) in the Atlantic ( $0\text{-}80^\circ\text{W}$  and  $30\text{-}70^\circ\text{N}$ ) and Pacific ( $140\text{-}230^\circ\text{E}$  and  $30\text{-}70^\circ\text{N}$ ) sectors of the composites in figure 4.5. Similar and more pronounced patterns have been observed in the lower-level geopotential thickness (in figure

4.2) and absolute vorticity distributions (not shown), the latter of which additionally indicates both types of breaking during the M regime.

Having established that the jet regimes do exhibit different eddy anisotropy and different dominant types of wave breaking, it is of interest to investigate whether these changes in eddy characteristics lead to the jet shifts, rather than just resulting from them. As mentioned in the introduction, the horizontal **E**-vector components usefully indicate the eddies' barotropic influence on the mean flow and they can both be involved in shifting the jet. By the **E**-vector definition (equation 4.1), both components are dependent on eddy tilt and aspect ratio (Hoskins *et al.*, 1983; Orlandi, 1998). This dependence, however, is not the same for the two components. For example, the zonal component can be altered considerably by meridional stretching and zonal thinning of an eddy, while the meridional component remains largely unchanged by the form of eddy decay (Orlandi, 1998). It was shown by Orlandi (1998) that the meridional **E**-vector component denotes the negative meridional momentum flux and its divergence indicates flow acceleration (or latitudinal deviation if the divergence is not symmetrical about the jet axis), while the zonal component promotes a quadrupole structure in the flow. Combining the averages of these two components organises the flow into a structure reminiscent of the time-mean trough-ridge pattern observed above both the Atlantic and Pacific ocean basins (Orlandi, 1998). Not only the divergence of these two components but also their relative magnitude is therefore important for determining the deflection of the jet.

The composites of the horizontal **E**-vector components averaged for the jet regimes are shown in figure 4.6. The meridional momentum convergence (indicating the location of the jet axis) is also displayed. Using Orlandi's (1998) theory, the large zonal component and the relatively large northward momentum flux of the N regime imply a northward deflection of the jet, as the trough-ridge structure becomes more pronounced. The meridional momentum convergence is relatively small and peaks at the beginning of the storm track, indicating a low jet speed downstream of the storm track during this regime. The M regime has a weaker zonal component but stronger poleward momentum flux compared to the N regime. However, Orlandi (1998) finds that the zonal component is more effective at deflecting the jet north in the North Atlantic, which would explain why the jet is at a lower latitude in the M regime than during the N regime. The M regime also exhibits a large convergence of the meridional momentum towards the downstream end of the storm track, resulting in strong flow acceleration there, as observed. During the S

	S	M	N
S	1.00	-0.42	-0.27
M	-0.42	1.00	0.16
N	-0.27	0.16	1.00

**Table 4.1:** Pattern correlation scores for the PV anomaly for the S, M and N jet regimes for the Atlantic sector.

	S	M	N
S	1.00	0.95	0.88
M	0.95	1.00	0.92
N	0.88	0.92	1.00

**Table 4.2:** Pattern correlation scores for the PV anomaly for the S, M and N jet regimes for the Pacific sector.

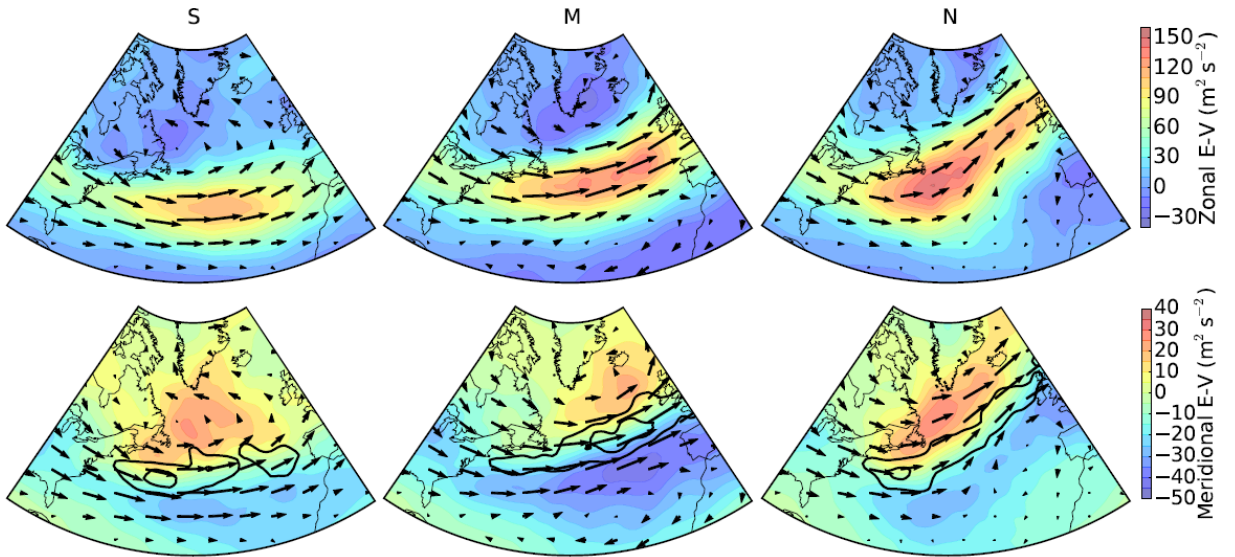


**Figure 4.6:** Composites of the horizontal E-vector components at 250 hPa for the S, M and N regimes. The upper panel shows the zonal component, and the lower panel shows the meridional component with its convergence marked by the solid black contours ( $3 \times 10^{-5}$  and  $5 \times 10^{-5} \text{ m s}^{-2}$ ). The overall relative direction of the horizontal E-vectors is shown by the arrows. From Novak *et al.* (2015).

regime both the zonal component and the poleward momentum flux are relatively small and more zonally symmetrical along the latitude circle compared to the other two regimes, resulting in a relatively zonal jet. These inferences concur with direct observations of the jet from the reanalysis data, implying that the eddies are, at least to some extent, responsible for this variability of the jet latitude and intensity. It is also notable the direction of the arrows is more polewards relative to the jet axis during the S regime and more equatorwards in the N regime. Such patterns agree with those found by Thorncroft *et al.* (1993) for the LC2 and LC1 scenarios, associated with different absorptive properties of the upper-level critical layer and thus different wave breaking (as discussed in Chapter 2).

Using the discussion in Chapter 2, the above results suggest that through an upstream effect of

reducing the baroclinicity, variations in heat flux induce changes in eddy properties that steer the jet to different latitudes further downstream. To confirm this directly, the PDF of the heat flux was split into the three jet regimes (figure 4.7). It is apparent that the S regime is most dominant when the heat flux is low and the N regime is most dominant when the heat flux is high.

To investigate whether this apparent relationship between the upstream heat flux and the downstream jet can be used to indicate the jet deflection from the heat flux values alone, the heat flux PDF was further divided into terciles, which were then used to split the time series of the lower-level latitudinal profiles of the downstream jet (as in figure 4.3). Averaging the profiles of each heat flux tercile produces three profile composites, as shown in figure 4.8. The highest heat flux tercile yields the most northern jet, whereas the lowest tercile yields the most southern jet. The differences between the jet latitudes are not as extreme as those defining the jet regimes (figure 4.3a). This is, however, expected since the latter was partitioned optimally to show the latitudinal deviations of the jet. Additionally, partitioning the PDF into terciles is not wholly representative of the frequency at which the jet regimes occur. In reality, the M regime is found to be most common while the N regime is found to be least common (Franzke *et al.*, 2011). It can nevertheless be concluded that heat flux has a strong downstream barotropic influence on the jet's latitudinal position.

This analysis was repeated using a 5-day cut-off Lanczos filter to define eddies. Although the results were similar, the equivalent figure to figure 4.8 (not shown) showed a less well defined separation between the zonal wind profiles, with the profiles of the high and middle terciles almost merging at the same latitude. This corroborates Rivière and Orlanski's (2007) findings that the intermediate-frequency (with a period between 5 and 12 days) synoptic eddies are strongly associated with anticyclonic breaking and therefore northward deflection of the jet, so that their removal leads to a less well defined northward jet deflection.

A better understanding of the extent to which heat flux affects the downstream behaviour of the flow can be achieved by comparing the flow observed during the jet regimes and that observed for the heat flux terciles. Figure 4.9 shows composites of stream function anomalies from the climatological mean averaged for the three respective regimes and heat flux terciles. As expected from the literature (e.g. Woollings *et al.*, 2010), the jet regime composites show similar patterns to the teleconnections, such as the North Atlantic Oscillation. Although somewhat weaker, the heat

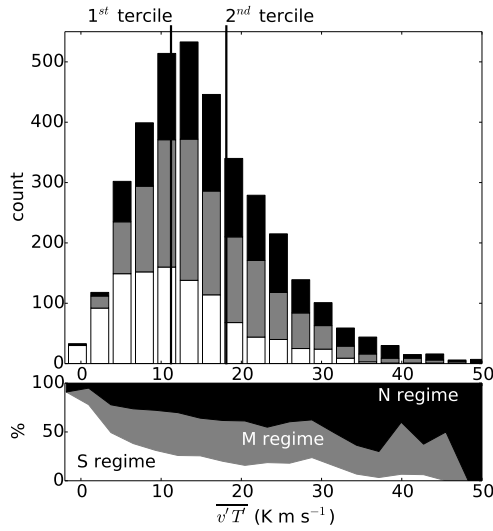


**Figure 4.7:** PDF of the 10-day filtered heat flux (averaged between 40 and 70°W, and 35 and 50°N), showing the occurrences of the S (white), M (gray) and N (black) jet regimes including the division of the PDF into terciles, with the lower panel displaying the relative importance of the regimes (as a percentage) in each bin. From Novak *et al.* (2015).

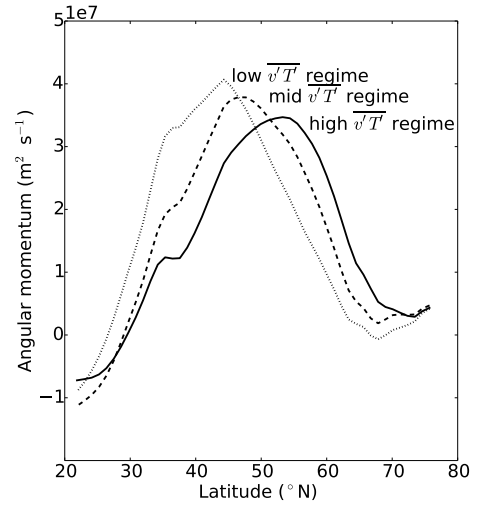


**Figure 4.8:** Composites of the lower-level relative angular momentum profiles (averaged between 0 and 30 °W, and between 925 and 700 hPa) averaged for the low (dotted line), middle (dashed line) and high (solid line) heat flux terciles. From Novak *et al.* (2015).

flux terciles also produce meridionally oriented barotropic patterns very similar to those of the jet regimes. Pattern correlation scores (calculated as per von Storch and Zwiers, 1999) are shown in tables 4.3 and 4.4 for a more quantitative comparison. The S jet regime therefore corresponds to the lowest heat flux tercile, the M regime to the middle heat flux tercile and the N regime corresponds to the highest heat flux tercile. The similarity between the S regime and the low heat flux tercile is strongest. This can be explained by inspecting the heat flux PDF (figure 4.7), which suggests that low values are almost entirely dominated by the S regime whereas in the higher part of the PDF, the N regime dominates but the M regime is also common. In addition to this, the stream function patterns in the M and N regimes are more strongly anticorrelated with the S regime than with each other (not shown). This agrees with the finding of Woollings *et al.* (2010) that while the S regime resembles the negative phase of the NAO, the other two regimes both weakly project onto the positive phase of the NAO. This implies that the S regime is more separable from the other two regimes. Furthermore, the partition into heat flux terciles is not fully representative of the frequency at which the regimes occur and could therefore be another source of the M and N regimes not being as strongly correlated with their respective heat flux terciles. The upper-level PV and absolute vorticity composites equivalent to figure 4.9 (not shown) also

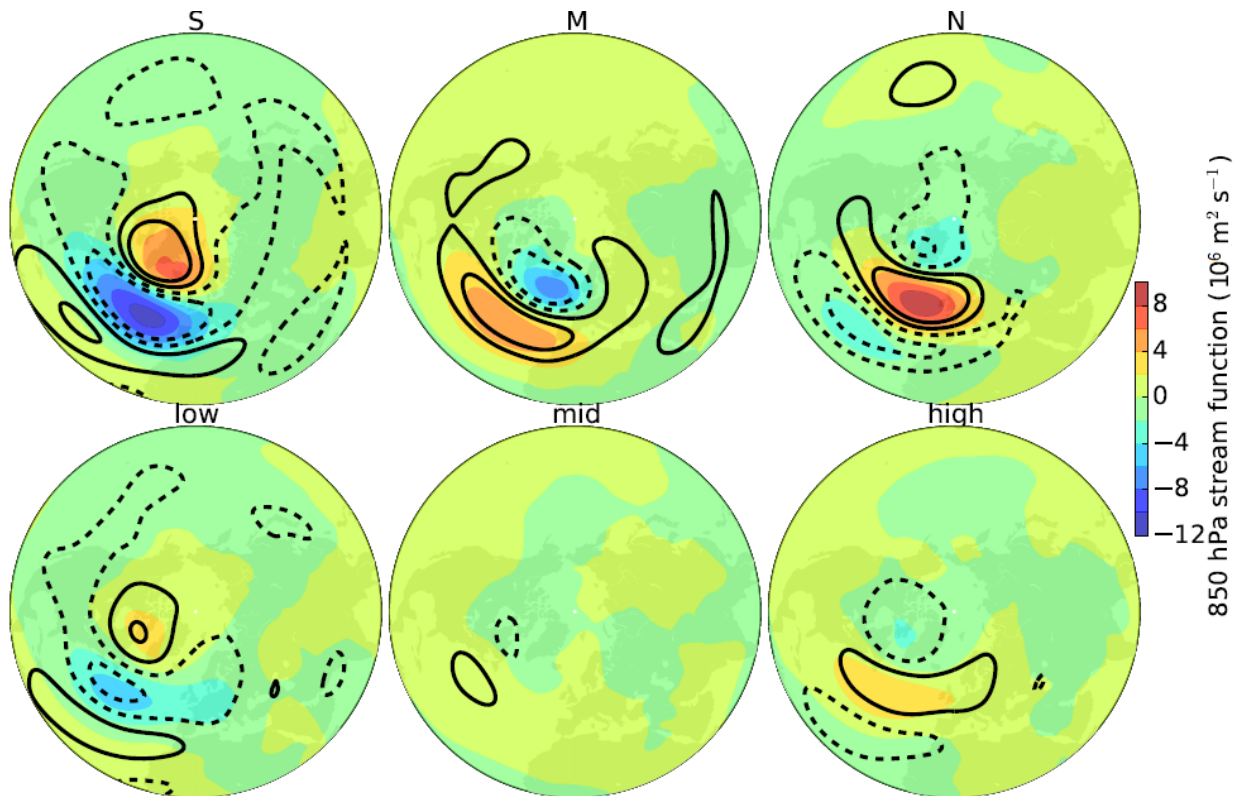


**Figure 4.9:** Stream function anomaly composites for the jet regimes (upper panel) and heat flux terciles (lower panel) at the 250 hPa level (thick black contours showing  $-6 \times 10^6$ ,  $-2 \times 10^6$ ,  $2 \times 10^6$  and  $6 \times 10^6$   $\text{m}^2 \text{s}^{-1}$ , with dashed being negative) and at the 850 hPa level (colour). From Novak *et al.* (2015).

revealed a considerable similarity between the jet regimes and heat flux terciles.

It is worth noting that streamfunction perturbations calculated using the 10-day filter (rather the climatological mean as above) provide an interesting insight into the timescales involved. Figure 4.10 shows these streamfunction perturbations composited into the three jet regimes, and the heat flux terciles based on both the filtered heat flux ( $\overline{v'T'}$ ) and the unfiltered (instantaneous) heat flux ( $v'T'$ ). The jet regime plots (top panels) show a similar picture to that described above for the anomalies from the climatological mean, with teleconnection-like patterns dominating in the North Atlantic. The unfiltered heat flux (bottom panels) shows a very different picture of meridionally extended baroclinic eddies with the characteristic banana-shaped structures as discussed in Chapter 2. The eddies become more barotropic towards the eastern part of the North Atlantic, as is consistent with the lifecycle theory. With more comparable values in the North Pacific, it is evident that the high frequency eddies propagate across the hemisphere, but are enhanced and modified as they enter and decay in the Atlantic. This is particularly evident during times of low heat flux. In contrast, the composites based on the terciles of the filtered heat flux

	low	mid	high
S	0.83	-0.58	-0.79
M	-0.37	0.57	0.32
N	-0.61	0.13	0.62

**Table 4.3:** Correlation scores for the 850 hPa streamfunction anomaly of the patterns in figure 4.9 for the S, M and N jet regimes and low, mid and high  $\overline{v'T'}$  terciles.

	low	mid	high
S	0.74	-0.27	-0.64
M	-0.25	0.41	0.11
N	-0.57	-0.07	0.60

**Table 4.4:** Correlation scores for the 250 hPa streamfunction anomaly of the patterns in figure 4.9 for the S, M and N jet regimes and low, mid and high  $\overline{v'T'}$  terciles.

(middle panels) produce anomalies that are less meridionally extended and less baroclinic, and in parts they begin to resemble the jet regime patterns, especially in the high heat flux tercile composites.

The above results imply that the transition from baroclinic to barotropic flow structures is associated with a transition of the nature of transient eddies to a lower frequency. In other words, while the reduction in the baroclinicity (and thus wind shear) may promptly respond to individual  $v'T'$  events, as shown in the previous chapter, the barotropic effect significantly shifting the jet's latitude operates predominantly at lower frequencies of the filtered heat flux ( $\overline{v'T'}$ ). In support of this, latitudinal profile composites of the lower-level jet (averaged between 700 and 925 hPa and between 0 and 30°W) centred around the high peaks (30 k m s<sup>-1</sup> or higher) in both  $v'T'$  and  $\overline{v'T'}$  were plotted, along with the composites of heat flux and baroclinicity, in figure 4.11. Both cases exhibit a similar behaviour of heat flux and baroclinicity. Consistent with the nonlinear oscillator mechanism of the previous chapter, the build up of baroclinicity is shortly followed by a rapid increase in the heat flux. Following this substantial increase in the heat flux the baroclinicity falls to low values. Consequently, the heat flux is reduced and the baroclinicity increases again. It is apparent, however, that this oscillation cycle of heat flux and baroclinicity in the  $\overline{v'T'}$ -centred composite operates on a longer timescale. It is also evident from the figure that only a small change in the jet latitude can be observed for the  $v'T'$ -centred composite following the short-term dip (of less than 3 days) in baroclinicity, whereas the jet was found to move north by approximately 5° a day after the peak in  $\overline{v'T'}$  and a longer term dip (of approximately 6 days) in baroclinicity.

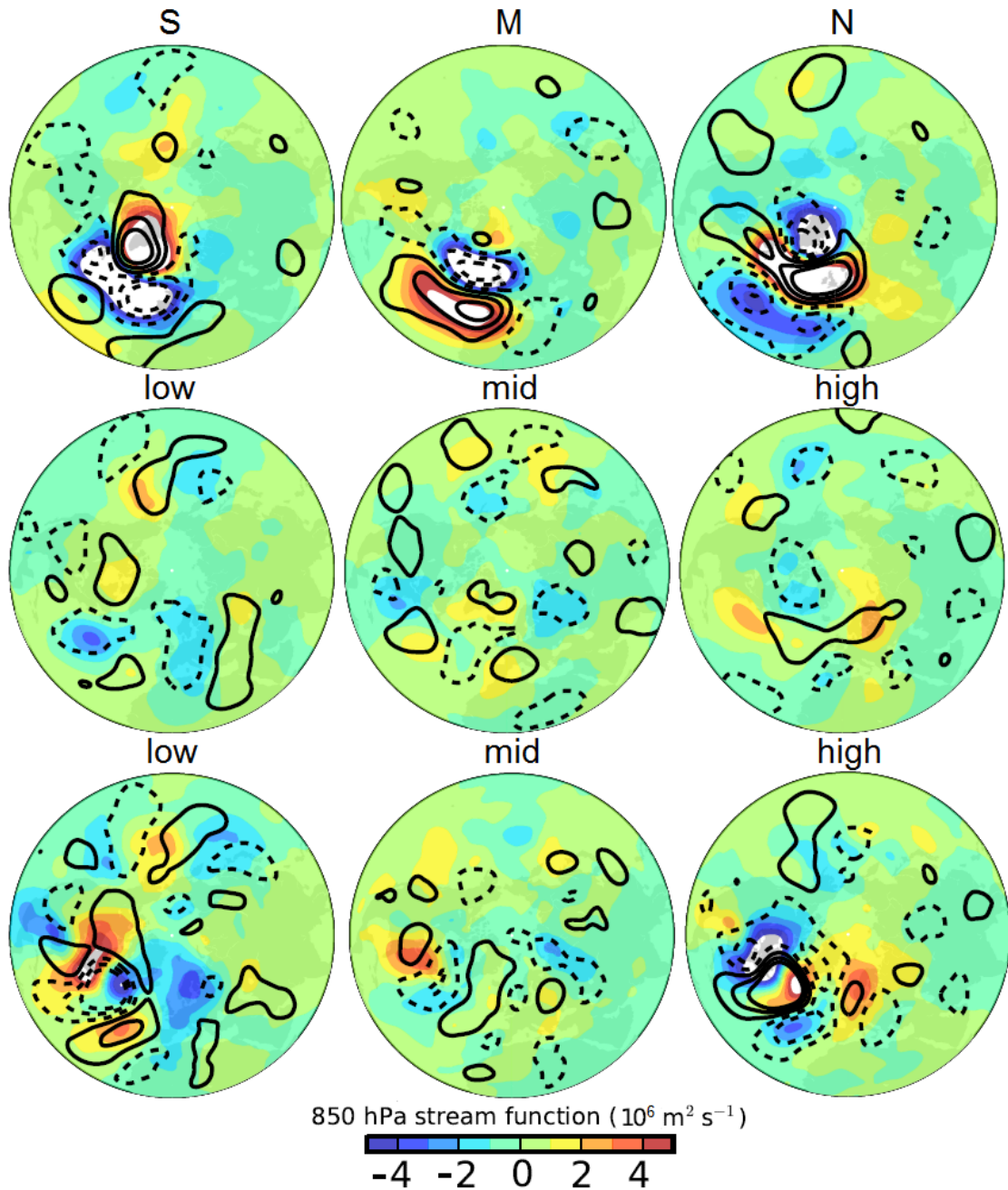


**Figure 4.10:** Stream function 10-day anomaly (computed using the Lanczos filter) composites for the jet regimes (upper panel), filtered heat flux terciles (middle panel) and unfiltered heat flux terciles (lower panel) at the 250 hPa level (thick black contours showing  $-10^7$ ,  $-6 \times 10^6$ ,  $-2 \times 10^6$ ,  $2 \times 10^6$ ,  $6 \times 10^6$  and  $10^7 \text{ m}^2 \text{ s}^{-1}$ , with dashed being negative) and at the 850 hPa level (colour).

In the previous section it was noted that the filtered heat flux is composed of an accumulation of  $v'T'$  events or one large event. To test this all of the 10-day windows that were used to produce figure 4.11b were examined using a simple algorithm. For each window, this algorithm uses a 1-2-1 filter to smooth  $v'T'$  and then counts all peaks in the smoothed  $v'T'$  that are higher than the maximum value of the  $\overline{v'T'}$  in that window. It additionally neglects the marginal points of days -5, -4, 4 and 5. Although it is difficult to define an individual spike unequivocally, visual inspection confirmed that this is a reasonable method of counting the major spikes. The results are shown in table 4.5. It is apparent that over a half of the  $\overline{v'T'}$  peaks are composed of 2- $v'T'$ -spike events and about a quarter are composed of 1- $v'T'$ -spike events. The rest are mostly 3- $v'T'$ -spike events. We also plotted the equivalent of figure 4.11b for the 1-spike, 2-spike and 3-spike events (not shown) and found that they all yield a similar northward shift in the jet. This implies that even one strong storm is capable of shifting the jet. Inspection of the  $v'T'$  PDF (not shown) revealed that such high  $v'T'$  spikes are common in both the M and N regimes but are more frequent during the latter regime.

This section suggests that the cycling between the jet regimes is, at least to some extent, a result of the longer-term effect of the nonlinear equilibration of zonally-oriented synoptic baroclinic eddies. These eddies cumulatively give rise to meridionally oriented patterns (as suggested by Benedict *et al.*, 2004), similar to those in Hannachi *et al.* (2012) which represent different phases of the North Atlantic Oscillation (NAO) and the East Atlantic Oscillation (EA). This concurs with the results of Athanasiadis and Ambaum (2009), which suggest that the only way synoptic eddies (associated with propagating wavetrains across the hemisphere) can contribute to teleconnections is through interaction with lower-frequency waves. The jet regime and heat flux tercile sets are not identical, but it can be concluded that high heat flux events are associated with a more northern shift of the jet, whereas low heat flux events are associated with a southern shift of the jet.

1 spike	2 spikes	3 spikes	4 spikes
33	73	25	2

**Table 4.5:** Count of  $\overline{v'T'}$  events over  $30 \text{ K m s}^{-1}$  that were composed of 1, 2, 3 and 4  $v'T'$  spikes over that value. More detail of the method employed to obtain these counts is given in the text.

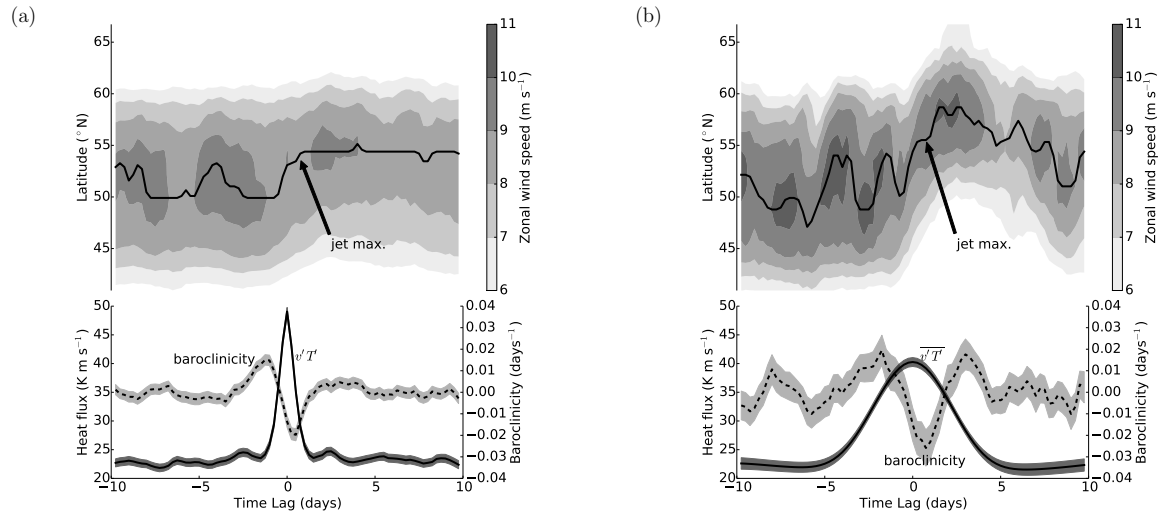


**Figure 4.11:** Lower panels: composites of the unfiltered (a) and filtered (b) heat flux (solid, averaged between 40 and 70°W, and 35 and 50°N), and baroclinicity (dashed, averaged between 30 and 90°W, and 30 and 50°N). The composites are centred around the maxima (higher than 30 K m s<sup>-1</sup>) of the respective heat flux variables. Baroclinicity is the excess baroclinicity as defined in the previous chapter and the mean offset is 0.52 day<sup>-1</sup>. The shading indicates the standard errors of the mean. Upper panels: composites of the lower-level zonal wind (averaged between 30 and 0°W, and 700 and 925 hPa) are marked by the grey-scale filled contours and the jet maximum is also displayed. For higher temporal resolution, these figures are based on 6-hourly ERA-40 data. From Novak *et al.* (2015).

#### 4.4 Sensitivity to the Choice of Frequency Bands to Define High-frequency Eddies

As a preliminary indication of whether the above mechanism, whereby higher eddy heat fluxes are associated with a higher latitude of the jet, applies to other scales of eddies, the length of the running-mean Lanczos filter was varied when computing the eddy heat flux ( $\overline{v'T'}$ ). Figure 4.12 shows that most filter lengths are associated with the dominance of the northern jet regime when the heat flux is high and the dominance of the southern regime when the heat flux is low. This agreement is particularly good for filter lengths between 5 and 15 days, justifying the usage of a 10-day cut-off in the above analysis.

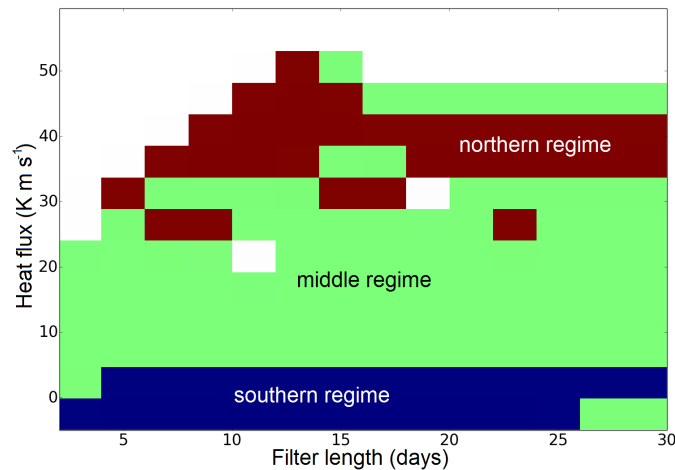


**Figure 4.12:** The dominating jet regimes of the heat flux PDF categories for different lengths of the running-mean filter used for calculating eddy heat flux. Only categories with counts larger than 150 are displayed.

## 4.5 Discussion and Conclusions

The results of this study suggest that variations in storm track activity (in particular lower-level meridional heat flux) during the North Atlantic jet regimes have a dual effect on the jet characteristics: a direct upstream baroclinic effect that strengthens and weakens the jet's wind shear (and thus baroclinicity), and a downstream barotropic effect that results in shifts in the jet's latitude and intensity.

The upstream baroclinic effect is not in a steady state, but oscillates due to the predator-prey relationship between the heat flux and lower-level baroclinicity, as proposed in the previous chapter. On longer timescales of the filtered heat flux, this relationship yields preferred transitions between the jet regimes that are from M to N, N to S and S to M (as suggested by Franzke *et al.*, 2011). High baroclinicity during the M regime produces high storm track activity. These storms will develop further and mix the temperature down-gradient and thus reduce baroclinicity, corresponding to the N regime. The storm track activity will eventually weaken as the low baroclinicity can no longer sustain it. This corresponds to the S regime with low storm track activity and a replenishing baroclinicity. Further increases in baroclinicity will lead to further increases in storm track activity and the cycle repeats.

The downstream effect of the storm track activity variability on the jet is closely dependent on the

upstream effect and is based on the idea that different values in baroclinicity may induce different eddy anisotropy and wave breaking that would result in latitudinal shifts in the jet (Orlanski, 2003). The eddy anisotropy, PV distribution and E-vectors were therefore studied to test whether this mechanism is responsible for the changing jet characteristics during the jet regimes. It was found that the N regime is most dominated by anticyclonic wave breaking and the S regime experiences most extensive cyclonic wave breaking, with the M regime exhibiting a strong influence of both wave breaking types. These patterns are consistent with what would be expected from the observed baroclinicity patterns according to Orlanski's (2003) theory. The E-vectors further show that high-frequency eddies are at least to some extent responsible for these large scale patterns and latitudinal jet deflection during the regimes.

The above cyclical spatio-temporal changes in eddy properties, propagation and breaking during the jet regimes can be viewed as the lifecycle of the storm track. The different stages of this lifecycle can be described as follows. Baroclinicity is continuously replenished by diabatic forcing. When the storm track activity is low, the baroclinicity will increase and start to form round and coherent eddies. This will contribute to the strengthening of the large scale trough over the west Atlantic inducing large scale cyclonic wave breaking (associated with an anticyclonic anomaly over Greenland and a cyclonic anomaly over the storm track), which will steer the jet south (S regime). Further increases of baroclinicity will further enhance cyclonic breaking. However, at the same time eddies will become more vigorous and propagate further downstream beyond the region of high baroclinicity. Consequently, the influence of the cyclonic breaking on the poleward side of the jet is overridden by the influence of the increased anticyclonic breaking on the equatorward side of the jet, due to the enhanced eddy deformation. The resultant jet position is slightly more poleward (M regime). In the next stage, eddy activity becomes so large that the eddy mixing rapidly reduces the baroclinicity, overriding the replenishing effect of the diabatic forcing. The reduced baroclinicity inhibits the production of new storms and enables the eddies to deform further upstream. The anticyclonic breaking starts to dominate as the large-scale ridge in the east Atlantic strengthens (and induces an anticyclonic anomaly over the end of the storm track and a low over Greenland), steering the jet further poleward (N regime). Once the remaining eddy activity decays, the baroclinicity can be replenished by the diabatic forcing again (S regime) and the cycle repeats.

Because the downstream effect is dependent on the upstream effect, both effects will oscillate

in time. However, these oscillations do not correlate completely due to their inherently different timescales. The upstream erosion of baroclinicity by high heat flux events occurs almost immediately (as shown in the previous chapter), resulting in high-frequency correlated variability in both variables. This study demonstrated that an accumulation of such heat flux events also results in lower-frequency oscillations of both heat flux and baroclinicity, which have an approximately weekly timescale that is similar to that of the jet regimes. While it was found that a short-term heat flux event is only followed by a slight shift in the jet latitude, this shift is significantly magnified when an accumulation of such events (or a particularly large one) precedes it. It has been found that a dominant type of wave breaking can persist for longer than an individual eddy, thereby enabling a transition from high- to low-frequency variability (Thorncroft *et al.*, 1993; Benedict *et al.*, 2004), most likely related to the absorptive properties of the critical layer, as discussed earlier. This cumulative effect may explain why the downstream effect of shifting the jet is much more prominent on the longer timescales, while the nonlinear oscillator relationship between heat flux and baroclinicity operates on both short and long timescales.

As hinted at in Section 4.3 and confirmed in previous studies (e.g., Woollings *et al.*, 2010), the jet regimes are related to the teleconnection patterns, such as the NAO and EA. While teleconnections are not the focus of this chapter, it is useful to compare its results to the existing literature to strengthen the validity of the above conclusions. For example, Pinto *et al.*'s (2009) analysis of cyclone 'Daria' shows that its onset in the western Atlantic was shortly followed by an increase in the NAO index which translates to a northern shift of the jet. Several days later the NAO index decreased as the storm left the upstream region, reflecting the characteristics of the S regime. Similarly, Woollings *et al.* (2011) find an increase in eddy activity in situ immediately before the onset of enhanced anticyclonic upper-level wave breaking (i.e., northern shift in the jet), without the need of preconditioned flow from the Pacific. In addition, Mailier *et al.* (2006) emphasize that there is a strong link between teleconnections and clustering of extratropical cyclones, which is associated with changing values of baroclinicity. Further support comes from Feldstein (2003), who suggests that high-frequency eddies are essential for driving low-frequency patterns, such as the NAO. Similarly, Athanasiadis and Ambaum (2010) showed that high-frequency eddies contribute to teleconnection tendencies by a nonlinear transfer from high to low frequencies. All the above studies confirm the conclusion that local variability of high-frequency eddy activity can induce lower-frequency variability in the downstream jet.

Throughout this study it is suggested that the cyclic behaviour of the storm track is a purely local phenomenon. However, it is clear (for example, from the time series in figure 3.5) that these storm track lifecycles are irregular and that other sources of variability must be present. It is inevitable that, unlike in the simplified nonlinear oscillator model, the diabatic heating that replenishes the region of enhanced baroclinicity will vary on many timescales. Furthermore, as suggested in Chapter 2, there are other mechanisms (other than modifying baroclinicity) that can induce transitions between different types of wave breaking and therefore cause latitudinal shifts in the jet. For example, several studies (for instance, Thorncroft *et al.*, 1993; Franzke *et al.*, 2004; Rivière and Orlanski, 2007; Pinto *et al.*, 2011) suggest that preconditioning the flow with barotropic shear can play a significant role in determining the polarity of the NAO index (and thus the jet latitude). This study, however, only reveals a weak variability outside of the North Atlantic basin during the jet regimes, which would imply that the North Atlantic and North Pacific jets are not strongly linked on the timescales of the jet regimes (as found, for example, by Blackmon *et al.*, 1984, Ambaum *et al.*, 2001). It is speculated here that while high-frequency eddies propagate across the hemisphere as zonally-oriented wavetrains (for example, Gerber and Vallis, 2007), their enhancement and shaping across the North Atlantic basin is a local phenomenon (Chang *et al.*, 2002) that will affect local patterns of teleconnections and thus induce lower-frequency variations in the local jet's latitude. It is nevertheless still possible that the averaging methods employed in this investigation obscured some external variability outside of the North Atlantic. In addition, while Wittman *et al.* (2004) conclude that stratospheric changes yield a relatively small response in the tropospheric flow, they note that constant exposure during several baroclinic lifecycles may produce a more significant tropospheric response. This aspect was not studied here and requires further attention.

In terms of broader applicability, the anomalous spikes in heat flux can be observed for all terrestrial storm tracks (Messori and Czaja, 2013), but not all exhibit the observed trimodal fluctuations in jet latitude (Woollings *et al.*, 2010). For example, the Pacific-North American pattern is largely dominated by the pulsation of the jet rather than the latitudinal shifts, as a consequence of the stationary eddies being dominant (Franzke and Feldstein, 2005) and it being more confined to the latitude of the subtropical jet (as discussed in Chapter 2). It is likely that these fluctuations in jet intensity in the Pacific region are also a result of baroclinicity erosion by heat flux. The two storm tracks do not appear to be significantly correlated, meaning that different timescales would apply. Woollings *et al.* (2010) find that the latitudinal PDFs of the jets in the South Pacific

and central North Pacific both exhibit a bimodal structure, corresponding to whether or not the eddy-driven jet is merged with the subtropical jet. They associated the trimodal structure of the North Atlantic jet to the stationary wave configuration that tilts the storm track (and the jet) more polewards than in any of the other regions. It is therefore possible that while the organisation into flow regimes is a general characteristic of all storm tracks, the relatively weak subtropical jet over the North Atlantic and the stationary wave forcing allow the North Atlantic jet to exhibit a more complex latitudinal variability due to transient eddies. Additional investigation of the other two storm tracks may separate the individual roles played by stationary and transient eddies, and determine more generally their relative contribution to the spatio-temporal lifecycle of the storm track.

## Chapter 5

# Energetics of the Storm Track Lifecycle

*Apart from the precise formulation of the local APE and its decomposition into the eddy and mean APE components (developed by the author's supervisor), the unquoted work in this chapter was performed by the author and there are plans to publish it in two publications: one describing the time-mean distribution of the local energetics and one focusing on the energetics lifecycle of the storm tracks from the local energetics perspective.*

## 5.1 Introduction

It was demonstrated in the previous chapters that different dynamical processes dominate in different regions of the storm track, and during different stages of its lifecycle. This indicates the diverse nature of the atmospheric dynamics involved. Energetics allows simplification of the complex primitive equations into a set of scalar evolution equations, and is therefore used here to provide a more concise and complementary picture of the storm track behaviour. A local energetics framework is employed here to examine the steady-state spatial distribution of the energetics, as well as the temporal variation of the energetics during the storm track lifecycle. Furthermore, this chapter demonstrates that the nonlinear oscillator relationship also exists between the eddy and mean energy components. This is shown using theoretical arguments as well as observations of the North Atlantic storm track and an idealised storm track of a simplified global circulation model (GCM). In addition, this chapter will demonstrate a more continuous link between the dynamics at the beginning of the storm track (discussed in Chapter 3) and those at the end of the storm track (discussed in chapter 4) during the storm track lifecycle.

The concept of energy was introduced into thermodynamics in its modern sense at the beginning of the 19th century by the work of Rumford and Young, and half a century later the first law

of thermodynamics developed from the works of Mayer, Joule, Helmholtz and Clausius (review provided in Muller, 2007). This law implies that a closed system will conserve its total energy, whilst still allowing conversion between its kinetic and potential components. This is the basis of the arguments presented in this chapter. In the atmosphere, the kinetic energy (KE) manifests as wind and its maxima are within jet cores. The total potential energy is the sum of internal and gravitational potential energies, and about 0.5% of it is available for conversion into the kinetic energy in the atmosphere (Lorenz, 1955). This conversion is the mechanism via which incoming solar radiation drives the global circulation.

In atmospheric research, the study of energetics gained substantial momentum after the study of Margules (1903), who considered the conservative transfer between the potential and kinetic energies in a closed system under adiabatic conditions; the idea being that if the atmosphere was to be rearranged adiabatically to be completely statically stable and vertically stratified, the required kinetic energy would be equal to the maximum amount of the total potential energy of the original state that is available for conversion. Lorenz (1955) called this energy the “available potential energy” (referred to as APE hereafter), and defined it formally as the difference between the total global potential energy of the actual state of the atmosphere and its adiabatically rearranged reference state. Using this definition, Lorenz (1955) showed that the global APE is proportional to the pressure variance on constant isentropes to the leading order. This in turn can be related to the temperature variance on isobaric surfaces and the inverse square of static stability. Assuming a flat topography, the Lorenz APE per unit area for a hydrostatic atmosphere composed of an ideal gas can therefore be written as:

$$\begin{aligned} \overline{APE}_{\text{Lorenz}} &= \overline{TPE} - \overline{TPE}_R = \frac{c_p}{g p_0^\kappa} \frac{1}{(1 + \kappa)} \int_0^\infty \overline{p^{\kappa+1}} - \bar{p}^{\kappa+1} d\theta \\ &\approx \frac{1}{2} \frac{\kappa c_p}{g p_0^\kappa} \int_0^{p_0} p^{-(1-\kappa)} \left( -\frac{\partial \bar{\theta}}{\partial p} \right)^{-1} \overline{\theta'^2} dp, \end{aligned} \quad (5.1)$$

where the averaging is over isentropic and isobaric surfaces in the second and third equalities, respectively. The total potential energy (TPE) is defined as:

$$TPE = \int_0^\infty \rho g Z dZ + c_v g^{-1} \int_0^{p_0} T dp = (1 + \kappa)^{-1} p_0^{-\kappa} g^{-1} c_p \int_0^\infty p^{\kappa+1} d\theta, \quad (5.2)$$

where  $c_p$  and  $c_v$  refer to the specific heat under constant pressure and constant volume respectively,  $R$  is the specific gas constant for dry air,  $\kappa$  is the ratio of  $R$  to  $c_p$ ,  $g$  is the gravitational

constant,  $p$  is pressure,  $p_0$  is the pressure at the surface,  $\theta$  is potential temperature,  $T$  is temperature,  $\rho$  is density and  $Z$  is geopotential height.

Lorenz further used the approximation in equation 5.1 for the APE and partitioned it into its zonal mean and eddy parts (though other kinds of commutable averaging can also be employed). The same partition was applied to the KE. By manipulating the thermodynamic and momentum equations, Lorenz was then able to derive a closed set of evolution equations for the four resultant energy terms: mean APE, eddy APE, mean KE and eddy KE. This set of equations delineates the forcings on and the conversions between the four energy terms, and is called the “Lorenz cycle”. It is depicted in figure 5.1. The mean and eddy heating terms feed into their respective APE terms, and similarly mean and eddy KE loss ensues from the mean and eddy friction terms, respectively. The conversions between the APE terms (CA), between the KE terms (CK), between the mean terms (CM) and between the eddy terms (CE) are also indicated. It has been observed (e.g. by Oort, 1964 and Li *et al.*, 2007) that the preferred flow of energy in the Earth’s global atmosphere is as indicated by the thickness of the arrows, i.e. from the mean APE to its eddy counterpart, and then into the eddy KE. A large part of the latter is then dissipated as friction but some of it is returned to the mean flow as mean KE.

This is concurrent with local synoptic observations of baroclinic instability as follows. The storm track regions are collocated with an enhanced mean diabatic forcing (e.g. the western boundary currents or the land-sea contrast) that sharpens meridional temperature gradients, steepens the isentropes and therefore enhances the mean APE (Brayshaw *et al.*, 2009). This enhanced mean APE can then be utilised by eddies, thereby enhancing the total eddy energy (sum of the eddy APE and eddy KE) within the storm tracks. The eddy energy can be further enhanced by pre-existing eddies in the form of eddy heating (e.g. Hoskins and Valdes, 1990). Most of the eddy energy is then dissipated as eddy friction, but some is returned to the mean flow via eddy anisotropy and wave breaking, inducing convergence of momentum fluxes as discussed in the previous chapters. The conversion between mean APE and mean KE is small and the direction of conversion is unclear. As will be shown below, this term results from a large cancellation between the thermally direct Hadley cell and the thermally indirect meridional mean circulation induced by eddies within the Ferrel cell (James, 1994). A similar energetics cycle can be derived in the wave-number domain (e.g. Saltzman, 1970).

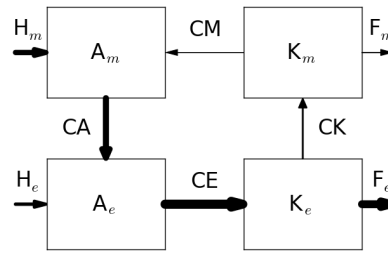


**Figure 5.1:** Lorenz energy cycle, indicating the direction and magnitude of the conversion and generation terms. Adapted from James (1994).

The Lorenz cycle therefore provides a useful insight into the dynamical processes of the global atmosphere, and it has been widely used to study individual lifecycle events in idealised scenarios. For example, the seminal study of Simmons and Hoskins (1978) used the Lorenz energy conversion terms to study the nonlinear lifecycles of baroclinic waves using a multi-layer primitive equation model on a sphere (as described by Hoskins and Simmons, 1975). The authors found the traditional picture of baroclinic growth being dominated by the conversion between the potential energies (CA), and the decay being more barotropic and exhibiting the conversion between the kinetic energies (CK) as the eddies return energy back into the mean flow and strengthen the upper-level jet. It is also apparent from their study that the conversion between the mean energies (CM) varies substantially, with a considerable amount of the mean KE being converted to the mean APE (especially during the decay stage). This is related to the indirect circulation induced by the intensified eddy activity. Using a similar setup, Tanaka's (1995) work, using spectral representation of the nonlinear lifecycle, extended Hoskins and Simmons's (1975) study by separating the vertical structure of the flow into its barotropic and baroclinic modes, and then splitting these modes into their zonal means and the perturbations thereof. The experiments with a zonal baroclinic field that was allowed to restore revealed oscillations in the zonal barotropic energy, the total eddy energy and the conversion terms between them. These oscillations had approximately weekly timescales, similar to those discussed in the previous chapters.

More recent applications of Lorenz energetics have focused on studying the idealised and observed behaviour of the current and future climates, both dry and moist (e.g. Hu *et al.*, 2004; Li *et al.*, 2007; Schneider and Walker, 2008; O'Gorman and Schneider, 2008; Hernandez-Deckers and von Storch, 2010; Veiga and Ambrizzi, 2013). Pearce (1978) further extended the Lorenz

energy cycle to allow for changes in static stability and vertical heat fluxes, but the comparison to the original Lorenz term showed a qualitatively similar result.

However, despite its usefulness for idealised storm tracks and global statistics, the globally integrated nature of the Lorenz energetics means that its applicability for regionally confined processes is limited. In such cases, interference and cancellation between key features of the flow can occur when globally integrated. For example, the presence of several storm tracks (as in the Northern Hemisphere) may make their individual behaviours less apparent.

Plumb (1983) discussed the possibility of using the locally definable mean total potential energy instead of the mean APE, the latter being dependent on the state of the entire domain whereas the former is not. The zonal mean-based eddy APE and the kinetic energies of the Lorenz method are already locally definable. These locally definable energy components were compared to their equivalent terms in the transformed Eulerian mean (TEM) framework, which is formulated so as to omit the large cancellation between the convergence of eddy fluxes and adiabatic cooling (Andrews and McIntyre, 1976), as discussed in Chapter 2. The TEM framework was found to yield a substantially different structure of the conversion and flux terms, and Plumb (1983) emphasizes that examining individual conversion and flux terms separately, without considering all the relevant terms, may lead to incorrect interpretations. The author concludes that the Lorenz cycle has a limited usefulness. Similarly, Kao and Chi's (1978) study of the energetics of different wavenumbers highlights the dangers of mistakenly assigning causality when a large conversion term coincides with an increase of the respective energy term.

Despite the limitations of the Lorenz energy cycle approach, Plumb's (1983) framework of locally definable energetics has been used in observational research to produce sensible results by careful consideration of all terms in the evolution equations (e.g. Orlandi and Katzfey, 1991). Nonetheless, using the zonal averaging masks the longitudinally localised variability, which may be problematic in the presence of several features in the same latitudinal band, such as the storm tracks in the Northern Hemisphere. However, the eddy APE is only independent of the global state if a zonal mean-based partition is used, and so a different local definition of APE that allows other averaging methods (such as the time mean) is therefore required.

Li *et al.* (2007) attempted to study the local distribution of the (time mean-based) energetics us-

ing Lorenz's formulation but without global integration (presumably using equation 5.1 with the potential temperature variance being neither horizontally averaged nor vertically integrated). Although their method provided physically reasonable results, it seems more satisfactory to use a more formally complete definition. Other attempts of using the Lorenz energetics locally include spatial integrations over a local domain of an open system which is embedded within a global closed system (Johnson, 1970). In this exact framework the lateral boundaries are permeable to allow energy fluxes between the domain of interest and the environment, whilst ensuring a total energy conservation of the whole system. Gall and Johnson (1971) subsequently demonstrated the application of this framework for a single extratropical storm and highlighted the importance of sensible heating in increasing the storm's APE. A more comprehensive discussion of this approach can be found in Johnson (1982). Though useful for the above applications, the precise spatial distribution of the various energy, conversion and transport terms is still obscure in this framework. In addition, the Lorenz definition of the APE is based on differences between two large terms, which amplifies any initial errors and seems to have resulted in large discrepancies between different studies (e.g. the studies reviewed by Oort, 1964). The need for a different formulation of a local definition is therefore apparent.

Developing from classical physics, another useful concept, "exergy", has been introduced into the atmospheric and oceanic sciences. As Tailleux (2013a) summarises, exergy is defined as the convex part of the internal energy in the entropy-specific volume space, and measures the departure of a system from its thermodynamic and mechanical equilibria. Such equilibria can be identified by defining an isothermal reference state, which was advocated by many (e.g., Dutton, 1973; Pearce, 1978; Blackburn, 1983; Karlsson, 1997). This idea gained popularity due to its simple calculation and local character as opposed to the traditional Lorenz APE. However, as Tailleux (2013a) stresses, exergy is fundamentally different and is too large when compared to Lorenz's APE. This is due to exergy depending on the system being brought to a maximum state of entropy when computing the reference state, whereas Lorenz's APE depends on the system being adiabatically rearranged whilst conserving entropy.

Alternative approaches of defining local APE include those of Holliday and McIntyre (1981) for an incompressible fluid, and Andrews (1981) for a fully compressible stratified one-component fluid. The authors defined APE density as the vertically integrated buoyancy forces acting on each individual parcel between the actual and reference levels. Its precise definition (in units of  $\text{J kg}^{-1}$

and in the notation of Tailleux, 2013b) is:

$$E_a = \frac{g}{\rho_0} \int_{Z_r}^Z (\rho - \rho_r) dZ' \approx \frac{1}{2} N^2 \zeta^2, \quad (5.3)$$

where  $\rho$  is the density and the subscript  $r$  indicates the reference variables. It can be easily related to the small amplitude limit as shown by the last equality, where  $N$  is the buoyancy frequency and  $\zeta$  is the vertical displacement.

An equivalent quantity to APE density, “pseudoenergy”, was derived by Shepherd (1993) using the Hamiltonian formalism. This formulation was later shown to be equivalent to using an extended form of exergy based on a height dependent reference state (Kucharski (1997)), which yields more comparable values to the Lorenz APE than the classical form of exergy and additionally includes diabatic processes. Using this definition, Kucharski and Thorpe (2000) then presented the local distributions of the zonal mean-based energy and conversion terms in a primitive-equation model. However, analysis of the observed local energetics in the atmosphere remains limited.

The APE density framework was then further extended to a multicomponent fluid (Bannon, 2005; Tailleux, 2013b; Peng *et al.*, 2015). It was found that the addition of moisture (i.e. considering the atmosphere as a multicomponent fluid) would introduce the possibility for parcels to possess multiple reference states. This would have a significant impact on the value of the APE and it was found that moisture in general increases the overall value of the APE (Lorenz, 1979; Pauluis and Held, 2002; Bannon, 2005). Peng *et al.* (2015) presented an application of a positive definite definition of the moist local APE, based on using the virtual temperature in an idealised atmosphere, showing the marked difference between using the classical exergy and their APE density.

For the purposes of the present study of large-scale dynamics and energetics of the storm track lifecycle, the analysis in this chapter is limited to the dry (one-component) atmosphere, which should still preserve the general features of the large scale dynamics (Pavan *et al.*, 1999). Tailleux’s (2013b) definition of the APE density (equation 5.3) tailored to the dry system is therefore used here. That said, a more accurate picture would be achieved by including moisture, and the results of the dry energetics below pose a good motivation for such study (though this would be significantly more computationally expensive).

Two types of partition of the APE and KE energies into their mean and eddy components are used: zonal averaging and the 10-day Lanczos filter, which will be hereafter referred to as “zonal-mean framework” and “transient framework”, respectively. The two-dimensional zonal-mean framework is exact, but it suffers from losing one spatial dimension and thus there is a possibility of several storm tracks in a similar latitudinal location interfering with each other. This is likely to be the case when averaging the Northern Hemisphere. In order to reduce this effect, a preliminary experiment using a simplified aquaplanet GCM, PUMA, was performed. The setup was such that a low-level heating dipole produces a localised storm track in the mid-latitudes (more details can be found in Appendix A). The zonal-mean framework includes transient synoptic-scale systems but these are combined with low-frequency stationary waves. In contrast, the transient framework is based on filtering which is not completely commutative, and so the framework is only approximate. However, it does provide a three-dimensional view of the energetics, and its eddy quantities are representative of the synoptic transient disturbances which are the focus of the present study. This framework will therefore be used to analyse the real atmospheric observations, namely the daily ERA-40 and ERA-Interim data.

Furthermore, despite the findings of Plumb (1983) about the redundant nature of the energetics cycle in isolation, energetics will be used here in conjunction with the results of the previous chapters to form a complementary picture of the storm track lifecycle. The five main aspects of this chapter are as follows:

- 1. The Lorenz energy and conversion terms are studied and compared to their globally integrated local equivalents.**

Careful selection of the reference state should theoretically make the (approximate) Lorenz and globally integrated local energetics almost equivalent. Such a comparison can therefore be used as a test of accuracy of the numerical methods used to compute them.

- 2. The time-mean spatial distribution of the local energy density components of the observed data are studied.**

Thus far, such analysis of local energetics in real observations is rather limited and it is shown here that globally integrated energetics can lead to misleading interpretations of the steady-state energetics in the atmosphere.

- 3. The predator-prey behaviour of the energetics is explicitly revealed.**

The results of Simmons and Hoskins (1978) and Tanaka (1995) mentioned in the previous chapters are encouraging, as their numerical experiments imply that a predator-prey relationship may also be preserved in the energy equations, with the mean APE being the prey and the eddy energy being the predator. Here, this relationship is established more directly, and it is demonstrated that it exists in both the energy equations and the atmospheric data (of both the simplified PUMA model and the reanalysis data).

**4. The three-dimensional local spatio-temporal variability of the energetics during the storm track lifecycle is presented.**

This allows a better insight into the linkage between the dynamics of the upstream and downstream ends of the storm track during composite events of high storm track activity. The importance of the overturning circulation during the lifecycle is emphasized.

**5. Sums of all adiabatic terms in the evolution equations are computed to indicate the residual heating and friction terms.**

This enables identification of energy sinks and sources within the storm track, as well as testing that the energetics calculations are of the correct order of magnitude.

This chapter is structured as follows. The next section describes the conventional use of the Lorenz global energetics and compares the results of the current study to past literature. Section 5.3 then defines the local energy densities, the method of their calculation and their evolution equations. Section 5.4 presents one-year averaged spatial distributions of the energetics terms in the reanalysis and idealised GCM data, and compares the zonal-mean and transient frameworks. Section 5.5 focuses on the temporal variability of the energetics within winter storm tracks, including study of the existence of the nonlinear oscillator relationship between the mean and eddy energies in the real atmosphere and in the idealised GCM. The last section discusses the results and highlights the importance of a local but holistic approach when studying the energetics of storm tracks.

## 5.2 Lorenz Energetics in Data

The Lorenz energetics are studied in this section to allow comparison with the local energetics in the next section. The evolution of the Lorenz energy terms is depicted in figure 5.1, and the

precise formulation of the energy terms (expressed in  $\text{J m}^{-2}$ ) and conversions (expressed in  $\text{W m}^{-2}$ ) is:

$$A_m^{(\text{LR})} = \frac{c_p}{2} g^{-1} \int_0^{p_0} \gamma \langle \overline{T'^2} \rangle dp, \quad (5.4)$$

$$A_e^{(\text{LR})} = \frac{c_p}{2} g^{-1} \int_0^{p_0} \gamma \langle \overline{T^2} \rangle dp, \quad (5.5)$$

$$K_m^{(\text{LR})} = \frac{1}{2} g^{-1} \int_0^{p_0} \langle (u^2 + v^2) \rangle dp, \quad (5.6)$$

$$K_e^{(\text{LR})} = \frac{1}{2} g^{-1} \int_0^{p_0} \langle (\overline{u^2} + \overline{v^2}) \rangle dp, \quad (5.7)$$

$$CA^{(\text{LR})} = -c_p g^{-1} \int_0^{p_0} \gamma \left[ \left\langle \frac{\overline{u'T''}}{a \cos \phi} \frac{\partial \overline{T''}}{\partial \lambda} \right\rangle + \left\langle \overline{v'T''} \frac{\partial \overline{T''}}{a \partial \phi} \right\rangle + \left\langle \overline{\omega'T''} \frac{T}{\theta} \frac{\partial \overline{\theta''}}{\partial p} \right\rangle \right] dp, \quad (5.8)$$

$$CE^{(\text{LR})} = g^{-1} \int_0^{p_0} \langle \overline{\alpha' \omega'} \rangle dp, \quad (5.9)$$

$$CK^{(\text{LR})} = g^{-1} \int_0^{p_0} \left[ \left\langle \overline{u^2} \frac{\partial \overline{u}}{a \cos \phi \partial \lambda} \right\rangle + \left\langle \overline{u'v'} \cos \phi \frac{\partial \overline{u} \cos^{-1} \phi}{a \partial \phi} \right\rangle + \left\langle \overline{u' \omega'} \frac{\partial \overline{u}}{\partial p} \right\rangle \right. \\ \left. + \left\langle \overline{u'v'} \frac{\partial \overline{v}}{a \cos \phi \partial \lambda} \right\rangle + \left\langle \overline{u' \omega'} \frac{\partial \overline{v}}{\partial p} \right\rangle + \left\langle \overline{v'^2} \frac{\partial \overline{v}}{a \partial \phi} \right\rangle + \left\langle \overline{u'^2 \overline{v}} \frac{\tan \phi}{a} \right\rangle \right] dp, \quad (5.10)$$

$$CM^{(\text{LR})} = g^{-1} \int_0^{p_0} \langle \overline{\omega'' \alpha''} \rangle dp, \quad (5.11)$$

where the (LR) superscript refers to the Lorenz formulation,  $u$  and  $v$  are the horizontal velocities,  $\omega$  is the vertical velocity defined as the material derivative of pressure,  $\alpha$  is the specific volume,  $\phi$  refers to latitude,  $\lambda$  to longitude and  $a$  to the Earth's radius.  $\gamma$  is independent of the horizontal coordinates and is defined as:

$$\gamma(p) = -\frac{\theta}{T} \frac{R}{c_p} p^{-1} \left( \frac{\partial \langle \overline{\theta} \rangle}{\partial p} \right)^{-1}. \quad (5.12)$$

The bars and primes in the above equations refer to the mean quantities (zonal mean was used for the results below) and the deviations thereof, respectively. The angle brackets denote the average over a closed pressure surface and the double primes are the deviations from it. The derivation of the evolution equations is shown in Appendix F, and the reader is referred to Lorenz (1955) and Oort (1964) for more detail on their formulation.

The Lorenz energy and conversion terms for all seasons of year 2000 of ERA-40 and ERA-

Interim, and for year 20 of the PUMA experiment were computed. Only one year was selected so as to facilitate comparison with the more computationally expensive local framework presented in the next section. These values are shown and compared to those found in previous studies of relevance in table 5.1. It is apparent that the largest energy term is universally the mean APE. This is expected, as only about 10% of this energy reservoir is actually ever being utilised for conversion to other energy terms (Holton, 2004). It can be shown that the ratio between the APE and KE relates to the Burger number, which in most cases corresponds to around 4, a reasonable estimate (Cushman-Roisin and Beckers, 2011). The other three energy terms are comparable in magnitude. The magnitudes of the conversion terms agree with the arguments in the introduction section, with the baroclinic pathway, through the CA and CE conversions, being most prominent.

In terms of the more detailed differences between the datasets, the results from the ERA-Interim and ERA-40 data are very similar to each other. However, they differ somewhat from those of Li *et al.* (2007), who also used the ERA-40 reanalysis data. Their method yielded lower values of the mean quantities and a smaller conversion between the kinetic energies. Some of these differences occur because Li *et al.* (2007) only integrated the data up to 100 hPa whereas all vertical levels were included here. In addition, Li *et al.*'s (2007) study is based on an average of 23 years and uses a combination of the zonal-mean and transient frameworks, whereas the present analysis is based only on one year and uses only the zonal-mean framework. Oort's (1964) results are based on a different dataset, which is based on weather station data (daily analysis by the National Meteorological Center of the U.S. Weather Bureau), rather than reanalysis datasets (which are based on many different sources, including satellite observations) like the data discussed thus far. Oort's (1964) study also only considers data north of 20°N, excluding a large part of the Hadley cell. Oort's (1964) substantially different magnitudes of the energetics to those found here are therefore not surprising.

It should be noted that only using the Northern Hemispheric data is quite a common approach (e.g. Sheng and Hayashi, 1990; Hu *et al.*, 2004) which assumes that the inter-hemispheric energy exchange is negligible. This is desirable because the Southern Hemispheric data are often less well constrained and their inclusion increases errors of the estimates (Kistler and Coauthors, 2001). However, as will be shown below, the energy transport across the hemispheres does seem to be substantial and thus the hemispheric domains cannot be considered to be closed.

Source	AM	AE	KE	KM
<b>ERA-40 (year 2000) z. f.</b>	44.1 (2.1)	5.3 (0.6)	6.5 (0.7)	8.4 (0.6)
<b>ERA-In (year 2000) z. f.</b>	46.1 (2.4)	5.5 (0.6)	6.7 (0.7)	8.4 (0.7)
Oort (1964) z. f.	40	15	7	8
Li et al. (2007) t.-z. f.	43.2	5.5	6.6	7.8
Oort (1964) t.-z. f.	35	20	10	5
<b>PUMA (year 20) z. f.</b>	64.1 (12.3)	2.9 (0.6)	2.7 (0.9)	8.3 (1.7)

**Table 5.1:** Magnitudes of the Lorenz energetics terms. The bold text highlights the computations of the present study, “z. f.” refers to the zonal-mean framework and “t.-z. f.” is the combination of the transient and zonal-mean frameworks. The values in the brackets refer to the standard deviations in that time segment.

Source	CA	CE	CK	CM
<b>ERA-40 (year 2000) z. f.</b>	1.8 (0.4)	2.4 (0.3)	0.7 (0.3)	0.1 (0.3)
<b>ERA-In (year 2000) z. f.</b>	1.9 (0.4)	2.3 (0.4)	0.7 (0.3)	0.2 (0.3)
Oort (1964) z. f.	3.0	2.2	0.4	0.1
Li et al. (2007) t.-z. f.	1.79	2.01	0.20	0.05
Oort (1964) t.-z. f.	2.5	2.4	0.4	0.1
<b>PUMA (year 20) z. f.</b>	2.6 (1.1)	1.1 (0.5)	0.5 (0.3)	0.6 (0.4)

**Table 5.2:** Magnitudes of the Lorenz conversion terms. The bold text highlights the computations of the present study, “z. f.” refers to the zonal-mean framework and “t.-z. f.” is the combination of the transient and zonal-mean frameworks. The values in the brackets refer to the standard deviations in that time segment.

Despite its simplified nature, the PUMA GCM experiment yields comparable results to the reanalysis data, except that the mean APE term is greater by about a half and the eddy terms are smaller by a factor of two compared to the results from the reanalysis. This increases the Burger number by about a half of that observed on the Earth, and magnifies the dominance of stratification over rotation. It is apparent that the simplified setup of one storm track yields less eddy activity and results in these differences. The conversions are of a similar order of magnitude, but the conversion between the potential energies (CA) is now larger than the conversion between eddy energies (CE), implying some diabatic loss of eddy APE. Also, the conversion between the mean energies is somewhat higher, implying an increased influence of (or a greater asymmetry in) the mean overturning circulation. Despite some of these differences, the PUMA run yields sensible values and the next section will analyse whether these are associated with the same spatial distributions as are found in the reanalysis data.

Although the Lorenz framework provides a useful conceptual description of the overall processes involved in global atmospheric circulation, its reliance on the global integration is a limiting

factor. For example, the Hadley cell contributes negatively to the mean APE but the Ferrel cell acts to increase it. As mentioned above, in the global average these circulations mostly cancel out and the regional variability is obscured. This example also demonstrates how studies that limit their domain of integration to specific latitudes may obtain very different results from those when using the global data. With the view to avoid these problems due to global integration, the next sections investigate a local energy approach and demonstrate its applicability to storm tracks.

### 5.3 Local Energy Terms: Method

This section defines the local APE density, the numerical methods used to compute its eddy and mean components, and the formulation of the evolution equations of all four APE and KE energy components.

#### 5.3.1 Definition

As stated above, the definition of the KE in the Lorenz cycle without the global integration gives a measure of the local KE density. However, APE density requires a different definition, based on a local parcel-based approach which is independent of the global state. This study uses Holliday and McIntyre's (1981) definition of APE density ( $E_a$  in  $\text{J kg}^{-1}$ ), which is the vertically integrated buoyancy forces acting on each parcel between its actual level and its reference level. Following Tailleux (2013b) and working in pressure coordinates, this can be written as:

$$E_a = \int_{p_r}^p \alpha(\theta, p') - \alpha(\theta_r(p', t), p') dp', \quad (5.13)$$

where  $\alpha$  is the specific volume viewed as a function of potential temperature and pressure, and the subscript  $r$  indicates the reference variables. The method of computation is as follows.

The first step is to calculate the reference temperature profile  $\theta_r$  and the corresponding  $p_r$  using  $\theta_r(p_r, t) = \theta$ , i.e. the reference pressure (or the neutral level of buoyancy) of a parcel is the pressure at which the reference potential temperature is equal to the potential temperature of that parcel. Assuming a dry atmosphere, only one reference pressure level is possible for each parcel. Three methods were tested to calculate  $\theta_r$ : the "PDF method", the "Quicksort method"

and the “isobaric average method” (see Appendix G for a description and comparison). All three methods yield similar results and so the isobaric averaging method was selected for the study below, in order to make it more comparable to the Lorenz energy results above.

Because it is assumed that the parcels move adiabatically (so that the potential temperature of the parcel is conserved with  $p$ ), the first term in equation 5.13 can be calculated analytically as follows:

$$\int_{p_r}^p \alpha(\theta, p') dp' = \frac{c_p \theta}{p_0^\kappa} (p^\kappa - p_r^\kappa) = c_p (T - T_R) = h(\theta, p) - h(\theta, p_r), \quad (5.14)$$

noting that the specific volume for ideal gas is defined as  $\alpha = R p_0^{-\kappa} \theta p^{\kappa-1}$ . This term can therefore be written as the enthalpy ( $h$ ) difference between the actual pressure level and the reference pressure level. The second term of equation 5.13, on the other hand, cannot be calculated analytically because  $\theta_R$  is an unknown function of  $p$  and  $t$  (so it cannot be taken outside of the pressure integral). It is therefore necessary to estimate  $\alpha_r$  by numerical interpolation. Using linear spline interpolation,  $\theta_r$  was obtained for each time step as a smooth function of pressure. This enabled the estimation of  $\theta_r$  at  $p$ . The  $\alpha(\theta_r, p')$  was then integrated using the trapezoidal rule:

$$\int_{p_r}^p \alpha(\theta_r, p') dp' = \sum_{j=1}^{10} \left[ \frac{1}{2} \frac{R}{p_0^\kappa} \left( \theta_r(p_{[j]}) p_{[j]}^{(\kappa-1)} + \theta_r(p_{[j+1]}) p_{[j+1]}^{(\kappa-1)} \right) \frac{(p - p_r)}{10} \right], \quad (5.15)$$

where the difference  $(p - p_r)$  was divided into 10 smaller intervals,  $(p - p_r)/10$ , to improve the accuracy of the integration. This method was additionally tested on the first term of equation 5.13 and yielded a negligible difference between the analytical and numerical methods.

### 5.3.2 Separation of APE Density into Eddy and Mean Components

As stated in Tailleux et al. (to be submitted), in order to separate  $E_a$  into its eddy and mean components, it is useful to set a new reference pressure,  $\tilde{p}_r$ , which is independent of the averaging used. The averages used in this study are the zonal mean and the 10-day Lanczos filter for the zonal-mean and transient frameworks, respectively.  $\tilde{p}_r$  is found using  $\bar{\theta}_r(\tilde{p}_r, t) = \bar{\theta}$ , and is a function of time and the spatial coordinates (mirroring the dimensions of  $\bar{\theta}$ ). As shown in Tailleux

(to be submitted), the mean and eddy APE density can be partitioned as:

$$E_a^m = \int_{\bar{p}_r}^p \alpha(\bar{\theta}, p') - \alpha(\bar{\theta}_r(p', t), p') dp', \quad (5.16)$$

$$E_a^e = \overline{\int_{p_r}^{\bar{p}_r} \alpha(\theta, p') - \alpha(\theta_r(p', t), p') dp'}, \quad (5.17)$$

This eddy-mean partition is equivalent to that of Lorenz.

The same analytical and numerical methods as used for the total  $E_a$  above were used to compute these quantities. By definition, all  $E_a$ ,  $E_a^m$  and  $E_a^e$  are positive definite quantities and are based on the vertical integral of buoyancy forces, rather the differences between potential energies of the actual and reference states.

### 5.3.3 Local Evolution Equations

The evolution equations for local kinetic energy components are identical to that of Lorenz before the global averaging (as shown in Appendix F) and the procedure of their derivations will not be repeated here. The complete local mean KE density ( $E_k^m$ ) and eddy KE density ( $E_k^e$ ) evolution equations are:

$$\begin{aligned} \frac{\partial E_k^m}{\partial t} = & \nabla \cdot (\bar{u} \overline{u' \mathbf{u}'}) - \nabla \cdot (\bar{v} \overline{v' \mathbf{u}'}) - \bar{\mathbf{u}} \cdot \nabla E_k^m + \overline{u' \mathbf{u}'} \cdot \nabla (\bar{u}) + \overline{v' \mathbf{u}'} \cdot \nabla (\bar{v}) - \bar{\omega} \bar{\alpha} \\ & - \nabla \cdot (\bar{\mathbf{u}} \delta \Phi) + \bar{v} \bar{F}_y + \bar{u} \bar{F}_x, \end{aligned} \quad (5.18)$$

$$\begin{aligned} \frac{\partial E_k^e}{\partial t} = & -\bar{\mathbf{u}} \cdot \nabla E_k^e - \overline{\mathbf{u}' \cdot \nabla E_k^e} - \overline{u' \mathbf{u}'} \cdot \nabla (\bar{u}) - \overline{v' \mathbf{u}'} \cdot \nabla (\bar{v}) - \overline{\omega' \alpha'} - \nabla \cdot (\overline{\mathbf{u}' \delta \Phi'}) \\ & + \bar{v} \bar{F}_y + \bar{u} \bar{F}_x, \end{aligned} \quad (5.19)$$

where

$$E_k^m = \frac{1}{2} (\bar{u}^2 + \bar{v}^2), \quad (5.20)$$

and

$$E_k^e = \frac{1}{2} (\overline{u'^2} + \overline{v'^2}), \quad (5.21)$$

where  $\mathbf{u}$  is the three-dimensional velocity vector,  $\delta\Phi$  is the difference in the geopotential between the reference and actual level, and  $F_x$  and  $F_y$  represent frictional effects in the zonal and meridional directions respectively.

To derive the evolution equations for the mean APE density, the material (Lagrangian) derivative of the mean APE density equation (equation 5.16) is taken. Using the Leibniz integration rule (as shown in Tailleux, 2013b), it is found that:

$$\frac{D_M E_a^m}{Dt} = (\alpha(\bar{\theta}, p) - \alpha(\bar{\theta}_r(p, t), t)) \bar{\omega} + \int_{\bar{p}_r}^p \frac{R}{p_0^K} p'^{K-1} dp' \frac{D_M \bar{\theta}}{Dt} - \int_{\bar{p}_r}^p \frac{R}{p_0^K} p'^{K-1} \frac{\partial \bar{\theta}_r}{\partial t} dp', \quad (5.22)$$

where

$$\frac{D_M}{Dt} = \frac{\partial}{\partial t} + \bar{u} \frac{\partial}{\partial x} + \bar{v} \frac{\partial}{\partial y} + \bar{\omega} \frac{\partial}{\partial p} \quad (5.23)$$

is the mean material derivative.

The mean thermodynamic equation is:

$$\frac{D_M \bar{\theta}}{Dt} = -\nabla \cdot \bar{\mathbf{v}'\theta'} - \frac{\partial \bar{\omega}'\theta'}{\partial p} + \frac{\bar{\theta}}{\bar{T}} \bar{Q}, \quad (5.24)$$

so the second RHS term of equation 5.22 can be written as:

$$\begin{aligned} \int_{\bar{p}_r}^p \frac{R}{p_0^K} p'^{K-1} dp' \frac{D_M \bar{\theta}}{Dt} &= \frac{1}{\bar{\theta}} (h(\bar{\theta}, p) - h(\bar{\theta}, \bar{p}_r)) \frac{D_M \bar{\theta}}{Dt} = \frac{c_p}{\bar{\theta}} (\bar{T} - \bar{T}_r) \left( \frac{\bar{\theta}}{\bar{T}} \bar{Q} - \nabla \cdot \bar{\mathbf{v}'\theta'} - \frac{\partial \bar{\omega}'\theta'}{\partial p} \right) \\ &= \bar{Y} \bar{Q} - c_p \frac{\bar{T}}{\bar{\theta}} \bar{Y} \left( \nabla \cdot \bar{\mathbf{v}'\theta'} + \frac{\partial \bar{\omega}'\theta'}{\partial p} \right), \end{aligned} \quad (5.25)$$

where

$$\bar{Y} = \frac{\bar{T} - \bar{T}_r}{\bar{T}}, \quad \bar{Q} = c_p \frac{\bar{T}}{\bar{\theta}} \frac{D_M \bar{\theta}}{Dt} \quad (5.26)$$

It is noteworthy that the last term of equation 5.22 is cancelled if  $\bar{\theta}_r$  is independent of time.

As for the eddy APE density equation, the material derivative of equation 5.17 cannot be further simplified (due to the  $p_r$  being dependent on the averaging). Thus the evolution of  $E_a^e$  will be calculated by subtracting the  $E_a^m$  evolution equation (equation 5.22) from the mean total APE density evolution equation accordingly:

$$\frac{D_M E_a^e}{Dt} = \frac{D_M \overline{E_a^t}}{Dt} - \frac{D_M E_a^m}{Dt}, \quad (5.27)$$

where

$$\frac{D_M \overline{E_a^t}}{Dt} = \frac{\overline{D E_a^t}}{Dt} - \overline{\mathbf{u}' \cdot \nabla E_a^t}. \quad (5.28)$$

The first term on the RHS of equation 5.28 is:

$$\begin{aligned} \frac{\overline{D E_a^t}}{Dt} &= - \overline{\left( \frac{\partial(\overline{\delta\phi} + \delta\phi')}{\partial p} \right) (\overline{\omega} + \omega')} + \overline{\int_{p_r}^p \frac{R}{p_0^K} p'^{K-1} dp' \frac{D(\overline{\theta} + \theta')}{Dt}} - X \\ &= - \frac{\partial \overline{\delta\phi}}{\partial p} \overline{\omega} - \frac{\partial \overline{\delta\phi'}}{\partial p} \overline{\omega'} + \overline{YQ} - X, \end{aligned} \quad (5.29)$$

where

$$X = \overline{\int_{p_r}^p \frac{R}{p_0^K} p'^{K-1} \frac{\partial \theta_r}{\partial t} dp'}, \quad (5.30)$$

$$\int_{p_r}^p \frac{R}{p_0^K} p'^{K-1} dp' \frac{D(\overline{\theta} + \theta')}{Dt} = \frac{c_p}{p_0^K} (p^K - p_r^K) \frac{D\theta}{Dt} = \underbrace{c_p \frac{T}{\theta} \frac{D\theta}{Dt}}_Q \underbrace{\frac{T - T_r}{T}}_Y. \quad (5.31)$$

Again, if  $\theta_r$  was independent of time then the  $X$  term would vanish. After subtracting the mean equation, the eddy APE density equation is obtained:

$$\frac{D_M E_a^e}{Dt} = \overline{\omega' \delta \alpha'} + c_p \frac{\overline{T}}{\overline{\theta}} \overline{Y \nabla \cdot \mathbf{u}' \theta'} + \overline{Y' Q'} - X' - \overline{\mathbf{u}' \cdot \nabla E_a^t}, \quad (5.32)$$

where:

$$\overline{Y' Q'} = \overline{YQ} - \overline{Y} \overline{Q}. \quad (5.33)$$

The final set of the four energy density equations is therefore:

$$\frac{D_M E_k^m}{Dt} = \overline{\mathbf{v}' \mathbf{u}' \cdot \nabla \mathbf{v}} - \overline{\delta \alpha \overline{\omega}} - \nabla \cdot (\overline{\mathbf{v}} \overline{\mathbf{v}' \mathbf{u}'}) - \nabla \cdot (\overline{\mathbf{u}} \overline{\delta \Phi}) + \overline{\mathbf{v} \mathbf{F}}, \quad (5.34)$$

$$\frac{DE_k^e}{Dt} = -\overline{\mathbf{v}'\mathbf{u}'} \cdot \nabla \overline{\mathbf{v}} - \overline{\delta\alpha'\omega'} - \nabla \cdot (\overline{\mathbf{u}'\delta\Phi'}) + \overline{\mathbf{v}'\mathbf{F}'}, \quad (5.35)$$

$$\frac{D_M E_a^m}{Dt} = \overline{\delta\alpha'\omega} - c_p \nabla \cdot \left( \overline{\mathbf{u}'\theta'} \frac{\overline{T}}{\overline{\theta}} \overline{\mathbf{Y}} \right) + c_p \overline{\mathbf{u}'\theta'} \cdot \nabla \left( \frac{\overline{T}}{\overline{\theta}} \overline{\mathbf{Y}} \right) - \overline{X} + \overline{YQ}, \quad (5.36)$$

$$\frac{DE_a^e}{Dt} = \overline{\delta\alpha'\omega'} + c_p \nabla \cdot \left( \overline{\mathbf{u}'\theta'} \frac{\overline{T}}{\overline{\theta}} \overline{\mathbf{Y}} \right) - c_p \overline{\mathbf{u}'\theta'} \cdot \nabla \left( \frac{\overline{T}}{\overline{\theta}} \overline{\mathbf{Y}} \right) - \overline{X'} + \overline{Y'Q'}. \quad (5.37)$$

The conversion terms equivalent to the Lorenz conversions are highlighted in colour, with CA in magenta, CK in red, CE in blue and CM in green. When integrated globally, it can be shown that if  $\theta_r$  is constant in time then equations 5.34 - 5.37 are of the same form as the Lorenz equations and the system becomes closed (under no diabatic forcing). In contrast to the Lorenz APE definition, however, the local APE does not require a global integration to be formally correct and can therefore be considered in the local context. However, in the local framework additional flux and eddy energy advection terms appear in the evolution equations. These equations are expressed in the spherical coordinates in Appendix H and it is this form that is used for the computations from the data.

It has been noted by James (1994) and Plumb (1983) that the separation between the eddy components is unnecessary, and that the conversion between the mean and eddy components should be considered in terms of both heat and momentum flux divergences simultaneously as is done when using the Eliassen-Palm flux analysis (Andrews and McIntyre, 1976). However, it will become apparent later that retaining this separation provides a better understanding of the spatial dominance of different processes.

## 5.4 Time-mean Spatial Distribution

This section presents the globally integrated local energetics and a comparison with its Lorenz equivalents in the time mean of a single year (year 2000 for the ERA-40 and ERA-Interim reanalysis data and year 20 for the PUMA experiment). Using the same years, this section also compares the zonal-mean framework with the zonally averaged transient framework, and finally it shows the three-dimensional distribution of the local energetics of the transient framework in the time mean. The time-mean diabatic residual terms of the evolution equations are also included, showing energy sources and sinks.

### 5.4.1 Globally Integrated Energetics

Andrews (1981) shows that the volume integrated local APE density is greater than or equal to the (exact) Lorenz energy, depending on what reference state is chosen. In order to make results from the local and the (approximate) Lorenz methods more comparable, this study uses the isobaric average of the potential temperature to compute the reference state, rather than using adiabatic rearrangement (by averaging the pressure along the isentropes) that is used in the exact Lorenz formula. The globally integrated local energy densities and their conversions are displayed in tables 5.3 and 5.4, respectively.

Firstly, the local zonal-mean framework is compared to the Lorenz results in the previous section. Although the general magnitudes of the local energetics are comparable to the Lorenz equivalents, some differences emerge upon closer inspection. In particular, the mean and eddy APE terms are somewhat smaller for the local approach in the reanalyses. However, since only the approximate Lorenz definition was used here, exact agreement is not expected. Furthermore, numerical errors (especially when integrating between the relatively sparse pressure levels) are likely to contribute to this discrepancy. The same factors could also be responsible for the apparent substantial difference in the CA conversion between the two methods. The same comparison for the PUMA experiment yields even greater differences between the APE terms, and the CA and CM conversion terms are approximately twice as large for the Lorenz framework than in the PUMA experiment. This is not surprising since the resolution is much coarser than in the ERA data.

Comparing the zonal-mean and transient frameworks, it is apparent that the eddy quantities are substantially lower for the latter. This is expected, as the definition of the transient eddies here

Source	AM	AE	KE	KM
ERA-40 (year 2000) z. f.	38.0 (2.0)	3.9 (0.4)	6.5 (0.7)	8.4 (0.6)
PUMA (year 20) z. f.	46.1 (6.1)	1.5 (0.5)	2.7 (0.9)	8.2 (1.7)
ERA-40 (year 2000) t. f.	40.2 (2.1)	0.8 (0.1)	1.9 (0.2)	12.1 (0.9)
ERA-In (year 2000) t. f.	41.1 (2.2)	0.9 (0.1)	1.9 (0.2)	12.1 (0.9)

**Table 5.3:** Magnitudes of the local energetics terms. All computations were based on the global domain. “z. f.” and “t. f.” refer to the zonal-mean and transient frameworks, respectively. The ERA data is based on year 2000 and the PUMA results are based on year 20 of the experiment. The values in the brackets refer to the standard deviations in that time segment.

Source	CA	CE	CK	CM
ERA-40 (year 2000) z. f.	0.8 (0.2)	2.4 (0.3)	0.7 (0.3)	0.2 (0.2)
Local PUMA (year 20) z. f.	1.4 (0.6)	1.1 (0.4)	0.5 (0.3)	0.3 (0.2)
ERA-40 (year 2000) t. f.	0.4 (0.1)	1.0 (0.1)	0.4(0.1)	1.7 (0.3)
ERA-In (year 2000) t. f.	0.4 (0.1)	1.0 (0.1)	0.4 (0.1)	1.6 (0.3)

**Table 5.4:** Magnitudes of the local conversion terms. All computations were based on the global domain. “z. f.” and “t. f.” refer to the zonal-mean and transient frameworks, respectively. The ERA data is based on year 2000 and the PUMA results are based on year 20 of the experiment. The values in the brackets refer to the standard deviations in that time segment.

excludes a substantial part of the lower-frequency wave spectrum. Consequently, these lower-frequency waves are incorporated in the mean energies instead. This difference between the two frameworks is also reflected in the smaller conversions between the eddy energy terms and a greater conversion between the mean terms in the transient framework. Nevertheless, it is apparent that the sums of the eddy and mean quantities yield similar values in the two frameworks.

The comparison between ERA-40 and ERA-Interim shows a very good agreement, with ERA-Interim exhibiting slightly higher APE energies. This suggests some sensitivity of the APE computation to the dataset change, most likely due to their different resolutions, but this sensitivity is smaller here than for the Lorenz zonal-mean framework.

This subsection revealed an overall agreement of the amplitudes of the energetics between the local and Lorenz approaches. Greater differences emerged in the comparison between the zonal-mean and transient frameworks. Such differences are to some extent expected due to their different definitions, though it is difficult to identify sources of these discrepancies precisely based on a one-dimensional time series. The following subsections focus on the spatial distribution of the time-mean local energetics of the two frameworks to investigate these differences in more detail.

#### 5.4.2 Zonal-Mean View of the Energetics

This subsection outlines some differences in the local energetics between the zonal-mean and (zonally averaged) transient frameworks.

The comparison between the zonal-mean and transient frameworks shows relatively little difference in the distribution of the energy terms in the zonal-mean picture, as shown in figures 5.2 and

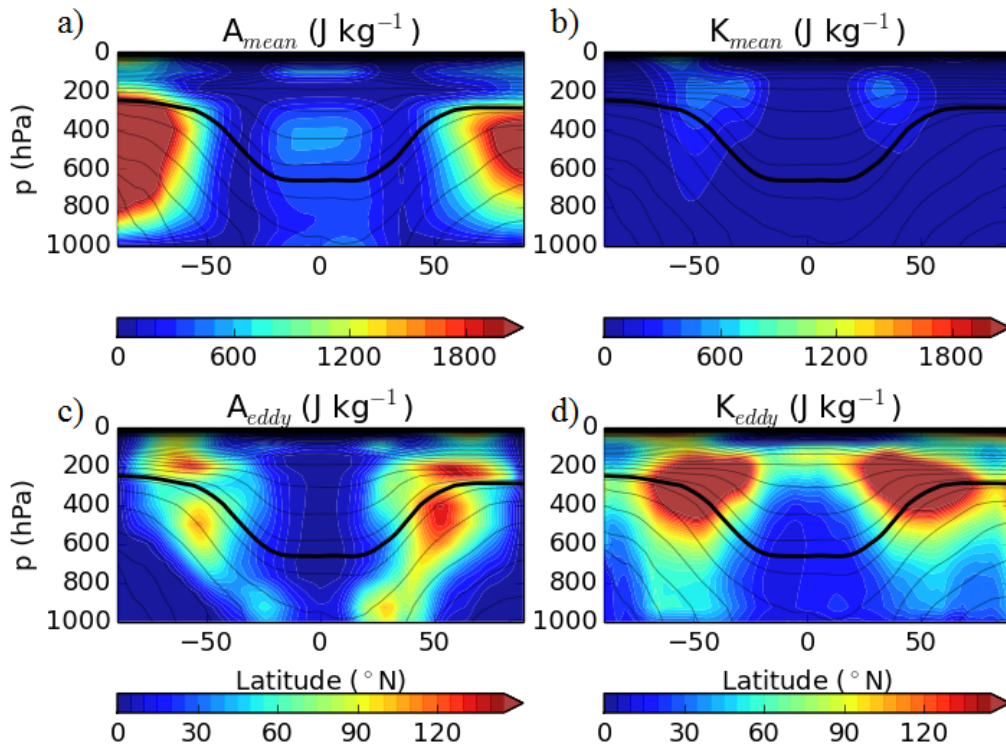


**Figure 5.2:** Pressure-latitude plot of a) mean APE, b) mean KE, c) eddy APE and d) eddy KE, partitioned using the zonal-mean framework and averaged for year 2000 of the ERA-40 reanalysis. The black contours represent zonally averaged potential temperature, with an interval of 10 K and the thick line denoting the 315 K isentrope.

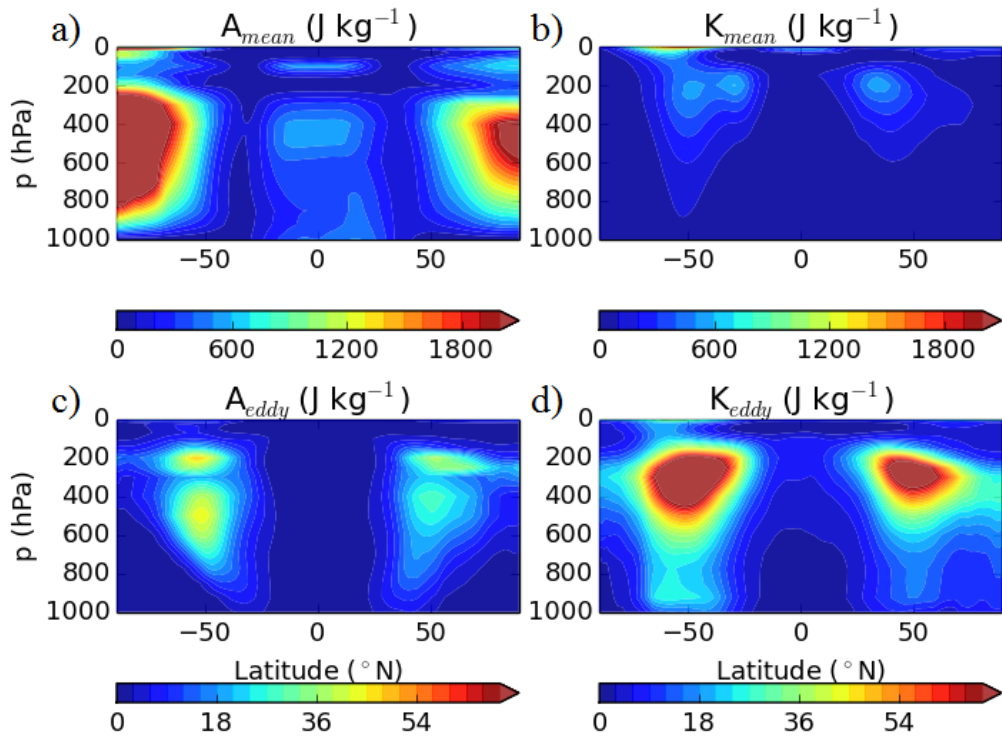


**Figure 5.3:** Same as figure 5.2, but partitioned using the transient framework.

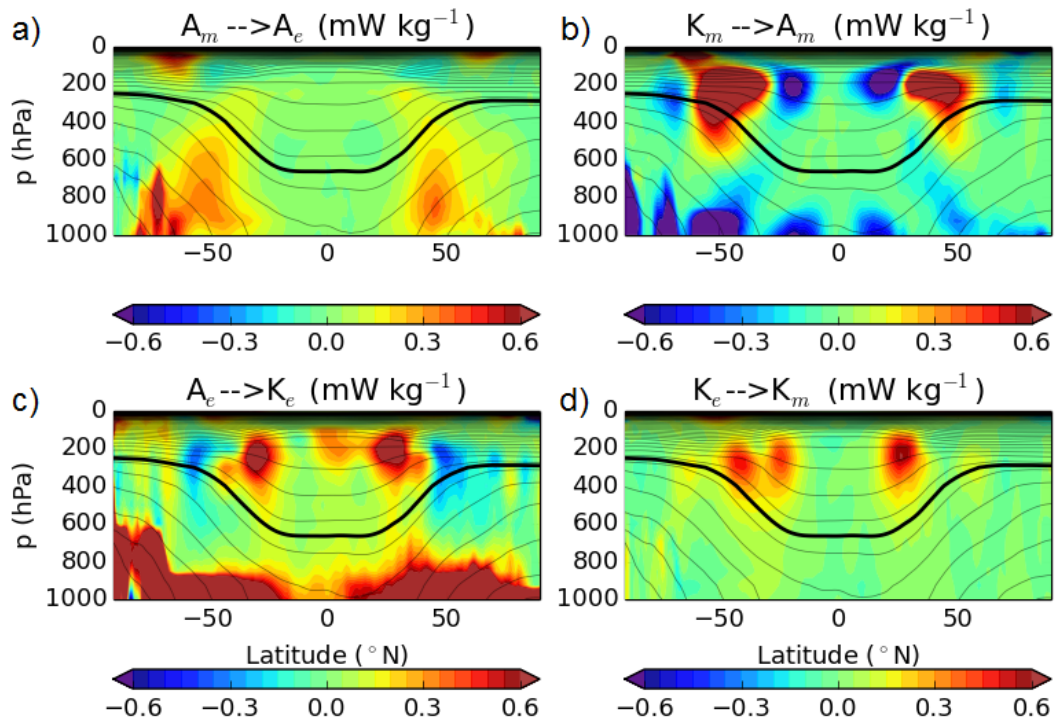


**Figure 5.4:** Pressure-latitude plot of a) CA, b) CM, c) CE and d) CK, partitioned using the zonal-mean framework and averaged for year 2000 of the ERA-40 reanalysis. The black contours represent zonally averaged potential temperature, with an interval of 10 K and the thick line denoting the 315 K isentrope.

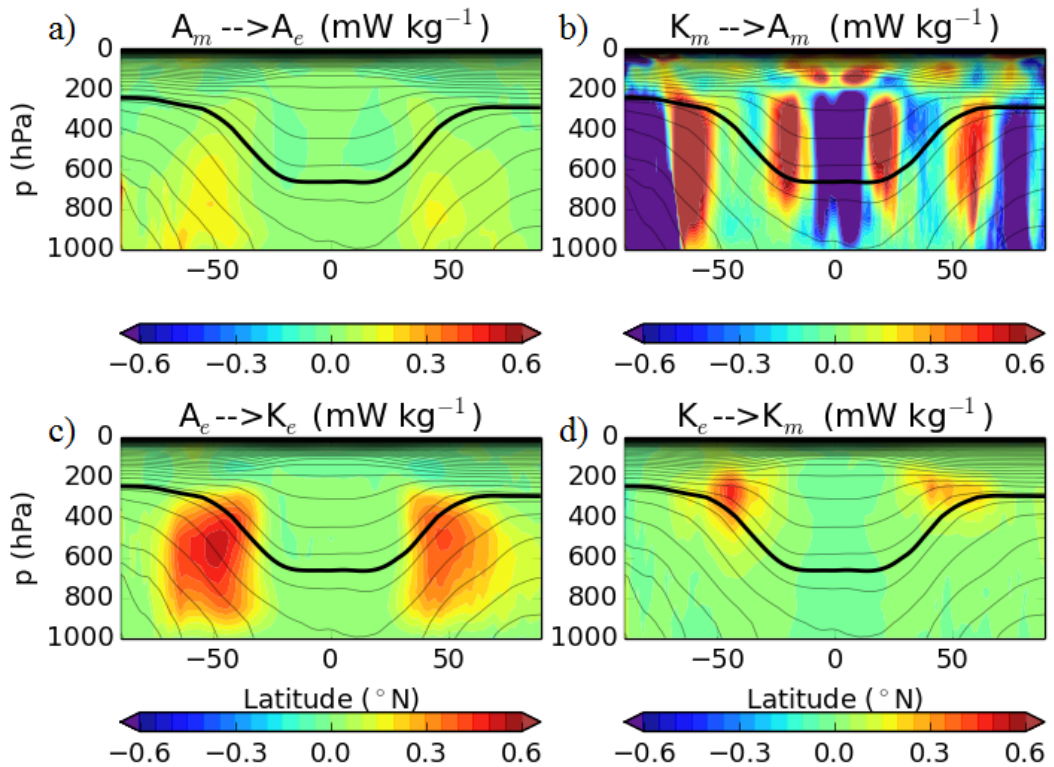


**Figure 5.5:** Same as figure 5.4, but partitioned using the transient framework.

5.3. The transient framework yields slightly sharper maxima of the upper-level jets, and the zonal mean-based eddy energies are more intense than their transient counterparts. As explained above, with the transient eddies only including the synoptic eddies here, this is expected. The zonal mean-based eddy APE also exhibits tertiary maxima near the surface (especially in the Northern Hemisphere). This is because it is associated with surface inconsistencies, such as heating and topography, which contribute to the stationary eddy field.

In terms of the conversion terms (figures 5.4 and 5.5), a greater difference is apparent between the zonal-mean and transient frameworks. In both cases the conversion from mean to eddy APE is mainly concentrated in the lower levels of the mid-latitudes (mirroring the distribution of the meridional heat flux), but in the transient framework it is much weaker due to the synoptic-eddy filtering effect discussed above.

The conversion between the eddy energies exhibits positive values in the mid- to upper-level mid-latitudes in the transient framework. However, in the zonal-mean framework this positive maximum is also accompanied by high positive values at the surface and negative values between 50 and 60 ° of latitude at the mid- to upper-levels. As opposed to the synoptic transient eddies, the zonal mean-based eddies include the effect of topography, which causes deviations from the zonal mean but not from the 10 day time-filtered time series. In addition, the zonal-mean eddies also include lower-frequency waves, which have a different imprint to the synoptic ones (e.g. Hoskins *et al.*, 1983) and may be responsible for the upper-level differences. Stationary eddies are also likely to be partially responsible for the small negative maxima in the upper levels at the eastern sides of the oceanic basins, where these eddies contribute to the storm track termination (Kaspi and Schneider, 2013) and some of the eddy KE is transferred to the eddy APE (as implied by the auxiliary material of Li *et al.*, 2007).

The conversion between the kinetic energies exhibits maxima that follow the maxima of the mean KE in the zonal-mean framework, but in the transient framework only one maximum appears in the Southern Hemisphere. This concurs with the idea that the synoptic transient eddies do not contribute to the subtropical jet very much, whereas any low-frequency meandering of the subtropical jet would imply stationary eddy activity.

The conversion between the mean energies is more vertically consistent in the transient case than

in the zonal-mean framework. In the zonal-mean framework the low levels are dominated by negative values, and there is a dipole in the upper levels on the boundary between the Hadley and Ferrel cells, agreeing with the results of Li *et al.* (2007). On the other hand, the subtropics in the transient framework experience a more dominant influence of the Hadley cell, implying that the thermally indirect circulation induced by the transient eddies in the mid-latitudes is insufficient to counteract the effect of the thermally direct circulation of the Hadley cell. This concurs with the globally integrated results. This insufficiency induces a barotropic pattern of the CM conversion that reflects the pattern of the thermally direct global circulation.

Since Li *et al.*'s (2007) results are based on a combination of both frameworks and are more comparable to the zonal-mean framework analysed here, it is suggested that the zonal-mean eddies have a more prominent influence on the steady-state and low-frequency energetics compared to the transients. In either case, it is noted that the magnitude of this conversion term between the mean energies is locally more influential than implied by its global integral.

Finally, the time-mean energetics in the PUMA model is investigated using the zonal-mean framework, to test to what extent it replicates the features in the real atmosphere. The energy distribu-

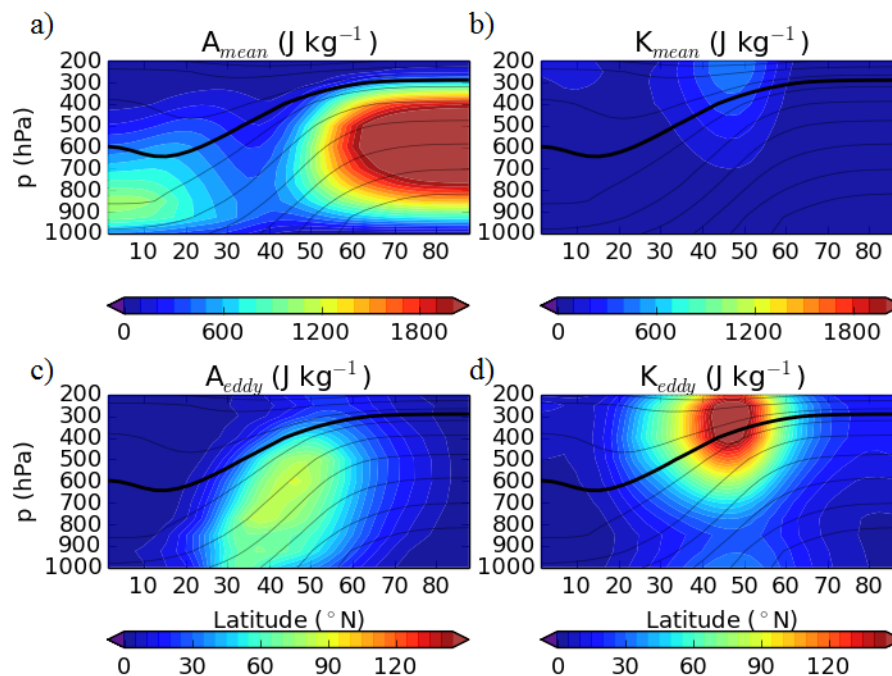


**Figure 5.6:** Pressure-latitude plot of a) mean APE, b) mean KE, c) eddy APE and d) eddy KE, partitioned using the zonal-mean framework and averaged for year 20 in the PUMA run. Black contours represent the zonally averaged potential temperature with an interval of 10 K and the thick contour denoting the 315 K.

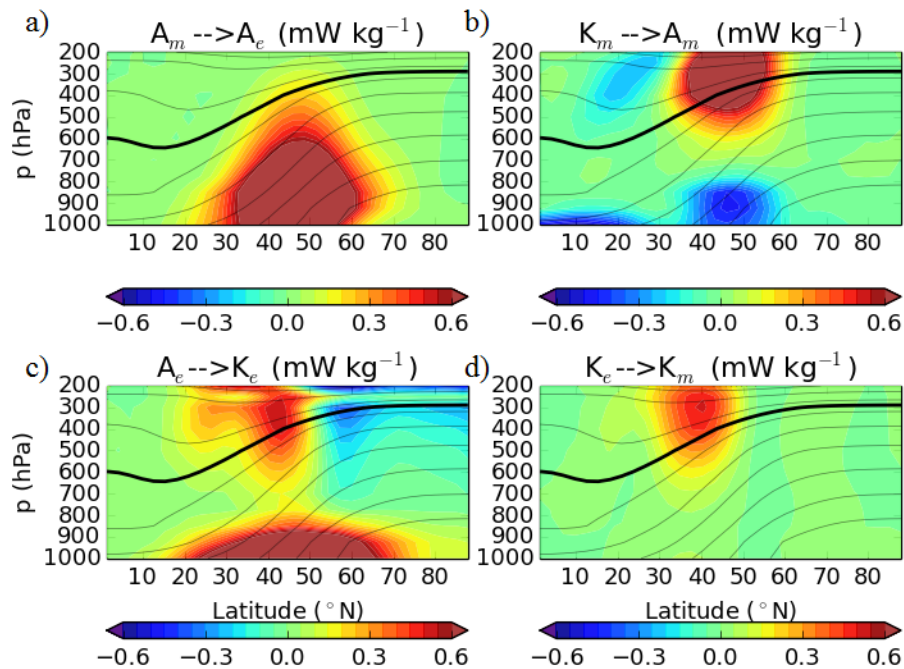


**Figure 5.7:** Pressure-latitude plot of a) CA, b) CM, c) CE and d) CK, partitioned using the zonal-mean framework and averaged for year 20 in the PUMA run. Black contours represent the zonally averaged potential temperature with an interval of 10 K and the thick contour denoting the 315 K.

tions are shown in figure 5.6. Despite the simplified nature of the model's setup, the distribution patterns and magnitudes of the observed energy components presented above are relatively well reproduced here (though the fields are smoother, reflecting PUMA's lower resolution). The mean APE again peaks over the pole with a secondary maximum over the tropics. However, the lack of accounting for moisture in PUMA prevents the effects of latent heat release in the upper-level tropics, which reduces the value of the mean APE estimate there (unlike the ERA reanalyses which incorporate this heating). It should also be noted that the mean APE is somewhat higher relative to the other terms, which is an artefact of a fairly strong heating dipole being imposed to produce the storm track. The APE and KE eddy energies peak again in the mid-latitudes, in the mid- and upper- troposphere respectively. The mean KE maximum marks a mean upper-level jet at 45°N.

The conversions (figure 5.7) also show a good agreement with the observed data. The conversion between the APE energies peaks at the latitude of the storm track in the lower levels, and so does the conversion between the KE terms but in the upper levels. The conversion between the eddy energies again exhibits high values near the surface and a dipole in the upper levels. Finally, the conversion between the mean energies has a maximum in the upper-level mid-latitudes and a negative region in the lower-level and upper-level subtropics. The low levels are dominated by

negative values as in the reanalysis plots.

In summary, most of the differences between the zonal-mean and transient frameworks arise due to the transient eddies being defined as only synoptic (high-frequency) deviations, whereas the zonal mean-based eddies additionally include some low-frequency variability and stationary eddies. Furthermore, although Li *et al.* (2007) investigated the Lorenz energetics without ultimately integrating globally (which may be considered formally imprecise), their results correspond relatively well with the results of the present analysis, namely with the zonal-mean framework. A good agreement in energy density distribution is also apparent between the results of the reanalyses and the PUMA experiment, as well as the idealised study of Kucharski and Thorpe (2000). The local transient framework provides an additional dimension for the spatial analysis and its precise distribution will be discussed in the next section.

### 5.4.3 Three-dimensional Energetics

This section investigates the three-dimensional variability of the Northern Hemisphere energetics in more detail, using the zonally averaged plots of the previous section in conjunction with a latitude-longitude view of the vertically integrated energetics of the transient framework.

As shown in figure 5.3a and 5.8a, the mean APE peaks at mid- to upper- levels in the polar regions, where the potential temperature departs most from the horizontal mean. There is a secondary maximum in the upper-level tropics where the potential temperature is anomalously high. The minima in the mean APE are apparent at the latitudes of the storm tracks, and these are particularly enhanced at the longitudes of their terminations. These values are consistent with those obtained for the extended energy of an idealised atmosphere by Kucharski (2001).

Although the mean KE (figures 5.3b and 5.8b) shows only one maximum in the zonal average of the Northern Hemisphere, it is apparent that there is localised separation between the subtropical and the eddy-driven jets, namely in the North Atlantic region. The jets gain more energy upon entering both storm tracks, which concurs with the arguments presented in the previous chapters.

The eddy energies peak at the latitudes of the storm tracks (figure 5.8c and d), with the North Atlantic storm track being confined to the eastern coast of North America, whereas the North

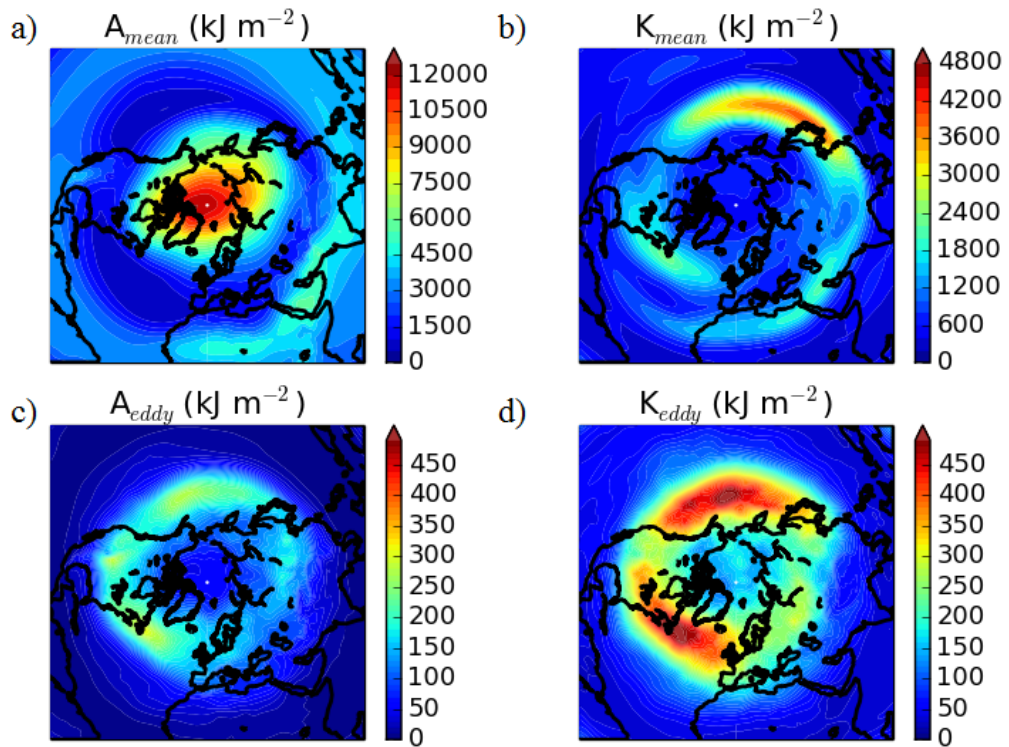


**Figure 5.8:** Energy terms, namely a) mean APE, b) mean KE, c) eddy APE and d) eddy KE. The energies were partitioned using the transient framework, vertically integrated between 1000 hPa and 1 hPa and averaged for year 2000 of the ERA-40 reanalysis.

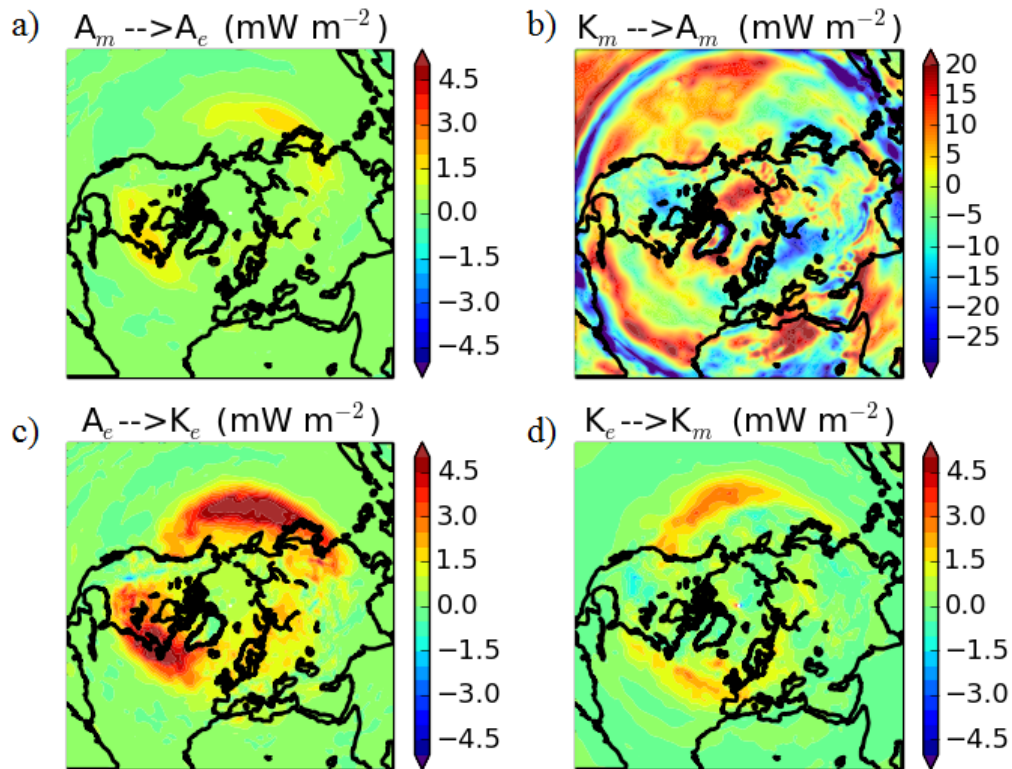


**Figure 5.9:** Same as figure 5.8 but for energy conversions, namely a) CA, b) CM, c) CE and d) CK.

Pacific storm track is more spread downstream and peaks in intensity in the centre of the Pacific (which agrees with the observed time-mean distribution of heat flux discussed in the previous chapters). The zonally averaged plots reveal that the eddy APE exhibits dual maxima, with one in the upper troposphere and one in the lower stratosphere, while the eddy KE peaks near the tropopause. It is also noted that the eddy energies peak near the edge of the polar maximum of the mean APE, suggesting that most of the converted mean APE originates from the polar regions (where it is being generated predominantly by radiative cooling).

In terms of the conversions, their zonally averaged and vertically integrated horizontal plots are shown in figures 5.5 and 5.9, respectively. The baroclinic (i.e. CA and CE) and kinetic (CK) conversions lie within the storm track regions, and their maxima are located more downstream and upwards from the storm tracks, in the order in which they would peak in a typical baroclinic lifecycle. They are of comparable magnitudes and do not exhibit any strong signals beyond the storm track regions. The CK conversion peaks at the downstream ends of the storm tracks, where occlusion of disturbances occurs and barotropic processes tend to dominate (Simmons and Hoskins, 1978).

On the other hand, the conversion between the mean energies has somewhat higher values, both within and outside of the storm tracks (note the different colour scales in the figure). As mentioned above, the cancellation between the Hadley and Ferrel cells causes this term to appear small in the Lorenz values, which gives an impression that this conversion term is almost negligible. However, it is evident that locally this term is very significant. Within the storm track, this term represents a conversion of the jet's kinetic energy back into the mean APE via a mean ageostrophic meridional circulation (that maintains the thermal wind balance). This effect partly counteracts the action of high-frequency eddies that reinforce the jet. The minima in this conversion at the Equator and the subtropics are associated with the thermally direct circulation of the Hadley cell (which is characterised by conversion of mean APE into mean KE).

To conclude, it is apparent that to understand the dynamics of individual storm tracks using energetics, the Lorenz framework is insufficient because it obscures a substantial part of the spatial variability in all of the energy and conversion terms. Although the transient framework is only approximate, it proves useful at indicating the horizontal distributions of the energetics terms, which tend to be very zonally variable in the Northern Hemisphere. These results showed to be

in good agreement with the local energy and conversion calculations of Kucharski and Thorpe (2000), who used an idealised system, and of Li *et al.* (2007) who used ERA-40 data. Unlike the results of the latter study, the results of the present study are based on a more exact definition of the mean APE density.

#### 5.4.4 Residual Diabatic and Frictional Terms

Since all adiabatic terms in the energy evolution equations 5.34 - 5.37 can be readily calculated from the data, it is possible to compute the diabatic and frictional terms as residuals: the mean APE generation ( $H_m$ ), the eddy APE generation ( $H_e$ ), the mean KE dissipation ( $F_m$ ) and the eddy KE dissipation ( $F_e$ ). This subsection studies these residuals in the one-year time mean using the transient framework (assuming only small leakage from the energy evolution equations) to further demonstrate its applicability, and to confirm that the framework yields reasonable residual values.

Figure 5.10 shows the zonally averaged residual terms and figure 5.11 shows their vertically

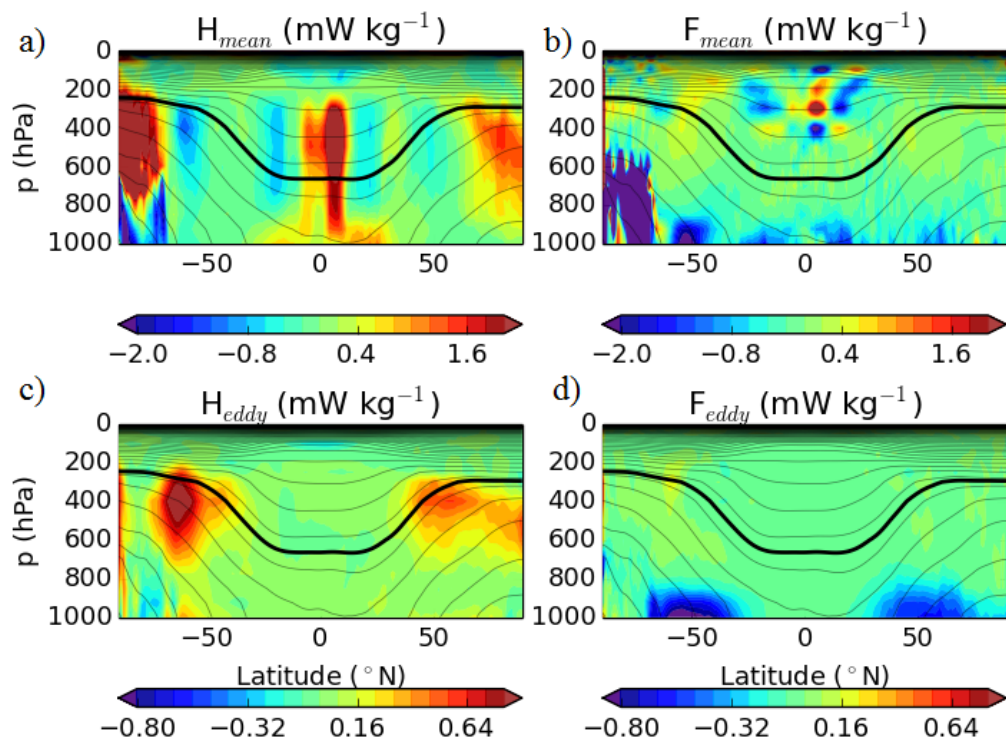


**Figure 5.10:** Pressure-latitude plot of the residual terms, namely a) mean APE generation, b) mean KE generation, c) eddy APE generation, and d) eddy KE generation. These terms were computed using the transient framework and averaged over year 2000 of the ERA-40 reanalysis. The black contours represent zonally averaged potential temperature, with an interval of 10 K and the thick line denoting the 315 K isentrope.

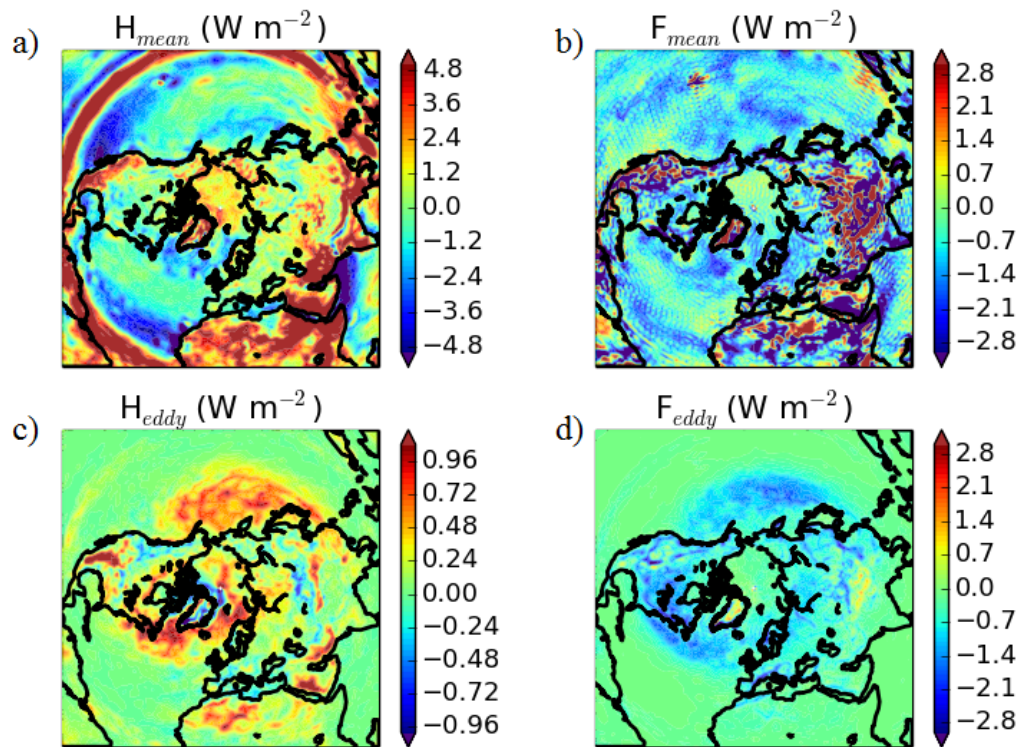


**Figure 5.11:** The low-level residuals, namely a) mean APE generation, b) mean KE generation, c) eddy APE generation, and d) eddy KE generation. The energies were partitioned using the transient framework, vertically integrated between 1000 and 700 hPa and averaged for year 2000 of the ERA-40 reanalysis.

integrated low-level counterparts. In the time mean, the APE energy is generated diabatically in the tropics and in upper-level polar regions. The former corresponds to the convective regions of the Hadley cell supplying sensible and latent heating to upper levels. The polar regions experience a cooling, which increases the temperature variance and thus APE. Friction mostly dissipates the mean KE at low levels, with some wave-like structures appearing in the tropical upper levels (likely stratospheric gravity waves). Eddy energy generation is collocated with the maxima in eddy activity in the upper level mid-latitudes, and eddy friction peaks at the surface at the same latitudes.

In terms of the low-level horizontal distribution, tropical heating dominates the APE production in the troposphere, and a closer look at the lowermost levels (not shown) reveals that there is a slight enhancement along the oceanic boundary currents. The mean APE generation term is negative at the western edges of the subtropical continents where oceanic gyres return relatively cold water equatorwards, inducing cooling at low latitudes and thus decreasing the mean APE there. The eddy APE generation peaks over the storm tracks but has relatively low values compared to the other terms (note the difference in the colour scales in the figure). The mean friction is enhanced

over land and reduced over the oceans, though care needs to be taken when interpreting areas with high topography, since some of the supposed data would in reality be below the surface. The eddy friction dominates the energy dissipation in the locations of the storm tracks. However, it is apparent that in general, beyond the storm tracks the mean friction can attain values comparable to those of eddy friction, which is not obvious from the Lorenz globally integrated terms (e.g. Oort, 1964).

As a basic check, figure 5.12 compares the mean heating (residual heating divided by the thermal efficiency) to the total heating calculated from the forecast net temperature tendencies in the ERA-40 Atlas (Kållberg *et al.*, 2005). Both the zonal-mean and vertically integrated (across the low levels) heating terms show a good overall agreement. The vertical and horizontal pattern of enhanced tropical heating and cooling at the western parts of subtropical continents are apparent. However, there are some differences, especially in the mid-latitudes, where small but positive values of the mean residual heating extend to the upper troposphere, whereas the ERA-40 Atlas shows that this heating only extends to mid-troposphere with small but negative values above. It is likely that the addition of the eddy residual heating would make up for this difference in the mid-latitudes. Furthermore, there are a number of anomalous discontinuities in the residual heating, especially in the mid-latitudes and the upper levels. This is due to the division by the thermal efficiency, which at most levels changes sign in the mid-latitudes. Any small inaccuracy when adding or averaging the resultant components (for example due to using the time filter which is not completely commutative) can then lead to extreme values upon division by the thermal efficiency. Nevertheless, the overall pattern and order of magnitude of the mean residual terms agree with the more directly derived terms.

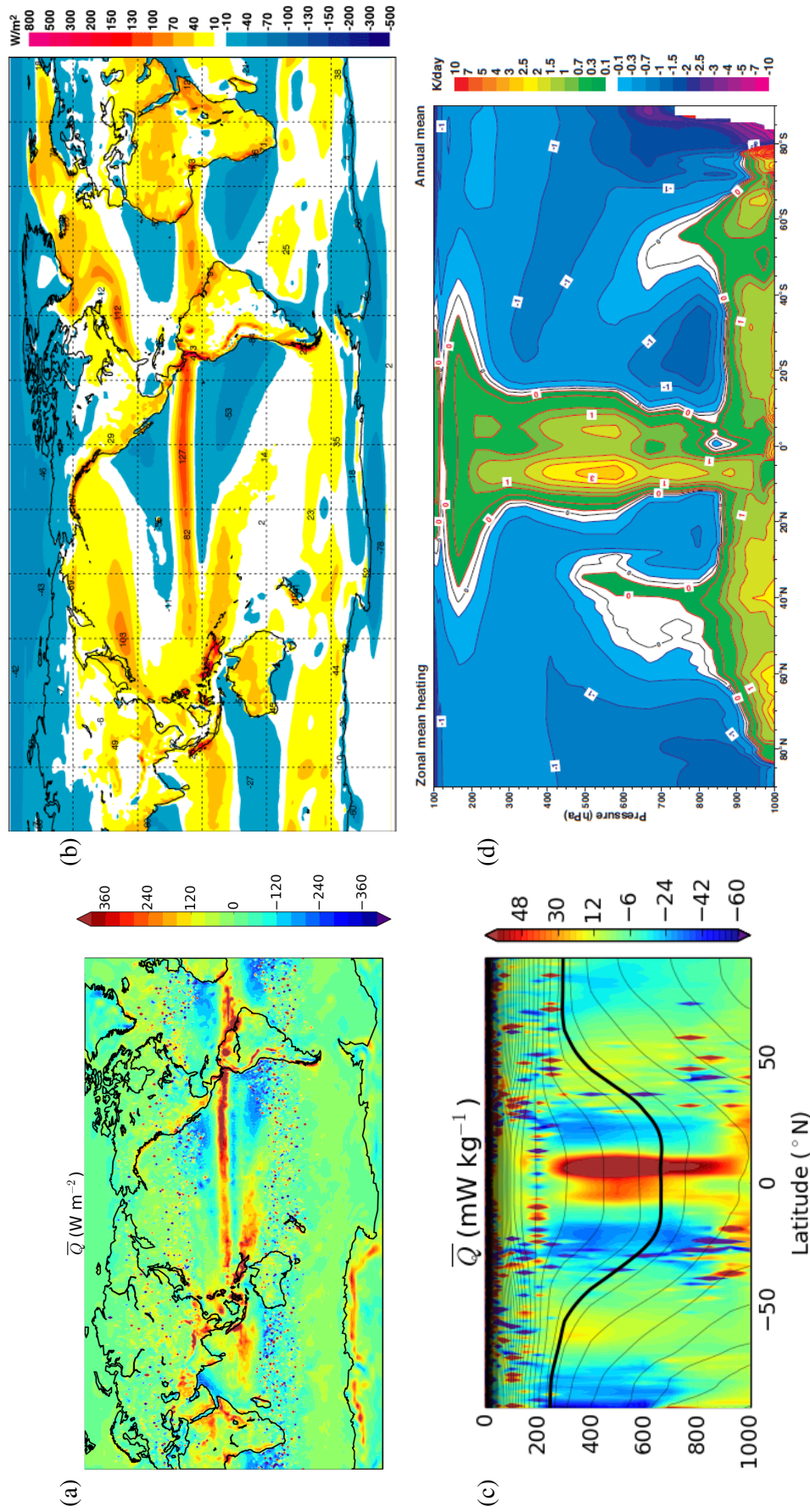


**Figure 5.12:** Vertically integrated between 1000 and 700 hPa (a) and the zonally averaged (c) residual mean heating (the mean APE generation term divided by the mean thermal efficiency) for year 2000 of the ERA-40; and the zonally averaged (b) and d, respectively) from Källberg *et al.* (2005) for the 45-year ERA-40 period.

## 5.5 Temporal Variability during the Storm Track Lifecycle

This section focuses on investigating the temporal behaviour of the eddy and mean energies and the associated characteristics of the flow during the storm track lifecycle. Although a similar behaviour would be expected in the Pacific, the focus of this section is on the North Atlantic storm track which was found to show a clearer oscillatory behaviour in the previous chapters due to its more longitudinally confined nature.

All analysis of the real observations in this section is based on the daily ERA-40 reanalysis, due to its longer data record than ERA-Interim. Lag composites of the energetics are computed and centred around the highest peaks (higher than  $30 \text{ K m s}^{-1}$ ) in the filtered low-level meridional heat flux of the North Atlantic storm track, using the same method as the one used to produce figure 4.11 in Chapter 4. Additionally, the PUMA experiment will be used when testing the zonal-mean framework, and its composites are centred around spikes larger than  $17 \text{ K m s}^{-1}$  of the meridional heat flux (averaged over  $30\text{-}60^\circ\text{N}$ ,  $160\text{-}200^\circ\text{E}$  and  $925\text{-}700 \text{ hPa}$ ). All analysis below is based on the daily winter (DJF) time series (45 winters of ERA-40 and 25 winters of the PUMA experiment) to enhance comparability with previous chapters.

It is specified here that throughout this section the beginning of the storm track (i.e. where eddy heat fluxes and baroclinicity peak) is referred to as the “upstream end” of the storm track, and the area of peaking momentum flux convergence where the eddy-driven jet fluctuates latitudinally is referred to as the “downstream end” of the storm track. Furthermore, throughout this section the zonal averaging and its perturbations are denoted by square brackets and stars, respectively. Similarly, the transient synoptic averaging and its perturbations are denoted by bars and primes, respectively, and the horizontal averaging (on closed pressure surfaces) and its perturbations are denoted by angle brackets and double primes, respectively.

The next section starts with a theoretical justification for the existence of the nonlinear oscillator model in the Lorenz APE energy equations using the zonal-mean framework. The chapter then proceeds to show that such oscillatory behaviour can be observed in the simplified PUMA model for the zonal-mean framework, as well as in the North Atlantic ERA-40 data for the transient framework. This is not surprising since this behaviour is consistent with the storm track lifecycle paradigm. It also discusses the variability of the kinetic energy, conversion and residual diabatic

terms associated with the changes during such a storm track lifecycle.

### 5.5.1 The Nonlinear Oscillator of the Energetics: Theory

The studies of idealised nonlinear storm lifecycles outlined in the introduction (Hoskins and Simmons, 1975; Schneider, 1981; Tanaka, 1995; Kucharski and Thorpe, 2000) provide motivation for testing whether the predator-prey relationship presented in chapter 3 exists in the energetics framework. These studies indicate that bursts in eddy energy are accompanied by fluctuations in the mean APE, analogous to the predator-prey relationship found between eddy heat flux and baroclinicity in the previous chapters. Since they are both measures of storm track activity, eddy heat flux and eddy energy vary in a similar fashion. Similarly, the mean APE and baroclinicity are also related by their dependence on the meridional temperature gradient and inverse static stability. This subsection uses two approaches to investigate more explicitly whether the nonlinear oscillator relationship can be found in the Lorenz energy equations.

#### 5.5.1.1 The “Constant Vertical Tilt” Method

A relationship between the mean APE and the eddy APE, similar to the nonlinear oscillator relationship, has been derived from the approximate Lorenz framework in Appendix I for a channel domain with impermeable meridional boundaries of  $y = -L_y, L_y$ , vertical impermeable boundaries of  $p = p_0, 0$ , and periodic boundaries in the zonal direction. The major assumptions are:

- approximately constant static stability in space and time (as per Schneider, 1981);
- a horizontally constant meridional gradient of the zonal-mean potential temperature (following Schneider, 1981);
- a reference potential temperature profile that is independent of the horizontal (as in Lorenz, 1955), so that  $[\theta](y, p, t) = [\theta]_R(p) + \Delta[\theta](y, t)$ ;
- a zonal perturbation potential temperature that can be defined as a geostrophically and hydrostatically balanced sinusoidal disturbance defined (following James, 1994, p. 125) as:

$$\theta^* \approx \left(\frac{p_0}{p}\right)^\kappa v^* \frac{f_0 p_0}{k \Delta p R} \sin \delta, \quad (5.38)$$

where  $\delta$  is the westward-upward eddy tilt,  $f_0$  is the Coriolis parameter,  $k$  is the zonal wavenumber, and  $R$  is the specific gas constant for dry air; and

- temporal changes in the vertical eddy tilt,  $\delta$ , are negligible.

The resulting equations are

$$\frac{L_y^2}{3} a_1^{-1/2} \frac{\partial \sqrt{A_m^{(LR)}}}{\partial t} = -\{\langle [v][\theta] \rangle\} - a_3^{-1} a_2^{-1} a_4 A_e^{(LR)} - c_p^{-1} \{\langle y[Q] \frac{\theta}{T} \rangle\}, \quad (5.39)$$

$$\frac{1}{2} a_2^{-1} \frac{\partial A_e^{(LR)}}{\partial t} = a_1^{-1/2} a_3^{-1} a_2^{-1} a_4 A_e^{(LR)} \sqrt{A_m^{(LR)}} - \{\langle [\theta^* \omega^*] \frac{\partial [\theta]}{\partial p} \rangle\} + c_p^{-1} \{\frac{\theta}{T} \langle [Q^* \theta^*] \rangle\}. \quad (5.40)$$

where the square brackets denote zonal averaging, angled brackets denote meridional averaging and curly brackets denote vertical averaging. The stars mark the perturbations from the zonal mean. The  $a$  terms are constants and  $Q$  is the diabatic warming rate (James, 1994).

Equations 5.39 and 5.40 suggest a temporal predator-prey relationship between the eddy APE and the square root of the mean APE that is analogous to the nonlinear oscillator model based on baroclinicity and heat flux (that was discussed earlier). Here the mean APE is increased by the diabatic forcing and eroded by eddies (as in the model), while some of it is being affected by the vertically integrated mean meridional flux of temperature. Were the zonal mean meridional velocity assumed to be negligible, as is often the case in baroclinic instability problems such as the Eady model, this term would disappear. The eddy energy is affected by the product of the eddy APE and the square root of the mean APE, and some of it is converted into eddy KE (most of which is then dissipated according to Oort's (1964) estimates). Eddy energy is also enhanced by eddy heating which is often considered to be relatively small (Oort, 1964).

It should be noted, however, that despite the promising arguments above, the assumptions that were used to obtain them could be deemed too crude. In particular, the assumption of a near-constant vertical eddy tilt over the horizontally averaged domain is unlikely to be fully accurate. In fact, the tilt is expected to decrease as waves develop, mature and decay (following the discussion in Chapter 2 pointing out that eddy tilt changes with the eddy heat flux). In addition, the assumption of a vanishing mean meridional wind implies a vanishing mean overturning circulation, which is clearly not the case in the real system. Despite these limitations, the next subsection presents a different and a more physically valid approach to this problem, and one which yields

similar results to equations 5.39 and 5.40.

### 5.5.1.2 The ‘‘Bounded Eddy Stress Tensor’’ Method

Another approach to investigate the relationship between the eddy and mean energy components is described in Marshall et al. (to be submitted) in the oceanic context, and their method can be readily applied to the atmosphere, as is demonstrated in this subsection. A periodic channel domain is taken with vertical boundaries of  $p = p_0, 0$  and meridional boundaries of  $y = -L/2, L/2$ . Working in the QG framework on pressure coordinates and assuming a spatially constant vertical zonal wind shear and a vanishing surface zonal mean wind, the zonal mean wind is:

$$[u](t) = u_t \left(1 - \frac{p}{p_0}\right) \quad (5.41)$$

where  $u_t(t)$  is the mean velocity at the top of the domain. Furthermore, the thermal wind balance yields:

$$[\theta]'' = -f\theta_0 g^{-1} p_0^{-1} y \frac{dp}{dz} u_t(t), \quad (5.42)$$

where, again,  $[\theta]''$  is the zonal-mean meridional perturbation of the potential temperature. The Lorenz mean APE can be written as:

$$\begin{aligned} A_m / \rho_0 &= -\frac{1}{2} c_p \int \int \int \gamma \frac{T^2}{\theta^2} \frac{1}{g\rho_0} [\theta]''^2 dx dy dp = \frac{1}{2} \int \int \int \frac{f_0^2 y^2}{p_0^2} \left( \frac{g}{\theta_0} \frac{\partial \langle [\theta] \rangle}{\partial p} \right)^{-1} u_t^2 dx dy dp \\ &= \frac{1}{24} \frac{f_0^2 L^2}{p_0} \left( \frac{g}{\theta_0} \frac{\partial \langle [\theta] \rangle}{\partial p} \right)^{-1} u_t^2 A, \end{aligned} \quad (5.43)$$

where the term in the square brackets is related to the static stability,  $A$  is the surface area of the domain,  $\rho_0$  is a constant density, and

$$\gamma = -\frac{\theta}{T} \frac{R}{c_p p} \left( \frac{\partial \langle [\theta] \rangle}{\partial p} \right)^{-1} \quad (5.44)$$

The mean KE equivalent is:

$$K_m / \rho_0 = -\frac{1}{2} \frac{1}{g\rho_0} \int \int \int [u]^2 dx dy dp = \frac{1}{6} \frac{1}{g\rho_0} p_0 u_t^2 A. \quad (5.45)$$

Combining the constants of equations 5.43 and 5.45 into one constant,  $c_1$ , allows the total mean energy ( $T_m$ ) to be written as:

$$T_m = c_1 u_t^2. \quad (5.46)$$

Using a bounded eddy stress tensor, Marshall *et al.* (2012) showed that meridional eddy potential vorticity flux ( $[v^*q^*]$ ) can be linked to the total eddy energy ( $T_e$ ) as follows:

$$\int [u][q^*v^*]dV = \alpha \frac{f_0 \rho_0 g}{N_0} A u_t T_e, \quad (5.47)$$

where  $\alpha$  is a constant non-dimensional parameter that is less than unity, and  $N_0$  is the constant static stability. Furthermore, using the Eliassen-Palm relation and the boundary conditions, the LHS of equation 5.47 can be written as:

$$\begin{aligned} \rho_0 \int [u][q^*v^*]dV &= - \int \frac{g f_0 \rho_0}{N_0^2 \theta_0} [v^* \theta^*] \frac{\partial [u]}{\partial z} dV \\ &= \int \int \int \frac{1}{g \rho_0 \theta_0} \left( \frac{\partial \langle [\theta] \rangle}{\partial p} \right)^{-1} [v^* \theta^*] \frac{\partial [\theta]''}{\partial y} dx dy dp = CA. \end{aligned} \quad (5.48)$$

Comparing with the equation 5.8, it is apparent that the last expression of equation 5.48 is equal to the dominant (i.e. the horizontal) component of the conversion between the mean APE and eddy APE ( $CA$ , in  $J s^{-1}$ ). In fact, assuming that  $[u]$  is constant in  $y$  cancels out the horizontal part of the EP flux in equation 5.48, which would otherwise also include the conversion between the kinetic energies (CK). It can therefore be written that:

$$\int \int \int \frac{1}{g \rho_0 \theta_0} \left( \frac{\partial \langle [\theta] \rangle}{\partial p} \right)^{-1} [v^* \theta^*] \frac{\partial [\theta]''}{\partial y} dx dy dp = CK + CA = CT = \alpha \frac{f_0 \rho_0^2 g}{N_0} A u_t T_e, \quad (5.49)$$

where equation 5.47 was used, and  $CT$  is the conversion between the total mean and eddy energies. According to the Lorenz cycle, the total mean and eddy energy evolution equations can therefore be written as:

$$\frac{\partial T_m}{\partial t} = H_m u_t - c_2 u_t T_e, \quad (5.50)$$

$$\frac{\partial T_e}{\partial t} = -c_2 u_t T_e - 2r T_e / c_3, \quad (5.51)$$

where it was assumed that the mean heating dominates the eddy heating, and that the eddy dissipation dominates the mean dissipation (concurring with Oort's (1964) observations).  $H_m(t)$  is a

function dependent only on time, related to Lorenz's (1955) mean heating:

$$H_m(t) = -\frac{f_0\theta_0 A}{g\rho_0} \int_0^{p_0} \gamma \frac{T}{\theta} \langle y \overline{Q''} \overline{T''} \rangle dp \quad (5.52)$$

and  $c_2$  is a constant

$$c_2 = \alpha A \frac{f_0 \rho_0 g}{N_0}. \quad (5.53)$$

A linear parametrisation of Lorenz's (1955) friction term was also used in the eddy dissipation term:

$$\int ([u^* F_x^*] + [v^* F_y^*]) dV = 2rK_e \approx 2rT_e/c_3, \quad (5.54)$$

where the scaling of  $A_e \approx (c_3 - 1)K_e$  with  $c_3$  being constant was used (Huang, 2010). Using equation 5.46, the equation set 5.50 and 5.51 can be written as:

$$\frac{\partial \sqrt{T_m}}{\partial t} = \frac{1}{\sqrt{c_1}} H_m - c_2 \frac{1}{\sqrt{c_1}} T_e, \quad (5.55)$$

$$\frac{\partial T_e}{\partial t} = \left( c_2 \frac{1}{\sqrt{c_1}} \sqrt{T_m} - \frac{2r}{c_3} \right) T_e, \quad (5.56)$$

Assuming a constant mean heating, these equations are identical in form to the nonlinear oscillator model in chapter 3. Furthermore, it can be shown that if only the available potential energies are considered in the method above, this method would yield the equation set derived in the previous subsection (equations 5.39 and 5.40), providing that the mean meridional overturning vanishes in the latter. In this section meridional overturning does not appear due to the fields being integrated vertically. As opposed to the method in the previous subsection, Marshall *et al.*'s (2012) method does not require the assumption of a constant phase tilt, which was deemed unsatisfactory in the previous subsection. In addition, this method does not require a constant diabatic heating, as was required in the nonlinear oscillator model.

Nevertheless, this method does have its own limitations. For example, the globally integrated nature of the components may obscure spatially important mechanisms. Furthermore, the reliance of this method on bounds of energy rather than absolute values, masks the variability of the system within those bounds. The arguments in this section should therefore be viewed as indicative of the presence of the oscillating behaviour, rather than a complete theoretical framework.

It is also noted that the nonlinear oscillator model is based on the predator-prey relationship be-

tween the meridional eddy heat flux and baroclinicity, whereas in the present section it is essentially based on baroclinicity and eddy energy. Eddy energy is therefore assumed to be proportional to the heat flux. Even though heat flux appears in the definition of the conversion between mean APE and eddy energy, it is the product of the eddy energy with the mean temperature gradient that defines the growth of eddy energy. In other words, if both heat flux and eddy energy scale with the square of eddy amplitude ( $a$ ) and if static stability is assumed to be constant then one can write:

$$\frac{1}{2} \frac{1}{v'T'} \frac{dv'T'}{dt} \propto \frac{1}{2} \frac{1}{AE} \frac{dAE}{dt} \propto \frac{1}{a} \frac{da}{dt} \propto s \propto \sqrt{AM} \propto -\frac{dT}{dy}. \quad (5.57)$$

It will be shown in the next sections that both heat flux and eddy energies peak on average on the same day in spatially confined storm tracks, supporting this proportionality.

To conclude the theoretical speculations above, using two different methods this section showed that an approximate predator-prey relationship between mean energy (prey) and eddy energy (predator) is embedded within the Lorenz energy equations. This relationship represents nonlinear oscillations between the eddy energy and the square root of the mean energy, and it is qualitatively analogous to the system of the nonlinear oscillator model if one assumes a constant heating and a linear drag. Using the method above, it can be shown that a similar nonlinear oscillatory relationship exists between the eddy APE and the square root of the mean APE (in which case eddy APE is converted to eddy KE rather than being dissipated). Given the close connection between the Lorenz and local energy systems, the local energetics are expected to exhibit this behaviour at least to some extent. This aspect is investigated using the reanalysis data and the PUMA experiment in the rest of this chapter.

### 5.5.2 PUMA Experiment: Zonal-mean Framework

The theories above suggest that the predator-prey relationship between the eddies and the mean flow should apply to the eddy and mean APE. This section investigates whether this is indeed the case for the zonal-mean framework (which was used in the theory-based arguments above). In addition, a comparison between the Lorenz APE and local APE energy density approaches is provided, with the local energy density approach additionally enabling a spatial insight into the processes involved during the composite of intense heat flux events. Because the zonal-mean framework averages features on the same circle of latitude, using the reanalysis data would likely

cause interference between the two storm tracks. Thus an idealised setup of the 25 winter aquaplanet PUMA experiment (described in section A) was used instead, where only one localised storm track was imposed in the mid-latitudes of the northern hemisphere.

Figures 5.13 a and b show composites centred around the major heat flux events of the four energy components for the Lorenz and local approaches, respectively. The local energy densities are integrated globally for better comparison with the Lorenz energies. Note that all terms were subtracted from the time mean of the composite window in order to emphasize their relative changes. The mean APE is substantially more variable than the other variables, and was therefore allocated a separate axis. By definition, the kinetic energy components are identical in the two plots. It is apparent that the total energy is not completely conserved for either of the two frameworks in this experiment. The APE terms during the composite event fluctuate in a similar manner for both Lorenz and local approaches, with the eddy term peaking a day after the peak in heat flux whilst the mean APE dips during this time. These fluctuations are more pronounced for the Lorenz framework. This behaviour of the APE components is suggestive of the predator-prey behaviour mentioned above, and is reminiscent of the baroclinicity-heat flux composites in the previous chapters. However, the lag between the mean APE dip and peaks in eddy energies is not very apparent. The eddy energies seem to peak approximately a day after the peak in the heat flux. This delay in eddy energy has been observed only in the PUMA experiment, whereas in the North Atlantic eddy energies seem to peak at the same time as the heat fluxes (as is shown in the next section). It should be noted that the PUMA storm track is less locally confined due to its idealised setup, compared to the North Atlantic. The maxima in the eddy energies are therefore more downstream of the maximum in the heat flux compared to the North Atlantic, which may cause the temporal delay. Nevertheless, a small time offset between the mean APE dip and eddy energy peak is still apparent for the local framework in PUMA and may become clearer for higher temporal resolution.

It is also apparent from figure 5.13 that all variables exhibit substantial fluctuations at larger lags, concurring with the periodicity of the nonlinear oscillator model. The time period of these fluctuations is approximately 10 days, as was the case with the fluctuations of heat flux and baroclinicity composites discussed in the previous chapter.

It is of interest to investigate the predator-prey relationship between the mean and eddy APE

terms in more detail. The 25 detrended winter time series were therefore used to construct phase plots for the two Lorenz and local approaches in figure 5.14 a and b, respectively, using the same phase-space filtering method as in chapter 3. The circulating trajectories of both plots in the clockwise direction reinforce the predator-prey argument, where the growth of the mean APE induces growth of eddies, which then feed on the mean APE reservoir. Once this reservoir is sufficiently depleted the eddies reduce in intensity and the eddy energy also reduces, at which point the mean APE reservoir can be replenished again and the cycle repeats. As opposed to the phase plots of the ERA-40 untransformed heat flux and baroclinicity in chapter 3, these phase plots seem to tilt slightly. Such tilting was also observed in the transient framework (not shown), implying that there is a weak inverse relationship between the mean and eddy APE, and that the phase shift between the latter two quantities is slightly larger than  $90^\circ$ , as was indicated in the lagged composites above. This general inverse relationship, however, must not be confused with the relationship between the oscillation amplitudes of the two APE components. It is apparent from the trajectories of the phase plots that the larger the amplitude of the mean APE, the larger the amplitude of the eddy APE, agreeing with Schneider's (1981) results. The thickness of the trajectories also indicates an irregular increase of speed of oscillation with amplitude, demonstrating the nonlinear nature of the oscillations.

The power spectra for the Lorenz and local frameworks (in figure 5.15 a and b, respectively) experience an increase at very low frequencies (below  $0.2 \text{ rad day}^{-1}$ ) for the mean APE, similar to the frequency recovered for baroclinicity and heat flux in chapter 3. The local eddy APE also peaks at this frequency, similar to the Atlantic heat flux power spectrum. However, the spectrum of the Lorenz eddy APE exhibits a dominant peak at a somewhat higher frequency than its mean APE. That being said, it still possesses a substantial power that coincides with the greatest spectral

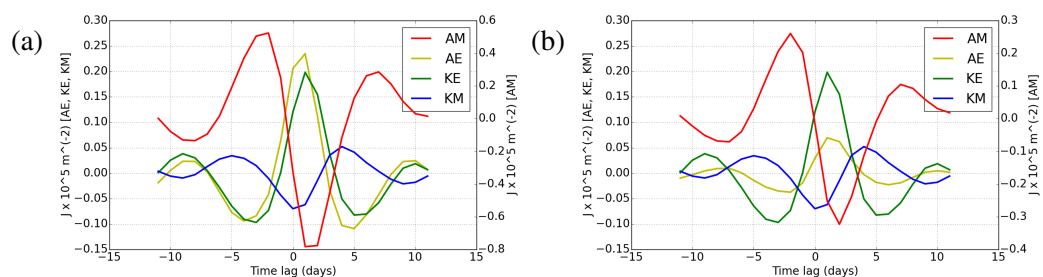


**Figure 5.13:** Lag composites around the highest spikes in heat flux (above  $17 \text{ K m s}^{-1}$ ) for a) the Lorenz energetics, and b) the globally integrated local energy densities, both calculated using the zonal-mean framework from the 25 winter data of the PUMA experiment. The values represent detrended perturbations from the time mean of the 21-day window.

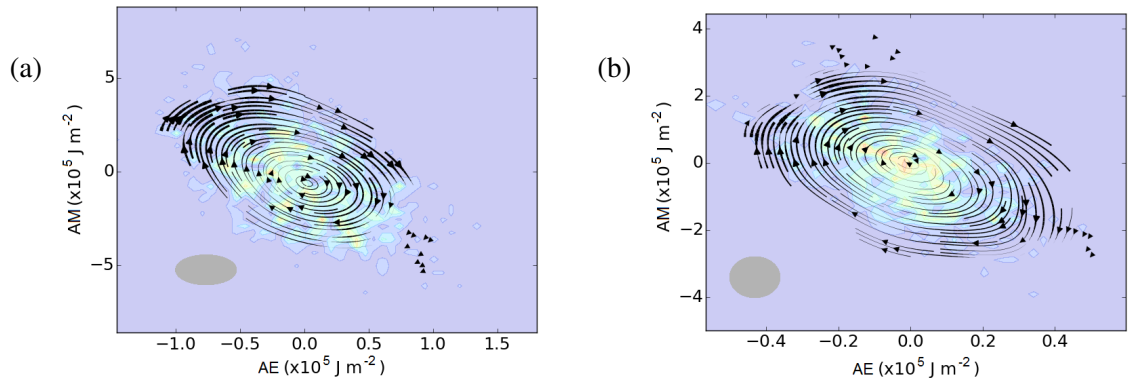


**Figure 5.14:** Phase plots of the mean and eddy APE for the a) Lorenz and b) local approaches, using the 25 winters of the PUMA experiment and the zonal-mean framework. The colour shading indicates the density of points that comprise the phase plot, with warmer colours indicating higher values. The grey ellipse indicates the standard deviation of the filter that was used to average the time series over the phase space.

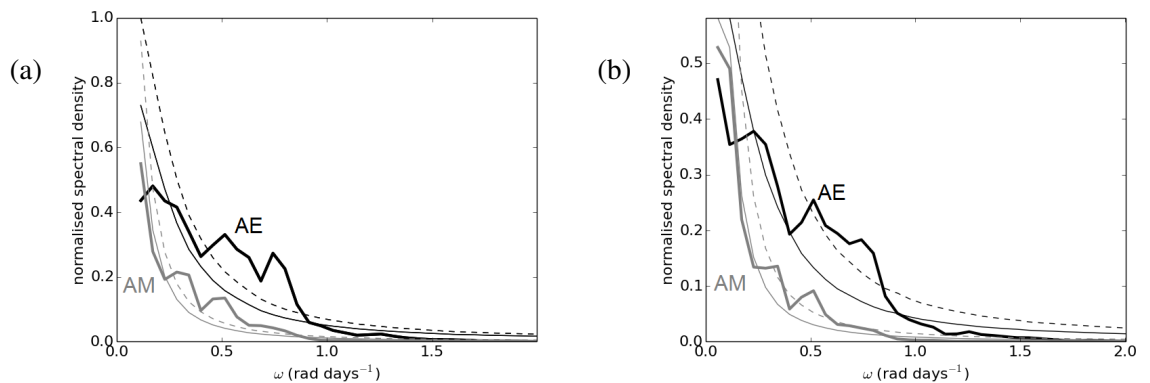


**Figure 5.15:** Power spectra for the a) Lorenz and b) local approaches, using the 25 winters of the PUMA experiment and the zonal-mean framework, with mean APE in grey and eddy APE in black.

increase in the mean APE. The spectral density peak in the eddy APE at frequencies of small mean APE spectral density represents additional variability, which introduces more structure into the phase plots and reveals the diverse nature of the eddy scales involved. As in chapter 3, the very low-frequency increases in the power spectra of both quantities are similar to the red noise spectra (calculated using the same method as in chapter 3), which is reflected in the quasi-periodicity of the system.

Next, the spatial variability during the composite heat flux event is investigated. Figure 5.16 shows composites of the local energy densities during the heat flux event maximum (at lag=0). The time mean of the 21-day window surrounding the heat flux event was subtracted in order to highlight the transient anomalies. At this time the mean APE is reduced greatly between 50

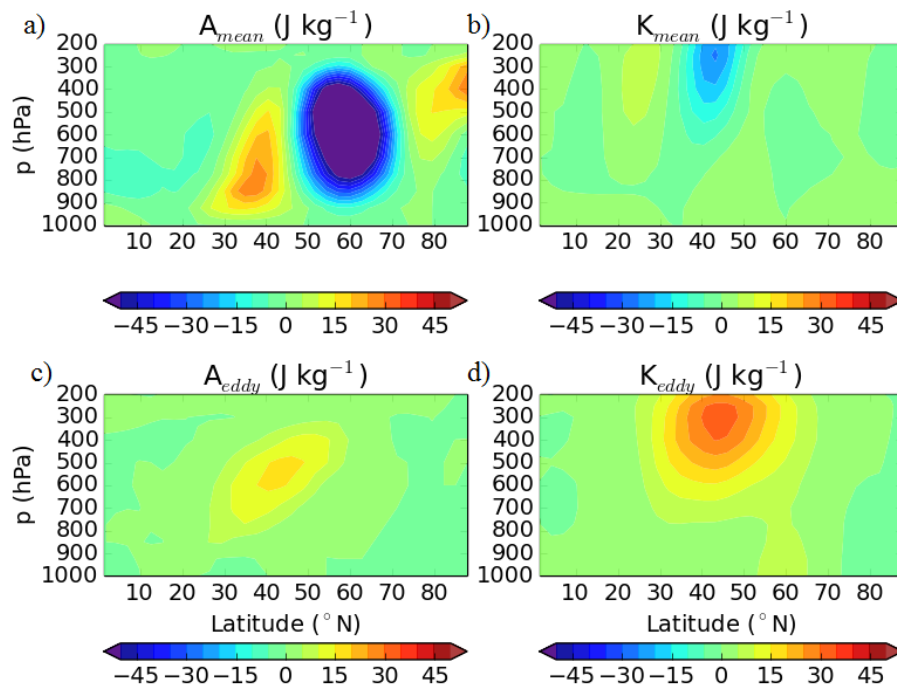


**Figure 5.16:** Zonal-mean energy density anomalies, namely a) mean APE, b) mean KE, c) eddy APE and d) eddy KE, at the peak of the heat flux composite event (lag=0). These terms were plotted as perturbations from the time mean of the 21-day window around those events, using the 25 winter time series of the PUMA experiment. The corresponding red noise power spectra and the 99% confidence intervals are included as the solid and dashed thin lines, respectively.

and 70 °N, as it is being consumed by the eddy activity there. The secondary maxima north and south of this minimum are a side effect of the overall flattening of the isentropes (not shown). Simmons and Hoskins (1978) used an idealised GCM and found a similar pattern, which the authors attributed to the limited extent of the meridional disturbances. This suggests that the mean APE is rearranged, as well as consumed, by the eddies. It should be noted that the mean APE negative anomaly is north of the eddy energy maxima, suggesting that most of the APE that is consumed by the eddies originates from the polar regions.

As expected at this time lag, both available potential and kinetic eddy energies are high at the latitude of the storm track, at the lower and upper levels respectively, as the eddies flux energy downstream and upwards whilst becoming more barotropic. The KE of the mean flow at this lag is affected negatively as the upper-level jet weakens and moves slightly more equatorwards.

In order to gain more insight into the time evolution of the above anomalies, cross sections were taken across the maxima of the energy terms in figure 5.16 (at 500 hPa for mean and eddy APE, and 300 hPa for the mean and eddy KE) and plotted against the time lag of the composite. This

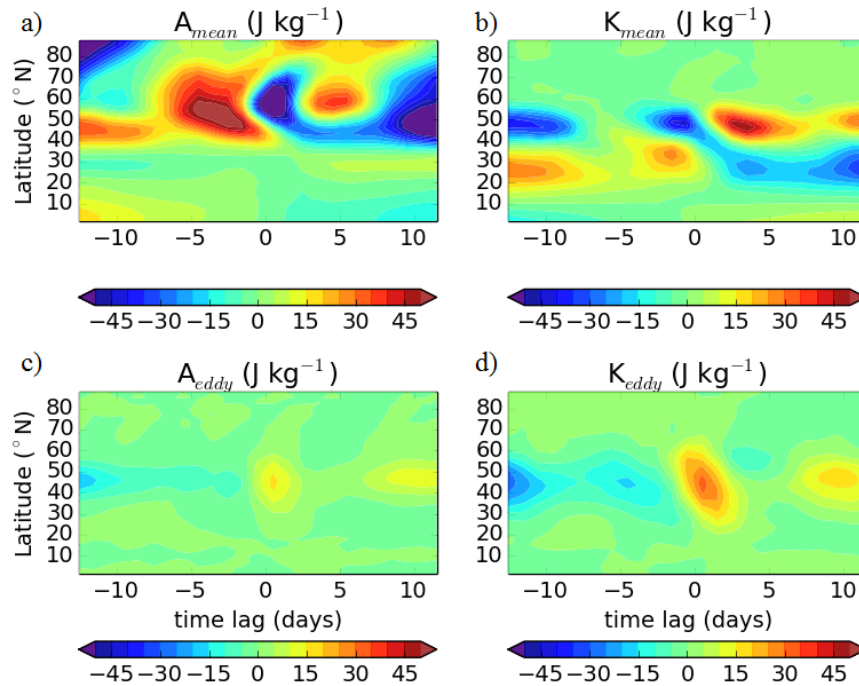


**Figure 5.17:** Hovmöller plot using the cross sections of the terms in figure 5.16, namely using the 500 hPa level for the eddy and mean APE, and the 300 hPa level for the eddy and mean KE.

was possible because the zonal-mean anomalies remained at the same vertical levels throughout the duration of the composite (not shown). The resulting Hovmöller plots are shown in figures 5.17. Although all terms exhibit high-frequency oscillations with a period of around 10 days, an underlying lower-frequency pattern is apparent. This is especially evident in the mean KE, which implies a northward shift of the mean jet that persists following the event (which is consistent with the observations of the North Atlantic jet in the previous chapter). Additionally, eddy activity is generally higher after the event. This lower-frequency variability is also reflected in the switch of the sign of the mean APE at the latitude of (and also equatorward of) the storm track.

Furthermore, the mean APE initially dips sharply north of the storm track as eddies become intense, and then its minimum moves equatorwards. This is most likely due to the eddy activity rearranging the mean APE southwards, the latter then becoming available for further eddy activity.

This section indicates that the nonlinear oscillator behaviour between the mean and eddy energy components exists in the simplified setup of the aquaplanet PUMA model for the zonal-mean framework. However, there is an underlying low-frequency variability which is reflected in shift-

ing of the eddy-driven jet. It was also revealed that it is the mean APE from the high latitudes that is being consumed by the eddies, rather than that originating in the tropics.

### 5.5.3 The North Atlantic: Transient Framework

This section examines the North Atlantic storm track using the transient framework, in order to investigate the interactions between the energies of synoptic transients and the mean flow. In particular, it is of interest to investigate to what extent the nonlinear oscillator relationship between the eddy energy and the mean APE applies to real observations, and to test whether the arguments about the storm track lifecycle based on the Lorenz cycle hold locally for the storm track domain alone.

The energetics terms are first investigated as spatially integrated quantities over a domain that is restricted to the most intense part of the storm track (280 - 320°E, 20 - 80°N, and 1000 - 200 hPa). The energy and conversion terms composited around the highest peaks in heat flux are shown in figure 5.18. Again, the values plotted are the deviations from the time mean of the 21-day composite.

All values of the energy components are substantially lower than those of the zonal-mean framework, due to the spatially restricted domain. Nevertheless, the composite fluctuations are reminiscent of those of the zonal-mean framework, also indicating predator-prey behaviour with the eddy energies now peaking at the same time as the heat flux. The conversion terms in figure 5.18b

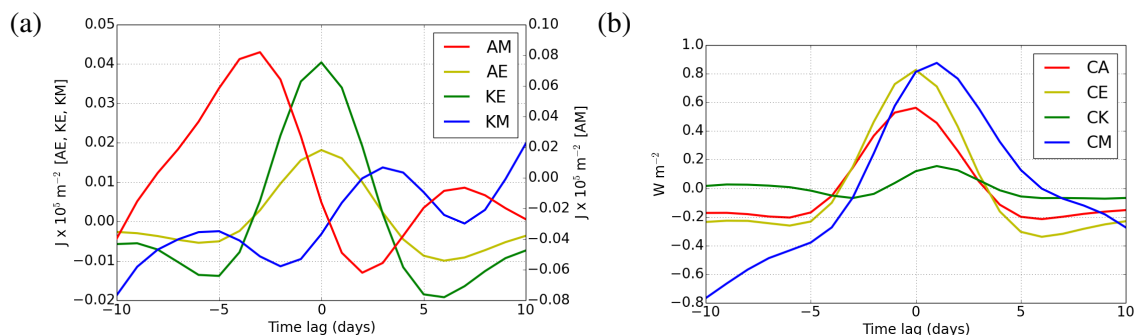


**Figure 5.18:** Lag composites around the highest spikes in heat flux ( $17 K m s^{-1}$ ) for the magnitudes of a) the local transient energy terms, and b) the associated conversion terms, integrated over a locally restricted domain (280-320°E, 20-80°N, and 1000-200 hPa), from the DJF time series of the ERA-40 data. All values are detrended and represent perturbations from the time mean of the 21-day window.

show a successive conversion from mean APE to eddy APE and eddy KE. This is then followed by an enhanced conversion from eddy to mean KE, as well as substantial conversion between the mean energies (with mean KE being converted to mean APE). This behaviour concurs with the arguments above and with lifecycle experiments (e.g. the PUMA experiment above; Simmons and Hoskins, 1978; Tanaka, 1995). One striking difference, however, is that the magnitude of the conversion term between the mean energies is somewhat larger here. Although this term is usually thought of as being small (e.g. Oort, 1964) due to cancellation between large values at different latitudes, the locally restricted integration over the storm track results in this term no longer cancelling to such a small value. Additionally, this term does not quite return to near its initial value at the end of the composite, suggesting a potential involvement of this term in the low-frequency variability of the storm track. Indeed, in such a spatially restricted open domain, it is difficult to make any conclusive statements without considering the detailed evolution of the additional terms of the eddy evolution equations, which is the subject of future work. Here the focus is on the existence of the predator-prey relationship between the APE components, which does seem to emerge in the composites above, with the APE recovering only partially after the eddy event, reflecting the different timescales of baroclinicity replenishment discussed in chapter 3.

In order to ascertain that the nonlinear oscillator relationship applies qualitatively to the mean and eddy APE, their phase plot is again constructed in figure 5.19a (using the same spatial averaging over the most intense part of the storm track as above). The familiar structure of a clockwise circulation is recovered, especially for smaller amplitudes, where the system spends most of the time. At large amplitudes the system becomes more irregular, exhibiting additional structure. Thus in general, the transient eddy energy and the associated mean energy also appear to follow the nonlinear oscillator model, as predicted by the theory based on the zonal-mean framework (as presented above). After comparison with the PUMA experiment it is notable that the phase plot is no longer tilted. In this case, the North Atlantic storm track is more longitudinally contained, which decreases the spatial and temporal delay between the maxima of the mean and eddy APE. As a result, the North Atlantic yields power spectra of the mean and eddy APE that are generally more similar to each other in terms of their shape (figure 5.19b). The red noise-like low-frequency (at around  $0.2 \text{ rad day}^{-1}$ ) spectral increase is again apparent for both quantities. The heat flux peaks at higher frequencies (in this case significantly different from the red noise spectrum) are now much less dominant.

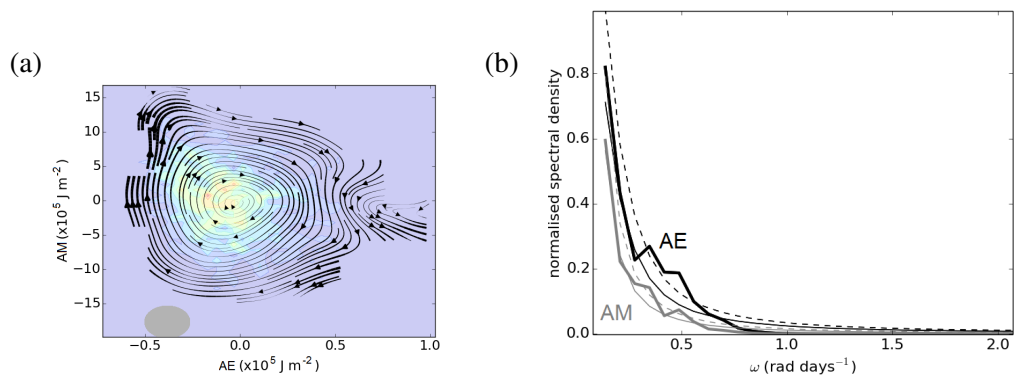


**Figure 5.19:** a) Phase plot of the mean and eddy APE for the transient framework from the 45 winters of the ERA-40 data. The colour shading indicates the density of points that comprise the phase plot, with warmer colours indicating higher values. The grey ellipse indicates the standard deviation of the filter that was used to average the time series over the phase space; b) the associated power spectrum with mean APE in grey and eddy APE in black.

To investigate the spatial characteristics of the behaviour described above, composites of the spatial distributions around the highest heat flux peaks were constructed for the energy densities and conversion terms. A horizontal polar view of the vertically integrated energy and conversion terms for the Northern Hemisphere is shown in figures 5.20 and 5.21, respectively, for the time of the peaking heat flux (time lag = 0). Again the quantities are plotted as deviations from the composite time mean. The eddy energy anomalies exhibit little variability outside of the North Atlantic basin. This is not the case, however, for the mean energy terms.

The mean APE anomaly in the region slightly north of the eddy energy maxima is substantially below average, but its values also increase markedly over northern Canada and over north-east Eurasia. A resultant quadrupole pattern centred over the polar region is apparent. It is evident that the anomalies of the mean APE are much higher than those of the other energy terms, suggesting that the changes in its advection, generation and dissipation are of a comparable importance as the conversion terms. In fact, preliminary analysis shows that the major positive maximum is mainly down to mean advection of the mean APE. Smaller increases in the mean APE are also apparent to the south-east of the storm track. This pattern concurs with that of the zonal-mean framework, where the edges of the storm track are associated with sharpened temperature gradients.

The mean KE again suggests a poleward shift in the eddy-driven jet in the North Atlantic. A similar but weaker signal can be observed in the Pacific. The subtropical jet gains mean KE in the eastern subtropics over both basins. The North Atlantic storm track activity therefore seems to be

associated with a hemispheric-wide imprint in the mean jets.

Aside from the conversion between the mean energies, the anomalies of the conversions (all three of which involve eddy activity) have a weak signal beyond the North Atlantic basin, and their maxima are positioned with distance downstream in the same order as they would occur in time according to the Lorenz cycle. Thus as the eddies move downstream, the energy is successively converted from mean APE to eddy energies and finally to mean KE, which is consistent with the traditional picture of the idealised energetics lifecycle (Simmons and Hoskins, 1978). As this framework is based on synoptic eddies, the conversion between the kinetic energies has no strong negative values, which agrees with Hoskins *et al.*'s (1983) findings that synoptic scale eddies tend to reinforce the mean flow along the storm track. The conversion term between the mean energies comprises very high positive and negative values in both basins, though the North Atlantic anomalies are greater. The latter are positive north of the beginning of the storm track and negative towards the downstream end, implying opposing effects on the mean flow by the associated ageostrophic circulation in these regions. This agrees with Orlanski and Katzfey's (1991) case study of a single storm, which revealed that the growth stage of the storm exhibited an increase of the energy available for eddy growth due to the associated ageostrophic circulation, whereas this energy was converted back to the mean KE during the decay stage.

To investigate the vertical structure of the energetics of the zero lag of the composite heat flux event, the anomalies from the composite time mean were zonally averaged for the beginning and downstream ends of the North Atlantic storm track, and plotted in figures 5.22 and 5.23, respectively. Along the whole storm track the eddy APE has two maxima, one in the upper troposphere and one in the lower stratosphere, whereas the eddy KE peaks near the tropopause, and both of these eddy energies reduce with distance downstream. The mean APE at the beginning of the storm track exhibits a deep tropospheric maximum at around 60 °N and is surrounded by strong minima on either side. This becomes almost entirely negative further downstream. At the beginning of the storm track the mean APE is expected to be higher and its anomaly is in fact being reduced overall at this time (as will be shown below). The mean KE is enhanced throughout the depth of the troposphere at around 50°N at the beginning of the storm track, but it is enhanced closer to the equator and weakly at high latitudes further downstream, indicating a split in the subtropical and eddy-driven jets (as was shown in the horizontal plots above). It is also worth noting that the mean energy components exhibit some weaker variability in the

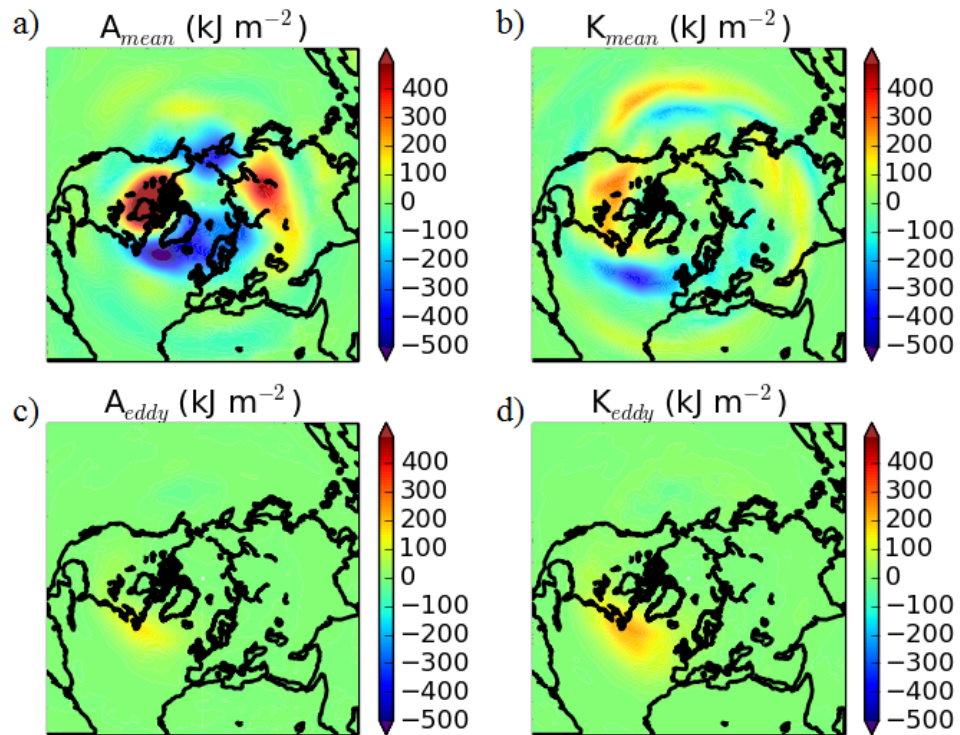


**Figure 5.20:** Horizontal view of local energetics, namely a) mean APE, b) mean KE, c) eddy APE and d) eddy KE, at time lag 0 of the heat flux composite, plotted as deviations from the time mean of the 21-day window, vertically integrated and based on the transient framework and the DJF data of ERA-40.

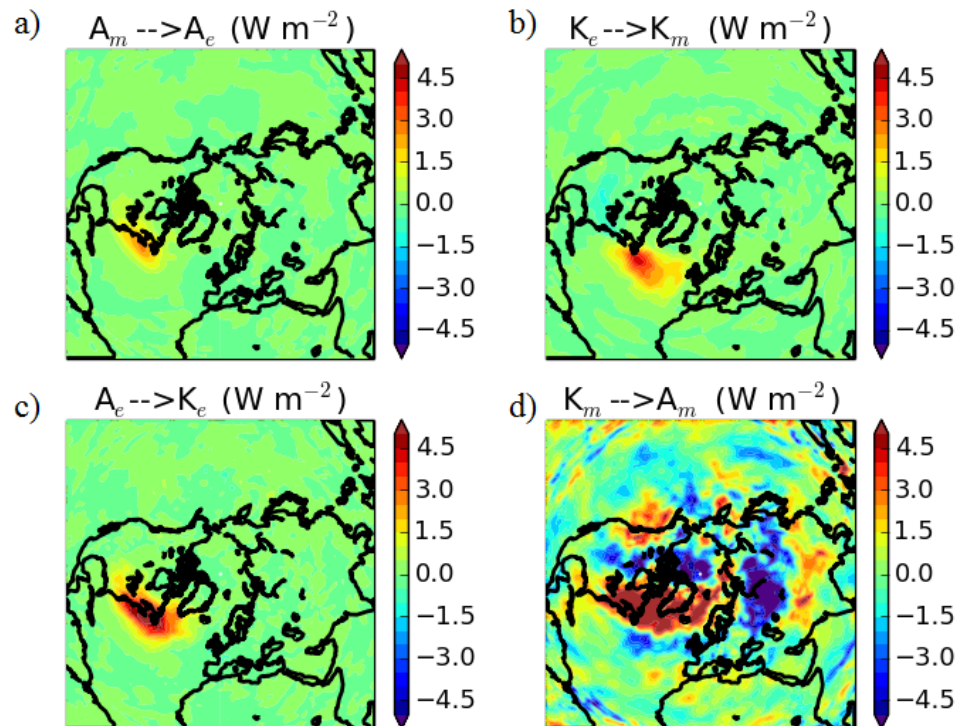


**Figure 5.21:** Same as figure 5.20 but for the local conversion terms, namely a) CA, b) CK, c) CE and d) CM.

Southern Hemisphere, suggesting a sensitivity of the global mean state to interactions in the North Atlantic. The mutual dependence of the hemispheres would explain the discrepancies between the Northern Hemispheric and the global integrals of the mean energetics that were discussed above. The Hovmöller plots presented below show that this interhemispheric connection is statistically significant.

Figures 5.24 and 5.25 show the equivalent zonal-mean figures for the upstream and downstream conversion terms, respectively. The conversion from mean APE to eddy APE is strongest in the low levels of the beginning of the storm track, and the conversion between the eddy energies is largest at a higher altitude and stretches over most of the tropospheric depth. The conversion between the kinetic energies is near the tropopause, whereas that between the mean energies extends throughout the troposphere. This agrees with the notion that energy conversion from mean APE to eddy APE to eddy KE follows the propagating disturbances upwards as they propagate downstream. The conversion between the mean energies tends to act against the conversion between the eddy energies via a mean meridional circulation, though it introduces some additional variability beyond the storm track latitude.

The time evolution of the energetics was studied using Hovmöller plots. Since the upstream anomalies discussed above are not very variable with height, a cross section was taken across the maxima of the variables of figures 5.22 and 5.24, and these were plotted against time to extract the evolution of those anomalies in time around the composite heat flux spike. Figures 5.26, 5.27 and 5.28 show the evolution of the upstream energy terms, downstream energy terms and the upstream conversions, respectively.

The mean APE increases prior to the eddy activity intensification, decreases substantially during it along all northern latitudes below  $70^{\circ}\text{N}$ , and recovers slightly following it. This was observed in the domain integrated energetics, as shown in figure 5.18. However, what was not shown previously is an apparent northward propagation of the anomalies of the mean APE from the latitude of the storm track, whilst south of it the anomalies are weaker and remain at the same latitude. A similar picture but with an inverted sign can be observed in the Southern Hemisphere, implying an associated global connection. This Northern Hemispheric pattern of the mean APE anomalies is somewhat different to that of the zonal-mean framework in the PUMA experiment, where these anomalies appear to propagate southward. This indicates that eddies use a little more

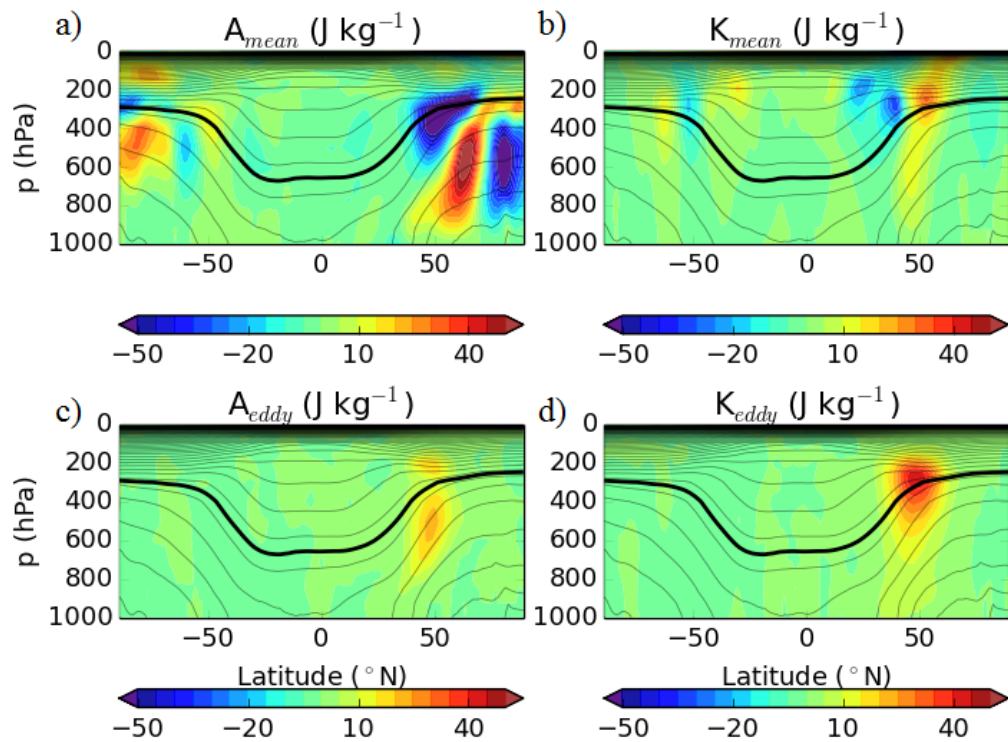


**Figure 5.22:** Zonal-mean view of local energetics, namely a) the mean APE, b) mean KE, c) eddy APE and d) eddy KE, at the beginning of the storm track (averaged between 280 and 320°E) at time lag 0 of the heat flux composite, plotted as deviations from the time mean of the 21-day window, vertically integrated and based on the transient framework and the DJF data of ERA-40. The black contours are potential temperature at this time, with an interval of 10 K and the thick line marking the 315 K isentrope.

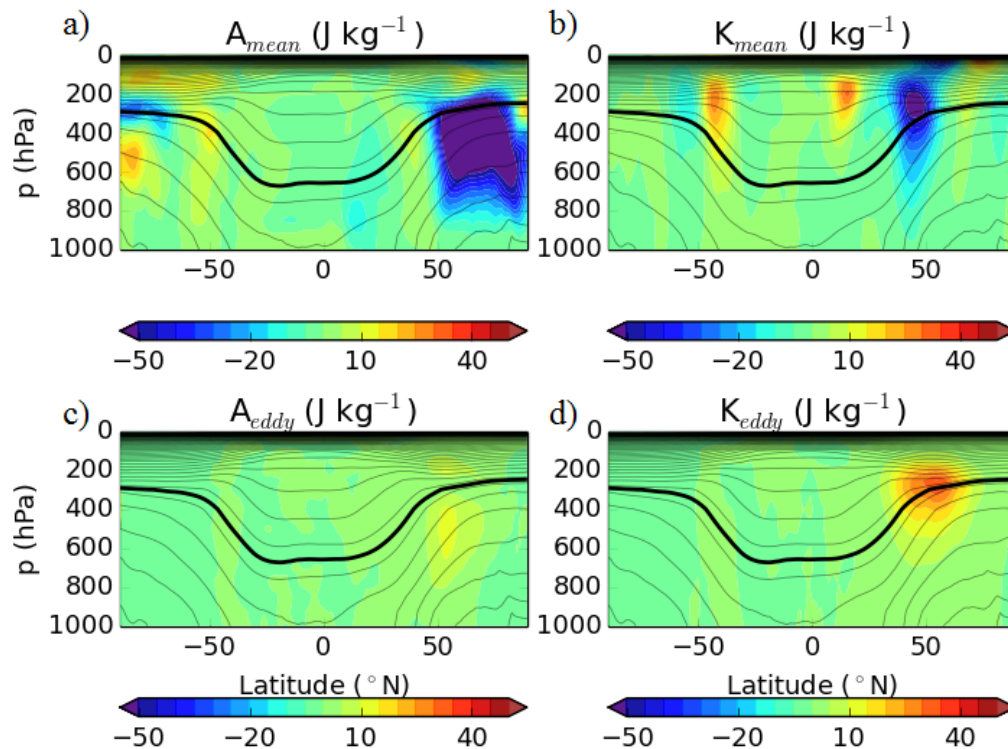


**Figure 5.23:** Same as figure 5.22, but for the end of the storm track (averaged between 320 and 360°E).

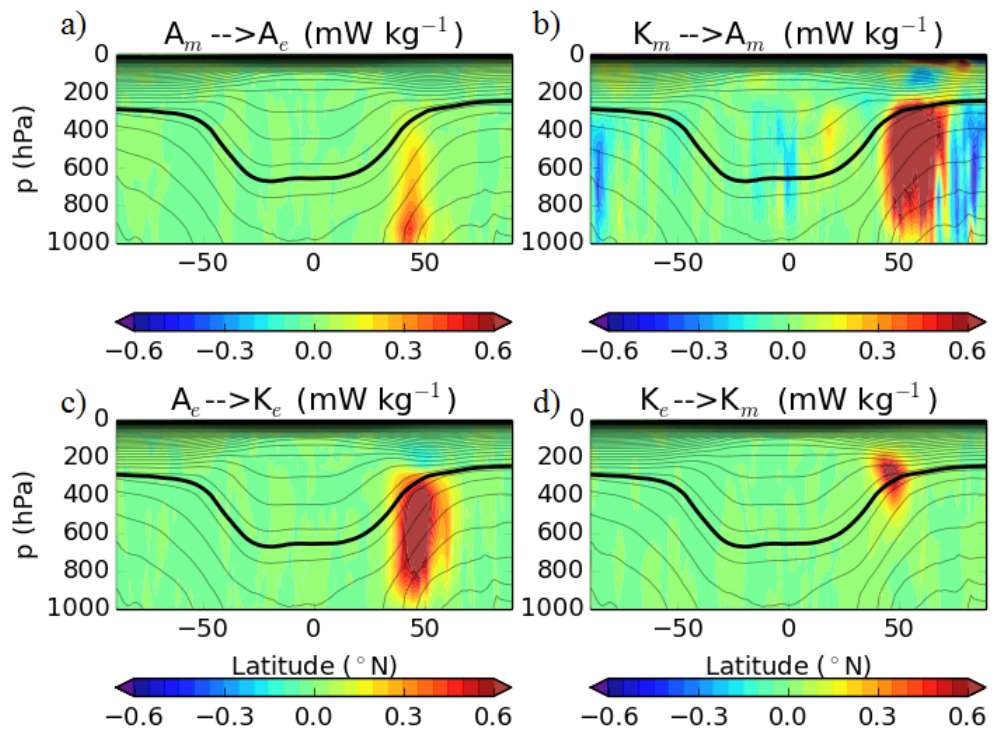


**Figure 5.24:** Zonal-mean view of local conversions, namely a) CA, b) CM, c) CE and d) CK, at the beginning of the storm track (averaged between 280 and 320°E) at time lag 0 of the heat flux composite, plotted as deviations from the time mean of the 21-day window, vertically integrated and based on the transient framework and the DJF data of ERA-40. The black contours are potential temperature at this time, with an interval of 10 K and the thick line marking the 315 K isentrope.

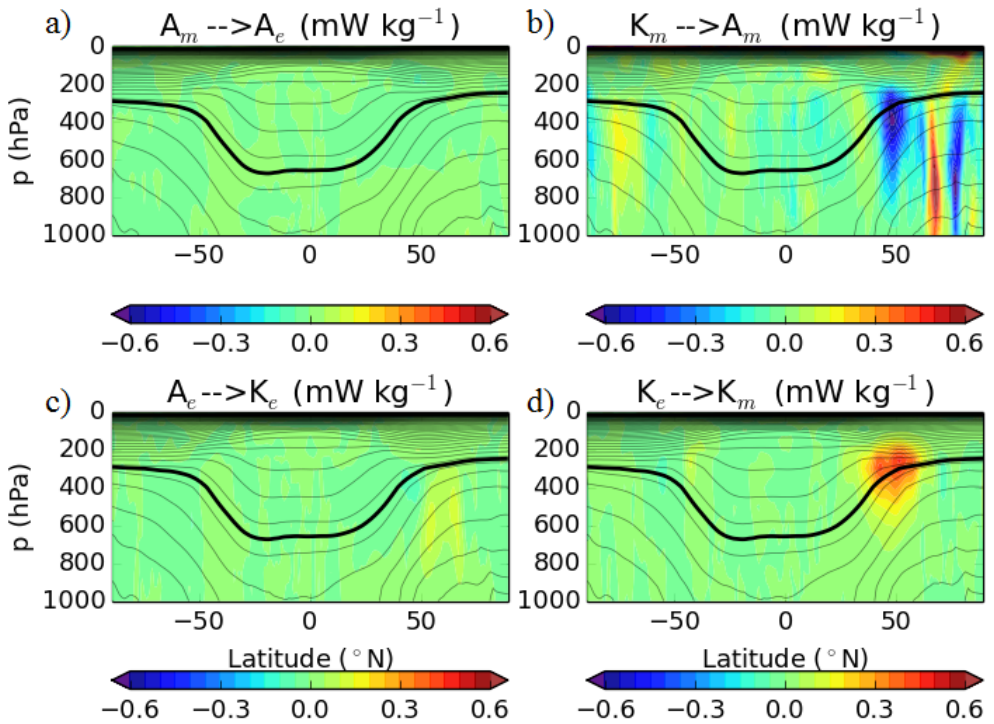


**Figure 5.25:** Same as figure 5.24, but for the end of the storm track (averaged between 320 and 360°E).

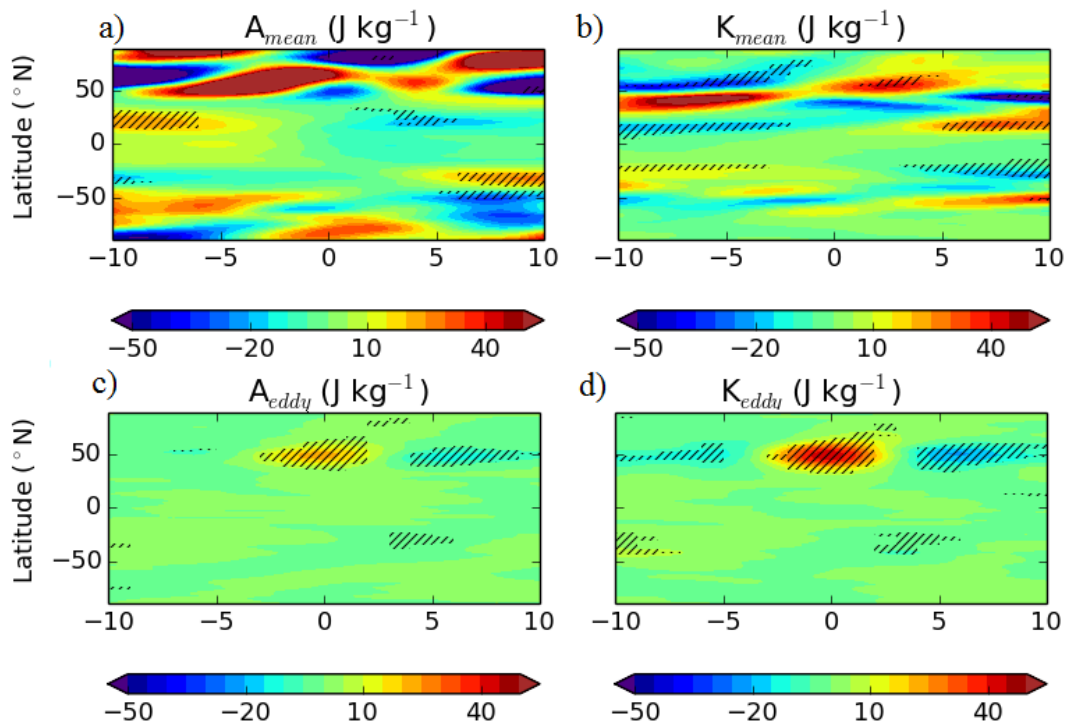


**Figure 5.26:** Hovmöller plots of cross sections of figure 5.22 representing the upstream (280-320°E) a) mean APE (at 500 hPa), b) mean KE (at 300 hPa), c) eddy APE (at 500 hPa), and d) eddy KE (300 hPa), as deviations from the composite mean. The hatched areas indicate significance at the 99% confidence level using the two-tailed Students t-test.

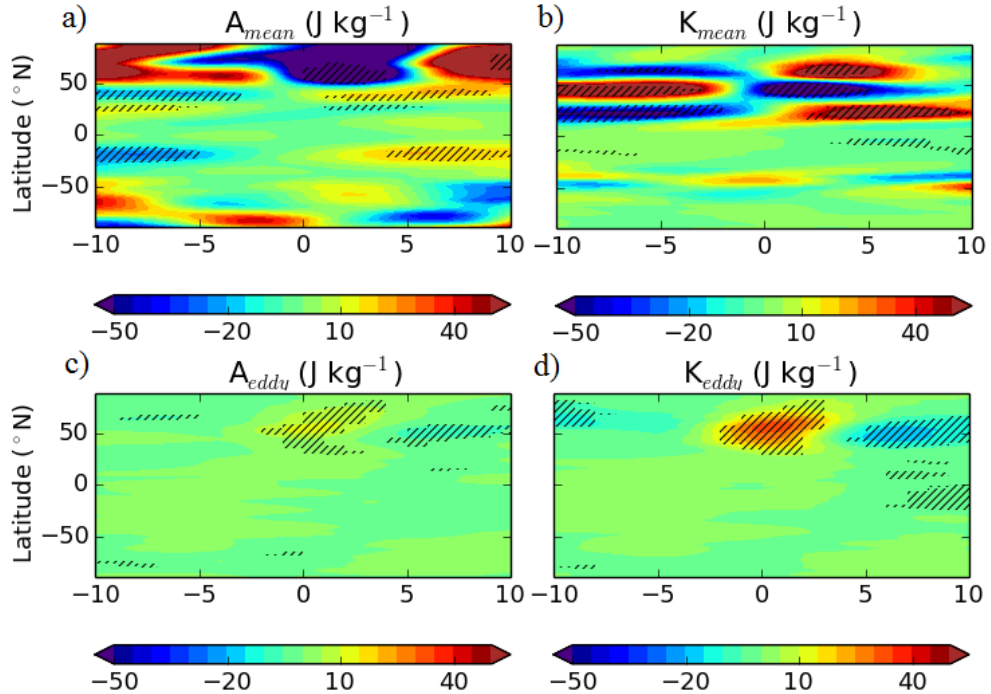


**Figure 5.27:** Same as figure 5.26 for the downstream (320-360°E) part of the storm track.

APE from the equatorward reservoir in the North Atlantic, though the consumption of the high-latitude mean APE still dominates. Turning to the same plot for the end of the storm track (figure

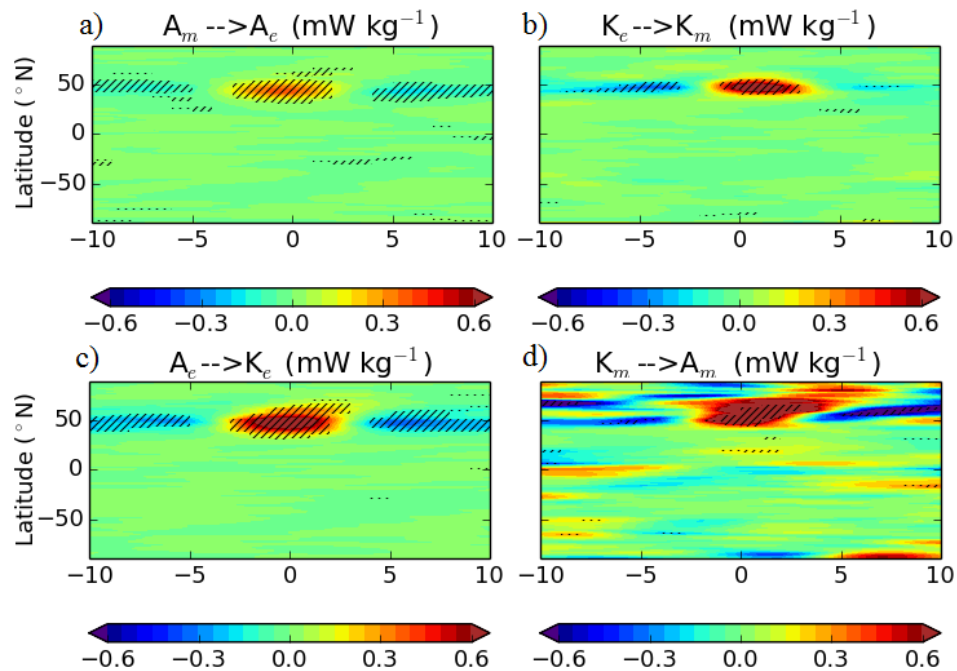


**Figure 5.28:** Hovmöller plots of cross sections of figure 5.24 representing the upstream (280-320°E) a) CA (at 850 hPa), b) CM (at 500 hPa), c) CE (at 500 hPa), and d) CK (300 hPa), as deviations from the composite mean. The hatched areas indicate significance at the 99% confidence level using the two-tailed Students t-test.

5.27), the northward propagation is no longer present and the pattern is more similar to the zonal-mean framework. Both plots additionally show that the mean APE exhibits a lower-frequency variability at latitudes equatorward of the storm track.

Similarly, the mean KE anomalies exhibit a lower-frequency pattern. The upstream positive anomaly moves northward following the heat flux spike, representing a northward shift in the eddy-driven jet which splits from the subtropical jet (the latter of which is shifted to around 25°N and strengthened substantially once the northward jet weakens). This split is even more apparent in the Hovmöller plot of the downstream end of the storm track. This northward jet shift is followed by a sharp jump equatorwards which is reminiscent of the transitions from the M to N and N to S jet regimes (as discussed in the previous chapter). In addition, the equatorward shift in the subtropical jet mirrors the changes in the mean APE mentioned above. A slight poleward shift of the eddy-driven jet in the Southern Hemisphere can also be observed.

The eddy energy anomalies are positive for about a week, peaking at a lag of zero. Despite the anomalies of the upstream mean energy terms migrating latitudinally in time, the eddy quantities stay at the same latitude at the beginning of the storm track, as suggested in the previous chapter.

The downstream evolution of the eddy energy terms is similar to that of the upstream terms with a slight shift northwards, following the jet.

The evolution of the conversion terms at the beginning of the storm track during the composite window is shown in figure 5.28. The above arguments are supported by the changes in these distributions, with the conversions involving eddies peaking at lag zero and only being of substantial magnitude at the constant latitude of the storm track. Conversely, the conversion between the mean energy terms peaks during the heat flux spike (as the thermally indirect circulation compensates for the high eddy activity and converts mean KE to mean APE to maintain the thermal wind balance), but also exhibits some substantial variability at other latitudes, including the Southern Hemisphere. This again highlights that the North Atlantic heat flux events are associated with global and lower-frequency variability in the mean energies, most likely associated with the meridional overturning circulation.

Finally, the composites of the low-level diabatic and frictional residual terms are briefly examined. These terms during the heat flux peak (lag=0) are displayed in figure 5.29. It is apparent that most of the mean production of APE is in the polar regions, in the tropics and over the continents, and that the overall friction acts to dampen the eddy-driven jet.

The low-level anomalies of the diabatic residuals (from the composite time mean) and their eddy and mean components are shown in figure 5.30. It is apparent that the largest anomalies of all terms occur in the North Atlantic region. The APE generation term (dominated by the mean component) exhibits a particularly large negative anomaly to the north of the storm track. It is apparent from the zonal-mean view of the upstream part of the storm track (figure 5.31) that this anomaly mainly resides in the upper half of the troposphere, and is opposite in sign to the corresponding eddy anomaly. Both of these anomalies peak with the heat flux spike, suggesting the presence of a diabatic feedback that is associated with the enhanced eddy activity. The eddy APE generation is likely due to the enhanced heating and sensible heat fluxes from previous storm activity (e.g. Hoskins and Valdes, 1990). The dissipation of the mean APE appears to be associated with an overall heating of the mid- to upper-level troposphere, which would increase the static stability of the atmosphere and thus decrease the mean APE. Furthermore, it was noted above that the mean APE increases at the beginning of the northward side of the storm track, and decreases more downstream. Since the mean APE generation term does not possess such a signal,

it can be concluded that the diabatic APE generation is not directly responsible for the observed mean APE anomalies.

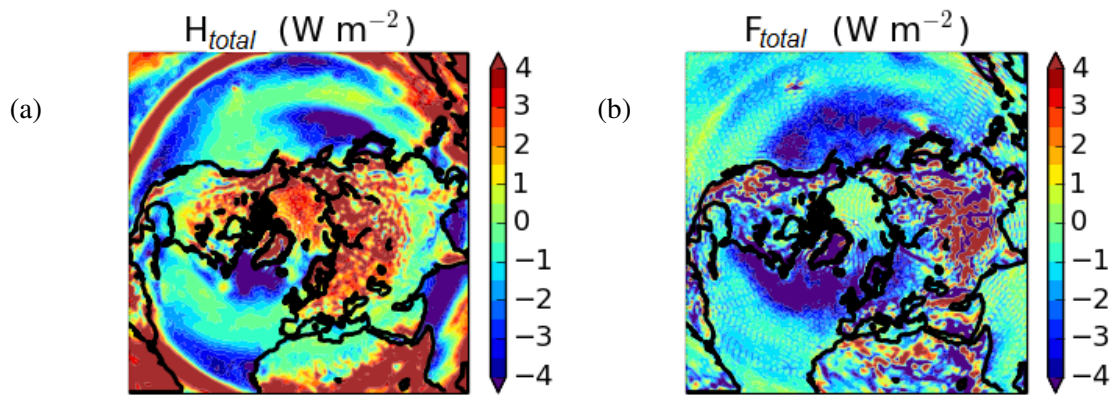


**Figure 5.29:** Horizontal view of the vertically integrated (between 1000 and 700 hPa) local residuals at time lag 0 of the heat flux composite. The mean and eddy terms have been summed up to show the total heating and dissipation acting on the system. The results are based on the transient framework and the DJF data of ERA-40.

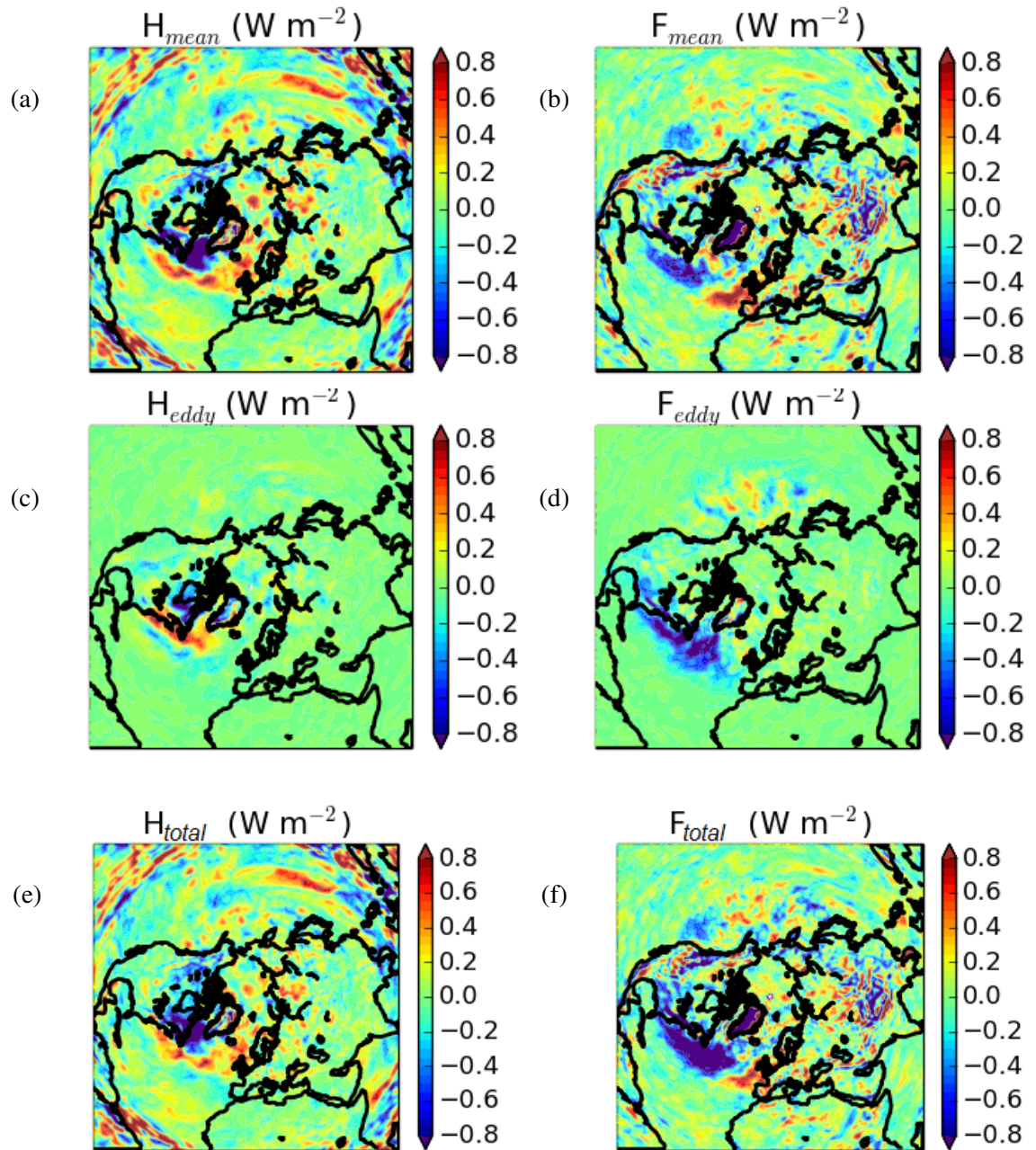


**Figure 5.30:** Horizontal view of the vertically integrated (between 1000 and 700 hPa) local residuals composited around the highest peaks in heat flux (day 0), namely the heating (left column) and frictional dissipation (right column) for the mean (top row), eddy (middle row) and mean plus eddy (bottom row) components. The residuals are plotted as deviations from the time mean of the 21 day window, based on the transient framework and the DJF data of ERA-40.

At low levels the eddy and mean frictional dissipation terms act in a similar manner by dissipating KE. Namely the KE is dissipated along the storm track (associated with the dissipation of eddy KE) and along the eddy driven jet (mainly associated with the dissipation of mean KE). At the upper levels of the beginning of the storm track (figure 5.31), the mean KE dissipation exhibits a large negative anomaly, whereas the eddy dissipation is positive. Both anomalies protrude into the lower stratosphere. In addition, investigation of the 21-day evolution of the composite (not shown) revealed that the mean KE dissipation anomaly propagates downwards in a burst-like manner during the event (as indicated by the black arrows) suggesting some influence from the stratosphere. Confirming such a suggestion would, however, require substantially more examination of the stratospheric processes, which would be beyond the scope of this thesis.

It is also noted that the APE generation and dissipation anomalies in general mimic the time-mean winter patterns of the absolute magnitudes of these variables in the mid-latitudes (not shown). This implies that the enhanced eddy activity and its related feedbacks generally dominate the time-mean diabatic and frictional structure of the atmosphere in the mid-latitudes.

Furthermore, although most of the variability of the residual terms during the North Atlantic heat flux events is contained within the North Atlantic, there is also weaker variability outside of it,

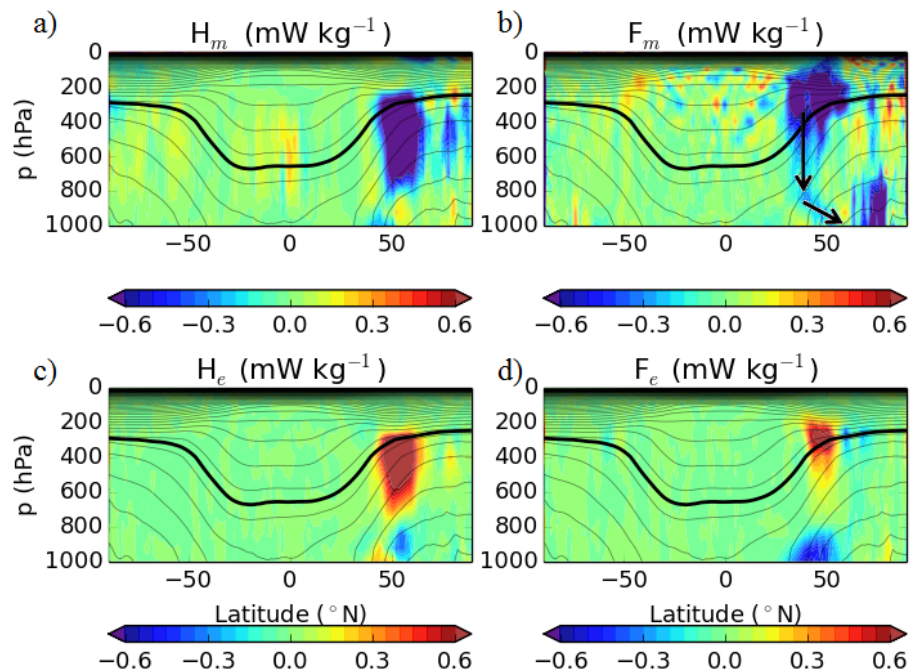


**Figure 5.31:** Zonal-mean plots of the residuals in figure 5.30 representing the upstream (280-320°E) vertically integrated between 700 and 1000 hPa. The residual terms are again plotted as deviations from the composite time mean.

especially in the mean terms. This suggests that the North Atlantic is not completely isolated from the diabatic processes taking place elsewhere.

Finally, the reader is reminded that the diabatic and frictional terms in this section were computed as residuals from the energetics evolution equations. Their precise values are therefore highly sensitive to any numerical errors or necessary assumptions (such as the assumption that the atmosphere has only one reference state, which would not be the case if moisture was considered). Nevertheless, their spatial patterns were shown to be physically plausible.

## 5.6 Summary and Conclusion

In this chapter, the lifecycle of the storm track was investigated from the perspective of local energetics, in order to provide a complementary picture to the analysis in the previous two chapters. As opposed to the traditional approach of using the globally integrated energetics introduced by Lorenz (1955), this work advocates Holliday and McIntyre's (1981) approach of using a locally-defined APE density, which is defined as the buoyancy forces vertically integrated between the actual level of a parcel and the neutral buoyancy level. It is noteworthy that the kinetic energy can be derived locally using the Lorenz approach, which is why this chapter focuses on the APE computational method. This local approach allows spatial, as well as temporal insight into the winter variability of the kinetic and available potential energies, and their eddy and mean components.

This method of defining the local APE is currently rarely used to diagnose real observations, which warranted a comparison with the more conventionally used Lorenz framework. For better comparison, the reference state of the local method was set to be equivalent to that used for the approximate Lorenz method (i.e. set by using averaging along the isobaric surfaces). The globally integrated local APE density should therefore yield comparable values to the Lorenz APE (Andrews, 1981). Although these values were of similar magnitudes in the reanalysis data in the time mean, they differed substantially in a simplified aqua-planet GCM (owing to the model's simplified nature and lower resolution).

Despite the differences in the absolute values in the idealised GCM, the Lorenz and local (zonal mean-based) approaches both yielded similar relative temporal variability of all globally inte-

grated energy components during a composite event of high North Atlantic heat flux. A dip in the mean APE during a peaking eddy energy and a consequent strengthening of the mean flow were observed during the composite. This is consistent with the lifecycle experiments of Simmons and Hoskins (1978) and Tanaka (1995). Furthermore, the temporal variability of the mean and eddy APE indicates the existence of a predator-prey relationship, as would be expected from heuristic arguments. More specifically, the mean APE is maintained by the mean diabatic processes and mean flow advection, whilst providing energy for the generation of eddies. When the eddies become intense enough, they flatten the isentropic slopes and thus decrease the mean APE. Depletion of the mean APE in the storm track region will eventually reduce eddy generation and thus the eddy energy decreases, which is followed by a replenishment of the mean APE and the cycle can repeat.

A more detailed inspection of the data revealed that the Lorenz approach exhibits more pronounced fluctuations in the mean APE and eddy APE, but both approaches produce phase plots with a clockwise circulation, indicating a generally oscillating behaviour of the system. A similar oscillatory behaviour was found for the three-dimensional synoptic transient framework in the spatially restricted domain of the North Atlantic storm track. The mean oscillation frequency is comparable to that found in the previous chapters, though a thorough quantitative comparison between the system based on the energetics and that based on heat flux and baroclinicity remains as future work.

The observation of oscillations in the real and GCM data is supported by a theoretical consideration of the Lorenz energy equations, which revealed a nonlinear oscillator relationship between the total eddy energy and the square root of the total mean energy. This is analogous to the relationship found in chapter 3 for heat flux and baroclinicity. In contrast to the latter, the nonlinear oscillator model derived using the energetics does not require a constant heating term, and can additionally be rewritten in terms of the eddy APE and the square root of the mean APE (where the eddy dissipation is replaced by the conversion from the eddy APE to the eddy KE). The existence of this predator-prey behaviour is consistent with the preferred flow of energy in the Lorenz cycle being along the baroclinic pathway (i.e. from APE generation to mean APE, to eddy energy, to eddy dissipation) as was observed (see review in Oort, 1964) and is depicted in figure 5.1. The lag composites in this study, however, suggest that a substantial additional interchange of energy occurs between the mean APE and KE during bursts in eddy activity. This interchange is related

to the ageostrophic circulation that maintains the thermal wind balance. Inclusion of this term may complicate the behaviour of the nonlinear oscillator model.

Further insight into the storm track lifecycle was gained by examining the three-dimensional energetics during the evolution of a composite event of high storm track activity. It is apparent that as the disturbances propagate downstream and upwards, the energy is converted from mean APE to eddy APE and eddy KE. Although the eddy APE and eddy KE are often considered together as one quantity, eddy energy (e.g. Plumb, 1983), it is apparent that the maximum of the eddy KE lies somewhat more downstream of the eddy APE maximum due to the more barotropic nature of the eddies further downstream. However, the global integrals of the two eddy energy components do peak at the same time in the composite. Furthermore, as well as the mean APE decreasing within the storm track during high storm track activity, the mean APE is also increased substantially on the northern and southern edges of the storm track due to the limited meridional extent of the disturbances (as was observed by Simmons and Hoskins, 1978). Some of these secondary centres can induce a prolonged eddy activity in those regions.

During the several days following the event, some of the eddy KE is converted into mean KE, returning energy to the mean flow and moving the eddy-driven jet north. This concurs with the analysis in the previous chapter. This northern position of the jet persists for longer than the individual events, indicating an underlying low-frequency variability. This agrees with the findings of Chen *et al.* (2007) who found that for instantaneously reduced friction in an idealised GCM, the eddy KE and the baroclinic nature of the flow would decrease within the first 10-20 days, whereas the latitudinal deflection would occur more slowly. The authors attribute this delay to a poleward shift of the subtropical critical latitude, corresponding to faster phase speeds of the dominant mid-latitude eddies.

The low-frequency variability of the system is also reflected in the mean APE at latitudes south of the storm track. It is worth noting that the precise formulation of APE depends on a globally-defined reference state, and so its individual variability in other parts of the globe may be merely an artefact of this global reference state being altered (rather than reflecting a real global signal). Having said that, the presence of the mean KE anomalies (which do not depend on the global state) in the North Pacific and the Southern Hemisphere suggests a real inter-hemispheric connection that is likely linked to the conversion between the mean energies. This connection appears to be

associated with exchange of energy between the Northern and Southern Hemispheres, and it is therefore not conservative to base the Lorenz energetics on anything other than the entire globe in this context. This was further confirmed by computing the time mean of the hemispheric (not shown) and global Lorenz terms, which yielded considerably different results.

It was also found that the magnitude of the conversion between the mean energies is highly spatially variable and is most likely responsible for inconsistencies between studies that use differently sized domains. Furthermore, the high spatial and temporal variability of this conversion term during events of high North Atlantic storm track activity suggests that the baroclinic pathway of the Lorenz energetics cycle (from mean APE to eddy energy which is then dissipated) does not necessarily dominate locally within the storm track. In fact, it is suggested that the conversion between the mean energies is responsible for ageostrophic circulation that converts the mean KE to APE at the beginning of the storm track and removes it further downstream, consistent with the findings of Orlanski and Katzfey (1991) for an individual storm. This suggests self-maintenance at the beginning of the storm track and self-termination towards its downstream end. This conversion may contribute to the observed partial quick recovery in the mean APE following the eddy events. The temporal variability of this conversion term also includes lower-frequency changes which are consistent with the variability of the mean energies outside of the North Atlantic. This nonlinear feedback is not included in the nonlinear oscillator model, and its inclusion is a focus of future work.

In summary, the results of this chapter are consistent with those of the previous chapter, as well as shedding some new light onto some of the key processes involved in the storm track lifecycle. More specifically, the issues that were clarified in this chapter are:

- the general predator-prey relationship previously found between the heat flux and baroclinicity also seems to exist between the total eddy energy and the square root of the total mean energy, though the relationship is somewhat less quantitatively consistent with the nonlinear oscillator model presented in chapter 3;
- this relationship was observed in atmospheric data and in a simplified aquaplanet GCM, indicating that it may be a fundamental feature of all storm tracks;
- zonal mean-based and synoptic transient eddies behave in a similar manner during the storm

track lifecycle, implying that synoptic transient eddies dominate at these timescales;

- the enhanced thermally indirect meridional circulation (which is usually assumed to be small, based on global estimates) provides additional mean APE to the storm track (by converting the mean KE). This may cause some secondary development and provide a nonlinear feedback that is not included in the nonlinear oscillator model;
- this feedback of the mean meridional circulation is likely to be connected to the variability of the mean energy components in the tropics and in the Southern Hemisphere;
- most of the mean APE that is converted into eddy energy originates at high latitudes, and it is suggested that the transport of this energy into the storm track is of more importance than the diabatic heating in forcing high storm track activity events. This implies that the assumption of a constant forcing of the APE (as in the nonlinear oscillator model in chapter 3) is insufficient;
- at the beginning of the North Atlantic storm track, eddy quantities remain anchored to their initial latitude, but more downstream they tend to follow the jet; and
- although some energy is dissipated as eddy friction following a high storm track activity event, some energy is returned to the mean flow in the upper levels. This return of energy is often associated with jet shifts on lower-frequency timescales.

Whilst the current chapter was focused on examining the existence of the nonlinear oscillator behaviour in the energetics variability, some additional interesting issues arose. These issues include the potential link between the North Atlantic storm track events and the Southern Hemispheric circulation, the precise involvement of the nonlinear feedback of the meridional circulation, the role of APE transport in setting the timescales of the storm track oscillations, and the effect of moisture. The work of this chapter provides significant motivation for pursuing these issues in the future.

## Chapter 6

# Conclusions

The focus of this thesis is on localised terrestrial storm tracks, and the spatial and temporal variability of their three-dimensional structure. In the light of the questions asked in the introduction chapter, this chapter summarises the results of this thesis in the following sections:

- observed periodic behaviour of storm tracks;
- modelling the predator-prey relationship between storm track activity and storm track growth rate;
- the effect of the periodic variability of the storm track on the latitudinal deflection of the eddy-driven jet; and
- interaction of storm tracks with other global regions.

## 6.1 Observed Periodic Behaviour of Storm Tracks

Despite the seemingly chaotic nature of local storm track variability, (quasi-)periodic behaviour of storm tracks was found in the North Atlantic, the North Pacific and an idealised aquaplanet global circulation model (GCM). It is suggested here that this periodicity is a result of nonlinear interactions between the storms and the mean flow, though it is characterised by different processes at the beginning and towards the end of the storm track.

At the beginning of the storm track the perturbations are mostly in their early stage of development which is primarily dominated by baroclinic instability (Chang and Orlanski, 1993). The maximum Eady growth rate is therefore a sufficiently appropriate measure of eddy growth rate (Hoskins and Valdes, 1990), which is referred to as baroclinicity here. The present study observes that the beginning of the storm track exhibits spatial maxima in baroclinicity and in storm track

activity, both of which oscillate quasi-periodically in intensity but not in latitude. The linear theory describing eddies within storm tracks as perturbations growing on a prescribed background baroclinicity therefore does not apply to storm tracks as a whole.

Oscillations on short timescales (lasting several days) between baroclinicity and storm track activity were captured in time lag composites centred around events of high storminess. It is apparent that the amplitude of these oscillations decays with lag time, likely due to the wide range of transient-eddy frequencies that are involved (Blackmon, 1976) and additional noise resulting in quasi-periodicity. Storm track activity was observed to occur in short-term bursts, agreeing with the findings of Swanson and Pierrehumbert (1997) and Messori and Czaja (2013). This burst-like nature of the storm track activity indicates that eddy dissipation is relatively fast compared to the recovery of the growth rate.

Evidence was also found for longer-term oscillations in storm track activity and baroclinicity, upon averaging of the phase space of the two quantities. Their approximately monthly time period of oscillation concurs with observations of Thompson and Li (2015) in the Northern Hemisphere. Although the precise oscillatory properties of the system are sensitive to the averaging method applied to identify the oscillations, the oscillatory behaviour undoubtedly exists within the observations.

This quasi-periodic oscillatory behaviour of storm tracks was observed in all storm tracks studied here, as well as for several different measures of storm track activity (such as low-level heat flux, mean sea level pressure variance, mid-level geopotential height variance, upper-level potential vorticity variance and upper-level velocity variances). It was also observed for the eddy and mean available potential energies. This universal picture suggests that quasi-periodic behaviour may be a general feature of all localised storm tracks.

On the other hand, towards the middle and end of the storm track, the storm track becomes more barotropic and its variability is dominated by highly nonlinear interactions, including eddy momentum fluxes. The meridional flux of zonal momentum is particularly important, as it helps to shift the associated eddy-driven jet. The quasi-periodic variability of the Northern Hemispheric mean jets has been noted by many (e.g. Namias, 1950; Lorenz and Hartmann, 2003), and it is characterised by the jets switching between two or three preferred latitudinal positions on weekly

to monthly timescales. This thesis mainly focused on the North Atlantic eddy-driven jet, which on average exhibits a cyclic sequence of transitions between its three preferred jet positions: from middle to north, north to south, and south to middle (Franzke *et al.*, 2011). It was observed here that storm track activity mirrors this latitudinal variability at the end of the storm track (unlike at the beginning where the storm track activity is more or less fixed in latitude).

## 6.2 Modelling the Predator-prey Relationship between Storm Track Activity and Its Growth Rate

Since baroclinicity and eddy heat flux represent storm track growth rate and activity, respectively, their mutual interaction can be viewed as a predator-prey relationship similar to the Lotka-Volterra system (Berryman, 1992 and references therein). It is this relationship that is proposed here to drive their mutual periodicity.

A nonlinear oscillator model is proposed to quantitatively describe this predator-prey relationship. It is shown that this model can be justified from first principles to some extent, using truncations of various analytical models, including the forced Phillips two-layer model, Lorenz-84 model and the model of Thompson (1987). This nonlinear oscillator model describes periodic oscillations in heat flux and baroclinicity, which possess a nonlinearity that is manifested in a burst-like temporal behaviour of the heat flux and a saw-tooth temporal variability in the baroclinicity for large amplitudes. These asymmetric oscillations reflect two separate timescales. The shorter timescale corresponds to the duration of one high heat flux event and the subsequent rapid dissipation of eddies. On the other hand, the second time scale corresponds to the longer-term replenishment of baroclinicity and the time between two heat flux events. Similarly to the observations, this model suggests that storm tracks oscillate around a threshold below which the baroclinicity is not strong enough to maintain the vigorous storm track activity. Both the model and observations suggest that storm tracks spend most of their time in the more quiescent regime, with the active regime manifesting itself as short-term bursts in eddy activity.

The qualitative temporal behaviour of the model is in a good agreement with the observed temporal variability of storm track activity and baroclinicity composited around the strongest storminess events. However, the frequency and amplitudes of the model oscillations for given initial condi-

tions do not vary in time (as the model is an energy conserving system), whereas the observed composite oscillations exhibit a much more diverse range of timescales and amplitudes. Similarly, a partial rapid replenishment in the observed baroclinicity following heat flux spikes reflects the different relaxation timescales involved in the real system.

Investigation of the model phase space produced additional means of comparison between the model and the reanalysis data. Comparison of the model with the average behaviour of the North Atlantic storm track shows a good agreement of the oscillatory properties, though less so for the North Pacific (likely due to this storm track being less longitudinally constrained). It was predicted and observed that under the same parameter setting, stronger storm events occur on average less frequently, though their onsets and terminations would be more rapid.

A study of the energetics within storm tracks revealed that the nonlinear oscillator model can also be retrieved from a simplification of the evolution equations of the eddy energy and the mean available potential energy (APE). This is not overly surprising as the former is another measure of storm track activity and the latter provides energy for eddy growth (and, like baroclinicity, depends on static stability and the tilt of isentropic surfaces). A transition from the heat flux-baroclinicity to eddy energy-mean APE equation systems is indicated. It is noted, however, that the theoretical links implied here are merely indicative of the presence of the nonlinear oscillator behaviour within the energy equations, rather than providing a formally complete theoretical framework.

Similar behaviour of dipping mean APE during high eddy activity and its subsequent recovery is also observed in the North Atlantic, and in aquaplanet GCM runs where the eddies were defined as anomalies from the zonal mean, which is the basis of the theoretical model. The qualitatively similar behaviour of the transient and zonal-mean based approaches indicates a dominance of the synoptic transient eddies on the timescales of the predator-prey behaviour.

The existence of nonlinearly oscillating behaviour of storm tracks also has implications for understanding the steady-state of the real system. According to the nonlinear oscillator model proposed here, the equilibrium value of baroclinicity is given by the dissipation of eddies, whereas the equilibrium point in storm track activity is given by the diabatic forcing. This seems counter-intuitive, as one may expect the mean baroclinicity to increase with the forcing that replenishes it. How-

ever, a thought experiment can show that this insensitivity of the steady state to the forcing has a viable physical interpretation. If the baroclinicity was increased by the forcing, the tendency to generate more intense eddies (and therefore their ability to erode the baroclinicity back towards a more stable state) would also intensify. Thus, the only way to increase the steady-state baroclinicity is to reduce its erosion by eddies through (in this case) increasing the eddy dissipation. This would bring the system to a different state of equilibrium baroclinic stability (with respect to the vigorous eddy events).

While the steady-state baroclinicity is predicted, and to some extent observed, to be insensitive to diabatic forcings, the amplitude and frequency of its temporal oscillations are highly dependent on it. It is therefore crucial to distinguish between the oscillation amplitude and steady-state magnitude of the baroclinicity, as each are forced by different mechanisms.

### 6.3 The Effect of the Periodic Variability of Storm Tracks on the Latitudinal Deflection of the Eddy-driven Jet

Towards the middle and end of the storm tracks, baroclinicity and heat fluxes are observed to be less prominent, and the dynamics are characterised more by fluctuations in eddy momentum fluxes. The storm tracks are therefore more latitudinally transient along with their associated jets, with the latter often exhibiting periodic latitudinal fluctuations. A particular focus was on the North Atlantic jet, because it exhibits a more varied trimodal behaviour of its latitude fluctuations compared to the bimodal behaviour of the other major terrestrial jets (Woollings *et al.*, 2010). This trimodal structure is a result of the combination of the weaker subtropical jet and stationary forcings in the North Atlantic allowing the eddy driven jet to move more freely in latitude, which makes it a desirable case study. However, preliminary GCM modelling results indicate that very similar results also apply to other storm tracks, even those with a bimodal structure.

It is suggested that the upstream effect of baroclinicity and heat flux cycling is to a large extent responsible for these downstream periodic jet deflections. It is found that low heat flux is on average associated with a slight equatorward deflection of the jet, and a high heat flux is associated with a northern deflection. This downstream jet-deflecting effect is accompanied by a transition of the system to lower-frequency variability, due to the mean flow mostly responding to the cumulative

effect of the eddies. It is found, however, that a single sufficiently strong storm event can also move the jet to a more northern position.

In terms of the responsible mechanism, it is proposed that upstream oscillations in baroclinicity induce variability in the eddy properties further downstream which is conducive to different fluxes of momentum at different times. The observed variability in eddy anisotropy is consistent with Orlandi's (2003) theory, whereby sufficiently high baroclinicity induces round eddies and cyclonic wave-breaking, and low baroclinicity induces stretched eddies conducive to anticyclonic wave breaking.

This mechanism of baroclinicity-controlled jet shifts can help explain the preferred direction of cycling of the North Atlantic between its preferred latitudinal positions. Increasing baroclinicity during periods of low eddy activity (southern jet regime) is conducive to cyclonically (north-west to south-east) stretched flow structures, due to the asymmetry between cyclones and anticyclones allowing the cyclones to become more intense under a baroclinic forcing (Orlandi, 2003). As the baroclinicity increases further (middle jet regime), the eddies become more active and begin to counteract the forcing that restores the baroclinicity. At this point the baroclinicity stops growing and the deformation of the eddies starts experiencing more of the (default) anticyclonic wave breaking, though cyclonic wave breaking remains strong north of the jet. As the excess baroclinicity is still positive, the eddies continue to grow until baroclinicity reaches its steady-state value (northern jet regime). The minimal baroclinic forcing means that anticyclonic wave breaking dominates at this point. Eventually, storm track activity also reduces, baroclinicity starts being restored by the forcing, and the cycle repeats.

This cycle appears to be characterised by the system cyclically drifting between being baroclinically active and quiescent, as the flow switches between being dominated by baroclinicity restoration (southern regime), both baroclinicity restoration and eddy activity (middle regime) and eddy forcing alone (northern regime). This is somewhat reminiscent of Namias's (1950) index cycle.

The upstream oscillations in storm track activity and baroclinicity and the downstream oscillations in the eddy-driven jet are therefore closely linked, and can be viewed as describing the spatio-temporal lifecycle of storm tracks. Both of these types of quasi-periodic variability were observed in several relatively different localised storm tracks, namely the North Atlantic storm track, the

North Pacific storm track and an idealised mid-latitude storm track in an aquaplanet GCM. This universal observation indicates that this quasi-periodic behaviour applies to all localised storm tracks.

There are two types of timescales that characterise the storm track lifecycle. First, there is the rapid response of the eddies and the mean wind shear, which describes the upstream predator-prey dynamics between the eddies and their growth rate. The second timescale is related to the downstream deflections of the jet latitude.

These timescales are reminiscent of the findings of Chen *et al.*'s (2007) idealised modelling study. The authors recovered two adjustment timescales due to an instantaneous reduction in surface friction. The first (fast) timescale was associated with a fast adjustment of the mean flow, with the latter becoming less baroclinic and being accompanied with a marked reduction in the storm track activity. On the other hand, the second (slower) timescale in Chen *et al.*'s (2007) study characterises a barotropic latitudinal jet shift. The authors attribute the delay in the shifting of the barotropic jet to the dependence of the jet latitude on the poleward movement of the subtropical critical latitude, which occurs more slowly. The storm track activity is largely independent of the horizontal wave breaking (and thus the subtropical critical layer latitude), and so it can change on shorter timescales (Thorncroft *et al.*, 1993). Based on the arguments in chapter 2, similar reasoning can be used to speculate that the longer timescales of the jet shifts observed in the present study are a consequence of low-level baroclinicity fluctuations modifying the critical layer in a quasi-periodic manner.

## 6.4 Interaction of Storm Tracks with Other Global Regions

It has been observed here that strong North Atlantic events may be linked to some variability in the mean flow in other regions of the globe, including the Southern Hemisphere. In particular, mean available and kinetic energies were found to vary outside of the storm track regions in the lagged composites that were centred around the largest events of storm track activity in the North Atlantic. Changes in the mean circulation, including a slight jet shift of the Southern Hemisphere mid-latitude jet were observed, while the eddy energies varied only locally within the storm track. The connection of the North Atlantic with the Southern Hemisphere and the North Pacific remains

to be fully explored, but a likely candidate responsible for the interhemispheric connection is the mean overturning circulation.

It is also emphasised here that local energetics shed more light on the storm track lifecycle, as opposed to the global framework which obscures many aspects of the related variability. For example, the conversion between the mean energies (associated with the mean overturning circulation) appears negligible in the global framework due to large scale cancellations. However, it has been shown that this term can be dominant locally within the storm track.

Furthermore, the energetics also indicates that the mean APE that is eventually converted into eddy energy is initially transported mostly from the high latitudes, rather than being generated locally due to diabatic forcing. A more detailed study of the energetics budgets is required for more conclusive results, though it seems likely that other processes and timescales may need to be considered in future work on the nonlinear oscillator. Such processes include upstream vorticity fluxes of pre-existing storms, the influence of the stratospheric vertical shear, imposition of horizontal wind shear along the storm track, variability in the oceanic circulation, mean potential vorticity fluxes from the polar regions, and fluctuations in the outer Hadley cell edge. External sources can therefore affect the flow variability from all of the boundaries of the storm track domain, and the nonlinear oscillator model explains only a part of this variability. Nevertheless, its striking consistency with the average observed variability is an encouraging result, indicating that the predator-prey relationship plays a major part in the storm track lifecycle.

## 6.5 Future Work

This study shows that storm tracks should be viewed as nonlinear forced-dissipative systems and proposes an analytical nonlinear oscillator model to describe their observed periodic behaviour. Although this model generally agrees well with the ERA-40 and ERA-Interim reanalysis data, its theoretical justification is still in its early stages. In particular, the assumption of a constant restoring forcing on baroclinicity seems insufficient, and therefore extending the system to allow for its variation is planned as future work.

Furthermore, the parallels drawn in this study between the nonlinear oscillator model and that

of Thompson (1987) need to be explored further. It was shown here that the nonlinear oscillator model is a truncation of Thompson's (1987) model. However, due to its five degrees of freedom, Thompson's (1987) model can additionally exhibit chaotic behaviour (Fleming, 2014), and it would be a good starting point to analyse its parameter space using bifurcation theory in the context of the predator-prey mechanism. For example, oscillations in both models are dependent on a diabatic forcing and an eddy dissipation rate, and exploring the sensitivity to different values of these parameters would unveil the underlying dynamics more explicitly.

As well as analysing the reanalysis data, this study provides further evidence for the existence of the predator-prey behaviour within storm tracks by analysing an idealised storm track in a dry-core aquaplanet GCM (PUMA) with a heating dipole. However, the preliminary results presented here from this experiment are mostly qualitative. Quantitative analysis of the baroclinicity-heat flux phase space (as was performed for the reanalysis data) may require less extreme averaging, which may be possible due to its simplified setting. This may reveal a more precise value for the natural frequency of the average oscillations, and the sensitivity of that frequency to changes in the strength of the heating dipole. Including realistic features in the model, such as the presence of continents and a more complex structure of the diabatic heating, would provide valuable insight. Additionally, an experiment with no eddy-eddy interactions (in a zonally symmetric case) may verify that these interactions are not necessary for the observed quasi-periodicity of the storm tracks.

To complete the hierarchy of the models used to test the quasi-periodic variability of storm tracks, comprehensive climate model runs are planned, and will be examined under different parameter settings. Investigating the sensitivity of the storm track temporal oscillations to changes in the diabatic forcing that are consistent with the future climate scenarios is one of the primary goals of future work.

Additionally, investigating the steady states of the atmospheric and oceanic systems in the context of the nonlinear oscillator model may be particularly valuable for climate change research. It is predicted that in the Northern Hemisphere the effect of greenhouse gases is to decrease the low-level meridional temperature gradient (due to polar amplification of temperatures) due to Arctic ice melt and higher static stability at higher latitudes, but increase the upper-level meridional temperature gradient due to tropical tropospheric warming from an increased release of latent heat

(Held, 1993). One may initially presume that the steady-state isentropic slopes would be directly affected by (future) changes in the meridional temperature gradient, but in fact these slopes are predicted to be rather insensitive to such changes due to eddies adjusting the thermal structure of the mean flow (e.g. Jansen and Ferrari, 2013). With the predicted reduced surface meridional temperature gradient under polar amplification, one may therefore expect weaker storm tracks but not necessarily a weaker baroclinicity, whereas the opposite may be expected for the upper levels. Although some of these features have been captured by climate models (e.g. Harvey *et al.*, 2013; Chang *et al.*, 2012), the diverse response of different storm tracks to such a forcing still warrants further investigation.

The investigation of the steady state of the nonlinear oscillator model may shed more light on the dynamics behind the predicted response of storm track under climate change. The implication of this model is that in both the atmosphere and oceans large-scale turbulence maintains the flow at a particular level of baroclinic instability by mixing temperature down-gradient whenever the instability becomes too vigorous. The nonlinear oscillator model assumes a constant static stability, in which case eddies would baroclinically adjust both the baroclinicity and isentropic slopes by eroding the meridional temperature gradient at times of high baroclinic activity (as in Stone, 1978). However, a number of studies have suggested that Stone's (1978) baroclinic adjustment does not necessarily apply to the atmosphere. For example, based on a modelling study Schneider and Walker (2008) have suggested that the insensitivity of the atmospheric isentropic slopes to changes in the Equator-pole temperature gradient is due to a compensation between horizontal and vertical temperature gradients (as eddies stabilise the atmosphere), rather than the insensitivity of the meridional temperature gradient.

Nevertheless, Jansen and Ferrari (2013) used scaling arguments to show that for Earth-like parameters the changes in isentropic slopes are primarily governed by eddies modifying the meridional temperature gradient, while the static stability stays more or less constant. Therefore, although Stone's (1978) baroclinic adjustment may not be a feature of all baroclinically unstable atmospheres, it is still highly likely that the observed constancy of the isentropic slopes is due to the predator-prey relationship described by the nonlinear oscillator model. It would therefore be insightful to diagnose in reanalysis data and climate models the extent to which the baroclinic adjustment and the compensation between the meridional and vertical temperature gradients dominate the insensitivity in the isentropic slopes.

The steady-state nonlinear oscillator model further implies that baroclinicity and storm track activity are independent of each other. While this would support the eddy saturation phenomenon observed in the oceans (e.g. Munday *et al.*, 2013), Schneider and Walker's (2008) idealised modelling experiments and O'Gorman's (2010) comprehensive climate modelling study both suggest that mean APE (related to baroclinicity) and eddy energy (measure of storm track activity) are directly proportional to each other in the steady state. This suggests more complexity in the predator-prey behaviour of atmospheric storm tracks and requires further attention.

Another topic for future work is the effect of the quasi-periodic behaviour of storm track activity on the jet's structure. The North Atlantic jet was the focus of this study, while the other jets were not examined directly. It is possible that the response of the North Pacific jet, for example, would be somewhat different due to the different stationary wave forcings involved in the two storm tracks (Chang, 2009).

As an additional point, the mechanisms responsible for latitudinal jet shifts through fluctuations in low-level baroclinicity were induced here implicitly, based on Orlandi's (2003) theory. However, it may be speculated that the fluctuations in the baroclinicity would also be reflected in the wave phase speeds and the latitudinal movement of the critical and reflective levels (Chen *et al.*, 2007; Lorenz, 2014). Analysing these wave properties may therefore show a more explicit link between the changes in the baroclinicity and those in eddy anisotropy, the latter of which are already explicitly linked to changes in the dominant type of wave breaking and latitudinal shifts of the jet (e.g. Hoskins *et al.*, 1983; Thorncroft *et al.*, 1993). A more quantitative link between baroclinicity and eddy anisotropy would allow the downstream effect of momentum fluxes and jet shifting to be incorporated into the nonlinear oscillator model, perhaps in the form of a coupled box model, to simulate the full lifecycle of the storm track.

In terms of the steady state of the system, the response of the latitudinal jet shifts to future climate change is very much at the forefront of current climate research. Polar amplification is predicted to lead to an equatorward shift in the jet, but upper-level sharpening of temperature gradients may lead to the opposite effect (Butler *et al.*, 2010). Chang *et al.* (2012) use a comprehensive multi-model ensemble projection and predict an overall poleward shift in the jets in both hemispheres due to global warming. This suggests that the changes in upper-level baroclinicity dominate in the steady state. A systematic examination of the wave properties in climate models and their

sensitivity to enhanced baroclinicity at different heights would help quantify the explicit mechanisms responsible for these predicted trends. Understanding these mechanisms would in turn help to identify any likely future changes in the quasi-periodic variability in the jet latitude.

The local energetics framework has proved to be valuable at providing a complementary view of the spatio-temporal lifecycle. However, a more detailed breakdown of the terms of the energy evolution equations would provide better insight into the spatial energy conversions and transports involved. Such a study of the energetics budget would be further improved by considering moisture, which would allow for the possibility of several neutral buoyancy levels when computing the available potential energy. A more precise estimate of the available potential energy would then be possible.

Despite the potential for improvement in the methods employed here, this study provides some useful insight. In particular, it reveals that storm tracks exhibit a quasi-periodic behaviour in their activity, characterised by oscillations around a state that could be described to be baroclinically neutral with respect to vigorous bursts in eddy activity. This is in contrast with the linear-theory view of storm tracks growing on an inviscid background flow, but agrees with nonlinear analytical and numerical models (e.g. Thompson, 1987; Tanaka, 1995) as well as growing observational evidence (Messori and Czaja, 2013; Thompson and Li, 2015). The proposed mechanisms behind this periodicity, and that of the associated eddy-driven jet, offer a new perspective on baroclinic instability and can be used to describe the spatio-temporal lifecycle of the storm track.

# Appendices

## Appendix A

# Setup of the PUMA Experiment

The Portable University Model of Atmosphere (PUMA, available from the Meteorological Institute of Hamburg University) is a dry dynamical core of Hoskins and Simmons's (1975) spectral global circulation model that uses a semi-implicit time integration scheme. Unless otherwise stated, the default settings of the PUMA model were used. Here, only the most relevant aspects of the setup are briefly outlined, but the reader is referred to the PUMA User's Guide (contained in the model documentation folder) for a more technical description of the default setting which was used here (unless otherwise stated).

The setup chosen for the experiment in this study uses the aquaplanet mode (i.e. without orography) with the T42 horizontal resolution (corresponding approximately to a  $2.8^\circ \times 2.8^\circ$  grid) and 10 equidistant sigma levels. The experiment contains 25 annual cycles, though the analysis in the main text only considers the DJF daily data and omits the winter of the first (spin-up) year. The tropopause height is parametrised to 12 km.

The diabatic effects are parametrised as Newtonian cooling and Rayleigh friction, where the temperature is relaxed to a restoration temperature profile  $T_R$  with a timescale,  $\tau_T(p, y)$ , as follows:

$$\frac{\partial T}{\partial t} = \dots - \frac{T - T_R}{\tau_T}. \quad (\text{A.1})$$

The frictional timescale increases exponentially with height from 0.5 days at the lowermost level to infinity at the 0.8 sigma level and above, and the thermal damping timescale ranges from 1.2 days at the lowermost level to 30 days in the uppermost level, following a similar setup to Fraedrich et al. (2005). The mean lapse rate in the restoration temperature,  $T_R$ , in the troposphere is set to be  $-6.5 \text{ K km}^{-1}$ . Hyperdiffusion of the temperature, vorticity and divergence is additionally included to account for unresolved eddy dissipation.

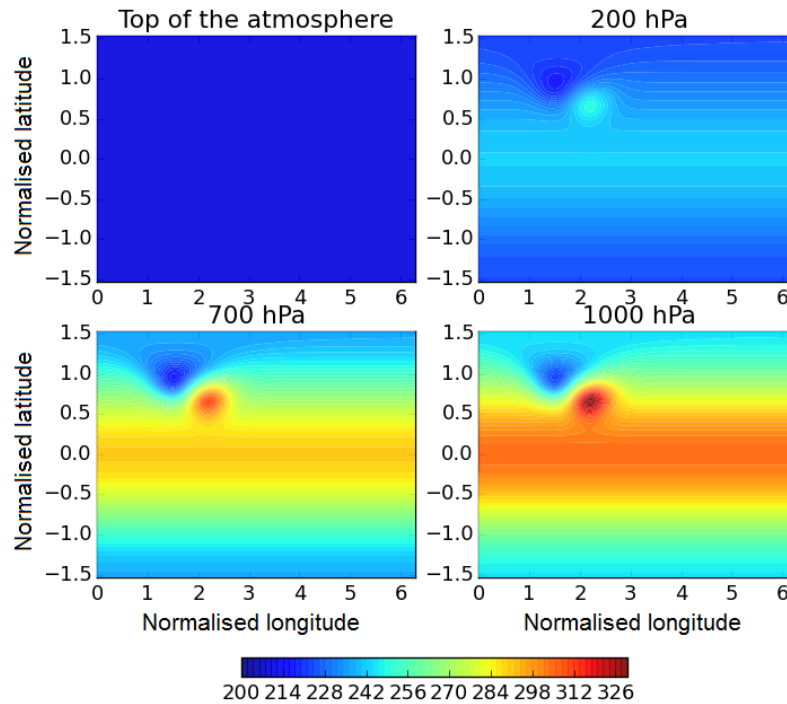


**Figure A.1:** Selection of levels displaying the horizontal profiles of the restoration temperature field (in Kelvin).

The restoration temperature profile is displayed in figure A.1 for a sample of vertical levels. It is based on a meridional temperature gradient replicating the Earth’s radiative imbalance, changing sinusoidally in time during the annual cycle. The temperature gradient also decreases with height and disappears at the tropopause. The equilibrium value of the Equator-pole temperature difference is 60 K. Additionally, following the formulation of Frisius *et al.*’s (1998) “NE case”, the restoration field was manually adapted to include a heating-cooling dipole (-50 and +50 K at the surface) in the mid-latitudes, such that the tightened isotherms between the positive and negative anomalies were at an angle, as shown in figure A.1. Such a tilted dipole of the restoration temperature field was found to induce a localised south west-north east oriented storm track, reminiscent of the North Atlantic setting.

The zonal mean zonal wind, temperature and the meridional overturning circulation shown in figures A.2 and A.3. Despite the simplified setup and coarse resolution, similar patterns and magnitudes of these quantities to their terrestrial equivalents can be observed (Källberg *et al.*, 2005). A mid-latitude jet bifurcates slightly in the lower troposphere and is associated with a descent of the Hadley cell in the subtropics. The Ferrel cell is also apparent in the Eulerian mean, with only a small descent in the polar region.

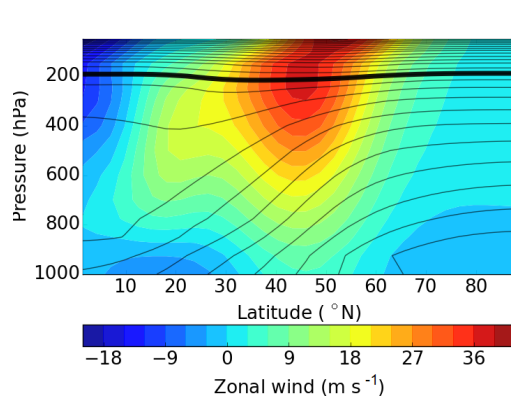


**Figure A.2:** 24 winter means of the zonal-mean profiles of the zonal wind (colours, in  $\text{m s}^{-1}$ ), and the potential temperature (black contours). The thick contour marks 315 K and the interval is 10 K.

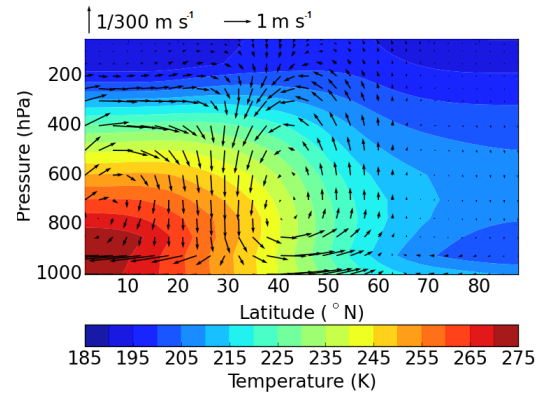


**Figure A.3:** 24 winter means of the zonal-mean profile of the temperature (colours, in K), and the meridional and vertical velocity in (arrows). The vertical velocity has been scaled by  $300 \text{ m s}^{-1}$ .

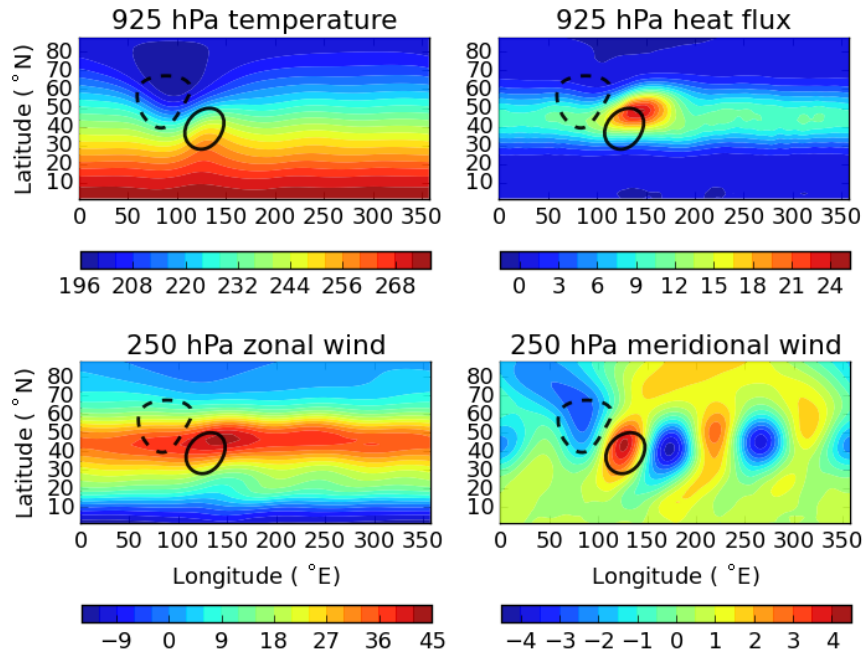


**Figure A.4:** Selection of horizontal profiles of the winter-averaged temperature at 925 hPa, low-level heat flux (vertically averaged between 700 and 925 hPa), zonal wind at 250 hPa, and meridional wind at 250 hPa. The black contours show the 40 K temperature anomalies in the low-level relaxation temperature field (with dashed being negative), marking the location of the heating dipole.

The horizontal view of the upper-level zonal and meridional wind, low-level temperature and the low-level high-frequency meridional heat flux are shown in figures A.4. Associated with the tightening of the temperature gradient is a strengthened zonal jet, maintaining the thermal wind balance. Unlike in the North Atlantic, the time-mean jet at this level does not seem to split and migrate polewards, so in this sense it is more like the Pacific. The jet meanders slightly

with a wavenumber of 3 or 4, which reflects the stationary waves induced by the heating dipole. These waves are more apparent in the meridional wind distribution that shows two wave trains propagating polewards and equatorwards with distance downstream, as they did due to orography in Hoskins *et al.*'s (1983) study mentioned in the introduction (figure 2.14). It is therefore apparent that this tilting induces momentum convergence in the jet core, as observed. With an increased baroclinicity is an increase in eddy activity. The eddy heat flux peaks slightly downstream of the sharpest temperature gradients, with a magnitude comparable to that in the North Atlantic.

The same or similar versions of this model have been relatively widely used to simulate the baroclinic interactions in the atmosphere and larger-scale storm track dynamics (e.g. James and Gray, 1986; Frisius *et al.*, 1998; Fraedrich *et al.*, 2005). Overall, the present setup outlined above yields suitable results for study of isolated storm tracks, and so it was chosen to test some of the theories in the main text where reanalysis data would yield ambiguous results (for example, when using zonal averaging).

## Appendix B

# An Example Attempt to Justify the Nonlinear Oscillator Model Using Normal Mode Analysis

Because of its simplicity, we attempted to derive our oscillator model equations using the nonlinear two-layer Phillips model. After combining the vorticity equations for the two layers with the thermodynamic equation, the model equations are:

$$\frac{\partial \nabla^2 \psi_M}{\partial t} + \mathbf{v}_M \cdot \nabla (\nabla^2 \psi_M) + \mathbf{v}_T \cdot \nabla (\nabla^2 \psi_T) = 0, \quad (\text{B.1})$$

$$\left( \frac{\partial}{\partial t} + \mathbf{v}_M \cdot \nabla \right) (\nabla^2 \psi_T - 2\lambda^2 \psi_T) + \mathbf{v}_T \cdot \nabla (\nabla^2 \psi_M) = 0, \quad (\text{B.2})$$

where  $\psi_M$  is the vertically averaged streamfunction and  $\psi_T$  is the baroclinic streamfunction representing the thermal wind shear.  $\lambda$  is the inverse Rossby radius of deformation (see Holton, 2004). Assuming that the flow can be partitioned into a zonal mean flow and perturbations therefrom, different shapes of the streamfunctions have been tested, but no exact general solution has so far been found. The  $y$  dependence of the streamfunction perturbations is essential for retaining the nonlinearities, and without it we obtain the linearised equation set in Holton (2004, p. 233). However, using perturbations dependent on both  $x$  and  $y$  yields nonlinear terms which introduce additional higher-wavenumber flow structures. Despite the lack of a general solution, we have found an approximated solution that is analogous to the idealised nonlinear oscillator model. This is obtained by assuming the following streamfunctions:

$$\psi_M = A(t) \cos(l y) \cos(k x), \quad (\text{B.3})$$

$$\psi_T = -u_T(t) y - B(t) \cos(l y) \sin(k x), \quad (\text{B.4})$$

where  $A$  and  $B$  are the time-dependent wave amplitudes,  $u_T$  is the zonal mean thermal wind, and  $k$  and  $l$  are the zonal and meridional wavenumbers, respectively. Note that the barotropic mean wind is zero, implying no net momentum supply into the jet. Using zonal averaging and substituting into equations B.1 and B.2, two perturbation equations can be obtained:

$$\frac{\partial A}{\partial t} = ku_TB, \quad (\text{B.5})$$

$$\frac{\partial B}{\partial t} = ku_TA \frac{2\lambda^2 - k^2}{2\lambda^2 + k^2}, \quad (\text{B.6})$$

and a zonal mean equation

$$\frac{du_T}{dt} = -\frac{1}{2}ABkl \frac{\sin(2ly)}{y} \approx -ABkl^2. \quad (\text{B.7})$$

The above approximation is only valid locally where  $\sin 2ly = 2ly$ . Scaling the above variables so that equation B.5 has the same form as equation B.6 yields:

$$s = ku_T \left( \frac{2\lambda^2 - k^2}{2\lambda^2 + k^2} \right)^{1/2}, \quad (\text{B.8})$$

$$\frac{d\hat{A}}{dt} = s\hat{B}, \quad (\text{B.9})$$

$$\frac{d\hat{B}}{dt} = s\hat{A}, \quad (\text{B.10})$$

$$\frac{ds}{dt} = -k^2l^2\hat{A}\hat{B}. \quad (\text{B.11})$$

Assuming  $\hat{A} = \hat{B}$ , we can derive the idealised unforced nonlinear oscillator model equations:

$$\frac{df}{dt} = 2sf, \quad (\text{B.12})$$

$$\frac{ds}{dt} = -k^2l^2f, \quad (\text{B.13})$$

where  $f = \hat{A}^2$  is proportional to heat flux and  $s$  is proportional to baroclinicity. Although the above approximation is relatively crude, this derivation is valid locally (near the jet core) and is a useful way of linking the idealised model to first principles. It shows that the  $y$  dependence of the perturbations is essential for retaining the nonlinearity and that, to the leading order, the real system near the jet core does exhibit the nonlinear oscillator behaviour.

## Appendix C

# Truncation of Thompson's (1987) Model

Thompson's (1987) model is based on the two-layer quasi-geostrophic model of a  $\beta$ -plane channel domain. By combining the vorticity and thermodynamic equations of the two layers (as in Holton, 2004), one can obtain:

$$\frac{\partial \nabla^2 \psi_m}{\partial t} + J(\psi_m, \nabla^2 \psi_m) + J(\psi_t, \nabla^2 \psi_t) + \beta \frac{\partial \psi_m}{\partial x} = \nu \nabla^2 \nabla^2 \psi_m, \quad (\text{C.1})$$

$$\begin{aligned} \frac{\partial \nabla^2 \psi_t - k_r \psi_t}{\partial t} + J(\psi_m, \nabla^2 \psi_t - k_r \psi_t) + J(\psi_t, \nabla^2 \psi_m) \\ + \beta \frac{\partial \psi_t}{\partial x} = \nu \nabla^2 (\nabla^2 \psi_t - k_r \psi_t) - \frac{\kappa_r^2 p_0 Q}{4f\rho\theta}, \end{aligned} \quad (\text{C.2})$$

where  $\nabla^2$  is the horizontal Laplacian and  $J$  is the horizontal Jacobian.  $k_r^2$  is the inverse square of the Rossby deformation radius,  $\nu$  is a constant eddy viscosity coefficient,  $p_0$  is the surface pressure,  $f$  is the Coriolis parameter and  $\beta$  is its northward derivative,  $\theta$  and  $\rho$  are the standard values of potential temperature and density on the inter-layer interface, and  $Q$  is the diabatic heating rate (dependent on  $t$  and  $y$  only). The barotropic and baroclinic geostrophic stream functions are:

$$\psi_m = \frac{\psi_1 + \psi_2}{2}, \quad \psi_t = \frac{\psi_1 - \psi_2}{2}, \quad (\text{C.3})$$

where 1 and 2 refer to the upper and lower layers, respectively. By splitting the flow into its zonal mean and perturbation components:

$$\psi_{m,t} = \Psi_{m,t}(y, t) + \phi_{m,t}(x, y, t) \quad (\text{C.4})$$

and assuming the following structure of the perturbations:

$$\phi_{m,t}(x, y, t) = S_{m,t}(t) \sin \lambda x \sin \frac{\pi y}{W} + C_{m,t}(t) \cos \lambda x \sin \frac{\pi y}{W}, \quad (\text{C.5})$$

where  $\lambda = k_x$  and  $\pi/W = k_y$  are the zonal and meridional wavenumbers respectively, Thompson obtained a closed system of five evolution equations for mean vertical wind shear, poleward heat flux, meridional kinetic energy, temperature variance and cross-correlation between temperature and geopotential. In the same order, these equations are:

$$\frac{\partial U_t}{\partial t} + 2k_y^2 \overline{v_m \phi_t} = -2k_y^2 \nu U_t - \frac{p_0}{4f\rho\theta} \frac{\partial Q}{\partial y}, \quad (\text{C.6})$$

$$\begin{aligned} \frac{\partial \overline{v_m \phi_t}}{\partial t} - \frac{(k_r^2 + k_y^2 - k_x^2)}{k_r^2 + k_x^2 + k_y^2} U_t \overline{v_m^2} - \frac{(k_x^2 - k_y^2)}{k_x^2 + k_y^2} U_t \overline{v_t^2} + \\ \frac{\beta k_r^2}{(k_x^2 + k_y^2)(k_r^2 + k_x^2 + k_y^2)} \overline{v_m v_t} + 2\nu(k_x^2 + k_y^2) \overline{v_m \phi_t} = 0, \end{aligned} \quad (\text{C.7})$$

$$\frac{\partial \overline{v_m^2}}{\partial t} - \frac{2k_x^2(k_x^2 - k_y^2)}{k_x^2 + k_y^2} U_t \overline{v_m \phi_t} + 2\nu(k_x^2 + k_y^2) \overline{v_m^2} = 0, \quad (\text{C.8})$$

$$\frac{\partial \overline{v_t^2}}{\partial t} - \frac{2k_x^2(k_r^2 - k_x^2 + k_y^2)}{k_x^2 + k_y^2 + k_r^2} U_t \overline{v_m \phi_t} + 2\nu(k_x^2 + k_y^2) \overline{v_t^2} = 0, \quad (\text{C.9})$$

$$\frac{\partial \overline{v_m v_t}}{\partial t} - \frac{\beta k_x^2 k_r^2}{(k_x^2 + k_y^2)(k_r^2 + k_x^2 + k_y^2)} \overline{v_m \phi_t} + 2\nu(k_x^2 + k_y^2) \overline{v_m v_t} = 0, \quad (\text{C.10})$$

where  $U_{m,t} = -(\partial \Psi_{m,t} / \partial y)$ , and  $v_{m,t} = (\partial \phi_{m,t} / \partial x)$ . This system therefore describes an interaction between a mean flow mode and four perturbation modes, and Thompson (1987) shows explicitly that such coupling between the mean and the perturbation fields leads to temporal oscillations of all modes (which is reminiscent of the predator-prey behaviour). It is therefore unsurprising that parallels can be drawn between Thompson's model and the nonlinear oscillator model, which is demonstrated as follows. It is first noted that the perturbation equations can be written in a matrix form as:

$$\frac{\partial A}{\partial t} = xAU_t - DA, \quad (\text{C.11})$$

where

$$\begin{aligned} A &= \begin{bmatrix} \overline{v_m \phi_t} & \overline{v_m^2} & \overline{v_t^2} & \overline{v_m v_t} \end{bmatrix}, \\ x &= \begin{bmatrix} 0 & q_1 & q_2 & -\beta q_3 / U_t \\ 2q_2 k_x^2 & 0 & 0 & 0 \\ 2q_1 k_x^2 & 0 & 0 & 0 \\ q_3 k_x^2 / U_t & 0 & 0 & 0 \end{bmatrix}, \end{aligned}$$

where  $q_1 = (k_r^2 + k_y^2 - k_x^2)/(k_r^2 + k_x^2 + k_y^2)$ ,  $q_2 = (k_x^2 - k_y^2)/(k_x^2 + k_y^2)$ , and  $q_3 = k_r^2/((k_x^2 + k_y^2)(k_r^2 + k_x^2 + k_y^2))$  are constants depending on the horizontal and vertical structure of the perturbations.  $D = 2\nu(k_x^2 + k_y^2)$  is a linear dissipation rate of the perturbations. It is apparent that under vanishing  $\beta$ , matrix  $x$  is independent of time and so equation C.11 attains the same shape as the perturbation equation of the nonlinear oscillator model (equation 3.3) and the evolution equation of  $\overline{v_m v_t}$  is decoupled from the system. If the remaining eddy quantities are then all approximately proportional to each other, then  $\overline{v_m \phi_t} \propto A$  in equation C.6. This approximation is supported by observations in chapter 5. If the term representing damping of the thermal wind in equation C.6 is assumed to be small, a system analogous to the nonlinear oscillator is obtained:

$$\frac{\partial U_t}{\partial t} = F - 2k_y^2 c A, \quad (\text{C.12})$$

$$\frac{\partial A}{\partial t} = x A U_t - D A, \quad (\text{C.13})$$

where  $F = p_0/(4f\rho\theta)(\partial Q/\partial y)$  and  $c$  is a constant of proportionality between  $\overline{v_m \phi_t}$  and  $A$ .

It is also noted by Thompson (1988) that the frequency of oscillation of the five-dimensional system can be approximated as:

$$\omega_i = [4N(R^2 + D^2)]^{1/4} \left(\frac{H}{D}\right)^{1/2}, \quad (\text{C.14})$$

where  $H$  and  $D$  are the dimensionless rates of heating and dissipation, respectively, and  $N$  and  $R$  are constants that under the limit of  $k_r \gg k_x, k_y$  reduce to 1. Thus for dimensionless friction less than 1, the frequency depends strongly on both the heating forcing and the friction. However, for friction much larger than 1 the frequency is approximately equal to the square root of twice the heating forcing alone. This is precisely the frequency of the nonlinear oscillator model, reflecting the similar nature of the two systems.

## Appendix D

# The Connection to the Lorenz-84 Model

van Veen (2003) showed that the model of Lorenz (1984) can be derived from a two-layer QG model, which after some truncation can be written in a three dimensional form as follows:

$$\frac{dX}{dt} = -aX - (Y^2 + Z^2) + aF \quad (\text{D.1})$$

$$\frac{dY}{dt} = -Y + bXZ + XY + G \quad (\text{D.2})$$

$$\frac{dZ}{dt} = -Z - bXY + XZ \quad (\text{D.3})$$

where  $X$  represents the thermal wind, and  $Y$  and  $Z$  represent the cosine and sine components of the phase of eddies respectively. The  $aF$  terms represents a constant mean symmetric thermal forcing, and  $G$  is a constant eddy asymmetric thermal forcing. The  $b$  terms represent mean advection of eddies by the westerly flow, with  $b$  being constant. If we multiply equation D.2 by  $Y$  and equation D.3 by  $Z$ , and then sum the two results together, we find the following equation set:

$$\frac{dU_T}{dt} = a(F - U_T) - 2A - aU_T, \quad \frac{dA}{dt} = 2A(U_T - 1) + GY, \quad (\text{D.4})$$

where  $u = X$ ,  $A = 1/2(Y^2 + Z^2)$ . Should the last terms of both equations disappear, we would obtain a system equivalent to the nonlinear oscillator model. This would occur if the mean Newtonian heating was balanced by the mean internal boundary frictional dissipation to produce an overall positive diabatic term (as suggested by Oort's (1964) results), and if the asymmetric thermal eddy forcing was absent ( $GY=0$ ).

## Appendix E

# Sensitivity of Oscillatory Properties to Kernel Phase-space Averaging

There are two parameters to which the quantitative analysis of the oscillatory properties in the phase space was found sensitive: the size and the shape of the Gaussian smoothing filter that was used to average over the phase space. To demonstrate the effect of changing filter size, Figure E.1a shows the change in frequency with amplitude for cases when fine, coarse and medium smoothing of the phase space was applied. It is apparent that excessive smoothing makes the decrease in frequency with amplitude very slow and it yields a lower natural frequency compared to the cases when smaller-sized filters are used. However, the smallest-sized filter exhibits a decrease in frequency that is no longer monotonous, reflecting the additional fine-scale structure of the phase space plot (Figure 3.7a and b). As mentioned earlier, one must compromise between losing the desired structure and gaining additional fine-scale noise. The focus in the main text is therefore on the optimal medium-sized filter. It should be noted that while the analysis of the frequency change with amplitude is rather sensitive to the filter size, the analysis of the  $y$ -tendency change with amplitude during the onset and termination of heat flux events is less sensitive (Figure E.1b).

The shape of the smoothing filter is closely related to the value of the scaling factor  $kl^2$ , which is used to scale baroclinicity to its non-dimensional equivalent ( $\sigma = 2s/\sqrt{2F} = 2s/\sqrt{2ckl^2\overline{v'T'}}$ , where  $c$  is an empirically determined constant which scales the time-mean heat flux to make it equal to the central point in the phase space plot). A proper scaling of the system should allow the use of a circular filter in the non-dimensional phase space. However, if the scaling factor was too small then the baroclinicity would be too stretched relative to the  $y$  variable (and the filter too compressed along the baroclinicity axis). In the case of an excessively stretched baroclinicity, the nonlinear oscillator model predicts that the trajectories would travel too far along the baroclinicity axis in the phase space into regions of higher energy (or Lyapunov function,  $E$ ) where the speeds

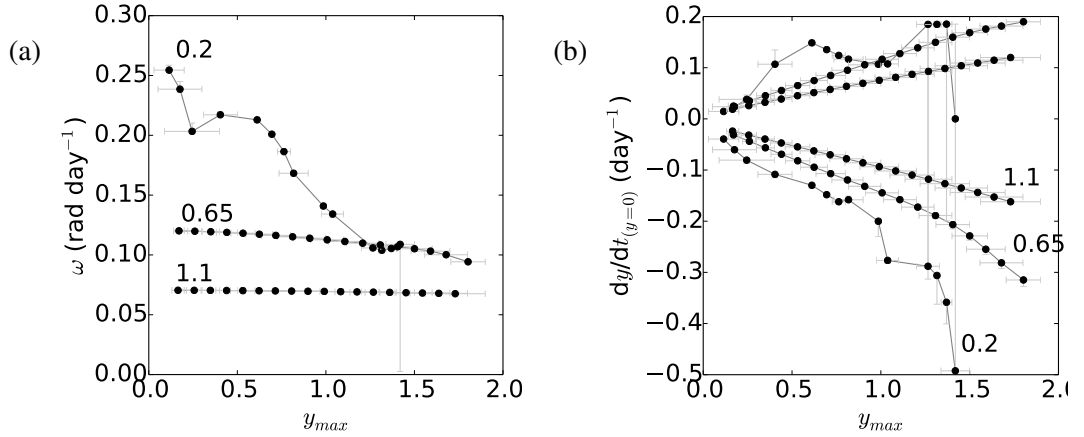


**Figure E.1:** Comparison of the effects of largest, medium and finest filtering on a) the frequency change with amplitude and b) the change in the  $y$  tendency at  $y = 0$  with amplitude. This comparison is based on the North Atlantic heat flux and baroclinicity, and the scaling factor  $kl^2 = 3.1 \times 10^{-13} \text{ K}^{-1} \text{ m}^{-1} \text{ s}^{-1}$  was selected. The numbers indicate the standard deviations of the filters. The medium filter changes are equivalent to Figure 3.8. Taken from Novak *et al.* (in review).

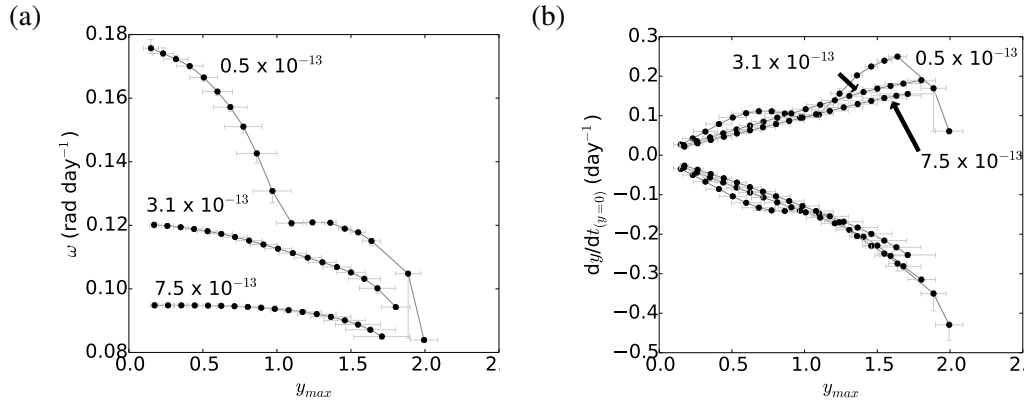


**Figure E.2:** As in Figure E.2 but comparing different values of the scaling factor (indicated in  $\text{K}^{-1} \text{ m}^{-1} \text{ s}^{-1}$ ),  $kl^2$ , for the medium-sized filter. Taken from Novak *et al.* (in review).

are higher, which could make the overall oscillation period shorter, and vice versa. In the data, this effect of baroclinicity stretching on the time period was found to be true for all reasonable filter sizes and amplitudes tested (Figure E.2).

As a further example, Figure E.3 shows how the natural frequency, obtained using the medium-sized filter, decreases as the scaling factor increases. This figure also shows the analytical relationship that  $\omega_0 = \sqrt{2F} = \sqrt{2ckl^2\bar{v}'T'}$  predicted by the nonlinear oscillator model. In this

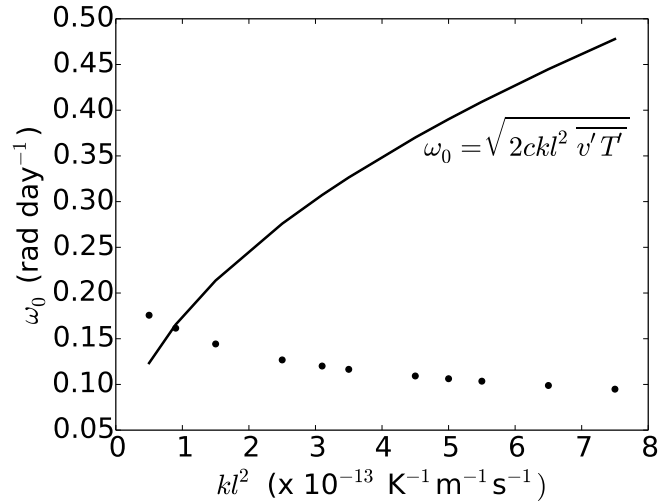


**Figure E.3:** Natural frequency change with the scaling factor,  $kl^2$ , tested for the North Atlantic heat flux and baroclinicity phase space, using the medium-sized filter. The analytical prediction of the relationship based on the nonlinear oscillator model is also shown (see text for more detail). Taken from Novak *et al.* (in review).

case  $c = 1.03$  since the time-mean heat flux lies very close to the central value. It is reasonable to expect that the convergence of the predicted analytical relationship with the observed (filter-dependent) values would indicate the appropriate value for the scaling factor. For the medium-sized filter the convergence is at  $ckl^2 = 0.9 \times 10^{-13} \text{ K}^{-1} \text{ m}^{-1} \text{ s}^{-1}$ . The corresponding variability of the Lyapunov function (estimated from data using equation 3.9) of a selection of trajectories of different amplitudes is shown in Figure E.4a. Each trajectory represents integrations in time (using the fourth-order Runge Kutta method), starting from the maximum heat flux when  $s = 0$ , until an entire cycle has been completed. It is apparent that when the trajectories reach the heat flux maxima and minima, the Lyapunov function for this particular scaling factor decreases substantially compared to the times when the trajectories are near the baroclinicity maxima and minima. This implies that the baroclinicity is still a little overstretched. The system was therefore further tested for slightly higher values of the scaling factor, with  $kl^2 = 3.1 \times 10^{-13} \text{ K}^{-1} \text{ m}^{-1} \text{ s}^{-1}$  yielding the least pronounced fluctuations in the Lyapunov function, as shown in Figure E.4b. Evidently, the Lyapunov function also varies at times when the trajectories are not at the maxima and minima of heat flux or baroclinicity, reflecting the additional structure in the data that is not characteristic of the nonlinear oscillator model. The overall Lyapunov function also decreases slightly in time mirroring the trajectory convergence towards the centre, as is shown in the corresponding phase space plot (Figure 3.7e). As noted in the main text, low-amplitude oscillations

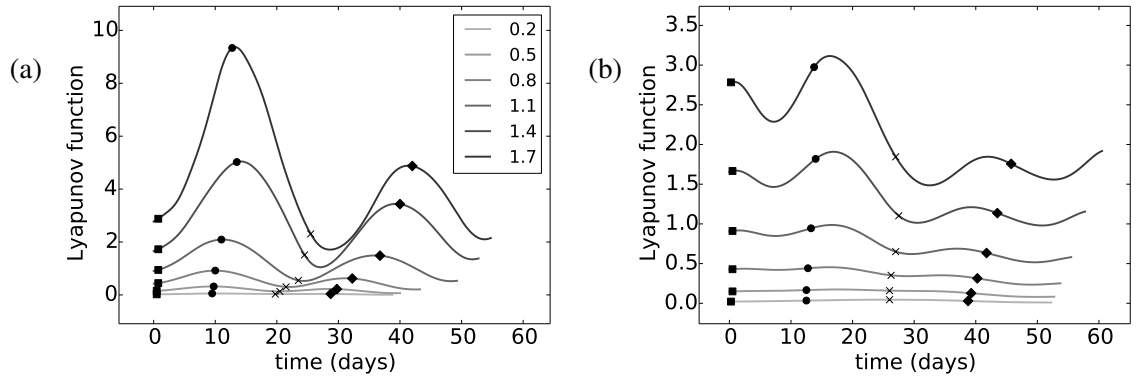


**Figure E.4:** Change of the Lyapunov function along the trajectories of one cycle in the phase space plot for different starting amplitudes of  $y_{\text{MAX}}$  for (a)  $kl^2 = 0.9e - 13 \text{ K}^{-1} \text{ m}^{-1} \text{ s}^{-1}$  and (b)  $kl^2 = 3.1e - 13 \text{ K}^{-1} \text{ m}^{-1} \text{ s}^{-1}$ . The legend indicates the initial amplitude ( $y_{\text{max}}$ ) of each trajectory. The points at which the trajectories reached the positive and negative heat flux at  $s = 0$  (squares and crosses, respectively), and positive and negative baroclinicity at  $y = 0$  (diamonds and circles, respectively) are also shown. Taken from Novak *et al.* (in review).

are almost linear and so they exhibit smaller fluctuations in the Lyapunov function, as well as a reduced overall decay of the latter.

It should be pointed out that if one explores the scaling of the  $kl^2$  factor, it can be found empirically that the value of the Eady scale  $k = 0.31g/(NT_0) \approx 0.78 \text{ m K}^{-1} \text{ s}^{-1}$  and  $c = 1.03$ . For  $kl^2 = 3.1 \times 10^{-13} \text{ K}^{-1} \text{ m}^{-1} \text{ s}^{-1}$ , this would therefore yield the meridional extent of the storm track (or half of the wavelength) of 5000 km. This seems excessive, but is the right order of magnitude. It should be noted that the maximum Eady growth rate is known to overestimate the length scales of cyclones (James, 1994), meaning that it may require larger than observed eddies to produce a more realistic baroclinicity. In addition, it is apparent that the data analysis includes a substantial amount of averaging of the phase space due to the additional noise of the data. It was shown that averaging reduces the natural frequencies and would thus increase the spatial scales of the disturbances estimated from the above scaling.

It was shown above that the filter can be tuned to adhere to the nonlinear oscillator model and the remnants of the data variability can be classed as noise. However, the model itself can be parametrised to adhere to the data. Thus it could be argued that there is no perfect precise size and shape of the filter. The results here merely state that a consistency between the nonlinear oscillator model and the observed data can be achieved by their mutual tuning. This consistency is

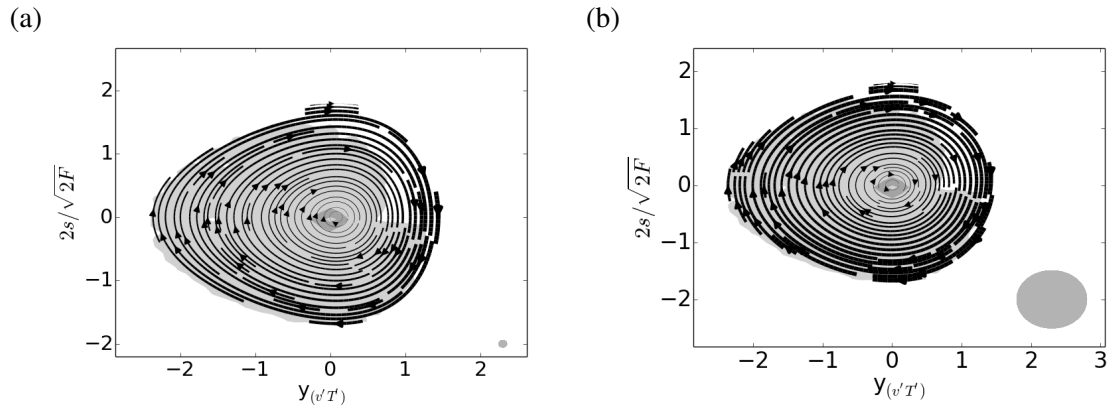


**Figure E.5:** Phase plots of the numerically integrated nonlinear oscillator model for fine (a) and coarse (b) filtering, with the radius of the grey ellipse indicating the standard deviation of the Gaussian phase space filter. The grey-scale shading indicates the two-dimensional histogram, marking values of 10, 50 and more points. The speed of oscillation is indicated by the thickness of the trajectories.

by no means obvious and not always perfectly achievable, as seen in the North Pacific storm track case in the main text. Additionally, a moderate consistency between the qualitative behaviour of the data and the model can be achieved without the mutual tuning, as long as a reasonable filter size and shape are selected (i.e. a filter that reflects the data point distribution adequately along both axes of the phase space). This consistency of the idealised nonlinear oscillator model with the observed storm tracks suggests that similar dynamics underline them. For more unequivocal results, it may be useful to analyse the remaining data variability (here viewed as noise) and isolate it from the phase-space oscillations in medium-complexity models. This is beyond the scope of this thesis.

The effect of the phase space filtering was also tested for timeseries extracted from the nonlinear oscillator model. It is apparent from figure E.5 that the main qualitative features of the circulation are retained, with a clockwise circulation around a single point exhibiting faster trajectories at higher amplitudes. It is apparent that the filtering makes the circulation less skewed and moves its centre slightly to the negative  $y$  values. Consistent with the analysis above, it was found that the coarser the filtering the smaller the changes with amplitude in the frequency and speed of oscillation (not shown). This analysis also showed that the natural frequency reduces with the coarseness of filtering (around 20% for a kernel of a normalised standard deviation of 1, as in figure E.5b). The coarse filtering also causes the frequency near the centre of the circulation to decrease (not shown), due to the Gaussian kernel filter selecting tendencies of the opposite direction. This effect appears only very slightly in the North Pacific, and not at all in the North

Atlantic or PUMA. As opposed to the idealised model, the observed data are very noisy near the centre of the phase plot and so the cancellation effect of opposing trajectories near the centre is not as pronounced. This analysis emphasizes that care needs to be taken when interpreting the precise value of the oscillating frequency obtained from this phase space filtering method, but the qualitative behaviour can be recovered relatively well, even for coarse filtering.

## Appendix F

# Derivation of Lorenz Evolution Equations

In order to investigate the conversion between the eddy and mean available potential and kinetic energy terms, it is useful to analyse their evolution. The evolution equations for the Lorenz APE and KE components are obtained using the momentum and thermodynamic equations, respectively. Working in the spherical pressure coordinates, the momentum equations are:

$$\frac{\partial u}{\partial t} + \frac{u}{a \cos \phi} \frac{\partial u}{\partial \lambda} + \frac{v}{a} \frac{\partial u}{\partial \phi} + \omega \frac{\partial u}{\partial p} - \frac{uv}{a} \tan \phi - \frac{u\omega}{a\rho g} = 2\Omega v \sin \phi + \frac{2\Omega}{g\rho} \omega \cos \phi - \frac{1}{a \cos \phi} \frac{\partial \Phi}{\partial \lambda} + F_x, \quad (\text{F.1})$$

$$\frac{\partial v}{\partial t} + \frac{u}{a \cos \phi} \frac{\partial v}{\partial \lambda} + \frac{v}{a} \frac{\partial v}{\partial \phi} + \omega \frac{\partial v}{\partial p} + \frac{u^2}{a} \tan \phi - \frac{v\omega}{a g \rho} = 2\Omega u \sin \phi - \frac{1}{a} \frac{\partial \Phi}{\partial \phi} + F_y, \quad (\text{F.2})$$

where the geopotential is  $\Phi = gZ$  and  $\omega \approx g\rho w$ . The continuity equation is of the form:

$$\frac{1}{a \cos \phi} \frac{\partial u}{\partial \lambda} + \frac{1}{a \cos \phi} \frac{\partial v \cos \phi}{\partial \phi} + \frac{\partial \omega}{\partial p} = 0, \quad (\text{F.3})$$

and the divergence of a vector  $\mathbf{Q} = (Q_x, Q_y, Q_p)$  is:

$$\nabla \cdot \mathbf{Q} = \frac{1}{a \cos \phi} \frac{\partial Q_x}{\partial \lambda} + \frac{1}{a \cos \phi} \frac{\partial Q_y \cos \phi}{\partial \phi} + \frac{\partial Q_p}{\partial p}. \quad (\text{F.4})$$

This is zero when integrated over a closed system (e.g. when integrated globally).

The mean kinetic energy is obtained by multiplying equations F.1 and F.2 by their respective mean (here running time mean) horizontal velocity components. Using the continuity equation

and averaging these equations F.1 and F.2 (using the same averaging operator) then leads to:

$$\begin{aligned} \frac{1}{2} \frac{\partial \bar{u}^2}{\partial t} + \frac{\bar{u}}{a \cos \phi} \frac{\partial(\bar{u}^2 + \overline{u'u'})}{\partial \lambda} + \frac{\bar{u}}{a \cos \phi} \frac{\partial(\bar{u}\bar{v} + \overline{u'v'}) \cos \phi}{\partial \phi} + \bar{u} \frac{\partial(\bar{u}\bar{\omega} + \overline{u'\omega'})}{\partial p} \\ - \bar{u} \frac{(\bar{u}\bar{v} + \overline{u'v'})}{a} \tan \phi - \frac{\bar{u}\bar{u}\bar{\omega}}{ag\rho} = - \frac{\bar{u}}{a \cos \phi} \frac{\partial \delta \Phi}{\partial \lambda} + \frac{2\Omega}{g\rho} \bar{u}\bar{\omega} \cos \phi + \bar{u}\bar{F}_x \end{aligned} \quad (\text{F.5})$$

$$\begin{aligned} \frac{1}{2} \frac{\partial \bar{v}^2}{\partial t} + \frac{\bar{v}}{a \cos \phi} \frac{\partial(\bar{u}\bar{v} + \overline{u'v'})}{\partial \lambda} + \frac{\bar{v}}{a \cos \phi} \frac{\partial(\bar{v}^2 + \overline{v'v'}) \cos \phi}{\partial \phi} + \bar{v} \frac{\partial(\bar{v}\bar{\omega} + \overline{v'\omega'})}{\partial p} \\ - \frac{\bar{v}\bar{v}\bar{\omega}}{ag\rho} + \frac{\bar{v}}{a} \tan \phi (\bar{u}^2 + \overline{u'^2}) = - \frac{\bar{v}}{a} \frac{\partial \delta \Phi}{\partial \phi} + \bar{v}\bar{F}_y \end{aligned} \quad (\text{F.6})$$

where  $\delta\Phi = \Phi - \Phi_r$  is the difference between the geopotential values of the actual and reference states, whose derivative in  $p$  is equal to the negative specific volume (Tailleux et al., to be submitted). The Coriolis terms have been cancelled out. Rearranging, integrating globally and adding these two equations together yields the mean kinetic energy equation:

$$\begin{aligned} \frac{\partial KM}{\partial t} = & \underbrace{\left\langle \frac{\overline{u'u'}}{a \cos \phi} \frac{\partial \bar{u}}{\partial \lambda} \right\rangle + \left\langle \overline{u'v'} \cos \phi \frac{\partial \bar{u} \cos^{-1} \phi}{a \partial \phi} \right\rangle + \left\langle \overline{u'\omega'} \frac{\partial \bar{u}}{\partial p} \right\rangle + \left\langle \frac{\overline{u'v'}}{a \cos \phi} \frac{\partial \bar{v}}{\partial \lambda} \right\rangle}_{\text{CK}} \\ & + \underbrace{\left\langle \overline{v'v'} \cos \phi \frac{\partial \bar{v} \cos^{-1} \phi}{a \partial \phi} \right\rangle + \left\langle \overline{v'\omega'} \frac{\partial \bar{v}}{\partial p} \right\rangle - (\bar{u}^2 + \overline{u'^2}) \bar{v} \frac{\tan \phi}{a}}_{\text{CK}} + \left\langle \frac{2\Omega}{g\rho} \bar{u}\bar{\omega} \cos \phi \right\rangle \\ & + \left\langle \frac{\bar{u}\bar{u}\bar{\omega}}{ag\rho} \right\rangle + \left\langle \frac{\bar{v}\bar{v}\bar{\omega}}{ag\rho} \right\rangle - \underbrace{\left\langle \bar{\omega}'' \bar{\alpha}'' \right\rangle}_{\text{CM}} + \underbrace{\left\langle \bar{u}\bar{F}_x + \bar{v}\bar{F}_y \right\rangle}_{\text{GKM}} \end{aligned} \quad (\text{F.7})$$

where the global averaging operator is

$$\langle X \rangle = \frac{1}{A} \int X dm = -\frac{1}{gA} \int \int \int X a^2 \cos \phi d\lambda d\phi dp \quad (\text{F.8})$$

and it gives the mass integrated  $X$  per unit area, where  $A$  is the surface area of the Earth. The globally integrated flux of a scalar  $X$  is zero:

$$\langle \nabla \cdot (\mathbf{u}X) \rangle = \left\langle \frac{1}{\cos \phi} \left( \frac{\partial}{a \cos \phi \partial \lambda} + \frac{\partial}{a \partial \phi} + \frac{\partial}{\partial p} \right) (\mathbf{u}X \cos \phi) \right\rangle = 0, \quad (\text{F.9})$$

$$KM = \frac{1}{2} \langle (\bar{u}^2 + \bar{v}^2) \rangle, \quad (\text{F.10})$$

$$\rho^{-1} = \alpha, \quad (\text{F.11})$$

$$\left\langle \frac{\bar{u}}{a \cos \phi} \frac{\partial \bar{\delta \Phi}}{\partial \lambda} \right\rangle + \left\langle \frac{\bar{v}}{a} \frac{\partial \bar{\delta \Phi}}{\partial \phi} \right\rangle = - \left\langle \bar{\omega} \frac{\partial \bar{\delta \Phi}}{\partial p} \right\rangle = \langle \bar{\omega} \bar{\delta \alpha} \rangle = \langle \bar{\omega}' \bar{\alpha}' \rangle. \quad (\text{F.12})$$

In red are the terms that are either cancelled out in the stationary framework or often neglected (e.g. Oort, 1964).

Similar techniques can be applied to calculate the eddy kinetic energy equation. The momentum equation multiplied by the perturbation horizontal velocity and averaged is:

$$\begin{aligned} \frac{1}{2} \frac{\partial \bar{u}'^2}{\partial t} = & - \frac{\overline{u'u'}}{a \cos \phi} \frac{\partial \bar{u}}{\partial \lambda} - \frac{\overline{u'v'} \cos \phi}{a} \frac{\partial \bar{u} \cos^{-1} \phi}{\partial \phi} - \overline{u'\omega'} \frac{\partial \bar{u}}{\partial p} - \frac{1}{2} \frac{\bar{u}}{a \cos \phi} \frac{\partial \bar{u}'^2}{\partial \lambda} - \frac{1}{2} \frac{\bar{v}}{a} \frac{\partial \bar{u}'^2}{\partial \phi} \\ & - \frac{1}{2} \bar{\omega} \frac{\partial \bar{u}'^2}{\partial p} + \frac{\overline{u'^2 \bar{v}} \tan \phi}{a} + 2 \frac{\overline{u'v'u}}{a} \frac{\tan \phi}{a} - \frac{\overline{u' \partial \delta \Phi}}{a \cos \phi} \frac{\partial \bar{u}}{\partial \lambda} + \overline{u' F'_x} + \frac{2\Omega}{g\rho} \overline{u'\omega'} \cos \phi + \overline{u' \frac{u\omega}{ag\rho}} \\ & + O_x(3) \end{aligned} \quad (\text{F.13})$$

$$\begin{aligned} \frac{1}{2} \frac{\partial \bar{v}'^2}{\partial t} = & - \frac{\overline{u'v'}}{a \cos \phi} \frac{\partial \bar{v}}{\partial \lambda} - \frac{\overline{v'v'} \cos \phi}{a} \frac{\partial \bar{v} \cos^{-1} \phi}{\partial \phi} - \overline{v'\omega'} \frac{\partial \bar{v}}{\partial p} - \frac{1}{2} \frac{\bar{u}}{a \cos \phi} \frac{\partial \bar{v}'^2}{\partial \lambda} - \frac{1}{2} \frac{\bar{v}}{a} \frac{\partial \bar{v}'^2}{\partial \phi} \\ & - \frac{1}{2} \bar{\omega} \frac{\partial \bar{v}'^2}{\partial p} - 2 \frac{\overline{u'v'u}}{a} \frac{\tan \phi}{a} + \frac{\overline{v'^2 \bar{v}} \tan \phi}{a} + \overline{v' \frac{v\omega}{ag\rho}} - \frac{\overline{v' \partial \delta \Phi}}{a} \frac{\partial \bar{v}}{\partial \phi} + \overline{v' F'_y} + O_y(3) \end{aligned} \quad (\text{F.14})$$

Adding equations F.13 and F.14 together, we obtain the equation for the eddy kinetic energy:

$$\begin{aligned} \frac{\partial KE}{\partial t} = & - \underbrace{\left\langle \frac{\overline{u'u'}}{a \cos \phi} \frac{\partial \bar{u}}{\partial \lambda} \right\rangle - \left\langle \frac{\overline{u'v'} \cos \phi}{a} \frac{\partial \bar{u} \cos^{-1} \phi}{\partial \phi} \right\rangle - \left\langle \overline{u'\omega'} \frac{\partial \bar{u}}{\partial p} \right\rangle - \left\langle \frac{\overline{u'v'}}{a \cos \phi} \frac{\partial \bar{v}}{\partial \lambda} \right\rangle}_{\text{CK}} \\ & - \underbrace{\left\langle \frac{\overline{v'v'} \cos \phi}{a} \frac{\partial \bar{v} \cos^{-1} \phi}{\partial \phi} \right\rangle - \left\langle \overline{v'\omega'} \frac{\partial \bar{v}}{\partial p} \right\rangle + \left\langle (\overline{u'^2} + \overline{v'^2}) \bar{v} \frac{\tan \phi}{a} \right\rangle + \left\langle \overline{v' \frac{v\omega}{ag\rho}} \right\rangle}_{\text{CK}} \\ & + \underbrace{\left\langle \overline{u' \frac{u\omega}{ag\rho}} \right\rangle + \left\langle \frac{2\Omega}{g\rho} \overline{u'\omega'} \cos \phi \right\rangle}_{\text{CE}} - \underbrace{\left\langle \overline{\omega' \alpha'} \right\rangle + \left\langle \overline{u' F'_x} \right\rangle + \left\langle \overline{v' F'_y} \right\rangle}_{\text{GKE}} + \langle O_x(3) \rangle + \langle O_y(3) \rangle \end{aligned} \quad (\text{F.15})$$

where

$$KE = \frac{1}{2} \langle (\overline{u'^2} + \overline{v'^2}) \rangle. \quad (\text{F.16})$$

The  $O(3)$  terms represent the triple perturbation products. In both of the kinetic energy equations,

the terms in red would either disappear upon zonal averaging or they would be neglected (Lorenz, 1955).

In order to obtain the equation for mean APE, the thermodynamic equation

$$\frac{\partial \theta}{\partial t} + \mathbf{v} \cdot \nabla_h \theta + \omega \frac{\partial \theta}{\partial p} = c_p^{-1} \frac{\theta}{T} Q \quad (\text{F.17})$$

is multiplied by the horizontal perturbation of the time mean potential temperature ( $\bar{\theta}''$ ) (as in Lorenz, 1955). Taking the required average (zonal mean or 10-day Lanczos filter in our work) of the resulting equation yields:

$$\begin{aligned} \frac{1}{2} \frac{\partial \langle \bar{\theta}''^2 \rangle}{\partial t} + \left\langle \frac{\bar{\theta}'' \bar{u}}{a \cos \phi} \frac{\partial \bar{\theta}}{\partial \lambda} \right\rangle + \langle \bar{\theta}'' \bar{v} \frac{\partial \bar{\theta}}{\partial a \phi} \rangle + \langle \bar{\theta}'' \bar{\omega} \frac{\partial \bar{\theta}}{\partial p} \rangle + \left\langle \frac{\bar{\theta}''}{\cos \phi} \frac{\partial \bar{u}' \bar{\theta}'}{a \partial \lambda} \right\rangle + \langle \bar{\theta}'' \frac{\partial \bar{v}' \bar{\theta}'}{a \partial \phi} \rangle \\ + \langle \bar{\theta}'' \frac{\partial \bar{\omega}' \bar{\theta}'}{\partial p} \rangle = c_p^{-1} \frac{\theta}{T} \langle \bar{\theta}'' \bar{Q}'' \rangle, \end{aligned} \quad (\text{F.18})$$

where  $\langle \rangle$  is the horizontal average. This can be simplified using the following:

$$\begin{aligned} \langle \bar{\theta}'' \bar{u} \frac{\partial \bar{\theta}}{a \cos \phi \partial \lambda} \rangle + \langle \bar{\theta}'' \bar{v} \frac{\partial \bar{\theta}}{a \partial \phi} \rangle + \langle \bar{\theta}'' \bar{\omega} \frac{\partial \bar{\theta}}{\partial p} \rangle = \underbrace{\langle \bar{\theta}'' \bar{u}'' \rangle \frac{\partial \langle \bar{\theta} \rangle}{a \cos \phi \partial \lambda} + \langle \bar{\theta}'' \bar{v}'' \rangle \frac{\partial \langle \bar{\theta} \rangle}{a \partial \phi}}_{=0} \\ + \langle \bar{\theta}'' \bar{\omega}'' \rangle \frac{\partial \langle \bar{\theta} \rangle}{\partial p} + \underbrace{\frac{1}{2} \langle \bar{u} \rangle \frac{\partial \langle \bar{\theta}''^2 \rangle}{a \cos \phi \partial \lambda} + \frac{1}{2} \langle \bar{v} \rangle \frac{\partial \langle \bar{\theta}''^2 \rangle}{a \partial \phi} + \frac{1}{2} \langle \bar{\omega} \rangle \frac{\partial \langle \bar{\theta}''^2 \rangle}{\partial p}}_{=0} \end{aligned} \quad (\text{F.19})$$

Equation F.18, multiplied by  $c_p \gamma (T/\theta)^2$  and integrated vertically, can therefore be written as:

$$\begin{aligned} \frac{c_p}{2} \frac{\partial \langle \bar{T}''^2 \rangle}{\partial t} = \underbrace{c_p \int_0^{p_0} \gamma \left\langle \frac{\bar{u}' \bar{T}''}{a \cos \phi} \frac{\partial \bar{T}''}{\partial \lambda} \right\rangle dp + c_p \int_0^{p_0} \gamma \left\langle \frac{\bar{v}' \bar{T}''}{a \partial \phi} \frac{\partial \bar{T}''}{\partial \phi} \right\rangle dp + c_p \int_0^{p_0} \gamma \left\langle \frac{\bar{\omega}' \bar{T}''}{\theta} \frac{\partial \bar{T}''}{\partial p} \right\rangle dp}_{\text{CA}} \\ + \underbrace{\int_0^{p_0} \langle \bar{u}'' \bar{\omega}'' \rangle dp}_{\text{CM}} + \underbrace{\int_0^{p_0} \gamma \langle \bar{Q}'' \bar{T}'' \rangle dp}_{\text{GAM}} \end{aligned} \quad (\text{F.20})$$

so that

$$\frac{\partial AM}{\partial t} = -CZ - CA + GAM, \quad (\text{F.21})$$

where

$$AM = \frac{c_p}{2} \int_0^{p_0} \gamma \langle \overline{T'^2} \rangle dp \quad (\text{F.22})$$

and

$$c_p \int_0^{p_0} \gamma \frac{T^2}{\theta^2} \langle \overline{\theta'' \omega''} \rangle \frac{\partial \langle \overline{\theta} \rangle}{\partial p} dp = - \int_0^{p_0} \langle \overline{\alpha'' \omega''} \rangle dp, \quad (\text{F.23})$$

where  $\alpha$  is the specific volume. The value of  $\gamma$  has been taken from Oort (1964):

$$\gamma = - \left( \frac{T}{\theta} \right)^2 \frac{R}{c_p p_0} \int_0^{p_0} \frac{T}{\theta} \frac{1}{p} \left( \frac{\partial \langle \overline{\theta} \rangle}{\partial p} \right)^{-1} dp \quad (\text{F.24})$$

because the original factor introduces additional (though likely unimportant terms).

Similarly, the eddy APE can be obtained by multiplying F.17 by the deviation of the potential temperature from the mean of interest (zonal mean or Lanczos filter in this study) and then averaging the resultant equation using that mean:

$$\frac{1}{2} \frac{\partial \overline{\theta'^2}}{\partial t} + \overline{\theta' \mathbf{v} \cdot \nabla \theta'} + \overline{\theta' \mathbf{v}' \cdot \nabla \bar{\theta}} + \overline{\theta' \omega \frac{\partial \theta'}{\partial p}} + \overline{\theta' \omega' \frac{\partial \bar{\theta}}{\partial p}} = c_p^{-1} \frac{\theta}{T} \overline{\theta' Q'} \quad (\text{F.25})$$

It is noted that upon global integration that:

$$\langle \overline{\theta' \mathbf{v} \cdot \nabla \theta'} + \overline{\theta' \omega \frac{\partial \theta'}{\partial p}} \rangle = \langle \frac{1}{2} \left( \overline{\mathbf{v} \cdot \nabla \theta'^2} + \overline{\omega \frac{\partial \theta'^2}{\partial p}} \right) \rangle = 0 \quad (\text{F.26})$$

using the continuity equation and that the globally integrated flux is zero. Horizontal averaging, multiplication by  $c_p \gamma (T/\theta)^2$  and vertical integration of F.25 then yield:

$$\begin{aligned} \frac{AE}{\partial t} = & - c_p \underbrace{\int_0^{p_0} \gamma \left\langle \frac{\overline{u' T''}}{a \cos \phi} \frac{\partial \overline{T''}}{\partial \lambda} \right\rangle dp - c_p \int_0^{p_0} \gamma \langle \overline{v' T''} \rangle \frac{\partial \overline{T''}}{\partial y} dp - c_p \int_0^{p_0} \gamma \langle \overline{\omega' T''} \rangle \frac{T}{\theta} \frac{\partial \overline{\theta''}}{\partial p} dp}_{CA} \\ & + \underbrace{\int_0^{p_0} \langle \overline{\alpha' \omega'} \rangle dp}_{CE} + \underbrace{\int_0^{p_0} \gamma \langle \overline{Q' T'} \rangle dp}_{GAE}, \end{aligned} \quad (\text{F.27})$$

where

$$AE = \frac{c_p}{2} \int_0^{p_0} \gamma \langle \overline{T'^2} \rangle dp \quad (\text{F.28})$$

and

$$c_p \int_0^{p_0} \gamma \frac{T^2}{\theta^2} \langle \theta' \omega' \rangle \frac{\partial \langle [\theta] \rangle}{\partial p} dp = - \int_0^{p_0} \langle \alpha' \omega' \rangle dp. \quad (\text{F.29})$$

The Lorenz equations are therefore:

$$\frac{\partial AM}{\partial t} = -CM - CA + GAM, \quad (\text{F.30})$$

$$\frac{\partial AE}{\partial t} = -CE + CA + GAE, \quad (\text{F.31})$$

$$\frac{\partial KE}{\partial t} = +CE - CK + GKE, \quad (\text{F.32})$$

$$\frac{\partial KM}{\partial t} = CM + CK + GKM. \quad (\text{F.33})$$

## Appendix G

# Methods for Calculating Reference Potential Temperature for the Local Framework

Three methods were considered for adiabatic rearrangement of the atmosphere to produce the reference potential temperature, which is only a function of pressure and time and is increasing with pressure.

The first method uses parcel sorting. For each time the global potential temperature is divided into parcels. For example, the ERA-40 dataset has a resolution of 320 longitude values, 160 latitude values and 23 pressure levels, giving 1,177,600 parcels. These parcels were then sorted using the Quicksort sorting algorithm for higher numerical efficiency, and in this order each parcel mass was then draped across the Earth's surface which yielded the height of each parcel and thus the sorted potential temperature profile increasing with height. Using linear interpolation, the reference potential temperature was then extracted.

The second method considers the probability distribution function (PDF) of the potential temperature for each time. The PDF was divided into sensibly large bins. The masses of the parcels were summed for each bin. The bins were then draped over the Earth's surface, giving bin thickness and thus the pressure levels of the ascending potential temperature values. The reference potential temperature profile for the pressure levels of the dataset was then obtained using linear interpolation.

The last method is using the latitudinally weighted isobaric averaging as was used by Lorenz (1955) and others, to account for the sphericity of the Earth. This method is the fastest of the

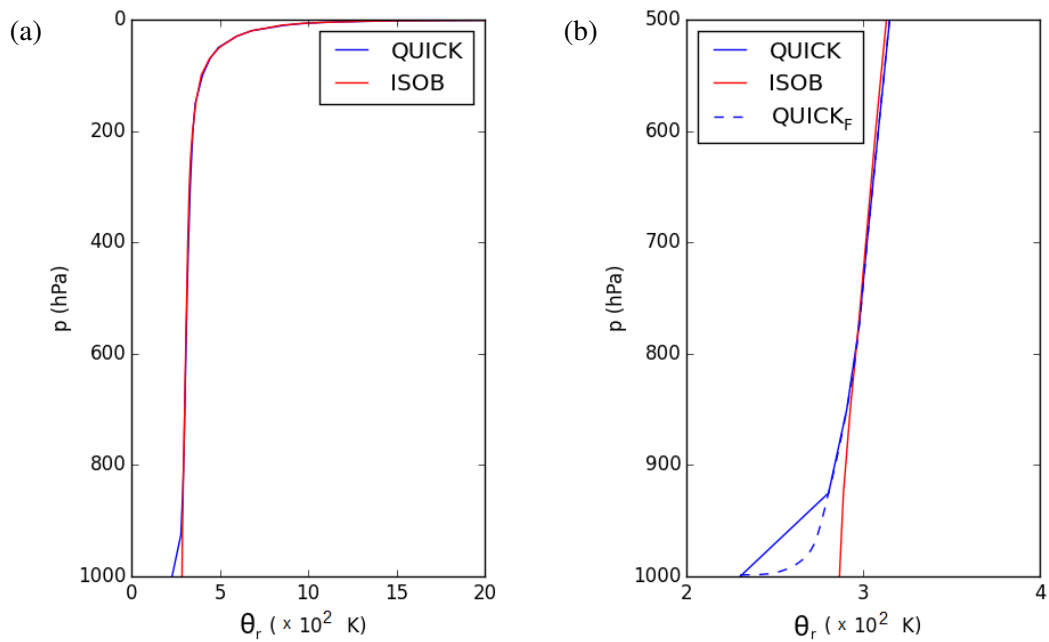


**Figure G.1:** Reference potential temperature profiles for the Quicksort (blue) and isobaric averaging (red) method averaged for 1-10 January 2000. Panel a) shows the full profile, and panel b) zooms in on low levels. The blue dashed line shown the profile based on the Quicksort method with higher vertical resolution.

three (with the PDF method being the slowest), though all methods can calculate one season of the energy and conversion terms in less than 10 minutes.

The PDF method is based on a similar principle as the Quicksort method, is less accurate and slower, and so only the Quicksort and isobaric averaging methods are compared here for ERA-40. The reference temperature profiles averaged for the first 10 days of January 2000 for both methods is shown in figure G.1a. It is apparent that both methods yield very similar profiles with a relatively small increase in the potential temperature throughout the troposphere and a sharp increase in the upper stratosphere and higher. There appears to be a small departure between the two methods near the surface (see the zoomed in plot in G.1b). The Quicksort method additionally decreases rapidly near the surface which is apparent more clearly if the profile is plotted against the finer resolution pressure levels (dashed) obtained from the parcel rearrangement. This rapid decrease is absent for the isobaric averaging method. The Quicksort method incorporates all values of the potential temperature for that time including the extremes, whereas the isobaric averaging method smooths out those extremes. Because the vertical resolution of the data is relatively coarse, the resultant profile of the Quicksort method exhibits a sharp step in the profile. Although the near-surface increase temperature change may be physical, the sharp step due to the coarse vertical resolution introduces significant errors.

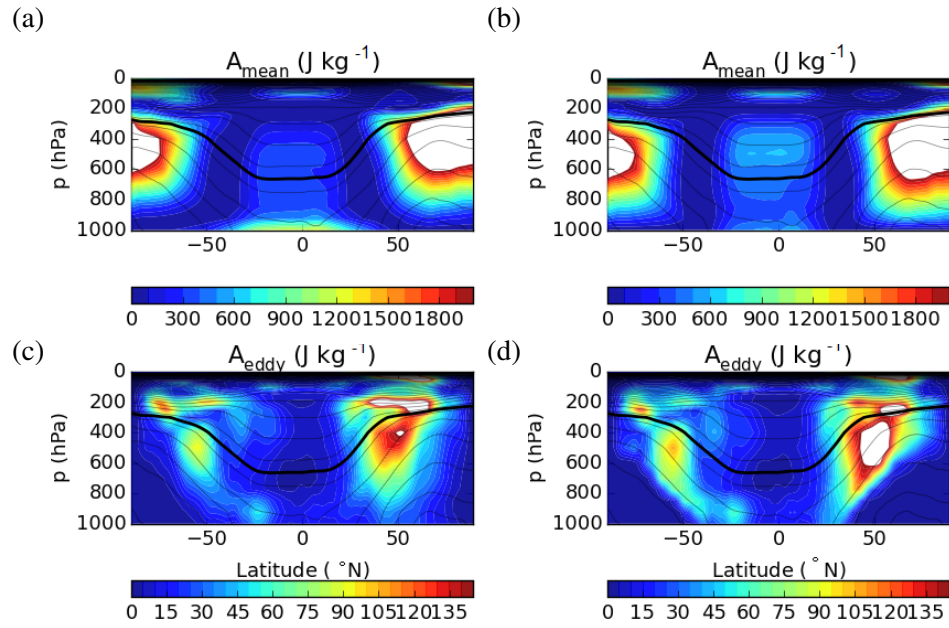


**Figure G.2:** Pressure-latitude plot of mean APE (a,b) and eddy APE (c, d) based on reference potential temperature calculated using the Quicksort (a,c) and isobaric (b,d) averaging methods for 1-10 January 2000. Eddies represent stationary eddies. Black contours represent zonal mean temperature for the same period.

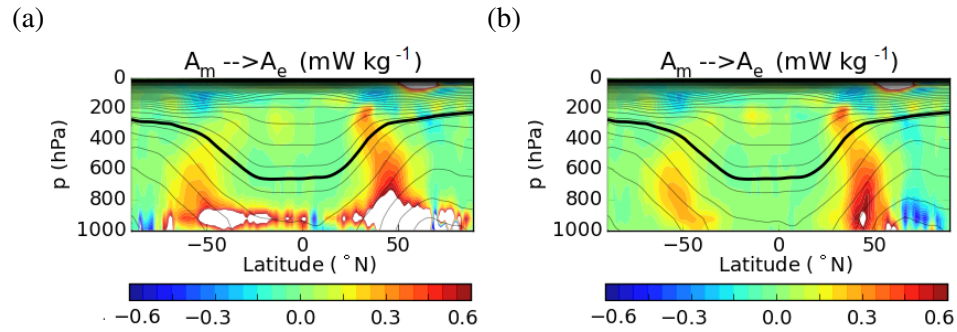


**Figure G.3:** Pressure-latitude plot of the CA conversion based on reference potential temperature calculated using a) the Quicksort method and b) the isobaric averaging method, for 1-10 January 2000. Eddies represent stationary eddies. Black contours represent zonal mean temperature for the same period.

For comparison of the local APE distributions of the two reference potential temperature profiles, figure G.2 a and b shows the mean and eddy APE values for the two methods, averaged for the first 10 days of year 2000 and for the stationary framework. The kinetic energies are not shown as they are not affected by the choice of the reference temperature profile. Overall the methods yield values comparable in both magnitude and spatial distribution. Their differences include low-level mean APE in the tropics for the Quicksort method, whereas higher tropical values dominate in the upper levels for the isobaric averaging method. In the mid-latitudes the eddy APE is slightly stronger in the troposphere for the isobaric averaging method whereas its maximum is near the

tropopause for the Quicksort method.

The equivalent zonal mean distributions for the CA conversion terms are displayed in figure G.3. This conversion is the only one affected by the choice of reference states and so the others were not included. The upper levels are in good agreement but the Quicksort method produces somewhat higher values closer to the surface. This is related to the rapid decrease in the reference potential temperature profile near the surface mentioned above. Although one could argue that the Quicksort method is more accurate, given the data resolution, we are only interested in the larger scale patterns in the energy and conversion terms. The smoother reference potential temperature profile is therefore adequate and it allows a more direct comparison with the existing literature which is usually based on the isobaric averaging method.

## Appendix H

# Local Energetics Evolution Equations in Spherical Coordinates

Working in spherical coordinates, the evolution equations for local kinetic energy components are identical to that of Lorenz before the global averaging (as shown in Appendix F). The complete local mean KE density ( $E_k^m$ ) and eddy KE density ( $E_k^e$ ) evolution equations are thus:

$$\begin{aligned}
 \frac{\partial E_k^m}{\partial t} = & -\cos^{-1} \phi \nabla \cdot (\bar{u} \overline{u' \mathbf{u}'}) \cos \phi - \cos^{-1} \phi \nabla \cdot (\bar{v} \overline{v' \mathbf{u}'}) \cos \phi + \bar{\mathbf{u}} \cdot \nabla E_k^m \\
 & - \cos^{-1} \phi \nabla \cdot (\bar{\mathbf{u}} \bar{u}^2 \cos \phi) - \cos^{-1} \phi \nabla \cdot (\bar{\mathbf{u}} \bar{v}^2 \cos \phi) + \cos \phi \overline{u' \mathbf{u}'} \cdot \nabla (\bar{u} \cos^{-1} \phi) \\
 & + \cos \phi \overline{v' \mathbf{u}'} \cdot \nabla (\bar{v} \cos^{-1} \phi) + \frac{\bar{u} \bar{u} \bar{\omega}}{a g \rho} + \frac{\bar{v} \bar{v} \bar{\omega}}{a g \rho} - (\bar{u}'^2 + \bar{v}'^2) \bar{v} \frac{\tan \phi}{a} - \bar{\omega} \bar{\alpha} \\
 & - \cos^{-1} \phi \nabla \cdot (\bar{\mathbf{u}} \bar{\delta} \Phi \cos \phi) + \bar{v} \bar{F}_y + \bar{u} \bar{F}_x + \frac{2\Omega}{g \rho} \bar{u} \bar{\omega} \cos \phi,
 \end{aligned} \tag{H.1}$$

$$\begin{aligned}
 \frac{\partial E_k^e}{\partial t} = & -\bar{\mathbf{u}} \cdot \nabla E_k^e - \bar{\mathbf{u}'} \cdot \nabla \bar{E}_k^e - \cos \phi \overline{u' \mathbf{u}'} \cdot \nabla (\bar{u} \cos^{-1} \phi) \\
 & - \cos \phi \overline{v' \mathbf{u}'} \cdot \nabla (\bar{v} \cos^{-1} \phi) + (\bar{u}'^2 + \bar{v}'^2) \bar{v} \frac{\tan \phi}{a} + \frac{\bar{u}' \bar{u} \bar{\omega}}{a g \rho} + \frac{\bar{v}' \bar{v} \bar{\omega}}{a g \rho} - \bar{\omega}' \bar{\alpha}' \\
 & - \cos^{-1} \phi \nabla \cdot (\bar{\mathbf{u}'} \bar{\delta} \Phi' \cos \phi) + \bar{v} \bar{F}_y + \bar{u} \bar{F}_x + \frac{2\Omega}{g \rho} \bar{u} \bar{\omega} \cos \phi,
 \end{aligned} \tag{H.2}$$

where

$$E_k^m = \frac{1}{2} (\bar{u}^2 + \bar{v}^2), \tag{H.3}$$

and

$$E_k^e = \frac{1}{2} (\bar{u}'^2 + \bar{v}'^2), \tag{H.4}$$

where  $\mathbf{u}$  is the three-dimensional velocity vector and

$$\frac{D_M}{Dt} = \frac{\partial}{\partial t} + \mathbf{u} \cdot \nabla = \frac{\partial}{\partial t} + \bar{u} \frac{1}{a \cos \phi} \frac{\partial}{\partial \lambda} + \bar{v} \frac{\partial}{a \partial \phi} + \bar{\omega} \frac{\partial}{\partial p} \quad (\text{H.5})$$

is the mean material derivative. The bars denote averages of choice and the primes are perturbations from them.  $\phi$  is latitude,  $\lambda$  is longitude and  $a$  is the Earth's radius.

Using the same methods as to those in the main text to manipulate the thermodynamic equation:

$$\frac{D_M \bar{\theta}}{Dt} = -\cos^{-1} \phi \nabla \cdot \overline{\mathbf{v}' \theta'} \cos \phi - \frac{\partial \overline{\omega' \theta'}}{\partial p} + \frac{\bar{\theta}}{\bar{T}} \frac{\bar{Q}}{c_p}, \quad (\text{H.6})$$

the local mean APE density ( $E_a^m$ ) and eddy APE density ( $E_a^e$ ) evolution equations in spherical coordinates are:

$$\frac{\partial E_a^m}{\partial t} + \bar{\mathbf{u}} \cdot \nabla E_a^m = \bar{\delta \alpha \bar{\omega}} - c_p \frac{\bar{T}}{\bar{\theta}} \bar{Y} \cos^{-1} \phi (\nabla \cdot \overline{\mathbf{u}' \theta' \cos \phi}) - \bar{X} + \bar{Y} \bar{Q}, \quad (\text{H.7})$$

$$\frac{\partial E_a^e}{\partial t} + \bar{\mathbf{u}} \cdot \nabla E_a^e + \overline{\mathbf{u}' \cdot \nabla E_a^{e'}} = \overline{\omega' \delta \alpha'} + c_p \frac{\bar{T}}{\bar{\theta}} \bar{Y} \cos^{-1} \phi \nabla \cdot \overline{\mathbf{u}' \theta' \cos \phi} - X' + \bar{Y}' Q'. \quad (\text{H.8})$$

## Appendix I

# Deriving the Energetics Nonlinear Oscillator Model Using the “Constant Vertical Tilt” Method

The nonlinear oscillator model is based on the interaction between eddy activity and mean shear of the flow, and so the first attempt to obtain the nonlinear oscillator relationship in the mean and eddy APE equations was to use similar techniques to Lorenz’s (1955) study (see Appendix F for the step by step method for the derivation of the Lorenz equations). We start with a channel model with impermeable meridional boundaries of  $y = -L_y, L_y$ , vertical impermeable boundaries of  $p = p_0, 0$ , and periodic boundaries in the zonal direction. Firstly, the continuity and thermodynamic equations in pressure coordinates are as follows:

$$\nabla_h \cdot \mathbf{v} + \frac{\partial \omega}{\partial p} = 0, \quad (\text{I.1})$$

$$\frac{\partial \theta}{\partial t} + \mathbf{v} \cdot \nabla_h \theta + \omega \frac{\partial \theta}{\partial p} = c_p^{-1} \frac{\theta}{T} Q, \quad (\text{I.2})$$

where  $\nabla_h$  marks the horizontal gradient on pressure surfaces.

The first (mean APE) evolution equation of the nonlinear oscillator is obtained as follows. Firstly, it is assumed that the zonal mean potential temperature can be partitioned into a pressure-dependent reference profile and the corresponding perturbation field which is a function of time and latitude:

$$[\theta](y, p, t) = [\theta]_R(p) + \Delta[\theta](y, t), \quad (\text{I.3})$$

where the second term can be expanded to the first order around  $y = 0$  as:

$$\Delta[\theta](y, t) = \Delta[\theta](0, t) + y \frac{\partial \Delta[\theta]}{\partial y}(0, t), \quad (\text{I.4})$$

The meridional average of  $[\theta](y, p, t)$  and the perturbation from it can be written as:

$$\langle [\theta] \rangle(p, t) = [\theta]_R(p) + \Delta[\theta](t), \quad [\theta]''(y, t) = \Lambda(t)y, \quad (\text{I.5})$$

where  $\Lambda(t) = (\partial \Delta[\theta] / \partial y)(0, t)$ . This approximation (first used by Schneider, 1981) requires that the zonal mean meridional temperature gradient is negligibly variable in  $y$ . Although seemingly crude at first sight, O’Gorman and Schneider (2008) showed that using this approximation to represent mean APE-like quantities in the climate of the Earth’s current atmosphere gives a realistic estimate. Returning to equation I.2, multiplying its zonal mean by  $[\theta]''$  and subsequently averaging meridionally yields:

$$\langle [\theta]'' \frac{\partial [\theta]''}{\partial t} \rangle = \langle [v\theta] \frac{\partial [\theta]''}{\partial y} \rangle - \langle \frac{\partial [\omega\theta][\theta]''}{\partial p} \rangle + \langle c_p^{-1} [\theta]'' [Q] \frac{\theta}{T} \rangle, \quad (\text{I.6})$$

where the continuity equation was used. Using equations I.5, equation I.6 can be written as:

$$\langle y^2 \rangle \Lambda \frac{\partial \Lambda}{\partial t} = \langle [v\theta] \rangle \Lambda - \langle \frac{\partial [\omega\theta][\theta]''}{\partial p} \rangle + \langle c_p^{-1} y [Q] \frac{\theta}{T} \rangle \Lambda, \quad (\text{I.7})$$

where the boundary conditions lead to  $\langle y^2 \rangle = L_y^2/3$ . This evolution equation for the zonal mean meridional temperature can be linked to the mean Lorenz APE (equation 5.4):

$$A_m^{(\text{LR})} = \frac{c_p}{2} g^{-1} \int_0^{p_0} \gamma \langle [T]''^2 \rangle dp = \frac{L_y^2 c_p}{3} g^{-1} \int_0^{p_0} \gamma \frac{T^2}{\theta^2} dp \Lambda^2 = a_1 (-\Lambda)^2, \quad (\text{I.8})$$

where the constants and the pressure integral (including the static stability) are absorbed in constant  $a_1$ . Combining equations I.8 and I.7 and vertically averaging yields:

$$\frac{L_y^2}{3} a_1^{-1/2} \frac{\partial \sqrt{A_m^{(\text{LR})}}}{\partial t} = -\{ \langle [v][\theta] \rangle \} - \{ \langle [v^* \theta^*] \rangle \} - c_p^{-1} \{ \langle y [Q] \frac{\theta}{T} \rangle \}, \quad (\text{I.9})$$

using curly brackets to denote vertical averaging and the fact that there is no flux divergence across the vertical boundaries.

The second (eddy APE) evolution equation of the nonlinear oscillator can be obtained by mul-

tipling the thermodynamic equation by the perturbation of potential temperature from its zonal mean and then averaging zonally. Further averaging meridionally yields:

$$\frac{1}{2} \frac{\partial \langle [\theta^{*2}] \rangle}{\partial t} + \frac{1}{2} \langle [\mathbf{v} \cdot \nabla_h \theta^{*2}] \rangle + \langle [\theta^* v^*] \rangle \frac{\partial [\theta]}{\partial y} + \frac{1}{2} \langle [\omega \frac{\partial \theta^{*2}}{\partial p}] \rangle + \langle [\theta^* \omega^*] \rangle \frac{\partial [\theta]}{\partial p} = c_p^{-1} \frac{\theta}{T} \langle [Q^* \theta^*] \rangle. \quad (\text{I.10})$$

This can be simplified using the continuity equation to:

$$\frac{1}{2} \frac{\partial \langle [\theta^{*2}] \rangle}{\partial t} = - \langle [\theta^* v^*] \rangle \frac{\partial [\theta]}{\partial y} - \langle [\theta^* \omega^*] \rangle \frac{\partial [\theta]}{\partial p} + c_p^{-1} \frac{\theta}{T} \langle [Q^* \theta^*] \rangle. \quad (\text{I.11})$$

The Lorenz eddy APE (equation 5.5) can be written as

$$A_e^{(\text{LR})} = \frac{c_p}{2} g^{-1} \int_0^{p_0} \gamma \frac{T^2}{\theta^2} \langle [\theta^{*2}] \rangle dp. \quad (\text{I.12})$$

Although Lorenz’s (1955) definition of  $\gamma$  is dependent on pressure, Oort (1964) suggests an alteration to this definition:

$$\gamma^{(\text{Oort})} = - \left( \frac{\theta}{T} \right)^2 \frac{R}{c_p P_0} \int_0^{p_0} \frac{T}{\theta} \frac{1}{p} \left( \frac{\partial \langle [\bar{\theta}] \rangle}{\partial p} \right)^{-1} dp, \quad (\text{I.13})$$

where the bar marks the long time average. Using this definition for  $\gamma$  allows rewriting equation I.12 as:

$$A_e^{(\text{LR})} = \frac{c_p}{2} g^{-1} \int_0^{p_0} \gamma^{(\text{Oort})} \frac{T^2}{\theta^2} \langle [\theta^{*2}] \rangle dp = a_2 \{ \langle [\theta^{*2}] \rangle \}, \quad (\text{I.14})$$

where all constants were combined into  $a_2$  and the curly brackets again denote the vertical average. After vertical averaging and using equation I.8, equation I.11 becomes:

$$\frac{1}{2} a_2^{-1} \frac{\partial A_e^{(\text{LR})}}{\partial t} = a^{-1/2} \{ \langle [\theta^* v^*] \rangle \} \sqrt{A_m^{(\text{LR})}} - \{ \langle [\theta^* \omega^*] \rangle \} \frac{\partial [\theta]}{\partial p} + c_p^{-1} \left\{ \frac{\theta}{T} \langle [Q^* \theta^*] \rangle \right\}. \quad (\text{I.15})$$

The final manipulation involves linking the heat flux to the eddy energy. Both of these quantities are evidently measures of eddy activity. An example of linking these is to define the perturbation potential temperature as a geostrophically and hydrostatically balanced sinusoidal disturbance, as described by James (1994, p. 125):

$$\theta^* \approx \left( \frac{p_0}{p} \right)^k v^* \underbrace{\frac{f_0 p_0}{k \Delta p R} \sin \delta}_{\text{ass. const.}} = a_3 \left( \frac{1}{p} \right)^k v^*, \quad (\text{I.16})$$

where  $\delta$  is the vertical tilt of the propagating disturbance and it is assumed that it changes negligibly in the horizontally averaged domain over the timescales considered. The other so far undefined constants of equation I.16 are the Coriolis parameter,  $f_0$ , the zonal wavenumber,  $k$ , and the specific gas constant,  $R$ . In the last equality the constants were absorbed into  $a_3$ . This allows the globally averaged heat flux to be written as:

$$\{\langle[\theta^*v^*]\rangle\} = a_3^{-1} \frac{1}{\Delta p} \int_0^{p_0} p^\kappa \langle[\theta^{*2}]\rangle dp. \quad (\text{I.17})$$

If the perturbation potential temperature is assumed to be proportional to the product of its height-dependent and time-dependent parts ( $\theta^* = \theta_i^* \theta_p^*$ ), as is often the case in normal mode analysis (e.g. Eady, 1949), the heat flux can be written in terms of the eddy APE:

$$\{\langle[\theta^*v^*]\rangle\} = a_3^{-1} a_2^{-1} a_4 A_e^{(\text{LR})}, \quad (\text{I.18})$$

where  $a_4 = \{p^\kappa \langle[\theta_p^{*2}]\rangle\} / \{\langle[\theta_i^{*2}]\rangle\}$ . Substituting for the heat flux in equations I.9 and I.15, the final set of equations is:

$$\frac{L_y^2}{3} a_1^{-1/2} \frac{\partial \sqrt{A_m^{(\text{LR})}}}{\partial t} = -\{\langle[v][\theta]\rangle\} - a_3^{-1} a_2^{-1} a_4 A_e^{(\text{LR})} - c_p^{-1} \{y[Q] \frac{\theta}{T}\}, \quad (\text{I.19})$$

$$\frac{1}{2} a_2^{-1} \frac{\partial A_e^{(\text{LR})}}{\partial t} = a_1^{-1/2} a_3^{-1} a_2^{-1} a_4 A_e^{(\text{LR})} \sqrt{A_m^{(\text{LR})}} - \{\langle[\theta^* \omega^*] \frac{\partial[\theta]}{\partial p}\rangle\} + c_p^{-1} \{ \frac{\theta}{T} \langle[Q^* \theta^*]\rangle \}. \quad (\text{I.20})$$

This equation set is equivalent to the nonlinear oscillator model in chapter 3 with some additional terms. Firstly, there is a mean meridional flux of temperature which would disappear if there was no mean meridional circulation. Secondly, the vertical eddy heat flux term is related to the conversion from eddy APE to the eddy kinetic energy (the vast majority of which then goes into eddy dissipation Oort, 1964). Finally there is an eddy APE diabatic generation term (which is again relatively small according to Oort’s (1964) calculations). The diabatic generation of the mean APE is the last term on the LHS of equation I.19 and it is equivalent to the diabatic forcing in the nonlinear oscillator model. It is noted that this term will only increase mean APE if heating occurs in the southern part of the domain (where  $y < 0$ ) or if cooling occurs in the northern part (where  $y > 0$ ). If heating is constant throughout the domain then no contribution to the meridional temperature gradient occurs, as expected.

Equations I.19 and I.20 therefore appear to include the nonlinear oscillator model, and using

equations I.8 and I.18 the mean and eddy APE can be converted into baroclinicity and heat flux.

## Appendix J

# Application of the Nonlinear Oscillator Model in the Oceans

The results of this thesis inspired collaboration with David Marshall and David Munday, focussing on applying the nonlinear oscillator model to the oceanic setting, namely the Antarctic Circumpolar Current and the associated eddy activity in a steady state. The ACC is an ocean current that encircles Antarctica and its variability can have severe implications on the current and future climate. For instance its strength contributes to the amount of upwelling of CO<sub>2</sub> from the deeper oceans (Ito and Follows, 2003) and its location can influence basal melting of Antarctica's ice shelves (Jacobs *et al.*, 2011). The importance of understanding its variability is therefore paramount.

The dynamics of the ACC setting may be expected to be somewhat similar to the baroclinic atmosphere discussed in the chapters above. However, some additional processes need to be taken into account, such as the presence of lateral boundaries and the inter-hemispheric mass transport. As Gnanadesikan (1999) outlines, five major processes contribute to the structure of the pycnocline (and thus the mean ACC transport): deep water formation at high latitudes (especially in the Northern Hemisphere), low-latitude upwelling, global vertical diapycnal diffusion, Southern Ocean wind shear and eddy activity. The first four components drive a meridional overturning circulation (MOC) whereby dense water from the North Atlantic (NADW) sinks and is transported southwards. Some of this water upwells in the Southern Ocean due to the wind stress forcing via Ekman pumping, with the remaining part of the NADW being advected upwards and equatorwards, which is balanced by a downwards diffusive heat flux due to turbulent mixing. The Southern Ocean wind forcing and eddy activity are processes that are local to the Southern Ocean.

In the Southern Ocean, the Ekman pumping-induced meridional circulation is such that it in-

creases the slopes of the isopycnals (lines of constant density) and therefore increases the available potential energy of the ACC. As in the mid-latitude atmosphere, this mean circulation is opposed by baroclinic eddies whose down-gradient buoyancy flux tends to flatten the isopycnals. This compensating effect between the mean circulation and the eddies has given rise to studies focussing on the residual circulation (e.g. Marshall and Radko, 2003).

Eddies are often not fully resolved in ocean models and their fluxes must therefore be parametrised, for instance using a first-order closure (e.g. Gent and McWilliams, 1990). Buoyancy fluxes can therefore be approximated as:

$$\overline{v'b'} = K \frac{\partial \bar{b}}{\partial y}. \quad (\text{J.1})$$

For a constant  $K$ , such models can predict a strong coupling between the wind stress forcing, the ACC transport and the MOC (Fyfe and Saenko, 2006), with wind stress increasing the ACC transport. For nonlinear models with a variable  $K$  this correlation is less clear, with the eddy compensation decreasing the sensitivity of the meridional circulation to the wind stress forcing (Kuhlbrodt *et al.*, 2012). However with an increasing computing power, the use of eddy resolving models is now more feasible and it produces interesting results. For a sufficiently high model resolution, the eddy intensity becomes highly sensitive to the wind stress forcing. In contrast, the steady-state ACC transport becomes almost insensitive to the wind stress changes (e.g. Munday *et al.*, 2013), as shown in figure J.1. This phenomenon has been called eddy saturation, and it implies a balance between the isopycnal sharpening by Ekman transport and isopycnal flattening by eddies.

While the effect of eddy compensation can be understood in terms of Ekman pumping and thermal wind balance restoration, the mechanism governing the eddy saturation phenomenon is less well understood. This section shows how the nonlinear oscillator model, developed for the storm tracks as shown above, can be used in its time-mean form to simulate this eddy saturation phenomenon.

The steady state nonlinear oscillator model is:

$$f = F, \quad s = D, \quad (\text{J.2})$$

where in the analogous ACC setting  $f$  is the eddy activity (or form stress),  $F$  is the wind stress

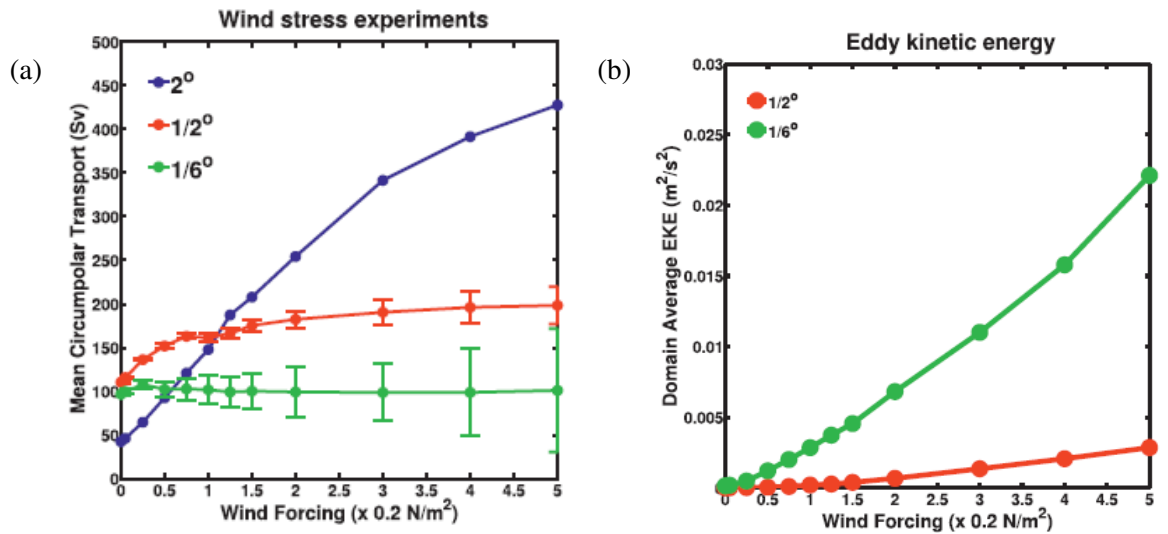


**Figure J.1:** Eddy saturation represented by reduced sensitivity of the ACC transport (a) and increased sensitivity of eddy intensity (b) with increased wind forcing for higher resolutions (colours) of the model. From Munday *et al.* (2013).

forcing,  $s$  is the baroclinicity set by the slope of the isopycnals and  $D$  is the eddy dissipation rate (corresponding to friction). It is noted that in this system the friction of the mean flow is assumed to be negligible compared to the eddy friction, as supported by observations of the global energetics (Oort, 1964). This model therefore implies that the steady-state eddy forcing is only dependent on the wind stress, whereas the baroclinicity is associated with the eddy friction. Equivalently, as shown in Chapter 5, the system can be written in terms of the energetics directly in the context of a globally integrated ACC (equations 5.55 and 5.56). The corresponding steady state of these equations is:

$$H_m = T_E, \quad T_M = \frac{4c_1 r^2}{c_2^2 c_3^2}, \quad (\text{J.3})$$

so that the wind stress forcing  $H_m$  is proportional to the total eddy energy,  $T_E$ , and the square root of the total mean energy (which is proportional to the ACC transport, assuming a constant Burger number so that the mean energies are proportional to each other),  $\sqrt{T_M}$ , is proportional to the eddy dissipation by bottom friction. It should be noted that a small constant correction needs to be applied in the case of a vanishing instability, so as to avoid having a zero background eddy activity (which is not realistic). Outside of the limit of weak wind stress, this model therefore predicts that the eddy saturation should occur and that it is the bottom friction that sets the steady state ACC transport.

The latter statement was confirmed by David Munday's preliminary runs of the ocean-only confi-

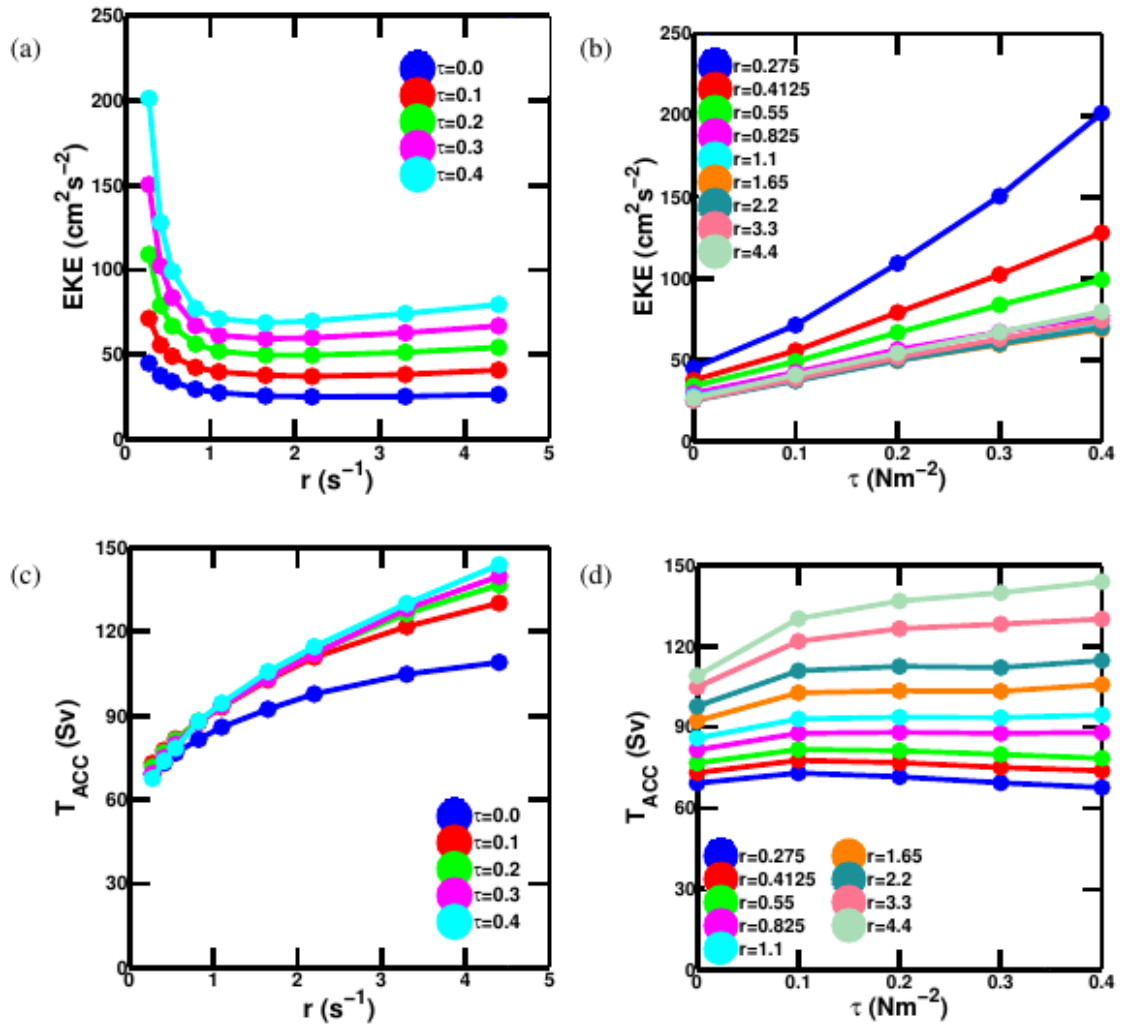


**Figure J.2:** Response of the eddy kinetic energy (a,b) and ACC transport (c,d) to changes in the bottom friction timescale ( $r$ ) and to changes in the wind forcing ( $\tau$ ). From D. Munday (personal communication).

uration of the Massachusetts Institute of Technology general circulation model (MITgcm) model that is eddy-resolving. The model geometry is highly idealised with the channel structure containing a ridge that provides orographic drag, an enhanced diffusivity at the northern boundary (parameterising the processes outside of the domain, such as high latitude deep water formation and diapycnal diffusion) and a superposed wind stress that is highest in the middle of the channel (see Munday *et al.*, 2015 for more details of the model setup).

A selection of David Munday's results are displayed in figure J.2. In general, the eddy kinetic energy increases markedly with increasing wind forcing, but is fairly insensitive to changes in the bottom friction. On the other hand, the ACC transport is very responsive to changes in the bottom friction but not to changes in the wind forcing. Evidently, this behaviour does not apply

in the limit of a vanishing friction or vanishing wind forcing. Nevertheless, moderate values of these parameters yield results that are consistent with the eddy saturation phenomenon and the behaviour of the steady state of the nonlinear oscillator model.

The finding that the steady-state ACC is proportional to the bottom friction seems counter-intuitive, and conflicts with Berloff *et al.*'s (2011) results who found that the latency (or weakness compared to the strength of the eddies) of a jet in their model is proportional to the bottom friction. However, the sharpened jets were observed to be associated with stronger flow in the opposite direction between the jets, suggesting that their results are associated with different strengths of momentum rearrangement (by eddies), rather than a domain-integrated increase in momentum (which is used to diagnose the ACC strength here).

Johnson and Bryden (1989) argue that the interfacial drag scales with the meridional heat flux (i.e. vertical EP flux). Consequently, eddies transport zonal momentum from the top layers to the bottom, deepening the ACC until the bottom drag is reached where the wind stress can be balanced.

This mechanism helps explain the likely links involved in the eddy saturation phenomenon. When wind forcing is increased, the isopycnal slopes will follow suit. However, this will also enhance the generation of baroclinic eddies, which will readily flatten the isopycnal slopes back to their original shape. The only way to stop eddies from flattening the slopes is to increase the eddy dissipation (in this case by bottom drag). Alternatively, increasing the bottom drag with the forcing staying constant would instantaneously increase eddy dissipation, making the eddies less efficient at flattening the isopycnals. The isopycnal slopes would in turn become sharper and allow the eddies to regain their original strength. The system therefore always equilibrates to a balance between eddy dissipation (bottom friction) and eddy generation (baroclinicity).

It should be noted that these are still very preliminary results, and work that includes more processes involved in the real ocean, such as the MOC, is still to be conducted. In addition, it would be interesting to apply such ideas to the atmospheric setting, where jets are less latent and bottom friction is smaller (Berloff *et al.*, 2011).

# References

- Ambaum, M. H. P. (1997). Isentropic formation of the tropopause. *J. Atmos. Sci.*, **54**, 555–568.
- Ambaum, M. H. P. and Hoskins, B. J. (2002). The NAO troposphere-stratosphere connection. *J. Climate*, **15**, 1969–1978.
- Ambaum, M. H. P. and Novak, L. (2014). A nonlinear oscillator describing storm track variability. *Quart. J. Roy. Meteor. Soc.*, **140**, 2680–2684.
- Ambaum, M. H. P., Hoskins, B. J., and Stephenson, D. B. (2001). Arctic Oscillation or North Atlantic Oscillation? *J. Climate*, **14**, 3495–3507.
- Andrews, D. and McIntyre, M. E. (1976). Planetary waves in horizontal and vertical shear: The generalised Eliassen-Palm relation and the mean zonal acceleration. *J. Atmos. Sci.*, **33**, 2031–2048.
- Andrews, D. G. (1981). A note on potential energy density in a stratified compressible fluid. *J. Fluid Mech.*, **107**, 227–236.
- Athanasiadis, P. and Ambaum, M. H. P. (2009). Linear contributions of different time scales to teleconnectivity. *J. Climate*, **22**, 3720–3728.
- Athanasiadis, P. J. and Ambaum, M. H. P. (2010). Do high-frequency eddies contribute to low-frequency teleconnection tendencies? *J. Atmos. Sci.*, **67**, 419–433.
- Balasubramanian, G. and Garner, S. (1997). The role of momentum fluxes in shaping the life cycle of a baroclinic wave. *J. Atmos. Sci.*, **54**, 510–533.
- Bannon, P. R. (2005). Eulerian available energetics in moist atmospheres. *J. Atmos. Sci.*, **62**, 4238–4252.
- Barnes, E. A. and Screen, J. A. (2015). The impact of arctic warming on the midlatitude jet stream can it has it will it. *WIREs Clim Change*, **6**, 277–286.
- Barry, L., Craig, G. C., and Thuburn, J. (2002). Poleward heat transport by the atmospheric heat engine. *Nature*, **415**, 774–777.
- Benedict, J. J., Lee, S., and Feldstein, S. B. (2004). Synoptic view of the North Atlantic Oscillation. *J. Atmos. Sci.*, **61**, 121–144.

- Bengtsson, L., Hodges, K. I., and Keenlyside, N. (2009). Will extratropical storms intensify in a warmer climate? *J. Climate*, **22**, 2276–2301.
- Berloff, P., Kamenkovich, I., and Pedlosky, J. (2009). A model of multiple zonal jets in the oceans: dynamical and kinematical analysis. *J. Phys. Oceanogr.*, **39**, 2711–2734.
- Berloff, P., Karabasov, S., Farrar, J. T., and Kamenkovich, I. (2011). On latency of multiple zonal jets in the oceans. *J. Fluid Mech.*, **686**, 534–567.
- Berryman, A. A. (1992). The origins and evolution of predator-prey theory. *Ecology*, **73**, 1530–1535.
- Blackburn, M. (1983). *An energetic analysis of the general atmospheric circulation*. Univ. Reading. PhD thesis.
- Blackmon, M. L. (1976). A climatological spectral study of the 500 mb geopotential height of the Northern Hemisphere. *J. Atmos. Sci.*, **33**, 1607–1623.
- Blackmon, M. L., Lee, Y.-H., and Wallace, J. M. (1984). Horizontal structure of 500 mb height fluctuations with long, intermediate and short time scales. *J. Atmos. Sci.*, **41**, 961–980.
- Brayshaw, D. J., Hoskins, B. J., and Blackburn, M. (2009). The basic ingredients of the North Atlantic storm track. part I: land-sea contrast and orography. *J. Atmos. Sci.*, **66**(9), 2539–2558.
- Brayshaw, D. J., Hoskins, B., and Blackburn, M. (2011). The basic ingredients of the North Atlantic storm track, part II: Sea surface temperatures. *J. Atmos. Sci.*, **68**, 1784–1805.
- Bretherton, F. P. (1966). Critical layer instability in baroclinic flows. *Q. J. Roy. Meteorol. Soc.*, **92**, 325–334.
- Butler, A. H., Thompson, D. W. J., and Heikes, R. (2010). The steady-state atmospheric circulation response to climate change-like thermal forcings in a simple general circulation model. *J. Climate*, **23**, 3474–3496.
- Cash, B. A., Kushner, P. J., and Vallis, G. K. (2005). Zonal asymmetries, teleconnections, and annular patterns in a GCM. *J. Atmos. Sci.*, **62**, 207–219.
- Chang, E. K. M. (2009). Diabatic and orographic forcing of northern winter stationary waves and storm tracks. *J. Climate*, **22**, 670–688.
- Chang, E. K. M. and Orlanski, I. (1993). Downstream development of baroclinic waves as inferred from regression analysis. *J. Atmos. Sci.*, **50**, 999–1015.
- Chang, E. K. M., Lee, S., and Swanson, K. L. (2002). Storm track dynamics. *J. Climate*, **15**, 2163–2183.
- Chang, E. K. M., Guo, Y., and Xia, X. (2012). CMIP5 multimodel ensemble projection of storm track change under global warming. *J. of Geophys. Res.*, **117**(D23). D23118.

- Charney, J. G. (1947). The dynamics of long waves in a baroclinic westerly current. *J. Meteor.*, **4**, 136–162.
- Charney, J. G. and DeVore, J. G. (1979). Multiple flow equilibria in the atmosphere and blockings. *J. Atmos. Sci.*, **36**, 1205–1216.
- Chemke, R. and Kaspi, Y. (2015). Poleward migration of eddy-driven jets. *J. Adv. Model. Earth Syst.*, **7**, 1457–1471.
- Chen, G., Held, I. M., and Robinson, W. A. (2007). Sensitivity of the latitude of the surface westerlies to surface friction. *J. Atmos. Sci.*, **64**, 2899–2915.
- Cushman-Roisin, B. and Beckers, J.-M. (2011). *Introduction to Geophysical Fluid Dynamics: Physical and Numerical Aspects*. Elsevier, Oxford.
- Czaja, A. (2003). On the time variability of the net ocean-to-atmosphere heat flux in midlatitudes. *Q. J. R. Meteorol. Soc.*, **129**, 2867–2878.
- Derome, J. and Wiin-Nielsen, A. (1971). The response of a middle-latitude model atmosphere to forcing by topography and stationary heat sources. *Mon. Wea. Rev.*, **99**, 564–576.
- Dritschel, D. G. and McIntyre, M. E. (2008). Multiple jets as PV staircases: The Phillips Effect and the resilience of eddy-transport barriers. *J. Atmos. Sci.*, **65**, 855–874.
- Drouard, M., Rivière, G., and Arbogast, P. (2013). The North Atlantic Oscillation response to large-scale atmospheric anomalies in the northeastern Pacific. *J. Atmos. Sci.*, **70**, 2854–2874.
- Drouard, M., Rivière, G., and Arbogast, P. (2015). The link between the North Pacific climate variability and the North Atlantic Oscillation via downstream propagation of synoptic waves. *J. Climate*, **28**, 3957–3976.
- Duchon, C. E. (1989). Lanczos filtering in one and two dimensions. *J. Appl. Meteor.*, **18**, 1016–1022.
- Dutton, J. A. (1973). The global thermodynamics of atmospheric motion. *Tellus*, **25**, 89–110.
- Eady, E. T. (1949). Long waves and cyclone waves. *Tellus*, **1**, 33–52.
- Farrell, B. F. and Ioannou, P. J. (2009). A theory of baroclinic turbulence. *J. Atmos. Sci.*, **66**, 2444–2454.
- Feldstein, S. B. (2003). The dynamics of nao teleconnection pattern growth and decay. *Quart. J. Roy. Meteor. Soc.*, **129**, 901–924.
- Feldstein, S. B. and Lee, S. (1998). Is the atmospheric zonal index driven by an eddy feedback? *J. Atmos. Sci.*, **55**, 3077–3086.
- Fleming, R. J. (2014). Explosive baroclinic instability. *J. Atmos. Sci.*, **71**, 2155–2168.
- Fraedrich, K., Kirk, E., Luksch, U., and Lunkeit, F. (2005). The Portable University Model

- of the Atmosphere (PUMA): Storm track dynamics and low frequency variability. *Meteorol. Zeitschrift*, **14**, 735–745.
- Frame, T. H. A., Ambaum, M. H. P., Gray, S. S., and Methven, J. (2011). Ensemble prediction of transitions of the North Atlantic eddy-driven jet. *Q.J.R. Meteorol. Soc.*, **137**(658), 1288–1297.
- Franzke, C. and Feldstein, S. B. (2005). The continuum and dynamics of Northern Hemisphere teleconnection patterns. *J. Atmos. Sci.*, **62**, 3250–3267.
- Franzke, C., Lee, S., and Feldstein, S. B. (2004). Is the North Atlantic Oscillation a breaking wave? *J. Atmos. Sci.*, **61**, 145–160.
- Franzke, C., Woollings, T., and Martius, O. (2011). Persistent circulation regimes and preferred regime transitions in the North Atlantic. *J. Atmos. Sci.*, **68**, 2809–2825.
- Frisius, T., Lunkeit, F., Fraedrich, K., and James, I. N. (1998). Storm-track organization and variability in a simplified atmospheric global circulation model. *Quart. J. Roy. Meteor. Soc.*, **124**, 1019–1043.
- Fyfe, J. C. and Saenko, O. A. (2006). Simulated changes in the extratropical Southern Hemisphere winds and currents. *Geophys. Res. Lett.*, **33**, L06701.
- Gall, R. L. and Johnson, D. R. (1971). The generation of available potential energy by sensible heating: a case study. *Tellus*, **23**(6), 465–482.
- Gent, P. R. and McWilliams, J. C. (1990). The generation of available potential energy by sensible heating: a case study. *J. Phys. Oceanogr.*, **20**, 150–155.
- Gerber, E. P. and Vallis, G. K. (2007). Eddy-zonal flow interactions and the persistence of the zonal index. *J. Atmos. Sci.*, **64**, 3296–3311.
- Gnanadesikan, A. (1999). A simple predictive model for the structure of the oceanic pycnocline. *Science*, **283**, 2077–2079.
- Griffies, S. M. (1998). The Gent-McWilliams skew flux. *J. Phys. Oceanogr.*, **28**, 831–841.
- Hannachi, A., Woolings, T., and Fraedrich, K. (2012). The North Atlantic jet stream: a look at preferred positions, paths and transitions. *Q.J.R. Meteorol. Soc.*, **138**, 862–877.
- Hart, J. E. (1972). A laboratory study of baroclinic instability. *Geophys. Fluid Dyn.*, **3**, 181–209.
- Hart, J. E. (1979). Finite amplitude baroclinic instability. *Annu. Rev. Fluid Mech.*, **11**(1), 147–172.
- Hartmann, D. L. (2007). The atmospheric general circulation and its variability. *J. Meteor. Soc. Japan*, **85B**, 123–143.
- Harvey, B., Shaffrey, L., and Woollings, T. (2013). Equator-to-pole temperature differences and the extra-tropical storm track responses of the CMIP5 climate models. *Clim. Dyn.*, **33**, 1171–

- 1182.
- Haynes, P. H. (1988). Forced, dissipative generalizations of finite-amplitude wave-activity conservation relations for zonal and nonzonal basic flows. *J. Atmos. Sci.*, **45**, 2352–2362.
- Haynes, P. H. (2003). Critical layers. In J. Holton, J. Pyle, and J. Curry, editors, *Encyclopedia of Atmospheric Sciences*. Elsevier.
- Haynes, P. H., McIntyre, M. E., Shepherd, T. G., Marks, C. J., and Shine, K. P. (1991). On the downward control of extratropical diabatic circulations by eddy-induced mean zonal forces. *J. Atmos. Sci.*, **48**, 651–678.
- Held, I. M. (1983). Stationary and quasi-stationary eddies in the extratropical troposphere: Theory. In B. J. Hoskins and R. Pearce, editors, *Large-scale processes in the atmosphere*. Academic Press, New York.
- Held, I. M. (1993). Large-scale dynamics and global warming. *Bull. Amer. Meteor. Soc.*, **74**, 228–242.
- Held, I. M. and Hou, A. Y. (1980). Nonlinear axially symmetric circulations in a nearly inviscid atmosphere. *J. Atmos. Sci.*, **37**, 515–533.
- Hernandez-Deckers, D. and von Storch, J. (2010). Energetics responses to increases in greenhouse gas concentration. *J. Atmos. Sci.*, **23**, 3874–3887.
- Hide, R. (1953). Some experiments on thermal convection in rotating liquid. *Quart. J. Roy. Meteor. Soc.*, **79**, 161.
- Hide, R. (1958). An experimental study of thermal convection in a rotating liquid. *Philos. Trans. R. Soc. London Ser.*, **250**, 442–478.
- Hirsch, M. W. and Smale, S. (1974). *Differential Equations, Dynamical Systems and Linear Algebra*. Elsevier Academic Press, London.
- Hitchcock, P. and Simpson, I. R. (2014). The downward influence of stratospheric sudden warmings. *J. Atmos. Sci.*, **71**, 3856–3876.
- Hitchcock, P., Shepherd, T. G., and Manney, G. L. (2013). Statistical characterization of Arctic polar-night jet oscillation events. *J. Climate*, **26**, 2096–2116.
- Hogg, A. M. C. and Blundell, J. R. (2006). Interdecadal variability of the Southern Ocean. *J. Phys. Oceanogr.*, **36**, 1626–1645.
- Holliday, D. and McIntyre, M. E. (1981). On potential energy density in an incompressible stratified fluid. *J. Fluid Mech.*, **107**, 221–225.
- Holton, J. R. (2004). *An Introduction to Dynamic Meteorology*. Elsevier Academic Press, London.

- Hoskins, B., James, I., and White, G. (1983). The shape, propagation and mean-flow interaction of large-scale weather systems. *J. Atmos. Sci.*, **40**, 1595–1612.
- Hoskins, B. J. (1983). Dynamical processes in the atmosphere and the use of models. *Quart. J. Roy. Meteor. Soc.*, **109**(459), 1–21.
- Hoskins, B. J. and Hodges, K. I. (2002). New perspectives on the northern hemisphere winter storm tracks. *J. Atmos. Sci.*, **59**, 1041–1061.
- Hoskins, B. J. and Hodges, K. I. (2005). A new perspective on Southern Hemisphere storm tracks. *J. Climate*, **18**, 4108–4129.
- Hoskins, B. J. and Karoly, D. J. (1981). The steady linear response of a spherical atmosphere to thermal and orographic forcing. *J. Atmos. Sci.*, **38**, 1179–1196.
- Hoskins, B. J. and Simmons, A. J. (1975). A multi-layer spectral model and the semi-implicit method. *Quart. J. Roy. Meteor. Soc.*, **101**, 637–655.
- Hoskins, B. J. and Valdes, P. J. (1990). On the existence of storm-tracks. *J. Atmos. Sci.*, **47**, 1854–1864.
- Hu, Q., Tawaye, Y., and Feng, S. (2004). Variations of the Northern Hemisphere atmospheric energetics: 1948-2000. *J. Clim.*, **17**, 1975–1986.
- Huang, R. X. (2010). *Ocean Circulation: Wind-Driven and Thermohaline Processes*. Cambridge University Press, Cambridge. pp. 293.
- Ingersoll, A. P., Beebe, R. F., Mitchell, Garneau, G. W., Yagi, G. M., and Shu, F. H. (1981). Interaction of eddies and zonal flow on Jupiter as inferred from Voyager 1 and 2 images. *J. Geophys. Res.*, **86**, 8733–8743.
- Ishioka, K. and Yoden, S. (1996). Numerical methods of estimating bounds on the non-linear saturation of barotropic instability. *J. Clim.*, **74**, 167–174.
- Ito, T. and Follows, M. J. (2003). Upper ocean control on the solubility pump of CO<sub>2</sub>. *J. Mar. Res.*, **61**, 465–489.
- Jacobs, S. S., Jenkins, A., Giulivi, C. F., and Dutrieux, P. (2011). Stronger ocean circulation and increased melting under pine island glacier ice shelf. *Nature Geoscience*, **4**, 519–523.
- James, I. N. (1987). Suppression of baroclinic instability in horizontally sheared flows. *J. Atmos. Sci.*, **44**, 3710–3720.
- James, I. N. (1994). *Introduction to Circulating Atmospheres*. Cambridge University Press, Cambridge. pp. 230.
- James, I. N. and Gray, L. J. (1986). Concerning the effect of surface drag on the circulation of a baroclinic planetary atmosphere. *Q.J.R. Meteorol. Soc.*, **112**, 1231–1250.

- Jansen, M. and Ferrari, R. (2013). Equilibration of an atmosphere by adiabatic eddy fluxes. *J. Atmos. Sci.*, **70**, 2948–2962.
- Johnson, D. R. (1970). The available potential energy of storms. *J. Atmos. Sci.*, **27**, 727–741.
- Johnson, D. R. (1982). On the energetics of open systems. *Tellus*, **34**, 458–470.
- Johnson, G. C. and Bryden, H. L. (1989). On the size of the Antarctic Circumpolar Current. *Deep-Sea Res.*, **36**, 39–53.
- Kao, S. K. and Chi, C. N. (1978). The mechanism for the growth and decay of long- and synoptic-scale waves in the mid-troposphere. *J. Atmos. Sci.*, **35**, 1375–1387.
- Karlsson, S. (1997). *Energy, entropy, and exergy in the atmosphere*. Chalmers Univ. Technol.
- Kaspi, Y. and Flierl, G. R. (2007). Formation of jets by baroclinic instability on gas planet atmospheres. *J. Atmos. Sci.*, **64**, 3177–3194.
- Kaspi, Y. and Schneider, T. (2013). The role of stationary eddies in shaping midlatitude storm tracks. *J. Atmos. Sci.*, **70**, 2596–2613.
- Kidston, J., Scaife, A. A., Hardiman, S. C., Mitchell, D. M., Butchart, N., Baldwin, M. P., and Gray, L. J. (2015). Stratospheric influence on tropospheric jet streams, storm tracks and surface weather. *Nature Geoscience*, **8**, 433–440.
- Kidston, J. W. (1988). Interannual variations in the Southern Hemisphere circulation. *J. Climate*, **1**, 1177–1198.
- Killworth, P. D. and McIntyre, M. E. (1985). Do Rossby-wave critical layers absorb, reflect, or over-reflect? *J. Fluid Mech.*, **161**, 449–492.
- Kim, B., Lim, G., and Kim, K. (2006). A new look at the midlatitude-MJO teleconnection in the northern hemisphere winter. *Q. J. R. Meteorol. Soc.*, **132**, 485–503.
- Kim, H. K. and Lee, S. (2001). Hadley cell dynamics in a primitive equation model. part II: Nonaxisymmetric flow. *J. Atmos. Sci.*, **58**, 2859–2871.
- Kistler, R. and Coauthors (2001). The ncep-ncar 50-year reanalysis: Monthly means cd-rom and documentation. *Bull. Amer. Meteor. Soc.*, **82**, 247–267.
- Kållberg, P., Berrisford, P., Hoskins, B., Simmonds, A., Uppala, S., Lamy-Thépaut, S., and Hine, R. (2005). *ERA-40 Atlas*. Number 19. ECMWF.
- Kucharski, F. (1997). On the concept of exergy and available potential energy. *Q. J. R. Meteorol. Soc.*, **123**, 2141–2156.
- Kucharski, F. (2001). The interpretation of available potential energy as exergy applied to layers of a stratified atmosphere. *Exergy Int. J.*, **1**, 25–30.
- Kucharski, F. and Thorpe, A. J. (2000). Local energetics of an idealised baroclinic wave using

- extended exergy. *J. Atmos. Sci.*
- Kuhlbrodt, T., Smith, R. S., Wang, Z., and Gregory, J. M. (2012). The influence of eddy parameterizations on the transport of the antarctic circumpolar current in coupled climate models. *Ocean Modell.*
- Landau, L. D. and Lifshitz, E. M. (1976). *Mechanics*, volume 1. Butterworth-Heinemann, Moscow, 3 edition.
- Lau, N. (1988). Variability of the observed midlatitude storm tracks in relation to low-frequency changes in the circulation pattern. *J. Atmos. Sci.*, **45**, 2718–2743.
- Lee, S. and Kim, H. K. (2003). The dynamical relationship between subtropical and eddy-driven jets. *J. Atmos. Sci.*, **60**, 1490–1503.
- Li, L., Ingersoll, A. P., Jiang, X., Feldman, D., and Yung, Y. L. (2007). Lorenz energy cycle of the global atmosphere based on reanalysis datasets. *Geophys. Res. Lett.*, **34**(16), 1–5.
- Li, Y. and Lau, N.-C. (2012). Impact of ENSO on the atmospheric variability over the North Atlantic in late winter role of transient eddies. *J. Climate*, **25**, 320–342.
- Li, Y. and Lau, N.-C. (2013). Influences of ENSO on stratospheric variability, and the descent of stratospheric perturbations into the lower troposphere. *J. Climate*, **26**, 4725–4748.
- Liberato, M. L. R., Pinto, J. G., Trigo, R. M., Ludwig, P., nez, P. O., Yuen, D., and Trigo, I. F. (2013). Explosive development of winter storm Xynthia over the subtropical North Atlantic ocean. *Nat. Hazard. Earth Sys.*, **13**(92), 2239–2251.
- Lorenz, D. J. (2014). Understanding midlatitude jet variability and change using Rossby wave chromatography: Poleward-shifted jets in response to external forcing. *J. Atmos. Sci.*, **71**, 2370–2389.
- Lorenz, D. J. and Hartmann, D. L. (2001). Eddy-zonal flow feedback in the Southern Hemisphere. *J. Atmos. Sci.*, **58**, 2212–3326.
- Lorenz, D. J. and Hartmann, D. L. (2003). Eddy-zonal flow feedback in the Northern Hemisphere winter. *J. Climate*, **16**, 1212–1227.
- Lorenz, E. N. (1955). Available potential energy and the maintenance of the general circulation. *Tellus*, **7**, 157–167.
- Lorenz, E. N. (1963a). Deterministic nonperiodic flow. *J. Atmos. Sci.*, **20**, 130–141.
- Lorenz, E. N. (1963b). The mechanics of vacillation. *J. Atmos. Sci.*, **20**, 448–464.
- Lorenz, E. N. (1979). Numerical evaluation of moist available energy. *Tellus*, **31**, 230–235.
- Lorenz, E. N. (1984). Irregularity: a fundamental property of the atmosphere. *Tellus*, **36A**, 98–110.

- Mailier, P. J., Stephenson, D. B., Ferro, C. A. T., and Hodges, K. I. (2006). Serial clustering of extratropical cyclones. *Mon. Wea. Rev.*, **134**, 2224–2240.
- Margules, M. (1903). U ber die energie der sturme. *Jahrb. Zentralanst.*, **51**.
- Marshall, D. P., Maddison, J. R., and Berloff, P. S. (2012). A framework for parameterizing eddy potential vorticity fluxes. *J. Phys. Oceanogr.*, **42**, 539–557.
- Marshall, D. P., Munday, D., Ambaum, M. H. P., and Novak, L. (to be submitted). On the physics of eddy saturation in the antarctic circumpolar current. *Nature Geoscience*.
- Marshall, J. and Radko, T. (2003). Residual-mean solutions for the Antarctic Circumpolar Current and its associated overturning circulation. *J. Phys. Oceanogr.*, **33**, 2341–2354.
- Martius, O., Schwierz, C., and Davies, H. C. (2007). Breaking waves at the tropopause in the wintertime Northern Hemisphere: Climatological analyses of the orientation and the theoretical LC1/2 classification. *J. Atmos. Sci.*, **64**, 2576–2592.
- Matsuno, T. (1970). Vertical propagation of stationary planetary waves in the winter Northern Hemisphere. *J. Atmos. Sci.*, **27**, 871–883.
- Mbengue, C. and Schneider, T. (2013). Storm track shifts under climate change: What can be learned from large-scale dry dynamics. *J. Climate*, **26**, 9923–9930.
- McIntyre, M. E. and Shepherd, T. G. (1987). An exact local conservation theorem for finite-amplitude disturbances to non-parallel shear flows, with remarks on Hamiltonian structure and on Arnolds stability theorems. *J. Fluid Mech.*, **181**, 527–565.
- Meehl, G. A., Arblaster, J. M., and Tebaldi, C. (2005). Understanding future patterns of increased precipitation intensity in climate model simulations. *Geophys. Res. Lett.*, **32**. L18719.
- Messori, G. and Czaja, A. (2013). On the sporadic nature of meridional heat transport by transient eddies. *Quart. J. Roy. Meteor. Soc.*, **139**, 999–1008.
- Met Office News Blog (2015). What are the prospects for the weather in the coming winter? <http://blog.metoffice.gov.uk/2015/10/29/what-are-the-prospects-for-the-weather-in-the-coming-winter/>. Accessed: 2-12-2015.
- Muller, I. (2007). *A History of Thermodynamics: The Doctrine of Energy and Entropy*. Springer, New York.
- Munday, D. R., Johnson, H. L., and Marshall, D. P. (2013). Eddy saturation of equilibrated circumpolar currents. *J. Phys. Oceanogr.*, **43**, 507–532.
- Munday, D. R., Johnson, H. L., and Marshall, D. P. (2015). The role of ocean gateways in the dynamics and sensitivity to wind stress of the early antarctic circumpolar current. *Paleoceanography*, **30**, 284–302.

- Nakamura, H. (1992). Midwinter suppression of baroclinic wave activity in the Pacific. *J. Atmos. Sci.*, **49**, 1629–1642.
- Nakamura, H. and Sampe, T. (2002). Trapping of synoptic-scale disturbances into the North-Pacific subtropical jet core in midwinter. *Geophys. Res. Lett.*, **29**, 8–1–8–4.
- Namias, J. (1950). The index cycle and its role in the general circulation. *J. Meteor.*, **7**, 130–139.
- Novak, L., Ambaum, M. H. P., and Tailleux, R. (2015). The lifecycle of the North Atlantic storm track. *J. Atmos. Sci.*, **72**, 821–833.
- Novak, L., Ambaum, M. H. P., and Tailleux, R. (to be submitted). Modelling the nonlinear oscillations of marginally stable storm tracks. *Quart. J. Roy. Meteor. Soc.*
- O’Gorman, P. A. (2010). Understanding the varied response of the extratropical storm tracks to climate change. *Proc. Natl. Acad. Sci. (USA)*, **107**, 19176–19180.
- O’Gorman, P. A. and Schneider, T. (2007). Recovery of atmospheric flow statistics in a general circulation model without nonlinear eddy-eddy interactions. *Geophys. Res. Lett.*, **37**. L22801.
- O’Gorman, P. A. and Schneider, T. (2008). Energy of midlatitude transient eddies in idealized simulations of changed climates. *J. Clim.*, **21**, 5797–5806.
- Okuno, A. and Masuda, A. (2003). Effect of horizontal divergence on the geostrophic turbulence on a beta-plane: Suppression of the Rhines effect. *Phys. Fluids*, **15**, 56–65.
- Oort, A. H. (1964). On estimates of the atmospheric energy cycle. *Mon. Weather Rev.*, **92**(11).
- Orlanski, I. (1998). Poleward deflection of storm tracks. *J. Atmos. Sci.*, **55**, 2577–2602.
- Orlanski, I. (2003). Bifurcation in eddy life cycles: Implications for storm track variability. *J. Atmos. Sci.*, **60**, 993–1023.
- Orlanski, I. and Katzfey, J. (1991). The life cycle of a cyclone wave in the Southern Hemisphere, part I: Eddy energy budget. *J. Atmos. Sci.*, **48**(17), 1972–1998.
- Osprey, S. M. and Ambaum, M. H. P. (2011). Evidence for the chaotic origin of Northern Annular Mode variability. *Geoph. Res. Lett.*, **38**. L15702.
- Panetta, R. L. (1991). Zonal jets in wide baroclinically unstable regions: Persistence and scale selection. *J. Atmos. Sci.*, **50**, 2073–2106.
- Pauluis, O. and Held, I. M. (2002). Entropy budget of an atmosphere in radiative-convective equilibrium. part II: latent heat transport and moist processes. *J. Atmos. Sci.*, **59**, 140–149.
- Pavan, V., Hall, N., Valdes, P., and Blackburn, M. (1999). The importance of moisture distribution for the growth and energetics of mid-latitude systems. *Ann. Geophysicae*, **17**, 242–256.
- Pearce, R. (1978). On the concept of available potential energy. *Q. J. R. Meteorol. Soc.*, **104**, 737–755.

- Pedlosky, J. (1970). Finite-amplitude baroclinic waves. *J. Atmos. Sci.*, **27**, 15–30.
- Pedlosky, J. (1982a). Finite-amplitude baroclinic waves at minimum critical shear. *J. Atmos. Sci.*, **39**, 555–562.
- Pedlosky, J. (1982b). A simple model for nonlinear critical layers in an unstable baroclinic wave. *J. Atmos. Sci.*, **39**, 2119–2127.
- Peng, J., Zhang, L., and Zhang, Y. (2015). On the local available energetics in a moist compressible atmosphere. *J. Atmos. Sci.*, **72**, 1521–1561.
- Phillips, O. M. (1972). Turbulence in a strongly stratified fluid is it unstable? *Deep-Sea Res.*, **19**, 79–81.
- Pinto, J. G., Zacharias, S., Fink, A. H., Leckebusch, G. C., and Ulbrich, U. (2009). Factors contributing to the development of extreme North Atlantic cyclones and their relationship with the NAO. *Clim. Dynam.*, **32**, 711–737.
- Pinto, J. G., Reyers, M., and Ulbrich, U. (2011). The variable link between PNA and NAO in observations and in multi-century CGCM simulations. *Clim. Dynam.*, **36**, 337–354.
- Plumb, A. R. (1983). A new look at the energy cycle. *J. Atmos. Sci.*, **40**, 1669–1688.
- Polvani, L. M. and Kushner, P. J. (2002). Tropospheric response to stratospheric perturbations in a relatively simple general circulation model. *Geophys. Res. Lett.*, **9**(7), 18–1–18–4.
- Porco, C. C., West, R. A., McEwen, A., Genio, A. D. D., Ingersoll, A. P., Thomas, P., Squyres, S., Dones, L., Murray, C. D., Johnson, T. V., Burns, J. A., Brahic, A., Neukum, G., Veverka, J., Barbara, J. M., Denk, T., Evans, M., Ferrier, J. J., Geissler, P., Helfenstein, P., Roatsch, T., Throop, H., Tiscareno, M., and Vasavada, A. R. (2003). Cassini imaging of Jupiters atmosphere, satellites, and rings. *Science*, **299**, 1541–1547.
- Proistosescu, C., Rhines, A., and Huybers, P. (2016). Identification and interpretation of nonnormality in atmospheric time series. *Geophys. Res. Lett.*, **43**(10), 5425–5434. 2016GL068880.
- Reed, R. J. and Albright, M. D. (1986). A case study of explosive cyclogenesis in the eastern Pacific. *Mon. Weather Rev.*, **114**, 2297–2319.
- Rhines, P. (1975). Waves and turbulence on a beta plane. *J. Fluid Mech.*, **69**, 417–443.
- Ringler, T. D. and Cook, K. H. (1997). Factors controlling nonlinearity in mechanically forced stationary waves over orography. *J. Atmos. Sci.*, **54**, 2612–2629.
- Rivière, G. (2009). Effect of latitudinal variations in low-level baroclinicity on eddy life cycles and upper-tropospheric wave-breaking processes. *J. Atmos. Sci.*, **66**, 1569–1592.
- Rivière, G. and Orlanski, I. (2007). Characteristics of the Atlantic storm-track eddy activity and its relation with the North Atlantic Oscillation. *J. Atmos. Sci.*, **64**, 241–266.

- Robinson, W. A. (2000). A baroclinic mechanism for the eddy feedback on the zonal index. *J. Atmos. Sci.*, **57**, 415–422.
- Ruddick, B. R., McDougall, T. J., and Turner, J. S. (1989). The formation of layers in a uniformly stirred density gradient. *Deep-Sea Res.*, **36**, 597–609.
- Salmon, R. (1980). Baroclinic instability and geostrophic turbulence. *Geophys. Astro. Fluid*, **15**(1), 167 – 211.
- Saltzman, B. (1970). Large-scale atmospheric energetics in the wave-number domain. *Rev. Geophys. Space Phys.*, **8**(2), 289–302.
- Salyk, C., Ingersoll, A. P., Lorre, J., Vasavada, A., and Genio, A. D. D. (2006). Interaction between eddies and mean flow in Jupiter’s atmosphere: Analysis of Cassini imaging data. *Icarus*, **185**(2), 430 – 442.
- Sanders, F. and Gyakum, J. R. (1980). Synoptic-dynamic climatology of the ”Bomb”. *Mon. Wea. Rev.*, **108**, 1589–1606.
- Sardeshmukh, P. D. and Hoskins, B. J. (1988). The generation of global rotational flow by steady idealized tropical divergence. *J. Atmos. Sci.*, **45**, 1228–1251.
- Schneider, E. K. (1981). On the amplitudes reached by baroclinically unstable disturbances. *J. Atmos. Sci.*, **38**, 2142–2149.
- Schneider, T. and Liu, J. (2009). Formation of jets and equatorial superrotation on Jupiter. *J. Atmos. Sci.*, **66**, 579–601.
- Schneider, T. and Walker, C. C. (2008). Scaling laws and regime transitions of macroturbulence in dry atmospheres. *J. Atmos. Sci.*, **65**, 2153–2173.
- Schopf, P. S., Anderson, D. L. T., and Smith, R. (1981). Beta-dispersion of low-frequency Rossby waves. *Dyn. Atmos. Oceans*, **5**, 187–214.
- Sheng, J. and Hayashi, Y. (1990). Observed and simulated energy cycles in the frequency domain. *J. Atmos. Sci.*, **47**, 1243–1254.
- Shepherd, T. G. (1987a). Non-ergodicity of inviscid two-dimensional flow on a beta-plane and on the surface of a rotating sphere. *J. Fluid Mech.*, **184**, 289–302.
- Shepherd, T. G. (1987b). Rigorous bounds on the nonlinear saturation of instabilities to parallel shear flows. *J. Fluid Mech.*, **196**, 291–322.
- Shepherd, T. G. (1993). A unified theory of available potential energy. *Atmos. Ocean*, **31**, 1–26.
- Simmons, A. J. and Hoskins, B. J. (1978). The lifecycle of some baroclinic waves. *J. Atmos. Sci.*, **35**, 414–432.
- Stewartson, K. (1981). Marginally stable inviscid flows with critical layers. *IMA J. Appl. Math.*,

- 27, 133–175.
- Stone, P. H. (1978). Baroclinic adjustment. *J. Atmos. Sci.*, **35**, 561–571.
- Straus, D. M. and Shukla, J. (1997). Variations of midlatitude transient dynamics associated with ENSO. *J. Atmos. Sci.*, **54**, 777–790.
- Swanson, K. L. and Pierrehumbert, R. T. (1997). Lower-tropospheric heat transport in the Pacific storm track. *J. Atmos. Sci.*, **54**(11), 1533–1543.
- Tailleux, R. (2013a). Available potential energy and exergy in stratified fluids. *Annu. Rev. Fluid Mech.*, **45**, 35–58.
- Tailleux, R. (2013b). Available potential energy density for a multicomponent Boussinesq fluid with arbitrary nonlinear equation of state. *J. Fluid Mech.*, **735**, 499–518.
- Tailleux, R., Novak, L., and Ambaum, M. H. P. (to be submitted). Local generalisations of Lorenz energy cycle. *Q. J. R. Meteorol. Soc.*
- Tamarin, T. and Kaspi, Y. (in press). The poleward motion of extratropical cyclones from a potential vorticity tendency analysis. *J. Atmos. Sci.*
- Tanaka, D., Iwasaki, T., Uno, S., Ujiie, M., and Miyazaki, K. (2004). Eliassen-Palm flux diagnosis based on isentropic representation. *J. Atmos. Sci.*, **61**, 2370–2383.
- Tanaka, H. L. (1995). A life-cycle of nonlinear baroclinic waves represented by a simple 3-D spectral model. *Tellus*, **47**(A).
- Taylor, G. I. (1915). Eddy motion in the atmosphere. *Phil. Trans. Roy. Soc. Lond.*, pages 1–23. A215.
- Thompson, A. F. and Young, W. R. (2007). Two-layer baroclinic eddy heat fluxes: Zonal flows and energy balance. *J. Atmos. Sci.*, **64**, 3214–3231.
- Thompson, D. W. J. and Barnes, E. A. (2014). Periodic variability in the large-scale Southern Hemisphere atmospheric circulation. *Science*, **343**, 641–64.
- Thompson, D. W. J. and Birner, T. (2012). On the linkages between the tropospheric isentropic slope and eddy fluxes of heat during Northern Hemisphere winter. *J. Atmos. Sci.*, **69**, 1811–1823.
- Thompson, D. W. J. and Li, Y. (2015). Baroclinic and barotropic annular variability in the Northern Hemisphere. *J. Atmos. Sci.*, **72**, 1117–1136.
- Thompson, D. W. J. and Wallace, J. M. (1998). The Arctic Oscillation signature in the wintertime geopotential height and temperature fields. *Geophys. Res. Lett.*, **25**, 1297–1300.
- Thompson, D. W. J. and Wallace, J. M. (2000). Annular modes in the extratropical circulation. part I: Month-to-month variability. *J. Climate*, **13**, 1000–1016.

- Thompson, D. W. J. and Woodworth, J. D. (2014). Barotropic and baroclinic annular variability in the Southern Hemisphere. *J. Atmos. Sci.*, **71**, 1480–1493.
- Thompson, P. D. (1987). Large-scale dynamical response to differential heating: Statistical equilibrium states and amplitude vacillation. *J. Atmos. Sci.*, **44**, 1237–1248.
- Thompson, P. D. (1988). Period and decay rate of amplitude vacillations in a low-order general circulation model. *J. Atmos. Sci.*, **45**, 1279–1282.
- Thorncroft, C. D., Hoskins, B. J., and McIntyre, M. E. (1993). Two paradigms of baroclinic wave life-cycle behaviour. *Quart. J. Roy. Meteor. Soc.*, **119**, 17–55.
- Townsend, R. D. and Johnson, D. R. (1985). A diagnostic study of the isentropic zonally averaged mass circulation during the first GARP global experiment. *J. Atmos. Sci.*, **42**, 1565–1579.
- Uppala, S. M., Kallberg, P. W., Simmons, A. J., Andrae, U., Bechtold, V. D., Florino, M., and et al. (2005). The ERA-40 re-analysis. *Quart. J. Roy. Meteor. Soc.*, **131**(612), 2961–3012.
- Vallis, G. K. (2006). *Atmospheric and Oceanic Fluid Dynamics: Fundamentals and Large-scale Circulation*. Cambridge University Press, Cambridge, UK.
- Vallis, G. K. and Maltrud, M. E. (1993). Generation of mean flows and jets on a beta plane and over topography. *J. Phys. Oceanogr.*, **23**, 1346–1362.
- van Veen, L. (2003). Baroclinic flow and the Lorenz-84 model. *International Journal of Bifurcation and Chaos*, **13**(08), 2117–2139.
- Veiga, J. A. P. and Ambrizzi, T. (2013). A global and hemispherical analysis of the Lorenz energetics based on the representative concentration pathways used in CMIP5. *Adv. Meteor.*, (485047).
- von Storch, H. and Zwiers, F. W. (1999). *Statistical Analysis in Climate Research*. Cambridge University Press, Cambridge.
- Warn, T. and Gauthier, P. (1989). Potential vorticity mixing by marginally unstable baroclinic disturbances. *Tellus A*, **41A**(2), 115–131.
- Williams, G. P. (2003). Jovian dynamics. part III: Multiple, migrating, and equatorial jets. *J. Atmos. Sci.*, **60**, 1270–1296.
- Wittman, M., Scott, R., and Charlton, A. (2004). Stratospheric influence on baroclinic lifecycles: Connection to the Arctic Oscillation. *Geophys. Res. Lett.*, **31**(16).
- Wittman, M., Charlton, A., and Polvani, L. (2007). The effect of lower stratospheric shear on baroclinic instability. *J. Atmos. Sci.*, **64**, 479–496.
- Woollings, T., Hoskins, B., Blackburn, M., and Berrisford, P. (2008). A new Rossby wave-breaking interpretation of the North Atlantic Oscillation. *J. Atmos. Sci.*, **65**, 609–626.

- Woollings, T., Hannachi, A., and Hoskins, B. (2010). Variability of the North Atlantic eddy-driven jet stream. *Quart. J. Roy. Meteor. Soc.*, **136**, 856–868.
- Woollings, T., Pinto, J. G., and Santos, J. A. (2011). Dynamical evolution of North Atlantic ridges and poleward jet stream displacements. *J. Atmos. Sci.*, **68**, 954–963.
- Woollings, T., Gregory, J. M., Pinto, J. G., Reyers, M., and Brayshaw, D. J. (2012). Response of the North Atlantic storm track to climate change shaped by ocean-atmosphere coupling. *Nature Geoscience*, **5**, 313–317.
- Yin, J. H. (2005). A consistent poleward shift of the storm tracks in simulations of 21st century climate. *Geophys. Res. Lett.*, **32**(18). L18701.